

Marco Limberger

**Ionosphere modeling from GPS radio occultations
and complementary data based on B-splines**

München 2015

**Verlag der Bayerischen Akademie der Wissenschaften
in Kommission beim Verlag C. H. Beck**



DGK Deutsche Geodätische Kommission
der Bayerischen Akademie der Wissenschaften

Reihe C

Dissertationen

Heft Nr. 755

Ionosphere modeling from GPS radio occultations
and complementary data based on B-splines

Von der Ingenieurfacultät Bau Geo Umwelt
der Technischen Universität München
zur Erlangung des akademischen Grades eines
Doktor-Ingenieurs (Dr.-Ing.)
genehmigte Dissertation

von

Marco Limberger

München 2015

Verlag der Bayerischen Akademie der Wissenschaften
in Kommission beim Verlag C. H. Beck

Adresse der Deutschen Geodätischen Kommission:



Deutsche Geodätische Kommission

Alfons-Goppel-Straße 11 • D – 80 539 München

Telefon +49 – 89 – 23 031 1113 • Telefax +49 – 89 – 23 031 -1283 / - 1100

e-mail hornik@dgfi.badw.de • <http://www.dgk.badw.de>

Prüfungskommission

Vorsitzender: Univ.-Prof. Dr.-Ing. Liqiu Meng

Prüfer der Dissertation: 1. Univ.-Prof. Dr. phil. nat. Urs Hugentobler

2. apl. Prof. Dr.-Ing. habil. Michael Schmidt

3. Prof. Dr. Claudio Brunini,
Universidad Nacional de La Plata, Argentinien

Die Dissertation wurde am 16.06.2015 bei der Technischen Universität München eingereicht
und durch die Ingenieur fakultät Bau Geo Umwelt am 25.09.2015 angenommen

Diese Dissertation ist auf dem Server der Deutschen Geodätischen Kommission unter <http://dgk.badw.de/>
sowie auf dem Server der Technischen Universität München unter
<<http://mediatum.ub.tum.de?id=1254715>> elektronisch publiziert

© 2015 Deutsche Geodätische Kommission, München

Alle Rechte vorbehalten. Ohne Genehmigung der Herausgeber ist es auch nicht gestattet,
die Veröffentlichung oder Teile daraus auf photomechanischem Wege (Photokopie, Mikrokopie) zu vervielfältigen.

Kurzfassung

Als Ionosphäre wird ein Bereich der Hochatmosphäre beschrieben, der sich ungefähr zwischen 50 km und 1000 km Höhe erstreckt und oberhalb in die Plasmasphäre übergeht. Die Ionosphäre zeichnet sich durch eine erhöhte Konzentration an geladenen Partikeln aus, die durch Ionisationsprozesse in Abhängigkeit von der solaren Einstrahlung entsteht. In der Regel befindet sich das Maximum der Elektronendichte zwischen 250 km und 450 km, einem Intervall das als F2-Schicht bezeichnet wird. Die Variation der ionosphärischen Elektronendichte wird durch Partikelemissionen der Sonne angetrieben und korreliert deshalb stark mit der solaren Aktivität. Sonneneruptionen, wie beispielsweise koronale Massenauswürfe, haben in der Vergangenheit bereits zur Emission von Partikelwolken geführt, die mit der Erde kollidierten und zu Überspannungen in Energieversorgungsnetzen sowie Interferenzen in der Radiokommunikation geführt haben. Abhängig von der Frequenz und Stärke der Ionisation werden außerdem elektromagnetische Signale in der Ionosphäre gebrochen, was zu Laufzeitverzögerungen führen kann. Davon betroffen sind diverse Anwendungsgebiete wie zum Beispiel die satellitengestützte Positionierung und Navigation. Eine wichtige Motivationsquelle für die vorliegende Arbeit leitet sich dementsprechend aus der Nachfrage nach verbesserten Ansätzen zur Beobachtung und Evaluierung der ionosphärischen Elektronendichtestruktur ab.

Mit dem Zeitalter der Satelliten wurde die Möglichkeit zur Sondierung der Ionosphäre aus dem Weltall geschaffen. Heutzutage trägt eine Vielzahl an Satellitenmissionen durch unterschiedliche geometrische Betrachtungswinkel, Datenverteilungen und Auflösungen zur Untersuchung der Ionosphäre bei. Die Analyse dieser Daten hilft beim Verständnis der umfangreichen physikalischen Zusammenhänge und erleichtert die Entwicklung von Algorithmen zur Beschreibung der Ionosphäre und Überwachung des Weltraumwetters.

Die vorliegende Arbeit beinhaltet die Ableitung ionosphärischer Information aus elektromagnetischen Signalen verschiedener, satellitengestützter Beobachtungstechniken. Darunter fallen ionosphärische Radio-Okkultationen (IRO) sowie Messungen globaler Satellitennavigationssysteme (GNSS), des Systems "Doppler Orbitography and Radiopositioning Integrated by Satellite" (DORIS) und der Radar Altimetrie (RA). Jede Technik hat eigene Vorzüge in Bezug auf die Sensitivität und räumlich-zeitliche Beobachtungsverfügbarkeit. Aus GNSS und DORIS lässt sich der integrierte totale Elektronengehalt (TEC) zwischen terrestrischen Empfangs- bzw. Sendestationen und den entsprechenden Satelliten ableiten, während RA den vertikalen TEC über Wasserflächen misst. Eine besonders wichtige Rolle in dieser Dissertation spielen Beobachtungen aus IRO, da sie die Ableitung der Elektronendichte entlang von Profilen und damit die Beschreibung der vertikalen Elektronendichteverteilung ermöglichen.

Um die individuellen Stärken der Techniken bestmöglich auszuschöpfen, wurde ein gemeinsames Ausgleichungssystem zur Schätzung ionosphärischer Schlüsselparameter entwickelt. Die Berücksichtigung relativer Gewichtungen zwischen den Beobachtungsgruppen ist in Form einer Varianzkomponentenschätzung realisiert. Aufgrund der typischerweise heterogenen Datenverteilung, spielt die Wahl der Basisfunktionen eine besonders wichtige Rolle. Dabei sollen Datenlücken entsprechend überbrückt, der Einflussbereich des Signals gleichzeitig aber möglichst lokal zugeordnet werden können. In dieser Arbeit wurden deshalb Tensor-Produkte aus polynomialen und trigonometrischen B-Splines zur mehrdimensionalen Parametrisierung der Zielgrößen gewählt.

Als Teil dieser kumulativen Dissertation, wurden essentielle Untersuchungen und Ergebnisse in den zugehörigen Publikationen Limberger et al. (2013), Limberger et al. (2014) und Limberger et al. (2015) sowie Dettmering et al. (2014b), Liang et al. (2014) und Liang et al. (2015) veröffentlicht.

Abstract

The ionosphere is a region of the Earth's upper atmosphere extending from about 50 km to 1,000 km with smooth transition into the plasmasphere. It can be characterized by an increased concentration of charged particles, ions and electrons, excited from photo ionization through solar radiation where the highest density of electrons is usually located in altitudes between 250 km and 450 km, an interval denoted as F2 layer. Ionospheric variations are mainly stimulated by particle emissions from the Sun and thus correlate strongly with the solar activity. It already happened in the past that particle clouds originating from eruptive processes on the Sun collided with the Earth and provoked stress in electric-power grids and interferences to radio communication. Furthermore, electromagnetic signals propagating through the ionosphere are refracted depending on the wave frequency and strength of ionization. As a consequence, measurements used in various application fields such as satellite-based positioning and navigation are disturbed by signal delays. One important source of motivation for this thesis follows from the demand for improved techniques to observe and evaluate the ionospheric electron density structure.

With the era of satellites, sounding the atmosphere from space became possible. Nowadays, a variety of different satellite missions contributes to ionospheric sensing featuring different geometrical viewing angles, measurement distributions and resolutions. The analysis of these data helps to understand the substantial physical relations and facilitates the development of algorithms to describe the ionosphere and monitor the space weather.

The scope of this thesis includes the extraction of ionospheric information from electromagnetic signals observed by different space observation techniques, specifically Ionospheric Radio Occultations (IRO), Global Navigation Satellite Systems (GNSS), Doppler Orbitography and Radiopositioning Integrated by Satellite (DORIS) and Radar Altimetry (RA). Each technique has its individual strength regarding sensitivity and spatio-temporal measurement availability. GNSS and DORIS provide the Total Electron Content (TEC) based on terrestrial receiver and transmitter networks, respectively, and RA measures the vertical TEC over the oceans. In this dissertation, special attention was paid to IRO which have a particular role allowing for the retrieval of electron density data along profiles for the resolution of the vertical electron density distribution.

To exploit the individual potentials of the observation techniques, a combined adjustment model aiming the determination of selected ionospheric key parameters has been developed. The relative weighting between different observation groups is considered by means of a variance component estimation. Due to the commonly heterogeneous distribution of the data, the selection of suitable basis functions is an important issue where data gaps should be properly handled while restricting the influence of the measured signal to its vicinity. Therefore, tensor products of localizing endpoint-interpolating polynomial and periodic trigonometric B-splines are chosen for the multidimensional parametrization of the target quantities.

As a part of this cumulative thesis, associated publications by Limberger et al. (2013), Limberger et al. (2014) and Limberger et al. (2015) as well as Dettmering et al. (2014b), Liang et al. (2014) and Liang et al. (2015) contribute essential studies and results.

Preface

Multidimensional, observation based ionosphere modeling is a highly topical subject where 4-D models, allowing for the description of the electron density distribution in space and time, are of particular importance. The development of an appropriate model is based on various criteria. Crucial aspects

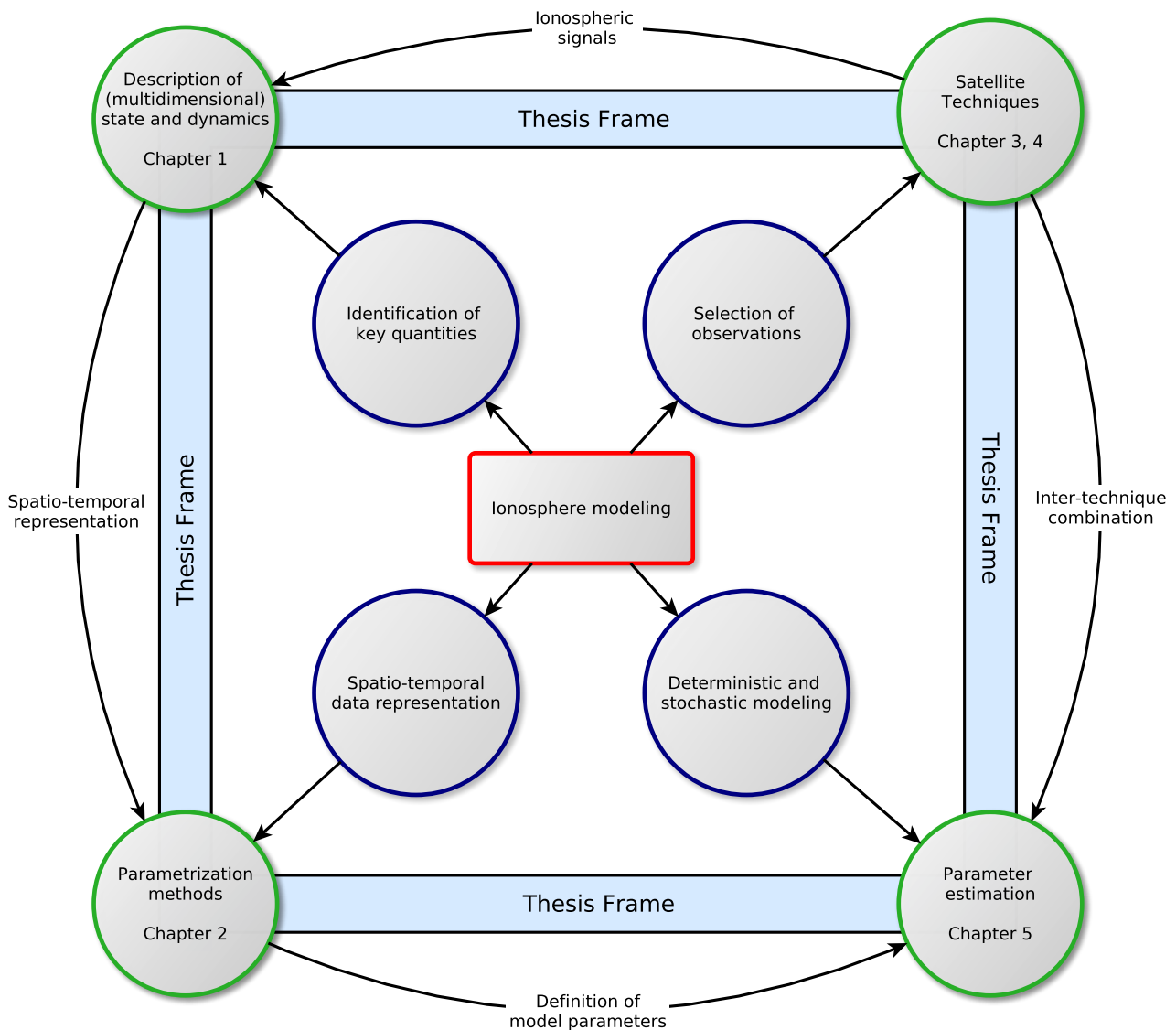


Figure 0.1: Interrelations of focus areas in ionosphere modeling constituting the framework of this thesis.

are embedded as blue bordered circles in the center of Fig. 0.1 and refer to (1) the identification of relevant key parameters, (2) the choice of observations that must feature a sufficient sensitivity for the model parameters, (3) the formulation of a suitable spatio-temporal data representation and (4) the definition of an appropriate deterministic and stochastic model.

Based on the identification of these requirements, a framework for this thesis composed of four main topics (green bordered circles in Fig. 0.1) can be defined which will be discussed within the chapters. The contents are related to

- the multidimensional ionospheric states and dynamics (Chapter 1),
- parametrization methods (Chapter 2),
- data processing of different satellite observation techniques (Chapter 3, Chapter 4) and
- the estimation of model parameters (Chapter 5).

This dissertation is cumulative, i.e. the following chapters describe theoretical aspects that are supplemented by publications in which the methodology is applied, analyzed and validated. Altogether six articles have been published as part of this thesis. To identify references to these papers, the common citation style has been extended in this work by prefixes P-I,...,P-VI. Both components together, methodology and publications, compose the dissertation. Each article is logically linked to one or more framework topics by accessing the subjects with selected methods. Consequently there exists a strong connectivity between the publications and the scope of the thesis. To disclose the coherence, a brief description of the scientific contents for each paper in chronological order is provided in the following. Blue and green font colors signalize the first- or co-authorship, respectively.

P-I

Limberger M., Liang W., Schmidt M., Dettmering D., Hugentobler U. (2013): **Regional representation of F2 Chapman parameters based on electron density profiles**. *Annales Geophysicae*, 31(12), 2215-2227, European Geosciences Union, DOI 10.5194/angeo-31-2215-2013.

Ionospheric radio occultation data can be exploited to resolve the electron density distribution where the data density can be increased by the combination of different occultation missions. This paper yields the combination of Formosat-3/COSMIC, GRACE and CHAMP data for regional 4-D electron density modeling. Quadratic polynomial B-splines are considered as base functions. This modeling method constitutes the basis for the adjustment system as part of the thesis and also for the studies contained in P-II: Limberger et al. (2014), P-V: Liang et al. (2014) and P-VI: Liang et al. (2015).

Keywords: Formosat-3/COSMIC ★ GRACE ★ CHAMP ★ Regional electron density model ★ B-splines ★ F2 Chapman parameters ★ Variance component estimation

P-II

Limberger, M., Liang, W., Schmidt, M., Dettmering, D., Hernández-Pajares M., and Hugentobler, U. (2014): **Correlation studies for B-spline modeled F2 Chapman parameters obtained from Formosat-3/COSMIC data**. *Annales Geophysicae*, 32, 1533-1545, DOI 10.5194/angeo-32-1533-2014.

The estimation of parameters within an adjustment process can be affected by the correlation of the target quantities in terms of a poor parameter separability. Correlations may be classified into physical and mathematical correlations where the latter one strongly depend on the parametrization. Investigations on the mathematical correlations between Chapman parameters as represented by B-spline base functions according to the model approach published in P-I: Limberger et al. (2013) are carried out in this publication.

Keywords: Formosat-3/COSMIC ★ Regional electron density model ★ Stochastic modeling ★ Correlations ★ B-splines ★ F2 Chapman parameters

P-III

Limberger M., Hernández-Pajares M., Aragón-Ángel A., Altadill D., Dettmering D. (2015): **Long-term comparison of the ionospheric F2 layer electron density peak derived from ionosonde data and Formosat-3/COSMIC occultations.** *Journal of Space Weather and Space Climate*, 5, A21, 2015, DOI 10.1051/swsc/2015023.

Many ionospheric models are driven by the combination of space observation techniques in favor of a high resolution and dense data distribution. In this context, radio occultations play an important role as allowing for the retrieval of electron density profiles. This paper includes a long-term validation of the ionospheric F2 peak derived from Formosat-3/COSMIC radio occultations. Important contributions of this paper to the thesis are the electron density retrieval and accuracy assessment of the derived Chapman F2 key parameters which will play a key role in the presented model approach.

Keywords: Formosat-3/COSMIC ★ Radio occultations ★ Electron density retrieval ★ Ionosondes ★ F2 peak assessment

P-IV

Dettmering D., Limberger M., Schmidt M. (2014): **Using DORIS measurements for modeling the Vertical Total Electron Content of the Earth's ionosphere.** *Journal of Geodesy*, 88(12), 1131-1143, DOI 10.1007/s00190-014-0748-2.

Several altimetry missions carrying a DORIS receiver capable of tracking continuous phase signals have been launched in recent years. Therefore, global models may benefit from the inclusion of additional DORIS tracks. This publication deals with the processing and study of TEC derived from DORIS carrier phase measurements, tracked by the missions Jason-2, Cryosat, Hy-2a and Saral. A study period of two months between 15 September 2013 and 15 November 2013 has been chosen to model and evaluate global TEC maps based on GPS and DORIS observations.

Keywords: Jason-2 ★ Cryosat ★ Hy-2a ★ Saral ★ DORIS TEC ★ Global TEC modeling ★ GPS and DORIS TEC combination

P-V

Liang W., Limberger M., Schmidt M., Dettmering D., Hugentobler U. (2015): **Combination of ground- and space-based GPS data for the determination of a multi-scale regional 4-D ionosphere model.** *International Association of Geodesy Symposia* (in press).

Probably the most powerful combination of satellite based observation techniques for ionospheric electron density modeling can be referred to GPS and occultation data. In this case, the strengths of both techniques are exploited: An appropriate continental data coverage through terrestrial GNSS tracking stations and the capability to resolve the vertical electron density distribution by means of occultations over continents and oceans. In this paper, the regional modeling strategy presented in P-I: Limberger et al. (2013) has been considered for the combination of GPS TEC and electron density data observed by CHAMP, GRACE and Formosat-3/COSMIC.

Keywords: GPS ★ Electron density profiles ★ Regional electron density model ★ TEC and electron density combination

P-VI

Liang W., Limberger M., Schmidt M., Dettmering D., Hugentobler U., Bilitza D., Jakowski N., Hoque M. M., Wilken V., Gerzen T. (2015): **Regional modeling of ionospheric peak parameters using GNSS data – an update for IRI**. *Advances in Space Research*, 55(8), 1981-1993, DOI 10.1016/j.asr.2014.12.006.

One of the most reliable sources for electron density data, at least below the ionization peak of the F2 region, are ionosondes. Therefore, ionosonde data are mostly favored for the validation of electron density models or estimated Chapman parameters. This paper takes up the methods of P-V: Liang et al. (2014) for an intensive validation of the model results with ionosonde data.

Keywords: TEC and electron density combination ★ Validation with ionosondes

Based on this work and in particular by means of the publications, different aspects in the field of ionosphere modeling are addressed. One topic discussed and investigated concerns the retrieval of the ionospheric electron density from GPS radio occultations which is in particular motivated by the demand for a global and reliable way for tracking electron density variations. This initial situation can be described by the following questions:

Electron density retrieval

- Which retrieval algorithms can be applied to derive the electron density from GNSS radio occultations?
- What accuracy can be expected from the electron density profiles, in particular for the ionospheric F2 layer?

Another aspect covered by this work refers to the selection of meaningful ionospheric parameters and the formulation of functional dependencies between the parameters, specifically the derivation of an observation equation related to the electron density. In particular, a description for the vertical structure of the electron density distribution is required. Furthermore, a suitable parametrization method is desired to enable the multidimensional data representation. Such aspects are covered by the questions:

Data representation

- How could an adequate representation of the electron density distribution, in particular for the vertical direction, look like?
- What kind of basis functions are suitable and meet the model requirements?

The sensitivity and distribution of input observations are responsible to resolve the spatio-temporal structure of selected ionospheric target parameters, i.e., the introduction of complementary data is often required. The combination of different datasets and individual weighting of the data are essential topics in this thesis that follow from the questions:

Parameter estimation and combination of observation techniques

- Which model approach is adequate to comply with the general requirements for the localization of the observed signal, continuous data representation and proper handling of data gaps?
- How can observation groups be combined and individually weighted?

It can be expected, that physically defined ionospheric parameters are governed by strong physical and, based on the selected model approach, also mathematical correlations that should be reflected in the stochastic component of the model. Specifically, investigations of the mathematical dependencies in terms of parameter correlations are carried out as part of this thesis. The motivation follows from the questions:

Aspects of stochastic modeling

- Which dependencies exist between the model parameters and base functions?
- What is the influence of variance components on the correlations?

Based on the aforementioned questions, categorized into four topics, the initial situation as a motivation of this thesis is formulated. The studies performed in this dissertation are related to these issues where the primary results and conclusions are summarized in Chapter 6.

Contents

Preface	5
1 The Earth atmosphere	13
1.1 Main sources of ionization	13
1.2 Plasma transportation	14
1.3 Ionospheric structure and variability	15
1.3.1 Vertical stratification	16
1.3.2 Dynamical features and irregularities	17
1.4 Mechanism of ionization	18
1.5 The Chapman function	20
1.6 Relevant key quantities	24
2 Parametrization	27
2.1 Spherical harmonics	28
2.1.1 Classical 2-D model	28
2.1.2 Spherical harmonics and empirical orthogonal functions	29
2.2 Grid modeling	30
2.2.1 Cells	30
2.2.2 Voxel model	31
2.3 B-splines	32
2.3.1 Normalized quadratic polynomial B-splines	33
2.3.2 Normalized periodic trigonometric B-splines	35
2.3.3 B-spline tensor products	36
2.4 Ionosphere modeling with B-splines	38
2.4.1 Total electron content	38
2.4.2 Electron density	40
3 Satellite techniques for observing the total electron content	44
3.1 Global Navigation Satellite Systems	44
3.2 Acquiring the ionospheric refraction from dual-frequency microwave signals . .	53
3.3 Doppler Orbitography and Radiopositioning Integrated by Satellite	57
3.4 Dual-frequency radar altimetry	60
4 Ionospheric GNSS radio occultations for observing the electron density	63
4.1 CHAMP, GRACE and Formosat-3/COSMIC	65
4.2 The Abelian inversion	67
4.3 Electron density retrieval from GNSS data	70
4.3.1 Based on the Doppler shift	71
4.3.2 Based on STEC	72

5	Modeling the ionosphere	77
5.1	Categorization of models	77
5.2	Observation equations for the discrete and integrated electron density	81
5.3	Parameter estimation	84
5.4	Handling data gaps	91
5.5	Combination of techniques or satellite missions	92
5.6	Adjustment sequence	93
5.6.1	Outer iteration: Linearization	94
5.6.2	Inner iteration: Variance component estimation	96
5.7	Parameter variances and correlations	97
6	Summary and Synthesis	99
6.1	Primary results of the papers	99
6.2	Conclusions and Outlook	107
7	Publications	110
7.1	P-I	
	Limberger M., Liang W., Schmidt M., Dettmering D., and Hugentobler U. (2013): Regional representation of F2 Chapman parameters based on electron density pro- files	110
7.2	P-II	
	Limberger, M., Liang, W., Schmidt, M., Dettmering, D., Hernández-Pajares M., and Hugentobler, U. (2014): Correlation studies for B-spline modeled F2 Chapman parameters obtained from Formosat-3/COSMIC data	126
7.3	P-III	
	Limberger M., Hernández-Pajares M., Aragón-Ángel A., Altadill D., and Dettmer- ing D. (2015): Long-term comparison of the ionospheric F2 layer electron density peak derived from ionosonde data and Formosat-3/COSMIC occultations	141
7.4	P-IV	
	Dettmering D., Limberger M., and Schmidt M. (2014): Using DORIS measure- ments for modeling the Vertical Total Electron Content of the Earth's ionosphere	157
7.5	P-V	
	Liang W., Limberger M., Schmidt M., Dettmering D., and Hugentobler U. (2015): Combination of ground- and space-based GPS data for the determination of a multi-scale regional 4-D ionosphere model	159
7.6	P-VI	
	Liang W., Limberger M., Schmidt M., Dettmering D., Hugentobler U., Bilitza D., Jakowski N., Hoque M. M., Wilken V., and Gerzen T. (2014): Regional modeling of ionospheric peak parameters using GNSS data — An update for IRI	161
	Abbreviations	163
	List of Figures	167
	List of Tables	170
	Software references	171
	Bibliography	172

1 The Earth atmosphere

Temperature is one of the most important parameters to describe the composition of the Earth's atmosphere as it controls the majority of physical and chemical processes. Up to approximately 15 km above the Earth surface, the temperature decreases with around 6.5°C per km, i.e., the air cools down to -65°C , until the upper boundary of the troposphere (also known as tropopause) is reached (Zolesi and Cander, 2014). Above, the temperature begins to increase and converges towards a local maximum of about 0°C that can be found at the upper boundary of the stratosphere (the stratopause) in an altitude of around 50 km. In the altitude interval between 50 km and 90 km, the temperature decreases again to reach its minimum of around -80°C at the mesopause, the upper boundary of the mesosphere. Above the mesosphere, the thermosphere extends from 90 km to altitudes between 500 km and 1,000 km and temperature increases. In the upper thermosphere, temperatures can range from about 500°C to $2,000^{\circ}\text{C}$ or even higher. However, due to the near-vacuum conditions in the upper thermosphere and adjacent exosphere, there is nearly no energy transfer.

In the mesosphere and particularly in the adjacent thermosphere layer, the density of matter starts to decrease and the temperature parameter therefore becomes rather meaningless. Ultraviolet (UV) radiation and X-rays cause an intense ionization of neutral particles to free electrons and positive ions in equal parts, especially above altitudes of approximately 200 km. In this region, the upper part of the mesosphere, the thermosphere and the uppermost layer, the exosphere, as defined in the temperature domain, overlap with the ionosphere and plasmasphere that are mainly characterized by the density of electrons.

1.1 Main sources of ionization

With a distance of around 150 million km¹, Sun is the closest star to Earth and the main driver for ionization processes in the ionosphere. As the Sun is a gaseous body, its surface and atmosphere is continuously changing. However, when looking to the Sun as an observer from Earth, the photosphere as a part of the Sun's surface appears as a yellow disc and reflects active convection processes as the source for energy radiation into space.

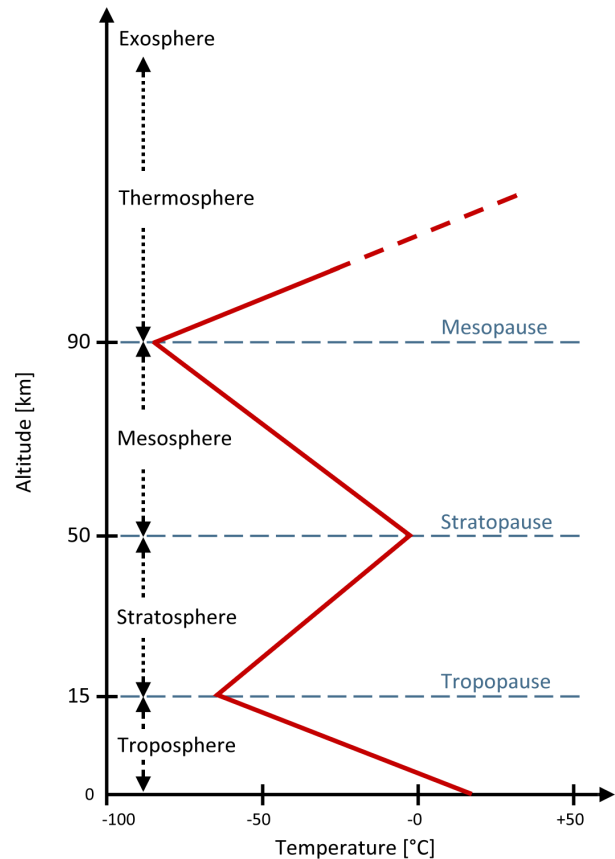


Figure 1.1: Scheme for height dependent temperature variations in the Earth atmosphere.

¹The Astronomical Unit (AU) is roughly the Earth-Sun distance and defined with $1 \text{ AU} = 149,597,870,700 \text{ m}$, i.e., around 150 million km.

An important phenomena that can be observed on the photosphere are sunspots. They are cooler than the environment and emit less visible light, meaning that sunspots appear for our eyes as small dark areas². Since the 19th century, the sunspot number is continuously recorded as an indicator for the Sun activity reflecting a periodical 11 year cycle with daily variations between 10 up to more than 100 spots.

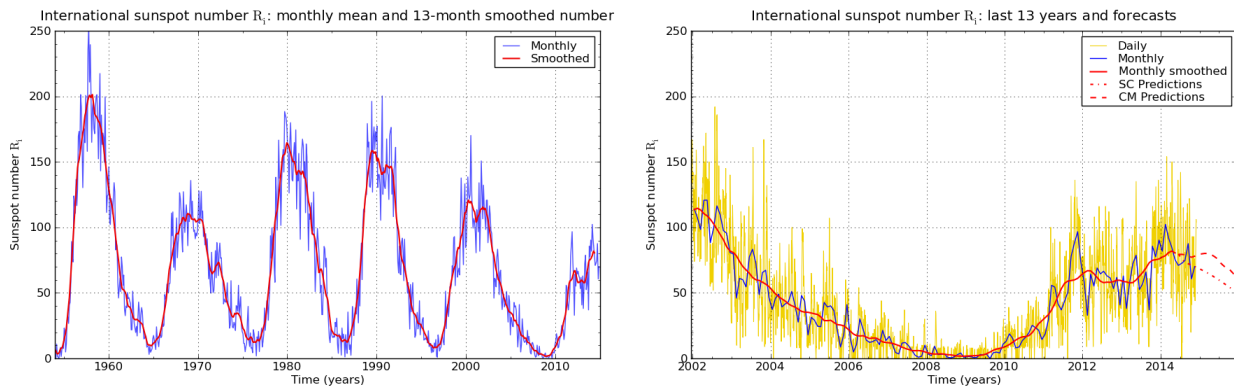


Figure 1.2: Monthly mean and daily total sunspot number, source: Sunspot Index and Long-term Solar Observations (SILSO) data/image, Royal Observatory of Belgium, Brussels (<http://www.sidc.be>)

The sunspot number of the last five cycles is provided by the left plot of Fig. 1.2 showing the monthly average (blue) together with the 13-months smoothed value (red). The right plot shows the daily sunspot numbers (yellow), the monthly averages (blue) as well as the smoothed monthly sunspot numbers (red). The dashed lines indicate predictions based on the sunspot number series only (small dashes) and taking additionally the geomagnetic index into account (large dashes). Both time series are provided by the Solar Influences Data Center (SIDC) in Brussels. Although being in a high solar activity period, it is obvious from the time series that we are currently facing very moderate conditions.

The presence of sunspots is often correlated with the incidence of large explosions emitting extremely hot plasma composed of protons and electrons. These explosions are denoted as solar flares and are typically located along magnetically neutral lines, i.e., at those positions where the Sun magnetic field polarization changes. The incidence of a Coronal Mass Ejection (CME) is mostly combined with solar flares including the emission of a tremendous amount of charged plasma into space. This event that can last up to several hours and the particle flow direction is typically oriented towards the Sun magnetic field lines. The described phenomena and their frequency of appearance, respectively, are strongly related to the solar activity and thus on the sunspot number but it shall be noted that it does not mean, that the features can be excluded during periods with low sunspot numbers.

1.2 Plasma transportation

The solar corona identifies the outer atmosphere of the Sun composed of extremely hot plasma as it consists of free electrons with high kinematic energy. The corona is driven through a continuous plasma flux emitted from the Sun. The Sun escape velocity v_{sev} yields 618 km/s, i.e., a particle requires at least a speed of v_{sev} to flee from the Sun in case that the depart is not prohibited by collisions with other particles (Moldwin, 2008).

Due to the heat in the corona, many particles are moving with supersonic velocity ($\approx 1,190$ km/h in dry air at standard temperature and pressure) and are able to escape into the entire solar system with hundreds of km/s while dragging the solar magnetic field into outer space. This flux is known as solar wind and for the reason that it is composed mostly of protons, helium nuclei and electrons,

²First telescope observation of sunspots by Galileo Galilei (15.02.1564 - 29.12.1641).

the solar wind is described as magnetized plasma. The solar wind streams off the Sun with about 400 km/s but its propagation velocity can vary between 300 km/s and 800 km/s, in particular due to solar wind interactions between slow and fast streams. Detailed studies about the solar wind speed variability as observed by different spacecrafts (IMP, Ulysses, Voyager-2) during more than three solar cycles have for instance been published by Rangarajan and Barreto (2000) and Richardson et al. (2001). The configuration of the Earth magnetic field can be approximated as a dipole where the magnetic field lines source in the South Pole and converge to the North Pole. The magnetic North pole is tilt by around 11° with respect to the Earth spin axis. From the collision of solar wind with the Earth, the magnetosphere is shaped and looks similar to a river encountering the Earth as a rock, i.e., forming a tail at the Earth night side. On the day side, a shock wave known as bow shock arises from the collision of the solar wind plasma with the magnetic field lines of the Earth. This interaction is schematically depicted in Fig. 1.3.

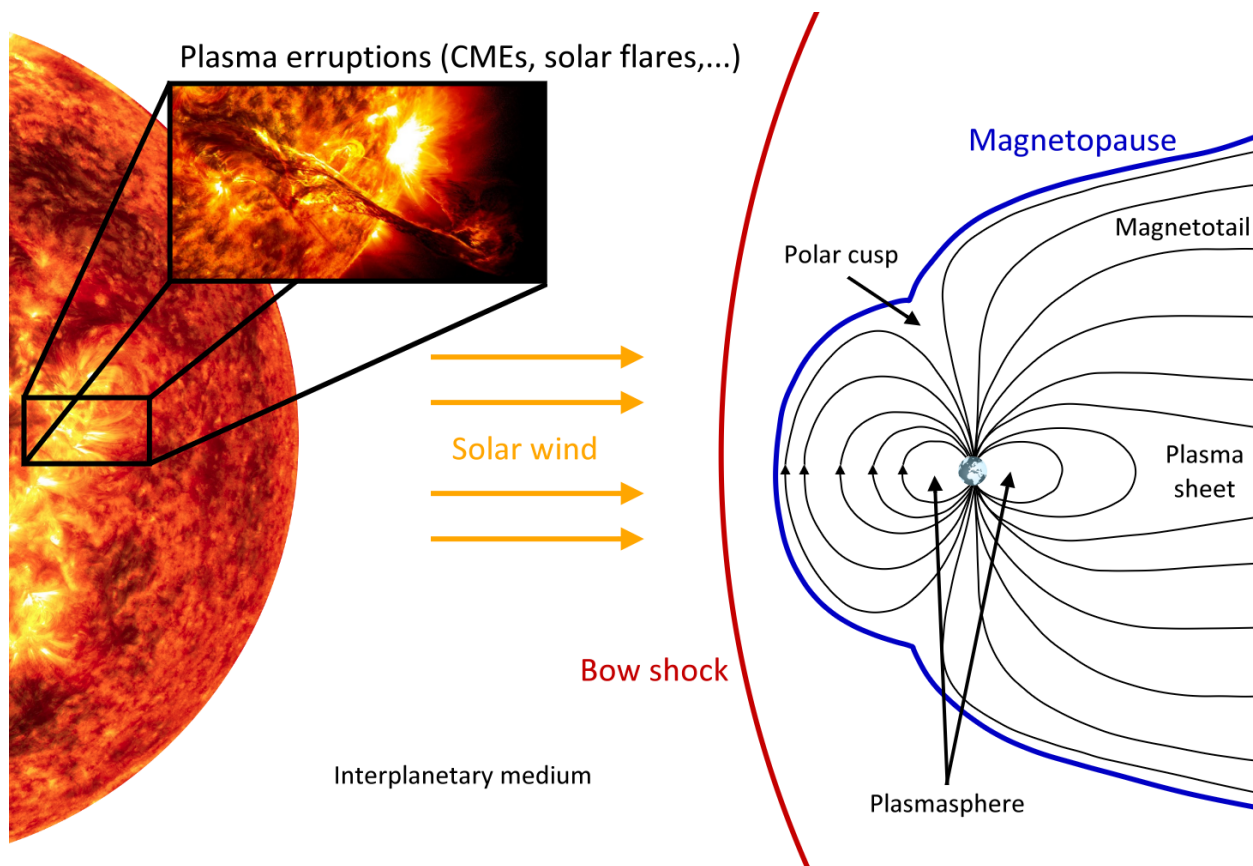


Figure 1.3: Scheme for the interaction between features of the Sun as ionization sources and the Earth's magnetic field, inspired by a representation of the European Space Agency (<http://sci.esa.in>).

For further details about solar phenomena, Sun-Earth interactions or the structure of planetary magnetics it shall be referred to Zolesi and Cander (2014), Brecke (2013) and Moldwin (2008).

1.3 Ionospheric structure and variability

With the solar irradiation, in particular the UV- and X-rays as the main sources of ionization, the ionospheric variations depend on the Sun position and the radiation intensity. It follows naturally that the intensity reaches a maximum when the Sun is located in the zenith and decreases towards the poles or day/night boundary. As described in Section 1.2, the flow of charged particles follows the magnetic field lines of the Earth and therefore the geomagnetic equator plays an important role as it forms the symmetry axis for ionospheric structures as a rough approximation. The geomagnetic equator is defined as a line connecting all points on Earth where the magnetic field inclination is zero.

1.3.1 Vertical stratification

The vertical stratification of the ionosphere is typically divided into mainly four layers: The D layer extending approximately from 50 km to 90 km followed by the E layer between 90 km and 130 km, the F1 layer from 130 km to 250 km and the F2 layer reaching from 250 km up to about 450 km with smooth transition into the plasmasphere. It should be noted, that these numbers are just approximations since the real height depends on the solar zenith angle, time (in particular daily and seasonal variations) as well as the solar cycle and solar activity.

D layer: This region is characterized by a comparably low electron density magnitude of about 10^2 el/cm³ to 10^3 el/cm³, controlled by variations in the diurnal, seasonal and solar cycle domain. Frequency modulated (FM) based radio signals can be scattered in this region during daytime whereas after sunset, the D layer vanishes within few minutes.

E layer: This layer contains densities of up to 10^5 el/cm³, reaches its daily maximum around noon and remains during night although stimulated by only weak ionization. Further drivers are seasonal variations and the solar cycle dependency. A special feature of the E-region is the infrequent occurrence of a sporadic E layer, namely the Es layer. It exceeds as the E layer from 90 km to 130 km and features a very diverse spatio-temporal pattern.

F layer: The F layers, containing the F1 and F2 components, include the maximum ionization region of the Earth's ionosphere and therefore must be considered as the main error source for applications related to radio communications, navigation and positioning. The F2 layer plays a dominant role as it is present for 24 hours a day with varying maximum densities between 10^4 el/cm³ and 10^6 el/cm³. F1 on the contrary shows an infrequent occurrence with stronger characteristics in summer than winter times and additionally merges with F2 during night. The F region can be influenced by long-term periodicities such as the solar cycle down to responses in the scale of seconds due to short-term disturbances.

An idealized profile of the vertical electron density distribution of the ionosphere including the characteristic layers is depicted in Fig. 1.4. The altitude is plotted along the y-axis as a function of the electron density in el/cm³. Prominent structures, e.g., the electron density maxima of the E layer and F2 layer are exposed in the profile.

At the beginning of this chapter, the atmospheric layer composition in the temperature domain has been introduced which is now extended by a definition in the ionization domain for the upper atmosphere. The relation of the electron density distribution as provided by Fig. 1.4 to these scales is schematically provided by Fig. 1.5. Beside the arrangement of layers, an altitude axis including the nominal orbit heights of different satellite missions, that will play a key role in this thesis, are depicted on the right. Taking into account that the satellites can be used as ionospheric sensors, the illustration shows that the selected missions are capable to contribute information for several or even all ionosphere layers.

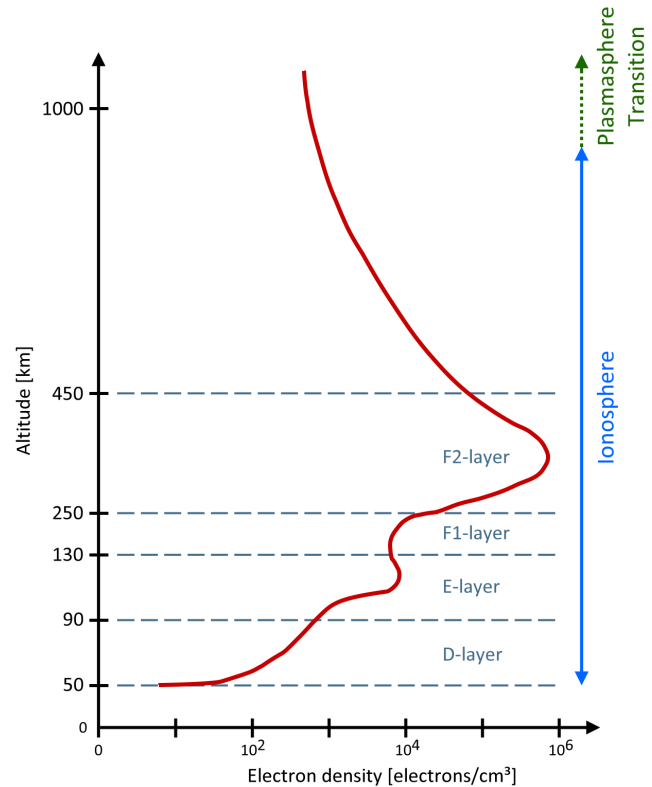


Figure 1.4: Ionospheric layer composition based on the vertical electron density distribution, here indicated by a schematic, idealized profile.

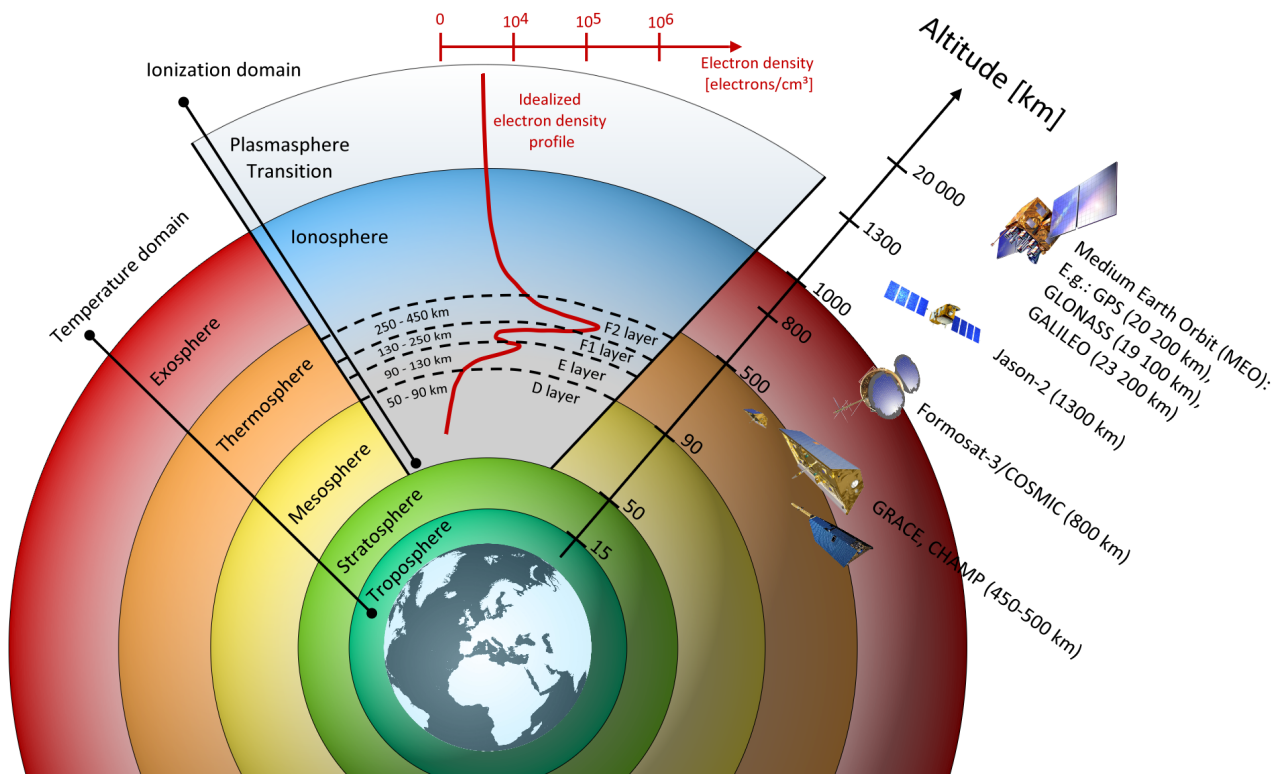


Figure 1.5: Composition of atmospheric layers in the temperature and ionization domain including an electron density distribution profile (red) with characteristic F2 and E peak occurrences. For comparison, orbit heights of different satellite missions, that will be described within this thesis, are provided on the right hand side. It should be noted, that this is just a sketch and the altitude as well as electron density axis is not linearly scaled.

1.3.2 Dynamical features and irregularities

Equatorial ionization anomaly: The most prominent feature that can even be classified as a periodic or regular event is known as the Equatorial Ionization Anomaly (EIA) that occurs within a region of approximately $\pm 20^\circ$ around the magnetic equator. It describes a trough of ionization in the F2 layer at the magnetic equator and crests at about $\pm 15^\circ$ in magnetic latitude. During daytime, solar heating and tidal oscillations in the lower ionosphere cause an upward electrodynamic drift of plasma at the magnetic equator that is carried by neutral winds into North and South direction and diffuses along the magnetic field lines under the influence of gravity and pressure gradients leaving a depression of ionization density at the equator (Bhuyan and Bhuyan, 2008). This phenomenon is often referred to as fountain effect or equatorial fountain.

Ionospheric storms: In case of a CME as for instance been released from solar flares, the solar wind typically is enhanced and causes large spatio-temporal variations in the ionospheric electron density if colliding with the Earth. These events are generally denoted as ionospheric storms. A severe storm happened on 30 October 2003, often denominated as Halloween storm, where large enhancements of the electron density in the magnetosphere and ionosphere have been recorded. The strongest impact encountered North America (during the storm, aurora could be seen from Texas and Florida) but also the European sector was affected. For instance, geomagnetically induced currents in the Earth's crust caused stress in the electric-power grids in North America, forcing system operators to take measures to prevent blackouts. The geomagnetic orientation used for directional oil and gas drilling was disrupted in Alaska. Some airline polar routes had to be canceled or changed to lower latitudes due to interferences with radio communication. The GPS accuracy was significantly degraded, affecting land and ocean surveys as well as commercial and military aircraft navigation. A protective operation mode has been set for several civilian and military satellites. Other satellites were damaged and a Japanese scientific satellite was permanently disabled. Astronauts onboard the International Space

Station (ISS) took precautionary shelter to avoid excessive levels of radiation.

Traveling ionospheric disturbances: Irregularities in the F-region appearing as ionospheric wave signatures with electron density oscillations slowly decaying in time are generally denoted as Traveling Ionospheric Disturbances (TIDs). TIDs can be classified into Large Scale Traveling Ionospheric Disturbances (LSTIDs) and Medium Scale Traveling Ionospheric Disturbances (MSTIDs), that differ by their existence time and motion speed. Following Zolesi and Cander (2014), LSTIDs occur for one to three hours, move with around 300 m/s and mainly depend on geomagnetic activity stimulated by gravity waves in polar regions. MSTIDs exist in shorter periods of 10 min to 1 hour (Hernández-Pajares et al., 2011) and move slower between 50 m/s and 300 m/s depending on the direction if horizontal (faster) or vertical (slower). They reach amplitudes of up to few Total Electron Content Units (TECU) during the solar cycle maxima (Hernández-Pajares et al., 2012). Stimulators of MSTIDs are meteorological phenomena such as neutral winds or the solar terminator³.

Scintillations: During high solar activity, rapid variations in the ionospheric index of refraction may occur. This effect is denoted as scintillation and may cause signal power fading, phase cycle slips, receiver loss of lock, etc., and degradation of the quality for satellite navigation systems. Thus, the consideration of scintillations plays an important role in the sector of integrity and public-safety applications (e.g. aviation) including Satellite Based Augmentation Systems (SBAS) (Skone and Knudsen, 2000).

Spread-F: The effect that the F region induces diffused, irregular scatters of the original radio waves can be associated to the occurrence of a spread-F layer. It appears as regions of irregularities that vary between 20 km up to more than 100 km related to solar activity, season and local time. Furthermore, the rate of appearance differs significantly with latitude (Zolesi and Cander, 2014).

1.4 Mechanism of ionization

The previous section described ionization sources and the transportation of charged plasma by solar wind towards Earth where the particles are trapped by the geomagnetic field. Additionally, the general layer structure and dynamical features of the ionosphere have been introduced. A physical and mathematical description of the ionospheric electron density distribution shall be derived in the following.

Atmospheric properties

At sea level, the standard atmosphere as a fluid composed of a mixture of gases has a pressure p of $1.01325 \cdot 10^5$ Pa ($1 \text{ Pa} = 1 \text{ N/m}^2 = 1 \text{ kg}/(\text{ms}^2)$ in SI⁴ units). It decreases with increasing altitudes z and is generally defined with

$$p(h_0) = \int_{h_0}^{\infty} g(z)\rho(z)dz \quad (1.1)$$

per unit surface as the weight of all air above the bottom height h_0 (Zolesi and Cander, 2014). p depends on the atmospheric density $\rho(z)$ and the gravitational acceleration $g(z)$, henceforth simply g , with a conventional standard value of $g = 9.80665 \text{ m/s}^2$. Both ρ and g are likewise decreasing with height. The pressure decrease with increasing heights is governed by the hydrostatic equilibrium. It follows for a cylindrical mass element with cross-section A [m^2] and height dz [m] including the number density n [m^{-3}] of molecules with the mass m [kg], that

$$[p - (p + dp)] A = nmgAdz \quad (1.2)$$

³The boundary that separates the portion of the Earth experiencing daylight from the portion experiencing darkness.

⁴SI = International System of Units

and consequently

$$dp = -nmgdz \quad (1.3)$$

where gravitational force and pressure are balanced to preserve static equilibrium (Brecke, 2013). An expression of the ideal gas law (Levine, 1985) is furthermore given by

$$pV = knT \quad (1.4)$$

as a relationship between the pressure, volume V , and temperature T for a fixed mass of gas including the Boltzmann constant $k = 1.38 \cdot 10^{-23}$ J/K. Merging Eq. (1.3) with Eq. (1.4) under considering of V as a unit volume leads to

$$\frac{dp}{p} = -\frac{mg}{kT}dz = -\frac{1}{H}dz \quad (1.5)$$

where the so-called scale height $H = kT/(mg)$ has been introduced (Brecke, 2013). The scale height varies between 8 km at the Earth's surface and several hundreds of kilometers in the upper ionosphere. The integration of Eq. (1.5) between the limits $[h_0, h]$ yields

$$\int_{h_0}^h \frac{dp}{p} = [\ln p]_{h_0}^h = \ln \frac{p(h)}{p(h_0)} = \int_{h_0}^h -\frac{1}{H}dz \quad (1.6)$$

or

$$p(h) = p_0 \exp\left(-\int_{h_0}^h \frac{1}{H}dz\right) \quad (1.7)$$

with $p_0 = p(h_0)$. For an isothermal atmosphere under the assumption of constancy for the gravitational acceleration and molecular mass, Eq. (1.7) can be solved as

$$p(h) = p_0 \exp\left(-\frac{h-h_0}{H}\right) \quad (1.8)$$

to obtain an approximation for the atmospheric pressure (Davies, 1990).

Photoionization and recombination

The sun emits UV rays as electromagnetic radiation that collide with neutral atoms leading to the detachment of electrons and positively charged ions by the UV energy. A simplified representation of this process, known as photoionization, is given by Fig. 1.6.

The rate of ionization depends mainly on two factors: (1) the neutral density decreases with height and (2) the in-coming solar radiation increases with height. The absorption rate L of the radiation, i.e., the loss of radiation intensity I along the Line-of-Sight (LOS) s from the Sun as the radiation source to a specific target height, can be defined as

$$L = \frac{dI}{ds} = -\sigma_f nI \quad (1.9)$$

where n is the density of a neutral particle and σ_f identifies the cross section of the radiation or photon absorption rate for the frequency f . With the proportionality between the absorption and the production rate Q of ions or electrons, respectively, we obtain

$$Q = -\frac{dI}{ds} = \sigma_f nI. \quad (1.10)$$

The recombination of free electrons with positive ions is a reversion of the photoionization as depicted in Fig. 1.6. Physically it is differentiated between two deionization processes, in particular

1. the **recombination** of a free electron with a positive ion to an atom or neutral molecule and
2. the **binding** of a free electron to an atom or neutral molecule resulting in a negative ion which barely has an influence to electromagnetic signals due to its mass

Since the effect of binding is relatively small, it can be neglected and the recombination process is the main driver to produce neutral atoms. In this case, we can also assume that the density of free electrons equals the density of positive ions.

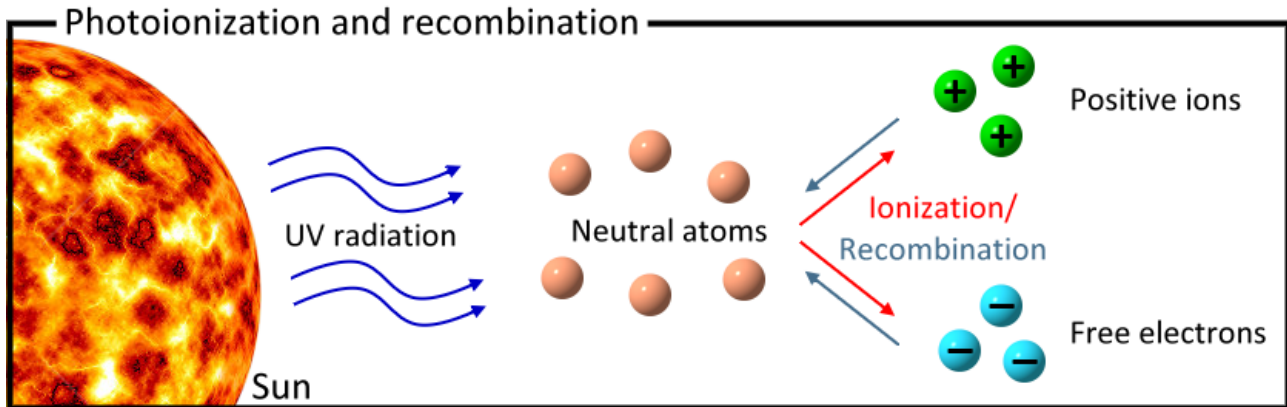


Figure 1.6: Schematic representation of the photoionization process.

1.5 The Chapman function

The formula for the production rate of ion pairs in a multi-component atmosphere has been published by Vanzandt (1967). For an atmosphere composed of an isothermal gas that is ionized by a single solar wavelength, Sydney Chapman⁵ found already in 1931 a formulation to approximate the variations of free electrons along the vertical. The corresponding methodology was published in Chapman (1931a,b) and Chapman and Mian (1942a,b). In comparison with other effects influencing the density of electrons, the Sun plays a key role and therefore the Chapman function (or Chapman profile) describes the electron density distribution depending on the Sun position. The basic regulations of the function include that the ion production will peak at some altitude and the maxima is reached when the Sun is located in zenith direction.

Some simplifications assumptions are taken into account for the mathematical description of the model, specifically that

- the atmosphere is composed of only one chemical element, i.e., as a isothermal one-component gas,
- the atmosphere is horizontally stratified and can be described by an undisturbed layer structure without diffusions or horizontal variations,
- the radiation is monochromatic and parallel,
- the temperature, gravitational acceleration and molecular mass are constant (see also Eq. (1.8)) so that the scale height $H = kT/(mg)$ is constant, too, and
- the electron production is caused only by photoionization and electron loss only through recombination.

The recombination theory (Hargraeves, 1992) can follow two different assumptions.

⁵Sydney Chapman (29.01.1888 - 16.06.1970) was a British physicist, astronomer and geophysicist.

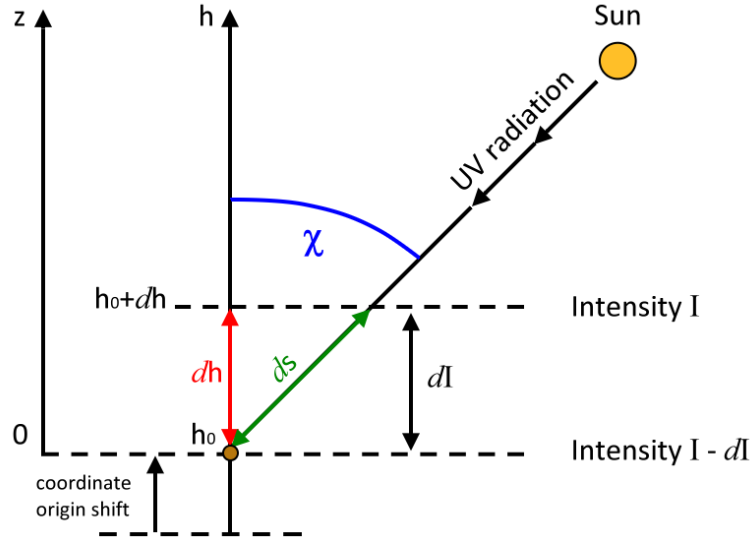


Figure 1.7: Loss of radiation intensity with respect to a path element ds or height interval dh .

(1) The loss rate ν_L or rate of recombination, respectively, can be expressed by

$$\nu_{L,\alpha} = \alpha N_e^2 \quad (1.11)$$

resulting from the recombination of free electrons e with positive ions N^+ while no negatively charged ions are present (Stankov et al., 2003). α is introduced as the so-called recombination coefficient.

(2) The linear loss rate is described by

$$\nu_{L,\beta} = \beta N_e \quad (1.12)$$

based on the assumption that the electron loss is coupled with the attachment of neutral particles. β is the attachment coefficient.

The electron density variation with respect to time can now be expressed from the difference between ionization and recombination (Davies, 1990) as depicted in Fig. 1.6. Based on $\nu_{L,\alpha}$, it follows that

$$\frac{dN_e}{dt} = Q - \alpha N_e^2 = \sigma_f n I - \alpha N_e^2 \quad (1.13)$$

where Q is the production rate introduced in Eq. (1.10).

The ionosphere of the Earth consists of weakly ionized gas. For low ionization levels it can be assumed that the atmospheric pressure, introduced by Eq. (1.8), also holds for the description of the neutral particle density n . Accordingly,

$$n = n_0 \exp\left(-\frac{h - h_0}{H}\right) \quad (1.14)$$

can be defined where n_0 is the neutral density at h_0 . According to Fig. 1.7, a coordinate shift $z' = h - h_0$ shall be introduced for simplification and the solar zenith angle χ is taken into account for the description of a subinterval along the irradiation path $ds = dh / \cos(\chi)$. Considering these modifications in Eq. (1.9) together with the substituting of n by means of Eq. (1.14) defines the radiation intensity decrease with

$$dI = -\sigma_f n I ds = -\frac{\sigma_f n_0 I}{\cos \chi} \exp\left(-\frac{z'}{H}\right) dz'. \quad (1.15)$$

$z' = \infty$ shall be introduced now to identify altitudes out of the atmosphere where absorption can be neglected. Then, the integration of Eq. (1.15) as

$$\int_{\infty}^z \frac{dI}{I} = -\frac{\sigma_f n_0}{\cos \chi} \int_{\infty}^z \exp\left(-\frac{z'}{H}\right) dz' \quad (1.16)$$

$$[\ln I]_{\infty}^z = -\frac{\sigma_f n_0}{\cos \chi} \left[-H \exp\left(-\frac{z'}{H}\right) \right]_{\infty}^z \quad (1.17)$$

$$\ln \frac{I_z}{I_{\infty}} = \frac{\sigma_f n_0 H}{\cos \chi} \exp\left(-\frac{z}{H}\right) \quad (1.18)$$

yields the radiation intensity in z where $\lim_{z' \rightarrow \infty} \left[-H \exp\left(-\frac{z'}{H}\right) \right] = 0$. It follows that

$$I_z = I_{\infty} \exp\left(\frac{\sigma_f n_0 H}{\cos \chi} \exp\left(-\frac{z}{H}\right)\right) \quad (1.19)$$

which can be used to substitute I in the electron production law provided by Eq. (1.10). Additionally, n can be expressed by means of Eq. (1.14) leading to

$$Q = \sigma_f n_0 I_{\infty} \exp\left(-\frac{z}{H} + \frac{\sigma_f n_0 H}{\cos \chi} \exp\left(-\frac{z}{H}\right)\right). \quad (1.20)$$

To find the peak height related to the maximum production rate Q_{\max} , the derivative of Eq. (1.20) may be calculated. Taking into account that Q_{\max} will be reached with the Sun located in the zenith and thus $\chi = 0^\circ$ yields

$$\frac{dQ}{dz} = \underbrace{\sigma_f n_0 I_{\infty}}_{>0} \underbrace{\exp\left(-\frac{z}{H} + \sigma_f n_0 H \exp\left(-\frac{z}{H}\right)\right)}_{>0} \underbrace{\left(-\frac{1}{H} \left(1 + \sigma_f n_0 H \exp\left(-\frac{z}{H}\right)\right)\right)}_{\text{only true if this term becomes zero}} \stackrel{!}{=} 0 \quad (1.21)$$

which is valid for

$$-\exp\left(\frac{z}{H}\right) \stackrel{!}{=} \sigma_f n_0 H. \quad (1.22)$$

With the height of the maximum ion production located in h_0 or $z = 0$, respectively, it can be considered from Eq. (1.22) that $\sigma_f n_0 H = -1$. Applying these relations to Eq. (1.20), a formulation for the maximum production can now be found with

$$Q_{\max} = \sigma_f n_0 I_{\infty} \exp(-1). \quad (1.23)$$

Furthermore, the expression

$$Q_{\max} = Q \exp\left(-1 + \frac{z}{H} + \frac{1}{\cos \chi} \exp\left(-\frac{z}{H}\right)\right) \quad (1.24)$$

is obtained after substituting $\sigma_f n_0 I_{\infty}$ by means of Eq. (1.20). Switching back the coordinate system and solving Eq. (1.24) for Q as an expression of the ion production for arbitrary heights leads finally to the Chapman production function

$$Q = Q_{\max} \exp\left(1 - \frac{h - h_0}{H} - \frac{1}{\cos \chi} \exp\left(-\frac{h - h_0}{H}\right)\right). \quad (1.25)$$

The profile shape for different function values is shown in Fig. 1.8 which shall be described in the following.

- χ : The top left subfigure shows the Chapman profile variation as a function of height h , plotted along the ratio Q/Q_{max} which indicates the magnitude of electron production. The profiles has been depicted here for different solar zenith angles $\chi = [0^\circ, 10^\circ, \dots, 80^\circ]$. The peak height and the scale height are fixed at $h_0 = 300$ km and $H = 80$ km, respectively. The curves clearly show the electron production decrease at increasing χ angles.
- H**: The second representation on the top right gives an overview of the function behavior regarding varying scale heights $H = [60$ km, 70 km, $\dots, 100$ km] while h_0 is again fixed at 300 km and the Sun is located in the zenith with $\chi = 0^\circ$. The plot shows that the profile curvature gets narrower with a decreasing scale height.
- h_0 : The bottom left illustration contains profiles for different peak heights at $h_0 = [200$ km, 250 km, $\dots, 400$ km] with $H = 80$ km and $\chi = 0^\circ$. h_0 can be interpreted as a shift parameter.
- Q_{max} : Finally, the Chapman function with respect to different electron production rates Q is shown in the bottom right representation. The varying parameter in this case is the maximum production rate $Q_{max} = [10^5$ el/cm³, $2 \cdot 10^5$ el/cm³, $\dots, 6 \cdot 10^5$ el/cm³] while $\chi = 0^\circ$, $h_0 = 300$ km and $H = 80$ km. Q_{max} can be interpreted as a scale factor.

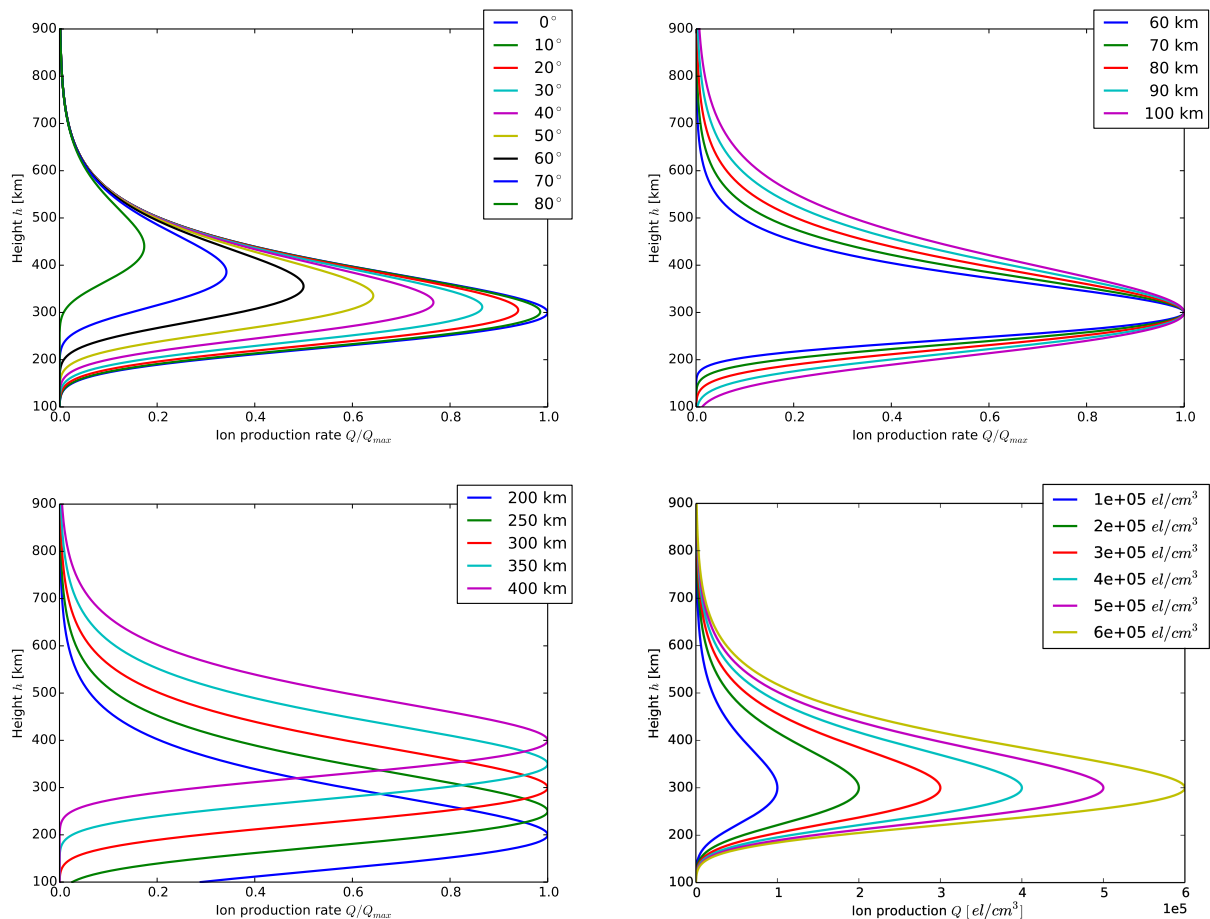


Figure 1.8: Chapman ion production profiles for different function parameters. Dependency with respect to the solar zenith angle $\chi = [0^\circ, 10^\circ, \dots, 80^\circ]$ (top left), scale height $H = [60$ km, 70 km, $\dots, 100$ km] (top right) and peak heights $h_0 = [200$ km, 250 km, $\dots, 400$ km] (bottom left) as functions of the Q/Q_{max} ratio. The ion production Q for different maximum rates $Q_{max} = [10^5$ el/cm³, $2 \cdot 10^5$ el/cm³, $\dots, 6 \cdot 10^5$ el/cm³] is given in the bottom right representation.

A relation between the production rate and the electron density can be obtained from the equilibrium assumption with $dN_e/dt = 0$ at a fixed time moment which can be applied in Eq. (1.13)

leading to $N_e = \sqrt{Q/\alpha}$. In case of the maximum electron density this relation gives accordingly $N_{e_{\max}} = \sqrt{Q_{\max}/\alpha}$. Together with Eq. (1.25), the Chapman production function can finally be obtained as

$$N_e = N_{e_{\max}} \exp \left(\underbrace{\frac{1}{2}}_c \left(1 - \frac{h - h_{\max}}{H} - \exp \left(-\frac{h - h_{\max}}{H} \right) \right) \right) \quad (1.26)$$

to describe the electron density under the assumption that the Sun is located in the zenith with $\chi = 0^\circ$. Here, $N_{e_{\max}}$ is the maximum electron density, h_{\max} the corresponding peak height and H the layer scale height. c identifies the type factor which depends on the electron recombination theory introduced with the Eqs. (1.11) and (1.12) (Stankov et al., 2003; Hargraeves, 1992). Here, a loss rate of $\nu_{L,\alpha} = \alpha N_e^2$ is considered and thus, a so-called α -layer with $c = 1/2$ is derived. Alternatively, $\nu_{L,\beta} = \beta N_e$ would have been taken into account leading to an alternative expression of Eq. (1.26) with type factor $c = 1$.

The α -Chapman layer is a well-known expression that has already been proposed for ionospheric modeling in the fifties by Martyn (1956). In the 1960s, Rishbeth and Garriot (1969) applied the original Chapman profile for modeling the ionospheric electron density under consideration of a fixed atmospheric scale height. The original function has been modified and extended over the years with sophisticated formulations accounting, e.g., for the distinction of the top- and bottomside shape controlled by the scale height. Ezquer et al. (1996) used for instance different coefficients to represent the α - and β -layer description for the bottom and topside, respectively. Huang and Reinisch (1996) expressed the electron density profile in terms of shifted Chebyshev⁶ polynomials including a logarithmic argument. Reinisch and Huang (2001) as well as Reinisch et al. (2007) improved the function by a continuous varying scale height and Jakowski (2005) extended the original α -Chapman profile by a slowly decaying plasmasphere term. The latter expression is applied in this work and will be specified in Chapter 5.

When comparing the production functions depicted in Fig. 1.8 with the electron density distribution in Fig. 1.4, it becomes obvious that the Chapman function provides an adequate approximation for vertical electron density profiles with only few, physically based, parameters. However, it shall be kept in mind that its validity is based on various physical assumptions which have been introduced at the beginning of Section 1.5. A summary including further details about these assumptions is for instance given by Wright (1960).

1.6 Relevant key quantities

For this thesis and within most of the associated publications, for instance in P-I: Limberger et al. (2013), P-II: Limberger et al. (2014), P-V: Liang et al. (2014) and P-VI: Liang et al. (2015), the Chapman function has been considered for modeling the vertical electron density structure of the ionospheric F2 layer. Accordingly, the Chapman parameters for the F2 representation as based on Eq. (1.26) are introduced as the predominant quantities that are identified with

- $NmF2$, as the maximum electron density of the F2 layer,
- $hmF2$, as the corresponding peak height and
- $HF2$, as the F2 scale height.

Then, the height dependent electron density distribution for the F2 layer can be described by means of Eq. (1.26) as

$$N_e(h) = NmF2 \exp \left(\frac{1}{2} \left(1 - \frac{h - hmF2}{HF2} - \exp \left(-\frac{h - hmF2}{HF2} \right) \right) \right) \quad (1.27)$$

⁶Pafnuty Lvovich Chebyshev (16.05.1821 - 08.12.1894) was a Russian mathematician.

where an α -layer type is taken into account.

Another key observable is the integrated electron density, defined as the Total Electron Content (TEC). TEC can for instance be derived from dual-frequency signals of GNSS, RA or DORIS measurements and describes the total amount of free electrons in a cylinder of 1 m^2 cross section with the ray path as the center axis. It is measured in TECU with $1 \text{ TECU} = 10^{16} \text{ el/m}^2$. It can further be differentiated between Vertical Total Electron Content (VTEC) and Slant Total Electron Content (STEC), depending on the ray path direction. Under consideration that a signal propagates through space along the ray path s between a transmitter at the position x^s towards a receiver located at x_r , STEC is defined as

$$\text{STEC}(x_r, x^s, t) = \int_{x_r}^{x^s} N_e(s, t) ds. \quad (1.28)$$

The relation of STEC and VTEC is commonly described by means of a so-called Single Layer Model (SLM). It is assumed, that all free electrons are concentrated in an infinitesimal thin shell above the Earth surface (Schaer, 1999) at an altitude (denoted as effective height) that is typically slightly above $hmF2$. Related to the SLM, a mapping function which defines the ratio

$$m = \frac{\text{STEC}}{\text{VTEC}} \quad (1.29)$$

as a conversion factor from STEC to VTEC is required. For instance, the Modified Single Layer Mapping (MSLM) function developed years ago at the Center for Orbit Determination Europe (CODE) (Hugentobler et al., 2008; Dach et al., 2012) is widely accepted and implemented in the Bernese software package⁷ (Dach et al., 2007). It approximates the Jet Propulsion Laboratory (JPL) Extended Slab Model (ESM) and is defined as

$$m(z) = \frac{1}{\cos z'} = \frac{1}{\sqrt{1 - \sin^2 z'}} = \left(1 - \left(\frac{R_e}{R_e + H} \sin \alpha z \right)^2 \right)^{-1/2} \quad (1.30)$$

with $\alpha = 0.9782$, single-layer height $H = 506.7 \text{ km}$ and mean Earth radius $R_e = 6,371 \text{ km}$. The mapping thus varies only with the zenith angle z at the receiver position and directed towards the transmitter. The intersection of a signal path connecting a transmitter and receiver (approximated

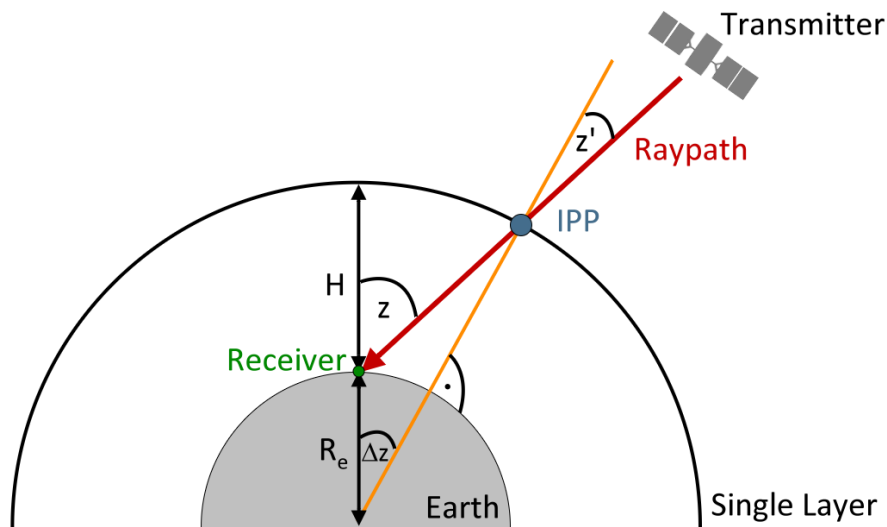


Figure 1.9: Scheme for a Single Layer Model.

as the LOS) with the single layer is denoted as Ionospheric Pierce Point (IPP). The corresponding geometrical disposition is shown by Fig. 1.9.

⁷<http://www.bernese.unibe.ch/>

$\Delta z = z - z'$ identifies the angle between the vectors connecting receiver and IPP with the geocenter. Based on this geometrical setup, VTEC can finally be computed from

$$\text{VTEC}(\varphi_{\text{IPP}}, \lambda_{\text{IPP}}, t) = m(z)^{-1} \text{STEC}(x_r, x^s, t) \quad (1.31)$$

and refers to the latitude φ and longitude λ of the IPP.

Summarizing this paragraph, we find a general mathematical relation between the Chapman parameters, electron density and TEC as

$$N_{e_{\max}}, h_{\max}, H \xrightarrow{\substack{\uparrow \\ \text{Chapman} \\ \text{function}}} } N_e \xrightarrow{\substack{\uparrow \\ \text{Integration} \\ \text{along ray path}}} \text{STEC} \xrightarrow{\substack{\uparrow \\ \text{Mapping}}} \text{VTEC}. \quad (1.32)$$

A key purpose of most geodetic ionosphere models refers to the spatio-temporal description of one or more of these parameters as derived for instance from space observation techniques. Therefore, appropriate parametrization functions to obtain a continuous regional or global representation are required and shall be introduced next in Chapter 2.

2 Parametrization

The initial state for empirical space-geodetic modeling can often be described by the situation, that there is a set of signals as scattered points on a spherelike surface S or subregion $S' \subset S$ which shall be approximated by a function s on the surface S or S' . Such a scenario can be representative for various planetary applications in geodesy or geophysics (gravity and magnetic field, wind models), oceanography (ocean currents) and meteorology (temperature variations) but also in the industrial (aircraft- and automotive design) or the medical (modeling organ shapes) sector. Selected modeling approaches for establishing an appropriate function basis are presented in the following. An overview of the selected methods is provided by Fig. 2.1.

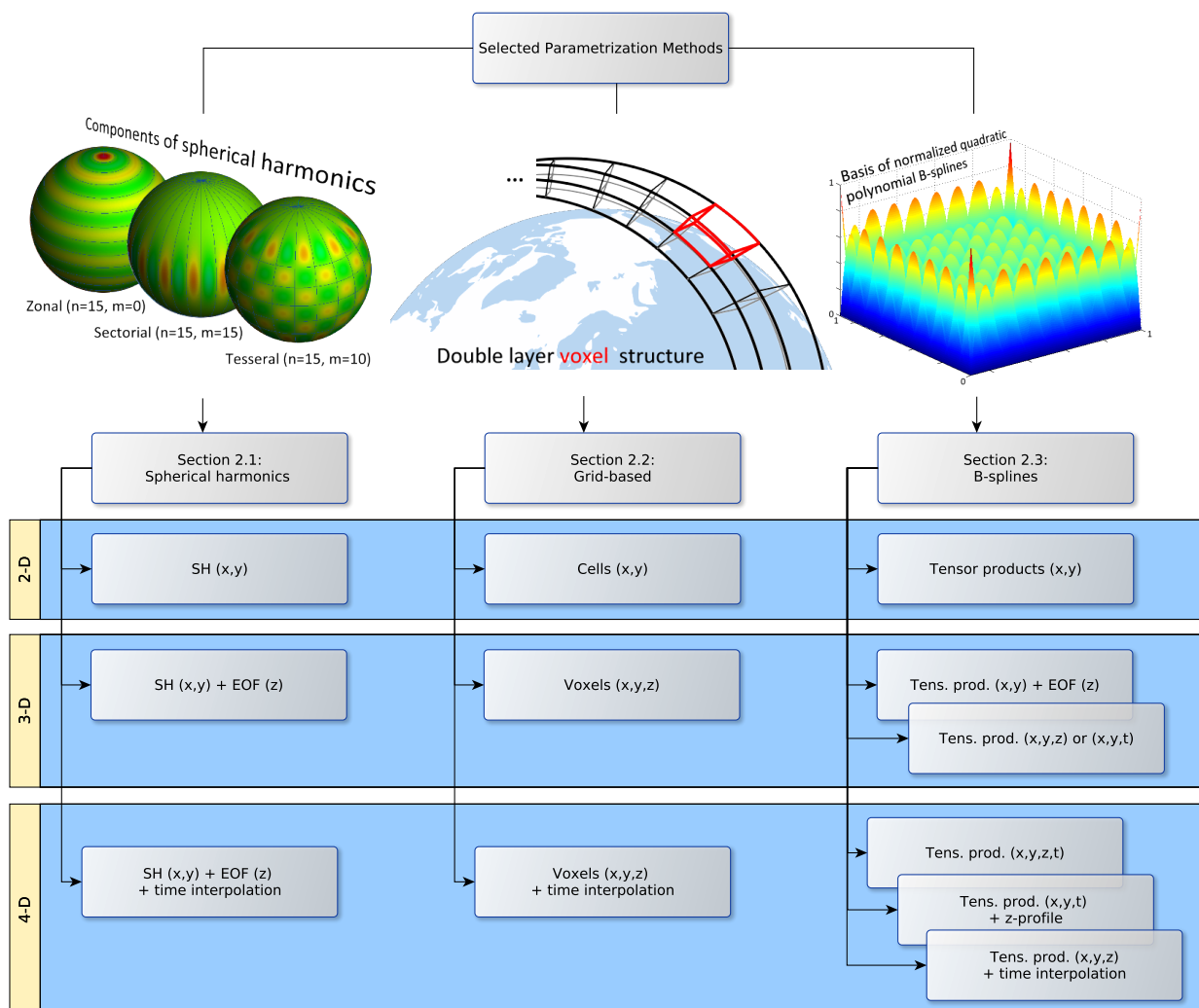


Figure 2.1: Overview of selected parametrization methods that will be discussed in Chapter 2. Three schematic representations are included which show different components (zonal, sectorial, tesseral) of spherical harmonics (left), the structure of a grid-based voxel band above Earth (middle) and a basis of normalized quadratic polynomial B-splines (right). The Spherical Harmonics (SH) structure is plotted with a visualization tool provided by International Centre for Global Earth Models (ICGEM) at <http://icgem.gfz-potsdam.de/ICGEM/>, the voxel structure is adapted from the 2-D representation in Hernández-Pajares et al. (1999).

2.1 Spherical harmonics

A classical and probably the most frequently used approach for representing data on a sphere is the consideration of a spherical harmonics series expansion with global support.

2.1.1 Classical 2-D model

The representation of an observation y_i defined in a 2-D space, for instance the VTEC related to latitude φ (geographic or geomagnetic reference system) and longitude λ (Earth-fixed or Sun-fixed reference system), based on a spherical harmonic expansion is given by

$$y_i + e_i = \text{VTEC}(\varphi, \lambda, t_i) = \sum_{n=0}^N \sum_{m=0}^n \bar{P}_{n,m}(\sin \varphi) \left(\bar{C}_{n,m}(t_i) \cos(m \cdot \lambda) + \bar{S}_{n,m}(t_i) \sin(m \cdot \lambda) \right). \quad (2.1)$$

Here, $\bar{P}_{n,m}$ is the normalized associated Legendre function of degree n and order m . The temporal dependency is not modeled here, i.e., the representation refers to a specific moment in time t_i . N defines the maximum degree and order of the expansion while $\bar{C}_{n,m}$ and $\bar{S}_{n,m}$ are the SH coefficients. In this formulation, the zero-degree SH coefficients \bar{C}_{00} can be interpreted as the global mean $\text{avg}(y)$. The total number of unknowns in the SH representation is defined by the number of coefficients $\bar{C}_{n,m}$ and $\bar{S}_{n,m}$, namely

$$U = (n_{\max} + 1)^2. \quad (2.2)$$

Furthermore, the spatial model resolution in latitude $\Delta\varphi$ and longitude $\Delta\lambda$ is controlled by n_{\max} in the sense that

$$\Delta\lambda = \Delta\varphi = 2\pi/n_{\max}. \quad (2.3)$$

The temporal modeling by the SH representation can, for instance, be carried out by the application of piece-wise linear functions as described in Schaer (1999).

Under consideration of a single layer model with a mapping function $m(z)$ as introduced in Section 1.6, Eq. (2.1) can be reformulated as

$$\begin{aligned} y_i + e_i &= \text{STEC}(x_r, x^s, t_i) \\ &= m(z) \sum_{n=0}^N \sum_{m=0}^n \bar{P}_{n,m}(\sin \varphi) \left(\bar{C}_{n,m}(t_i) \cos(m \cdot \lambda) + \bar{S}_{n,m}(t_i) \sin(m \cdot \lambda) \right). \end{aligned} \quad (2.4)$$

It is most likely, that the use of a SH expansion is the most prevalent approach for global ionosphere modeling. However, from the modeling point of view, the feature of global support brings at the same time some disadvantages:

1. The global support implies, that each spherical harmonic function differs from zero almost everywhere throughout the sphere.
2. According to the previous point, the spherical harmonic coefficients depend on all the data distributed around the entire sphere. With the Earth as the modeling surface it can be concluded that a single data point influences all coefficients and thus the representation on the entire globe. Therefore, all globally distributed coefficients must be taken into account to obtain the information at a specific position.
3. The definition of spherical harmonics in the global domain presupposes a rather uniform distribution of data with same accuracy.

2.1.2 Spherical harmonics and empirical orthogonal functions

The spherical harmonic model, introduced in Section 2.1, is appropriate to describe the global data distribution in latitude and longitude, e.g., to represent the spatial VTEC distribution. The model is not able to characterize the vertical data distribution, but can be expanded to a 3-D representation. This extended model may be denoted as tomographic model that requires the availability of measurements crossing the 3-D region of interest, here in the exterior space of our sphere. The model benefits significantly from a geometrically suitable data distribution with different viewing angles. To obtain discrete data points within the 3-D space, measurement inversion methods are applied. One realization of this concept is the application of SH together with Empirical Orthogonal Functions (EOFs) to model the horizontal and vertical distribution. This concept is based on a Principal Component Analysis (PCA) where EOFs can, e.g., be computed from a priori model data by means of an eigenvector and eigenvalue decomposition of the data covariance matrix (Schmidt, 2007). The methodology to derive SH and EOFs for a 4-D representation of the ionosphere has been published by Howe and Runciman (1998), Gao and Liu (2002) and Al-Fanek (2013) and shall not be further discussed in this work.

Based on the data points y_i , e.g., STEC measurements as introduced in Section 1.6, the observation equation of the tomographic model reads

$$y_i + e_i = \text{STEC}(x_r, x^s, t_i) = \int_{x_r}^{x^s} N_e(\varphi, \lambda, h, t_i) ds \quad (2.5)$$

where the N_e is integrated along the LOS from the satellite transmitter at x^s to the receiver x_r .

Table 2.1: Overview of the spherical harmonics parametrization for ionosphere modeling.

Spherical harmonics (Section 2.1)	
Static 2-D representation: $\text{VTEC}(\varphi, \lambda, t_i) =$	
SH	$\sum_{n=0}^N \sum_{m=0}^n \bar{P}_{n,m}(\sin \varphi) (\bar{C}_{n,m}(t_i) \cos(m \cdot \lambda) + \bar{S}_{n,m}(t_i) \sin(m \cdot \lambda))$
Static 3-D representation: $N_e(\varphi, \lambda, h, t_i) =$	
SH + EOF	$\sum_{k=1}^K \sum_{n=0}^N \sum_{m=0}^n \bar{P}_{n,m}(\sin \varphi) (\bar{C}_{n,m}(t_i) \cos(m \cdot \lambda) + \bar{S}_{n,m}(t_i) \sin(m \cdot \lambda)) \cdot c_k(t_i) \text{EOF}_k(h)$
<ul style="list-style-type: none"> • Classical and most widespread approach • Global support • Continuous and orthogonal • Resolution is controlled by SH degree n and order m • Unknowns are the SH coefficients which are sensitive for data of the entire globe • Not recommended in case of heterogeneous data density or quality • Data gaps can be bridged by prior information or adaption of the model resolution 	

The 3-D electron density distribution can now be constructed from

$$N_e(\varphi, \lambda, h, t_i) = \sum_{k=1}^K \sum_{n=0}^N \sum_{m=0}^n \bar{P}_{n,m}(\sin \varphi) \left(\bar{C}_{n,m}(t_i) \cos(m \cdot \lambda) + \bar{S}_{n,m}(t_i) \sin(m \cdot \lambda) \right) \cdot c_k(t_i) \text{ EOF}_k(h) \quad (2.6)$$

where Eq. (2.1) has been extended by EOFs and the corresponding series coefficients c . The observation equation for the STEC follows then as

$$y_i + e_i = \text{STEC}(x_r, x^s, t_i) = \int_{x_r}^{x^s} \sum_{k=1}^K \sum_{n=0}^N \sum_{m=0}^n \bar{P}_{n,m}(\sin \varphi) \left(\bar{C}_{n,m}(t_i) \cos(m \cdot \lambda) + \bar{S}_{n,m}(t_i) \sin(m \cdot \lambda) \right) \cdot c_k(t_i) \text{ EOF}_k(h) ds. \quad (2.7)$$

This tomographic model is one possible extension of the classical SH expansion introduced in Section 2.1 for modeling the global electron density distribution but naturally still lacks by the previously provided disadvantages.

As a summary of Section 2.1, Table 2.1 provides an overview of the spherical harmonic parametrization. Different representations for N_e and TEC with respect to global and regional modeling, the usage for representing data in different dimensions as well as strengths and drawbacks of the approaches are pointed out.

2.2 Grid modeling

Another representation can be achieved by decomposing the modeling surface by a grid with predefined cell width. Typically, 2-D cells or 3-D voxels are taken into account for grid based modeling.

2.2.1 Cells

For 2-D grid models, each data point y_i is located within a specific grid cell and may be described by its surrounding four grid points as

$$y_i + e_i = \sum_{k=0}^4 G_k \cdot w_k \quad (2.8)$$

where G_k is the value at a specific grid point k that is weighted by a function w_k . Equation (2.8) allows for the deployment of an equation system and solution for the grid point information.

In case of representing the ionosphere at a specific epoch t_i by means of a single layer as introduced in Section 1.6, we can apply this method to decompose the ionospheric shell into a grid of arbitrary resolution. Each IPP is then located within a specific 2-D grid cell. By means of a mapping function, every STEC observable can thus be expressed by

$$y_i + e_i = \text{STEC}(x_r, x^s, t_i) = m(z) \sum_{k=0}^4 \text{VTEC}(\varphi, \lambda, t_i)_k \cdot w_k \quad (2.9)$$

under consideration of the VTEC values at the surrounding four grid points. The model resolution depends on the cell size which should be adapted to the distribution of observations. This approach has been described for instance by Gao and Liu (2002) and is applied in the modeling strategy at the department Energy, Mines and Resources (EMR) of Natural Resources Canada (NRCAN).

2.2.2 Voxel model

As an extension of the previously described 2-D cell approach, Hernández-Pajares et al. (1998, 1999) and García-Fernández (2004) presented a tomographic ionospheric modeling technique depending on 3-D voxels, where the electron density is assumed to be constant within a specific voxel. Again, the voxel size defines the model resolution depending not only on the data distribution but also on the measurement sensitivity with respect to N_e , i.e., coarse vertical and high horizontal resolutions in case of terrestrial GNSS. Details about GNSS observables and the signal processing for ionospheric research will be provided in Chapter 3. At this point, it shall be already noted that Hernández-Pajares et al. (1999) proposed the use of phase observations only to account for the susceptibility of code pseudoranges for multipath, in particular in low elevations. Low elevation data carry important information about the vertical ionospheric structure though. Phase observations are less susceptible for multipath but are ambiguous. Therefore, differences to a reference observation STEC_R belonging to the same data arc are taken into account to eliminate the ambiguity term and model ΔSTEC . The observation equation yields

$$y_i + e_i = \Delta\text{STEC}(x_r, x^s, t_i) = \int_{x_r}^{x^s} N_e(\varphi, \lambda, h, t_0 + \Delta t_i) ds - \underbrace{\int_{x_r}^{x^s} N_e(\varphi, \lambda, h, t_0) ds}_{\text{STEC}_R} \quad (2.10)$$

where the reference observation is defined at t_0 and Δt_i refers to a subsequent epoch, i.e., the elapsed time since t_0 . Following Hernández-Pajares et al. (1998), the time shift is chosen relatively small (e.g. 720 s) to account for the assumption that the electron density does not change in the selected reference frame, preferably sun-fixed, but at the same time provides enough geometrical ray variation to solve for the electron densities. Introducing a voxel representation for Eq. (2.10) leads to the discrete approximation

$$y_i + e_i = \Delta\text{STEC}(x_r, x^s, t_i) = \sum_{V_\varphi} \sum_{V_\lambda} \sum_{V_h} [N_e(\varphi, \lambda, h, t_i) (\Delta s_{t_0 + \Delta t_i} - \Delta s_{t_0})]_{V_\varphi, V_\lambda, V_h} \cdot \quad (2.11)$$

Here, $V_\varphi, V_\lambda, V_h$ are indices to identify voxels with respect to geographical or geomagnetic latitude φ , earth- or sun-fixed longitude λ and height h . Δs defines the path length within a specific voxel.

This model approach with a double-layer voxel composition separated at 60 km, 740 km and 1,420 km is applied for the generation of Global Ionosphere Maps (GIMs) at the Universitat Politècnica de Catalunya (UPC) based on a Kalman Filter with random walk process. The consideration of two layers can be interpreted as a strategy to account for a variable, data driven effective height where the model in this setup primarily aims a 3-D description of VTEC. However, the concept generally allows for modeling also the N_e by increasing the voxel number and resolution.

Based on Eq. (2.10) and taking into account that an initial solution is required to level the relative data, the N_e can be determined for each voxel and finally VTEC can be modeled as

$$\begin{aligned} y_i + e_i &= \text{VTEC}(\varphi, \lambda, t_i) \\ &= m(z)^{-1} \text{STEC}(x_r, x^s, t_i) = m(z)^{-1} \sum_{V_\varphi} \sum_{V_\lambda} \sum_{V_h} [N_e(\varphi, \lambda, h, t_i)]_{V_\varphi, V_\lambda, V_h} \end{aligned} \quad (2.12)$$

by means of a mapping function $m(z)$.

Both the cell and voxel approaches score with a relatively simple implementation for the benefit of less computational burden but imply the drawback of possible discontinuities at the cell boundaries. As a summary of Section 2.2, Table 2.2 provides an overview of model equations and characteristics for the cell and voxel parametrization.

Table 2.2: Overview of the cell and voxel parametrization for ionosphere modeling.

Cells and Voxels (Section 2.2)	
Static 2-D representation: $VTEC(\varphi, \lambda, t_i) =$	
Cell	$\sum_{k=0}^4 VTEC(\varphi, \lambda, t_i)_k \cdot w_k$
Static 3-D representation: $STEC(x_r, x^s, t_i) =$	
Voxel	$\sum_{V_\varphi} \sum_{V_\lambda} \sum_{V_h} [N_e(\varphi, \lambda, h, t_i)]_{V_\varphi, V_\lambda, V_h}$
<ul style="list-style-type: none"> • Global and regional support due to localizing voxels • Resolution is controlled by the cell/voxel size • Unknown values are related to the voxels itself or to the corner points of each cell/voxel • Heterogeneous data distribution and data gaps can be handled efficiently, e.g., by introducing background information or adapting the cellsize • Voxel-layer composition as an effective way to consider vertical data structures • Possible discontinuities at the cell/voxel boundaries • Assumption of data constancy in a voxel or interpolation of corner point values • The voxel model can be characterized as a relatively simple but nevertheless efficient approach 	

2.3 B-splines

An alternative model has been adapted in this work. The main requirements of this approach are primarily defined by the disadvantages of the previously presented parametrization techniques:

1. The base functions shall only be different to zero in a local environment on the sphere to allow for the modification of present data or incorporation of new data into the model without causing a global effect.
2. The representation shall be continuous within the modeling region.

For this purpose, polynomial and trigonometric B-splines with local support have been selected as appropriate base function candidates for representing the ionospheric information derived from space-geodetic observations in the model space. In contrast to SH, which are defined on a sphere and related to latitude and longitude via the associated Legendre polynomials, B-spline base functions are commonly defined in the Euclidean space \mathbb{R}^2 and therefore need to be constrained in case of global modeling. However, since space observations for ionosphere modeling are typically available with heterogeneous distribution and quality, the feature of compact support clearly outweighs the issue of applying global constraints. Furthermore, the selected B-spline functions allow to generate a Multi-Resolution Representation (MRR) as shown by Lyche and Schumaker (2000) and Schmidt (2007) where the target parameters such as VTEC or N_e can be decomposed by successive low-pass filtering into a certain number of detail signals. Non-significant information can then be neglected facilitate data compression. A detailed comparison between the spherical harmonic and B-splines for modeling VTEC has for instance been performed by Schmidt et al. (2011) and shall not be the repeated here. For

the mathematical background of B-splines, it shall be referenced to Schumaker (1981), Schumaker and Traas (1990), Lyche and Schumaker (2000), Jekeli (2005) and Zeilhofer (2008).

The following sections focus on the use of B-splines for regional ionosphere modeling in accordance to P-I: Limberger et al. (2013) and P-II: Limberger et al. (2014) but besides, guidance for an application in the global domain is provided. In a first step, B-spline functions are introduced from a generally valid perspective before adapting the basis for ionosphere modeling in the following Section 2.4.

For the case of a 1-D representation, the approximation function $s(x)$ with $x \in [x_{\min}, x_{\max}]$ is now expressed as

$$s(x) = \sum_{k=1}^K d_k^J \Psi_k^J(x). \quad (2.13)$$

Ψ identifies a linearly independent set of 1-D scaling functions Ψ_1, \dots, Ψ_K of level J and d_k are associated series coefficients.

Two different kinds of B-spline base functions are introduced in the following Sections, namely the normalized quadratic polynomial B-splines and normalized periodic trigonometric B-splines. Both offer excellent features for ionosphere modeling in the regional and global domain.

2.3.1 Normalized quadratic polynomial B-splines

For regional modeling applications, we intend to consider normalized quadratic polynomial B-splines denoted by $\phi_k^{J_\phi}(x) = N_{k,m}^{J_\phi}(x)$ as 1-D basis functions for representing the signal within a bounded interval. $N_{k,m}^{J_\phi}$ are usual normalized B-splines of order m with

$$\sum_{k=1}^{K_\phi} N_{k,m}^{J_\phi}(x) = 1 \text{ where } x \in [0, 1] \quad (2.14)$$

where $J_\phi \in \mathbb{N}_0$ defines the B-spline resolution level and $k \in \{1, 2, \dots, K_\phi\}$ identifies a specific spline function. k is sometimes denoted as shift, e.g., in Schmidt et al. (2015). The model resolution is controlled by the level, i.e., the higher J_ϕ , the finer the signal structures that can be resolved. The total number of B-splines is computed from $K_\phi = 2^{J_\phi} + m - 1$. The basis is deployed by an increasing sequence of $K_\phi + m$ so-called knot points $v_k^{J_\phi} \in \{v_1^{J_\phi}, v_2^{J_\phi}, \dots, v_{K_\phi+m}^{J_\phi}\}$ where, at the boundaries, multiple knots may be linked to a specific coordinate point. The knot interval $v_{k+1}^{J_\phi} - v_k^{J_\phi}$ must not mandatory be constant. The basis for normalized quadratic polynomial B-splines is defined recursively (Schumaker and Traas, 1990; Stollnitz et al., 1995) with

$$N_{k,1}^{J_\phi}(x) = \begin{cases} 1 & v_k^{J_\phi} \leq x < v_{k+1}^{J_\phi}, \quad k = m, \dots, K_\phi \\ 0 & \text{otherwise} \end{cases} \quad (2.15)$$

$$N_{k,m}^{J_\phi}(x) = \frac{x - v_k^{J_\phi}}{v_{k+m-1}^{J_\phi} - v_k^{J_\phi}} N_{k,m-1}^{J_\phi}(x) + \frac{v_{k+m}^{J_\phi} - x}{v_{k+m}^{J_\phi} - v_{k+1}^{J_\phi}} N_{k+1,m-1}^{J_\phi}(x), \quad m \geq 2. \quad (2.16)$$

A uniform knot sequence is established as

$$\underbrace{0 = v_1^{J_\phi} = \dots = v_m^{J_\phi}}_{\text{Boundary multiplicity}} < \underbrace{v_{m+1}^{J_\phi} < \dots < v_{K_\phi}^{J_\phi}}_{\text{Internal sequence}} < \underbrace{v_{K_\phi+1}^{J_\phi} = \dots = v_{K_\phi+m}^{J_\phi} = 1}_{\text{Boundary multiplicity}} \quad (2.17)$$

where $K_\phi - m + 2$ distinct knots are taken into account. At the boundaries there is a multiplicity of m knots each that allow for the endpoint-interpolation. The knot distance $v_{k+1}^{J_\phi} - v_k^{J_\phi}$ yields consequently $(K_\phi - m + 1)^{-1}$ on the unit interval.

Normalized quadratic polynomial B-spline functions $\phi_k^{J_\phi}(x) = N_{k,3}^{J_\phi}(x)$ of order $m = 3$ have been considered by P-I: Limberger et al. (2013); P-II: Limberger et al. (2014) and P-V: Liang et al. (2014); P-VI: Liang et al. (2015). In case of $m = 3$, $K_\phi = 2^{J_\phi} + 2$ normalized B-spline functions anchored at $K_\phi + 3$ knot points are distributed on the unit interval.

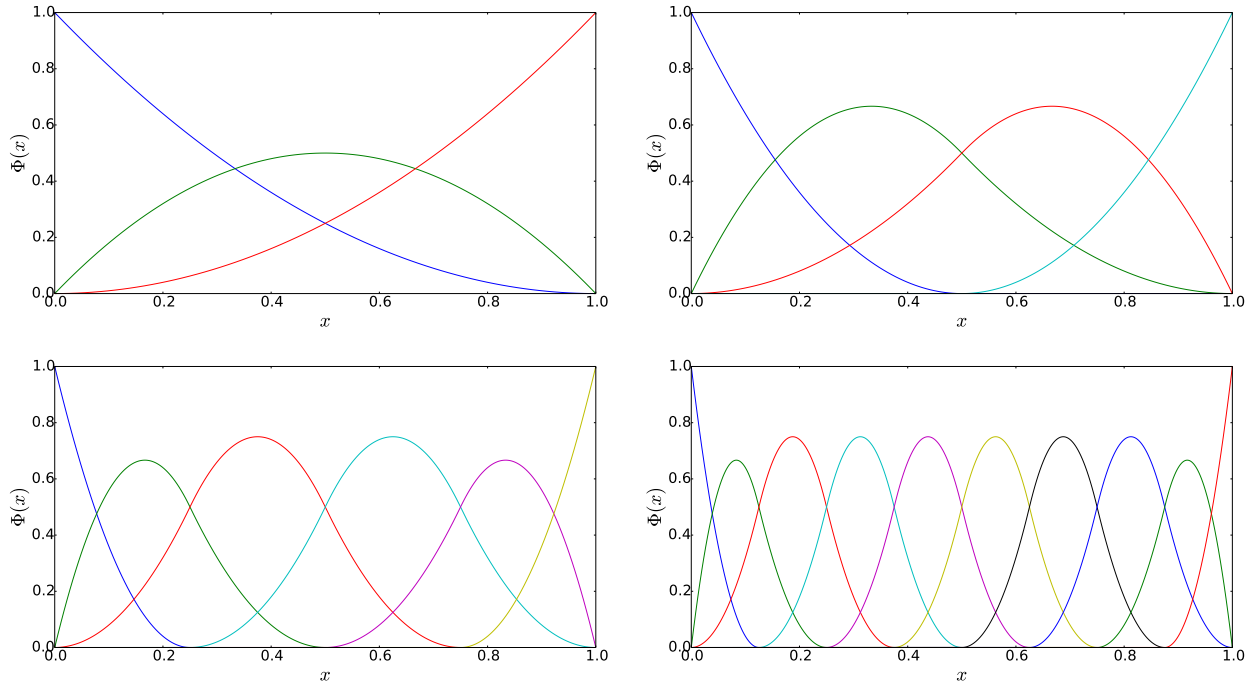


Figure 2.2: Normalized quadratic polynomial B-splines with different levels $J_\phi = 0, 1, 2, 3$ and accordingly different number of B-splines $K_\phi^J = 3, 4, 6, 10$.

Figure 2.2 provides examples of polynomial B-spline functions of $m = 3$ regarding different levels $J_\phi = 0, 1, 2, 3$. The number of splines varies with J_ϕ where the subplots are related to $J_\phi = 0 \rightarrow K_\phi^0 = 3$ (top-left), $J_\phi = 1 \rightarrow K_\phi^1 = 4$ (top-right), $J_\phi = 2 \rightarrow K_\phi^2 = 6$ (bottom-left) and $J_\phi = 3 \rightarrow K_\phi^3 = 10$ (bottom-right). Special features of polynomial B-splines are in particular given by the

- endpoint-interpolation, i.e., adaptation of the splines to a bounded interval, and
- localization, i.e., compact support only within a restricted interval.

It can be clearly seen from the plots, that the first two and last splines are different with respect to the interior spline functions contributing to the endpoint-interpolation in the bounded interval. Each spline differs from zero only within a certain interval according to the level J_ϕ . A comparison of all four figures demonstrates how the B-spline support interval changes with J_ϕ , i.e., the higher the level the smaller the influenced area and the sharper the peaks. For further details about the support interval, it shall be referenced to Mößmer (2009) and Schmidt et al. (2011).

From Fig. 2.2 it becomes visible that always three adjacent splines are overlapping, i.e., a single data point contributes to the determination of exactly three B-spline coefficients. The model resolution is defined by J_ϕ should be adapted to the input data density to overcome data gaps. For the case of a homogeneous data sampling, Schmidt et al. (2011) derived the relation

$$\Delta \text{si} = \frac{\text{si}_{\max} - \text{si}_{\min}}{K_\phi - 1} \quad (2.18)$$

with the sampling si on the interval $[si_{\min}, si_{\max}]$. This formulation can be transformed to

$$J_\phi < \log_2 \left(\frac{si_{\max} - si_{\min}}{\Delta si} - m + 2 \right) \quad (2.19)$$

under consideration of $K_\phi = 2^{J_\phi} + m - 1$. The level needs to be adapted to the observations density to minimize the data gaps and avoid the loss of significant information. For $m = 3$, the level can thus be derived from

$$J_\phi < \log_2 \left(\frac{si_{\max} - si_{\min} - \Delta si}{\Delta si} \right). \quad (2.20)$$

2.3.2 Normalized periodic trigonometric B-splines

As a second base function type, normalized periodic trigonometric B-splines $T_{k,m}^{J_T}(x)$ of odd order m shall be introduced (Schumaker, 1981; Schumaker and Traas, 1990). Trigonometric B-splines with resolution level $J_T \in \mathbb{N}_0$ are defined on a circle in the closed interval $[0, 2\pi]$ and have no knot multiplicity but comply with the constraint of $s(0) = s(2\pi)$. The number of spline functions is computed from $K_T = 3 \cdot 2^{J_T} + m - 1$ where altogether $K'_T = K_T - m + 1 = 3 \cdot 2^{J_T}$ complete splines are distributed on the basis interval, meaning that the interrupted boundary splines are completed by the corresponding opposing sub-spline to enable periodicity. The basis definition follows from

$$T_{k,1}^{J_T}(x) = \begin{cases} 1 & v_k^{J_T} \leq x < v_{k+1}^{J_T} \\ 0 & \text{otherwise} \end{cases}, \quad k = 1, \dots, K_T \quad (2.21)$$

$$T_{k,m}^{J_T}(x) = \frac{\sin\left(\frac{x - v_k^{J_T}}{2}\right)}{\sin\left(\frac{v_{k+m-1}^{J_T} - v_k^{J_T}}{2}\right)} \cdot T_{k,m-1}^{J_T}(x) + \frac{\sin\left(\frac{v_{k+m}^{J_T} - x}{2}\right)}{\sin\left(\frac{v_{k+m}^{J_T} - v_{k+1}^{J_T}}{2}\right)} \cdot T_{k+1,m-1}^{J_T}(x), \quad m \geq 2 \quad (2.22)$$

with the non-decreasing sequence of distinct knots

$$0 = v_m^{J_T} < v_{m+1}^{J_T} < \dots < v_{K_T}^{J_T} < v_{K_T+1}^{J_T} = 2\pi. \quad (2.23)$$

Additional constraints on the knot placement

$$\begin{aligned} v_i^{J_T} &= v_{K'_T+i}^{J_T} - 2\pi \\ v_{K'_T+m+i}^{J_T} &= v_{m+i}^{J_T} + 2\pi \end{aligned} \quad \text{for } i = 1, \dots, m-1 \quad (2.24)$$

are introduced for Eq. (2.23) to force periodicity.

Choosing the same order $m = 3$ as for the polynomial B-splines the number of trigonometric spline functions $T_{k,3}^{J_T}$ can be determined as $K_T = 3 \cdot 2^{J_T} + 2$. Periodic trigonometric B-splines are particularly suitable for global modeling applications due to special properties in the

- definition on the $[0, 2\pi]$ interval with "wrapping-around" condition and
- localization, i.e., compact support only within a restricted interval as also provided by the polynomial B-splines.

A set of trigonometric B-splines of $m = 3$ for different levels $J_T = 0 \rightarrow K_T = 5$ (top-left), $J_T = 1 \rightarrow K_T = 8$ (top-right), $J_T = 2 \rightarrow K_T = 14$ (bottom-left) and $J_T = 3 \rightarrow K_T = 26$ (bottom-right) is provided by Fig. 2.3. Similarities to the polynomial B-spline functions can be found in the local support and the overlapping of three splines in each point along x . The main difference is related

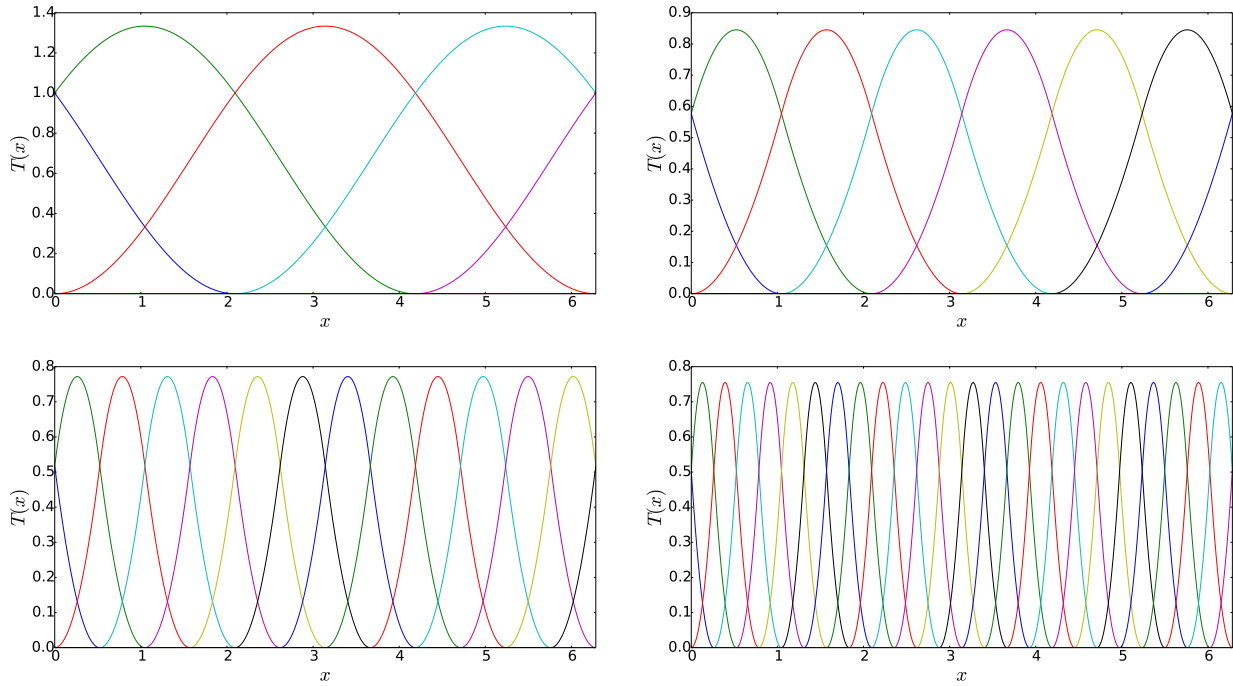


Figure 2.3: Trigonometric B-splines with different levels $J_T = 0, 1, 2, 3$ and accordingly different number of B-splines $K_T = 5, 8, 14, 26$.

to the boundary splines where, in contrast to the endpoint-interpolation of polynomial splines, the periodicity is visible. Although different colors have been chosen for each function, it can be clearly seen that every sub-spline at one boundary is continued at the opposite boundary. For instance in the top-left illustration for $J_T = 0$, the magenta spline on the right can be connected with the green spline on the left without any discontinuation.

Similarly to Eq. (2.19), the relation of the data density to the B-spline level can be derived from

$$J_T < \log_2 \left(\frac{si_{\max} - si_{\min} + \Delta si}{3 \Delta si} \right) \quad (2.25)$$

by substituting K'_T as the number of complete splines into Eq. (2.18).

2.3.3 B-spline tensor products

S_Ω shall identify a unit sphere as

$$R_{S_\Omega} := \{(\varphi, \lambda) : -\frac{\pi}{2} \leq \varphi \leq \frac{\pi}{2} \text{ and } 0 \leq \lambda \leq 2\pi\} \quad (2.26)$$

with polar coordinates φ and λ in an angular system mapped on a rectangle R_{S_Ω} in a 2-D space \mathbb{R}^2 . The representation of a subsurface of S'_Ω defined within $\varphi \in [\varphi_{\min}, \varphi_{\max}]$ and $\lambda \in [\lambda_{\min}, \lambda_{\max}]$ in the rectangular domain can be obtained with

$$R_{S'_\Omega} := \{(\varphi, \lambda) : \varphi_{\min} \leq \varphi \leq \varphi_{\max} \text{ and } \lambda_{\min} \leq \lambda \leq \lambda_{\max}\}. \quad (2.27)$$

In order to represent multidimensional information on the rectangular modeling surfaces R_{S_Ω} or $R_{S'_\Omega}$ as introduced by Eq. (2.26) and Eq. (2.27), tensor products of B-spline base functions shall be applied in an orthogonal coordinate system. Details about tensor product techniques for surface modeling can, e.g., be found in Dierckx (1984), Gmelig Meyling and Pfluger (1987) or Zeilhofer (2008).

For a 2-D case representation, the approximation function s can be constructed from

$$s(x_1, x_2) = \sum_{k_1=1}^{K_1} \sum_{k_2=1}^{K_2} d_{k_1, k_2}^{J_1, J_2} \Psi_{1_{k_1}}^{J_1}(x_1) \Psi_{2_{k_2}}^{J_2}(x_2). \quad (2.28)$$

Here, tensor products of two linearly independent 1-D B-spline functions $\Psi_{1_{k_1}}^{J_1}$ and $\Psi_{2_{k_2}}^{J_2}$ have been introduced together with the corresponding series coefficients d . It should be noticed that Ψ_1 and Ψ_2 may differ but can also be of the same type.

So far, the B-spline levels and numbers were expressed in relation to the B-spline type (J_T, K_T, J_ϕ, K_ϕ). From now on, the identification will be based on indices ($J_1, K_1, J_2, K_2, \dots$) to distinguish between B-splines of the same kind in the tensor product notation. Furthermore, the order will permanently be considered as $m = 3$.

At first, polynomial B-splines as defined in Section 2.3.1 are chosen on both, the x_1 and x_2 interval, with

$$x_1 \rightarrow \Psi_1 = \phi_{k_1}^2 \quad \text{and} \quad x_2 \rightarrow \Psi_2 = \phi_{k_2}^3 \quad (2.29)$$

for the levels $J_1 = 2$ and $J_2 = 3$. The corresponding basis is depicted in Fig. 2.4. Both plots show

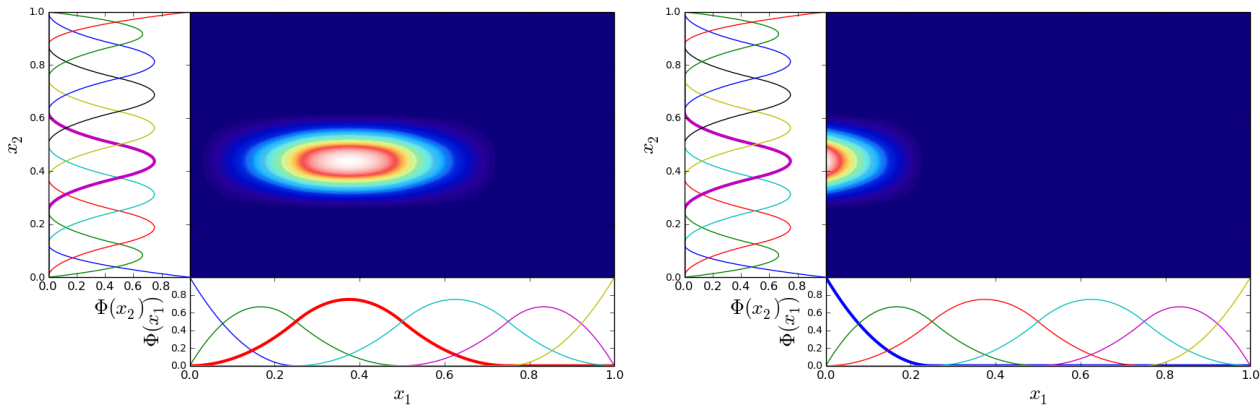


Figure 2.4: Polynomial B-splines $\phi_{k_1}^2(x_1)$ and $\phi_{k_2}^3(x_2)$ of order $m = 3$ with different levels $J_1 = 2$ and $J_2 = 3$. $\phi_3^2(x_1)$ (left), $\phi_1^2(x_1)$ (right) and $\phi_5^3(x_2)$ are emphasized to show the support area.

the support area spanned by the tensor product of two polynomial B-splines which are emphasized by thick lines. As can be clearly seen from the left illustration of Fig. 2.4, an ellipse shaped support area is spanned by $\phi_3^2(x_1)$ (red) and $\phi_5^3(x_2)$ (magenta). Choosing the same level in both directions naturally would result in a circle shaped area. The subfigure on the right, exemplarily depicts the support area at the boundary for $\phi_1^2(x_1)$ (blue) and $\phi_5^3(x_2)$ (magenta) constraint by endpoint-interpolation on the x_1 axis.

In a next step, the 2-D basis is generated from the combination of polynomial and trigonometric B-spline functions. The basis is defined as

$$x_1 \rightarrow \Psi_1 = T_{k_1}^2 \quad \text{and} \quad x_2 \rightarrow \Psi_2 = \phi_{k_2}^3 \quad (2.30)$$

for different levels $J_1 = 2$ and $J_2 = 3$ with endpoint-interpolation in the x_2 and continuity in the x_1 direction. Figure 2.5 shows the support area for $T_3^2(x_1)$ and $\phi_5^3(x_2)$ in this spline constellation. The right subplot additionally shows the 3-D shape of a 2-D tensor B-spline product basis related to the emphasized splines of the left graph.

For each additional dimension a new set of basis functions can be incorporated, i.e., the B-spline expansion can easily be adapted to higher or lower dimensions by means of the tensor product technique.

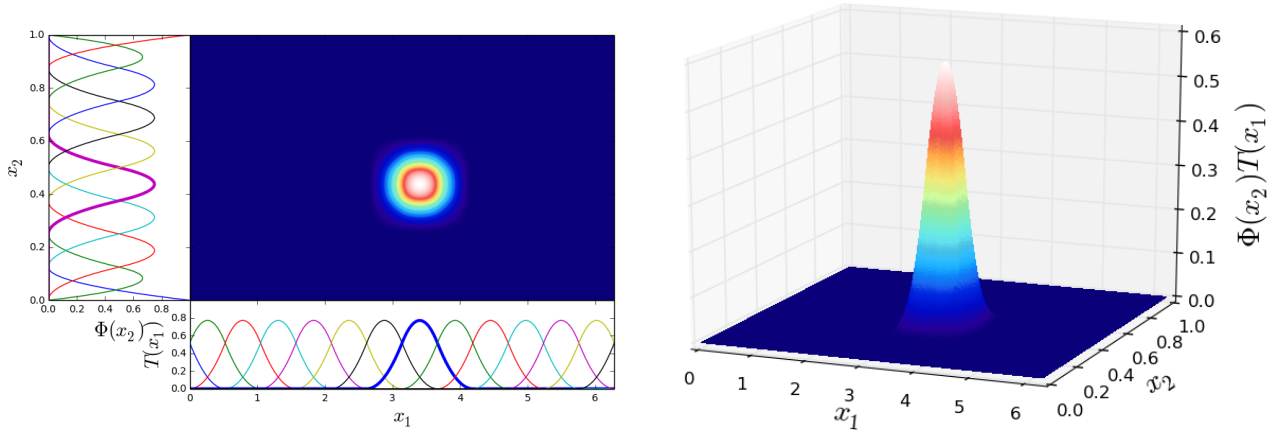


Figure 2.5: Combination of trigonometric B-splines with level $J_1 = 2$ and polynomial B-splines with level $J_2 = 3$. A specific spline combination identified by $k_1 = 5$ and $k_2 = 8$ has been highlighted and plotted in the center part of the left subplot. Accordingly, a 3-D representation of the tensor product is given on the right hand side.

A 3-D modeling basis is accordingly defined as

$$s(x_1, x_2, x_3) = \sum_{k_1=1}^{K_1} \sum_{k_2=1}^{K_2} \sum_{k_3=1}^{K_3} d_{k_1, k_2, k_3}^{J_1, J_2, J_3} \Psi_{1k_1}^{J_1}(x_1) \Psi_{2k_2}^{J_2}(x_2) \Psi_{3k_3}^{J_3}(x_3). \quad (2.31)$$

Further details about B-spline expansions for multidimensional modeling are, for instance, published by Schmidt et al. (2015). These generally derived formulations for basis representations with normalized quadratic polynomial B-splines and normalized periodic trigonometric B-splines, individual and combined in tensor products, will now be adapted for ionosphere modeling.

2.4 Ionosphere modeling with B-splines

Different function characteristics are crucial to select a suitable set of base functions. It has been shown that polynomial B-splines are rather convenient for regional modeling applications due to the endpoint-interpolation while trigonometric B-splines are preferable for global modeling. A more concrete formulation for ionosphere modeling is provided and tensor products of 1-D B-spline scaling functions for the multidimensional representation in the spatio-temporal domain are introduced.

2.4.1 Total electron content

Spatial TEC model

This section deals with the spatial modeling of TEC data in the regional and global domain without an explicit modeling of the temporal ionospheric behavior.

The regional 2-D representation of VTEC by means of polynomial B-splines can be expressed as

$$y_i + e_i = \text{VTEC}(\varphi, \lambda, t_i)_R = \sum_{k_1=1}^{K_1} \sum_{k_2=1}^{K_2} d_{k_1, k_2}^{J_1, J_2}(t_i) \phi_{k_1}^{J_1}(\varphi) \phi_{k_2}^{J_2}(\lambda) \quad (2.32)$$

where φ indicates the geographic or geomagnetic latitude and λ the geographic or sun-fixed longitude. A subscript R has been introduced to indicate the regional model space. Equation (2.32) refers to a static representation of the epoch t_i . A common approach for the generation of snapshots is the consideration of measurements within a certain time interval around t_i where the observation impact can, for instance, be controlled by step functions or piecewise interpolations.

A regional B-spline basis consisting of normalized quadratic polynomial B-splines, given for instance on a study area with $\varphi = [-30^\circ, +60^\circ]$ and $\lambda = [250^\circ, 340^\circ]$ is shown in Fig. 2.6. The levels are chosen as $J_1 = J_2 = 3$ leading to $K_1 = K_2 = 10$ splines in each direction. The figure provides two different perspectives where the representation on the left shows the basis structure from a slant viewpoint and the representation on the right is given in a bird view perspective. As can be seen in Fig. 2.6, tensor products of uniform B-splines result in a pattern of 3-dimensional knobs which are enhanced along the area boundary due to the endpoint interpolating functions.

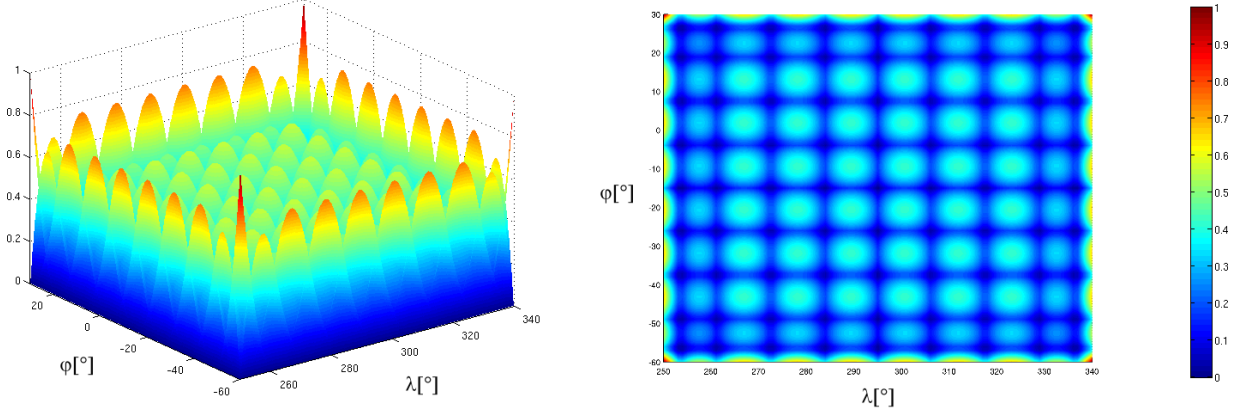


Figure 2.6: Normalized quadratic polynomial B-spline basis spanned to an exemplary study area of $\varphi = [-30^\circ, +60^\circ]$ and $\lambda = [250^\circ, 340^\circ]$ with B-spline levels $J_1 = J_2 = 3$. Two perspectives are given by a slant viewpoint (left) and bird view (right).

Now, the B-spline basis shall be applied for global modeling where quadratic trigonometric B-splines with periodicity are selected. The VTEC representation in the global domain is then formulated with

$$y_i + e_i = \text{VTEC}(\varphi, \lambda, t_i)_G = \sum_{k_1=1}^{K_1} \sum_{k_2=1}^{K_2} d_{k_1, k_2}^{J_1, J_2}(t_i) \phi_{k_1}^{J_1}(\varphi) T_{k_2}^{J_2}(\lambda) \quad (2.33)$$

where the longitude axis covers now $\lambda = [0^\circ, 360^\circ]$. In this case, the periodicity of trigonometric splines for a closed definition on the entire sphere is exploited. According to the indication of Eq. (2.32) for the regional application, a subscript G has been introduced here for the affiliation to global modeling. For the latitude axis, the polynomial B-splines are kept in relation to the fixed interval of $\varphi = [-90^\circ, 90^\circ]$.

Spatio-temporal TEC model

As an extension of Eq. (2.32) for considering the time dependency, an additional set of polynomial B-spline functions to model the temporal behavior of the TEC within a fixed interval can be introduced as

$$\text{VTEC}(\varphi, \lambda, t)_R = \sum_{k_1=1}^{K_1} \sum_{k_2=1}^{K_2} \sum_{k_3=1}^{K_3} d_{k_1, k_2, k_3}^{J_1, J_2, J_3} \phi_{k_1}^{J_1}(\varphi) \phi_{k_2}^{J_2}(\lambda) \phi_{k_3}^{J_3}(t). \quad (2.34)$$

The corresponding formulation for global modeling can once more be obtained by introducing trigonometric B-splines leading to

$$\text{VTEC}(\varphi, \lambda, t)_G = \sum_{k_1=1}^{K_1} \sum_{k_2=1}^{K_2} \sum_{k_3=1}^{K_3} d_{k_1, k_2, k_3}^{J_1, J_2, J_3} \phi_{k_1}^{J_1}(\varphi) T_{k_2}^{J_2}(\lambda) \phi_{k_3}^{J_3}(t). \quad (2.35)$$

2.4.2 Electron density

Spatial electron density model

The modeling of the spatial N_e distribution comes along with the consideration of an additional dimension, specifically the height h . One obvious solution might be the introduction of additional B-splines for modeling the vertical N_e distribution. For this purpose, Eq. (2.32) and Eq. (2.33) are enhanced to

$$N_e(\varphi, \lambda, h, t_i)_R = \sum_{k_1=1}^{K_1} \sum_{k_2=1}^{K_2} \sum_{k_3=1}^{K_3} d_{k_1, k_2, k_3}^{J_1, J_2, J_3}(t_i) \phi_{k_1}^{J_1}(\varphi) \phi_{k_2}^{J_2}(\lambda) \phi_{k_3}^{J_3}(h) \quad (2.36)$$

and

$$N_e(\varphi, \lambda, h, t_i)_G = \sum_{k_1=1}^{K_1} \sum_{k_2=1}^{K_2} \sum_{k_3=1}^{K_3} d_{k_1, k_2}^{J_1, J_2}(t_i) \phi_{k_1}^{J_1}(\varphi) T_{k_2}^{J_2}(\lambda) \phi_{k_3}^{J_3}(h). \quad (2.37)$$

For modeling the height dependency, polynomial B-splines have been considered here with respect to a bounded interval $h \in [h_{\min}, h_{\max}]$.

An alternative modeling approach can be found in the use of EOFs, similar to Eq. (2.6) where EOFs have been used in combination with spherical harmonics. A formulation for this method yields

$$N_e(\varphi, \lambda, h, t_i)_R = \sum_{k_1=1}^{K_1} \sum_{k_2=1}^{K_2} \sum_{k_3=1}^{K_3} d_{k_1, k_2, k_3}^{J_1, J_2, J_3}(t_i) \phi_{k_1}^{J_1}(\varphi) \phi_{k_2}^{J_2}(\lambda) \text{EOF}_{k_3}(h) \quad (2.38)$$

for the regional and

$$N_e(\varphi, \lambda, h, t_i)_G = \sum_{k_1=1}^{K_1} \sum_{k_2=1}^{K_2} \sum_{k_3=1}^{K_3} d_{k_1, k_2, k_3}^{J_1, J_2, J_3}(t_i) \phi_{k_1}^{J_1}(\varphi) T_{k_2}^{J_2}(\lambda) \text{EOF}_{k_3}(h) \quad (2.39)$$

for the global domain. The temporal N_e variation is not modeled and the Eqs. (2.36) - (2.39) describe static representations of the spatial N_e distribution at the epoch t_i . However, the time domain may be indirectly considered by interpolation between successive epochs.

Spatio-temporal electron density model

The highest dimension that shall be described here is related to a 4-D representation in latitude, longitude, height and time fully supported by B-splines. For this case, the electron density model is given through

$$N_e(\varphi, \lambda, h, t)_R = \sum_{k_1=1}^{K_1} \sum_{k_2=1}^{K_2} \sum_{k_3=1}^{K_3} \sum_{k_4=1}^{K_4} d_{k_1, k_2, k_3, k_4}^{J_1, J_2, J_3, J_4} \phi_{k_1}^{J_1}(\varphi) \phi_{k_2}^{J_2}(\lambda) \phi_{k_3}^{J_3}(h) \phi_{k_4}^{J_4}(t) \quad (2.40)$$

and

$$N_e(\varphi, \lambda, h, t)_G = \sum_{k_1=1}^{K_1} \sum_{k_2=1}^{K_2} \sum_{k_3=1}^{K_3} \sum_{k_4=1}^{K_4} d_{k_1, k_2, k_3, k_4}^{J_1, J_2, J_3, J_4} \phi_{k_1}^{J_1}(\varphi) T_{k_2}^{J_2}(\lambda) \phi_{k_3}^{J_3}(h) \phi_{k_4}^{J_4}(t) \quad (2.41)$$

referring to the regional and global representation, respectively. This modeling basis enables the representation in all four dimensions. It consists of four one-dimensional sets of B-spline functions and is, just as the other parametrization methods introduced so far, purely based on mathematics. With respect to the ionospheric target quantities as presented in Section 1.6, it would however be reasonable to consider physically driven processes, patterns and structures by means of appropriate physical-based expressions incorporated in the model equations. One possible method refers to the consideration of a physically-based profile function for the vertical N_e structure that shall be described in the following.

Table 2.3: Overview of the B-spline parametrization for ionosphere modeling.

B-spline parametrization (Section 2.3)	
Blue and red colored functions define specific regional and global components	
Static 2-D representation: $VTEC(\varphi, \lambda, t_i) =$	
B-splines	$\sum_{k_1=1}^{K_1} \sum_{k_2=1}^{K_2} d_{k_1, k_2}^{J_1, J_2}(t_i) \phi_{k_1}^{J_1}(\varphi) \phi_{k_2}^{J_2}(\lambda) T_{k_2}^{J_2}(\lambda)$
3-D: $VTEC(\varphi, \lambda, t) =$	
B-splines	$\sum_{k_1=1}^{K_1} \sum_{k_2=1}^{K_2} \sum_{k_3=1}^{K_3} d_{k_1, k_2, k_3}^{J_1, J_2, J_3} \phi_{k_1}^{J_1}(\varphi) \phi_{k_2}^{J_2}(\lambda) T_{k_2}^{J_2}(\lambda) \phi_{k_3}^{J_3}(t)$
Static 3-D representation: $N_e(\varphi, \lambda, h, t_i) =$	
B-splines	$\sum_{k_1=1}^{K_1} \sum_{k_2=1}^{K_2} \sum_{k_3=1}^{K_3} d_{k_1, k_2, k_3}^{J_1, J_2, J_3}(t_i) \phi_{k_1}^{J_1}(\varphi) \phi_{k_2}^{J_2}(\lambda) T_{k_2}^{J_2}(\lambda) \phi_{k_3}^{J_3}(h)$
empirical orthogonal functions:	
B-splines + EOFs	$\sum_{k_1=1}^{K_1} \sum_{k_2=1}^{K_2} \sum_{k_3=1}^{K_3} d_{k_1, k_2, k_3}^{J_1, J_2, J_3} \phi_{k_1}^{J_1}(\varphi) \phi_{k_2}^{J_2}(\lambda) T_{k_2}^{J_2}(\lambda) EOF_{k_3}(h)$
4-D: $N_e(\varphi, \lambda, h, t) =$	
B-splines	$\sum_{k_1=1}^{K_1} \sum_{k_2=1}^{K_2} \sum_{k_3=1}^{K_3} \sum_{k_4=1}^{K_4} d_{k_1, k_2, k_3, k_4}^{J_1, J_2, J_3, J_4} \phi_{k_1}^{J_1}(\varphi) \phi_{k_2}^{J_2}(\lambda) T_{k_2}^{J_2}(\lambda) \phi_{k_3}^{J_3}(h) \phi_{k_4}^{J_4}(t)$
empirical orthogonal functions:	
B-splines + EOFs	$\sum_{k_1=1}^{K_1} \sum_{k_2=1}^{K_2} \sum_{k_3=1}^{K_3} \sum_{k_4=1}^{K_4} d_{k_1, k_2, k_3, k_4}^{J_1, J_2, J_3, J_4} \phi_{k_1}^{J_1}(\varphi) \phi_{k_2}^{J_2}(\lambda) T_{k_2}^{J_2}(\lambda) EOF_{k_3}(h) \phi_{k_4}^{J_4}(t)$
with a vertical profile function:	
B-splines + Profile	$\vartheta(h, \kappa(\varphi, \lambda, t)_R \kappa(\varphi, \lambda, t)_G)$
<ul style="list-style-type: none"> • Global and regional supported by different B-spline characteristics • Continuity on the globe by using periodic trigonometric B-splines with "wrapping-around" property • For global modeling, additional pole and meridian constraints are required • The model dimension can easily be adapted by means of B-spline tensor products • Heterogeneous data distribution and data gaps can be handled efficiently due to the localization of B-splines • Resolution is controlled by the B-spline level J • Unknowns are related to the unknown series coefficients • Heterogeneous data distribution and data gaps can be bridged by prior information or adaption of the B-spline levels 	

Spatio-temporal electron density model with external height profile

The idea of combining mathematical B-spline base functions with an external N_e height profile has been realized for the studies presented in P-I: Limberger et al. (2013) and P-II: Limberger et al. (2014) where an α -Chapman layer, as introduced in Section 1.5, has been taken into account. It is certainly possible to introduce any other profile function and therefore we introduce this vertical function at present in a general notation with $\vartheta(h)$. $\vartheta(h)$ will naturally be driven by a set of model parameters κ_h with $h \in \{1, \dots, H\}$ contained in the vector κ that depends at least on the position coordinates, e.g., λ and φ , and the time t . A possible formulation for the spatio-temporal N_e distribution can then be obtained by

$$N_e(\varphi, \lambda, h, t) = \vartheta(h, \kappa(\varphi, \lambda, t)). \quad (2.42)$$

Taking into account that we intend to apply a B-spline basis to model each κ_h , the electron density representations in the regional and global domain are defined as

$$N_e(\varphi, \lambda, h, t)_R = \vartheta(h, \kappa(\varphi, \lambda, t)_R) \quad (2.43)$$

$$\text{with } \kappa_h(\lambda, \varphi, t)_R = \sum_{k_1=1}^{K_1} \sum_{k_2=1}^{K_2} \sum_{k_3=1}^{K_3} d_{k_1, k_2, k_3}^{J_1, J_2, J_3} \phi_{k_1}^{J_1}(\varphi) \phi_{k_2}^{J_2}(\lambda) \phi_{k_3}^{J_3}(t) \quad (2.44)$$

and

$$N_e(\varphi, \lambda, h, t)_G = \vartheta(h, \kappa(\varphi, \lambda, t)_G) \quad (2.45)$$

$$\text{with } \kappa_h(\lambda, \varphi, t)_G = \sum_{k_1=1}^{K_1} \sum_{k_2=1}^{K_2} \sum_{k_3=1}^{K_3} d_{k_1, k_2, k_3}^{J_1, J_2, J_3} \phi_{k_1}^{J_1}(\varphi) T_{k_2}^{J_2}(\lambda) \phi_{k_3}^{J_3}(t). \quad (2.46)$$

As a summary of Section 2.3, Table 2.3 provides an overview of the parametrization with B-spline tensor products. Different representations for N_e and TEC with respect to global and regional modeling, the usage for representing data in different dimensions as well as strengths and drawbacks of the approach are pointed out.

Global constraints

In contrast to spherical harmonics (Section 2.1), that are defined on a sphere by associated Legendre polynomials, B-spline functions are basically specified in the 2-D space, i.e., on a plane. For regional modeling with polynomial B-splines there is generally no need for constraints. Quite the contrary, the requirement for the base functions related to the definition on a finite interval is already fulfilled by the endpoint-interpolating feature. However, for the combined application of polynomial and trigonometric B-splines in terms of global modeling, we claim continuity throughout the globe with five conditions (Schumaker and Traas, 1990; Jekeli, 2005):

1. $s(\varphi, 0) = s(\varphi, 2\pi)$ for $-\pi/2 \leq \varphi \leq \pi/2$ (Meridian boundary equality),
2. $s(-\pi/2, \lambda) = s_s$ and $s(\pi/2, \lambda) = s_n, \forall \lambda$ (Pole value equality),
3. $s_\lambda(\varphi, 0) = s_\lambda(\varphi, 2\pi)$ for $-\pi/2 \leq \varphi \leq \pi/2$ (Meridian continuity),
4. $s_\lambda(-\pi/2, 0) = A_s \cos \lambda + B_s \sin \lambda$ for $0 \leq \lambda \leq 2\pi$ (South pole continuity),
5. $s_\lambda(\pi/2, 0) = A_n \cos \lambda + B_n \sin \lambda$ for $0 \leq \lambda \leq 2\pi$ (North pole continuity).

s_s and s_n are values for the south and north pole, respectively, A_s, B_s and A_n, B_n are constants, and s_λ is the partial derivative of s for the longitude. These considerations can be merged in a constraint matrix \mathbf{C} to be considered in a linear equation system as

$$\mathbf{C}d = \mathbf{0} \quad (2.47)$$

alongside with the normal equations. For further details it shall be referenced to Schumaker and Traas (1990) and Schmidt et al. (2011). The focus of this work is, however, on the regional representation and the estimation of B-spline coefficients as part of an adjustment system that will be explained in Chapter 5.

3 Satellite techniques for observing the total electron content

Inconsistencies of the ionosphere conditions affect the speed and curvature of microwave signal propagation and are known as the main error source in various application fields such as the space situation awareness, satellite-based communication, navigation and positioning or astronautics. An overview of error sources and an approximation of the corresponding impact on a pseudorange to a single satellite is provided by Table 3.1 as published by Novatel⁸.

Table 3.1: Error sources of GNSS signals.

Source	Pseudorange error
Satellite clocks	± 2 m
Orbit	± 2.5 m
Ionosphere	± 5 m
Troposphere	± 0.5 m
Receiver noise	± 0.3 m
Multipath	± 1 m

The determination of signal delays induced by the ionosphere from one or even multiple sounding techniques allows to obtain information about the ionospheric structure and its spatio-temporal variation. Such information can be used to correct measurements for the signal delay but also to monitor space weather processes and gain knowledge about physical phenomena. The following sections provide an overview of different space observation techniques, in particular GNSS, DORIS and RA, including the relevant preprocessing steps to derive the TEC. It shall be noted, that the deployment of a database from measurements only is often insufficient to develop a comprehensive description of relevant ionospheric target quantities, e.g., in the presence of data gaps. In this case, additional information based on external ionosphere models may be assimilated for the completion of the data basis. A selection of appropriate models will be introduced in Section 5.1.

3.1 Global Navigation Satellite Systems

GNSS are generally defined by three segments, specifically the space segment consisting of the GNSS satellites, the ground segment defined by terrestrial control sites and finally the user segment that comprises the GNSS receivers that are contributing with observations related to Positioning, Velocity and Timing (PVT).

The original and primary purpose for the deployment of a GNSS is related to applications in the scope of Positioning, Navigation and Timing (PNT). Extensive descriptions about the theory of GNSS signal processing for static and kinematic positioning can, e.g., be found in Hofmann-Wellenhof et al. (2008) or Xu (2010) and shall not be discussed here. However, the derivation of ionospheric information from

⁸GNSS error sources: <http://www.novatel.com/an-introduction-to-gnss/chapter-2-basic-gnss-concepts/step-4-computation>

GNSS measurements is of high relevance for this work and therefore, an overview about the presently active GNSS constellations is given in the following.

The GNSS are presently consisting of the four constellations

- Navigation Satellite Timing and Ranging Global Positioning System (NAVSTAR-GPS)
- Globalnaya Navigatsionnaya Sputnikovaya Sistema (GLONASS)
- Galileo⁹
- BeiDou¹⁰

providing continuously high frequent and globally distributed microwave signals on different frequencies linked between transmitting GNSS satellites and terrestrial receiver stations. A brief overview of the above mentioned constellations will be given in the following.

GPS

The Global Positioning System (GPS) is operational and fully deployed since decades and can be considered as the most important system with respect to data coverage and reliability. It has been designed for military and civilian purposes and is operated by the United States of America (USA).

Constellation specifications

The GPS constellation employs currently 31 satellites¹¹ of different block-types: IIA (5 operational), IIR (12 operational), IIR-M (7 operational), IIF (7 operational) which are located on one of six circular orbits in 20,200 km altitude above the Earth. The orbital planes are inclined with an angle of approximately 55° and with ascending nodes separated by 60° in argument of longitude. To guarantee a global visibility of at least four GPS satellites from any point on Earth, the core GPS constellation for Full Operational Capability (FOC) is designed with 24 unequally distributed spacecraft slots. A scheme of the GPS constellation is depicted in Fig. 3.1. The number of satellites has been expanded to increase the performance and maintain the global coverage in case of satellite service operations or satellite decommissioning. All GPS satellites are equipped with cesium and rubidium clocks. The nominal orbit period is 11 hours, 58 minutes and 2 seconds.

The GPS system uses the World Geodetic System 84 (WGS-84) for spatial referencing in an Earth-centered Earth-fixed (ECEF) frame. WGS-84 has been developed by the US Department of Defense (DoD), used by GPS since 1997 and received several updates during the years. In general, the International Terrestrial Reference System (ITRS) and its International Terrestrial Reference Frame (ITRF) realizations are identical to WGS-84 at one meter level. Newer versions even coincide with the ITRF at the centimeter level. However, there are no official transformation parameters (<http://itrf.ensg.ign.fr>). Further information about the WGS-84 reference ellipsoid can be found in the technical report of the U.S. National Imagery and Mapping Agency (2000) or Wong et al. (2012).

For the time reference, GPS Time (GPST) is considered as a continuous time scale starting from 5 January 1980 at 24:00:00 UTC and was at that time identical with the Coordinated Universal Time (UTC) while the difference between International Atomic Time (TAI) and UTC was 19 seconds. In order to align UTC with the Earth rotation, every one to six years a leap second has been added. This was however not considered in GPST. The International Earth Rotation Service (IERS) decided to introduce another leap second as of 30 June 2015 leading to a time difference of GPST = UTC + 17 s.

⁹In honor of the Italian physicist, mathematician, engineer, astronomer, and philosopher Galileo Galilei (15 February 1564 - 8 January 1642).

¹⁰Named after the Chinese expression for the Great Bear constellation.

¹¹GPS constellation status: <http://www.navcen.uscg.gov/?Do=constellationStatus>

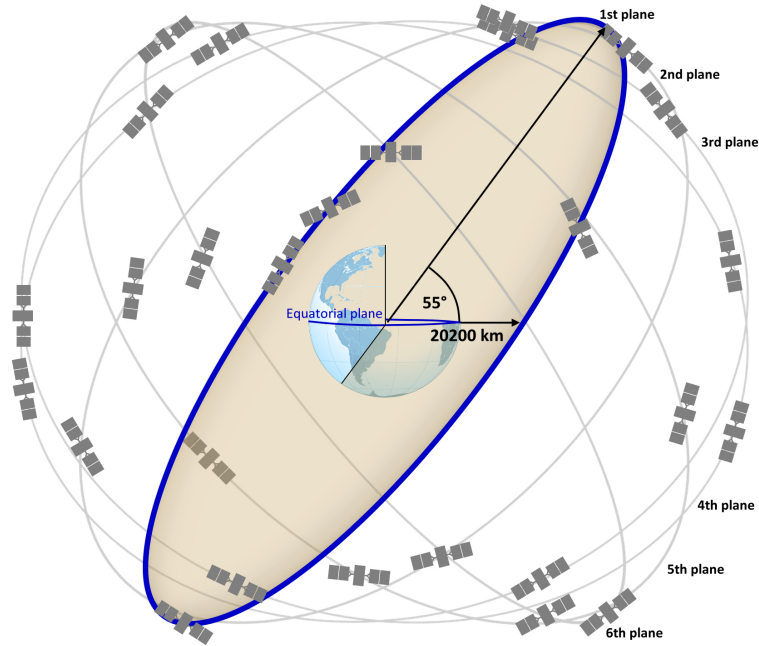


Figure 3.1: Extended GPS core constellation with 24+3 spacecraft slots as defined by the Standard Positioning Service (SPS) Performance Standard (graphical design inspired by <http://www.gps.gov>).

Signals

All GPS navigation signals are based on the fundamental frequency $f_0 = 10.23$ MHz, generated from on-board atomic clocks. Presently, three different signal links are transmitted by the modern spacecraft. The links are right-hand circularly polarized in the L-band and are denoted as L1, L2 and L5 with the corresponding frequencies f and wavelength λ

- L1: $f_1 = 154 \cdot f_0 = 1,575.42$ MHz; $\lambda_1 = c/f_1 = 0.190$ m
- L2: $f_2 = 120 \cdot f_0 = 1,227.60$ MHz; $\lambda_2 = c/f_2 = 0.244$ m
- L5: $f_5 = 115 \cdot f_0 = 1,176.45$ MHz; $\lambda_5 = c/f_5 = 0.255$ m

where a carrier specific factor is considered to derive f_1 , f_2 and f_5 from f_0 . c is the speed of light in vacuum with 299,792,458 m/s in SI units.

Each GPS carrier signal is modulated by Pseudorandom Noise (PRN) ranging codes and additional messages where the PRN sequence is used for the identification of GPS spacecrafts. For this work, modulated Coarse/Acquisition (C/A) and Precision (P) codes have been taken into account. The C/A code is modulated only on L1 carrier and to be used in terms of the SPS, e.g. for single-frequency positioning, whereas P code is modulated on both the L1 and L2 carriers defining the Precise Positioning Service (PPS) and reserved for military and authorized civilian users. In case of activated Anti-Spoofing (A/S), P code is encrypted to Y code.

The additional L5 link has been realized in modern block IIF and newer spacecrafts with respect to Safety-of-Life (SoL) applications. The signal is modulated with a new type and can be characterized by a high robustness against interferences and improved multipath resistance. For further information on the signal structure it shall be referred to Subirana et al. (2013).

In principal, the GPS observables are ranges which are derived from a code correlation technique in a so-called Delay Lock Loop (DLL) under consideration of the measured signal travel time or phase differences in the carrier signals resulting from a comparison of the emitted signal with a carrier replica, denoted as Phase Lock Loop (PLL), generated in the ground receiver. The signal travel duration can be derived from the difference of the broadcasted signal emission time as specified by the satellite atomic clock with the ground receiver clock, i.e., the calculated ranges are affected by

clock errors and therefore can be denoted as pseudoranges. Thus, it is generally distinguished by two types of observables: Code pseudoranges and carrier phase measurements.

The carrier phase can be obtained after removing the modulated PRN from the signal and performing additional filtering steps. There are various processing methods existing which can be used to derive code pseudoranges and reconstruct the unmodulated carrier wave, e.g., based on code correlation, cross correlation, squaring or z-tracking. These techniques can be classified into code-based and codeless methods where the first group assumes the knowledge of the P code and the latter ones are essentially required in case that A/S is activated.

Due to their availability on all satellites with modulated codes on both carrier signals, only the L1 and L2 links have been considered for the data processing in the framework of this thesis. Accordingly, the observable to be used in the data preprocessing are based on L1 and L2. Following the designation for GPS observables defined in the Receiver Independent Exchange Format (RINEX)¹² we can identify the observables as Φ_1 and Φ_2 for the carrier phases and C_1 , P_1 and P_2 for the modulated C/A and P code data. A summary of these GPS observations is given by Table 3.2.

Table 3.2: Overview on the legacy GPS signals

L1 link	
Φ_1	Carrier phase observation in cycle units [cyc] related to the L1 signal link with frequency $f_1 = 1,575.42$ MHz.
C_1	Pseudorange observation based on the C/A code modulated on the L1 carrier signal.
P_1	Pseudorange observation based on the precision code P modulated on the L1 carrier signal.

L2 link	
Φ_2	Carrier phase observation in cycle units [cyc] related to the L2 signal link with frequency $f_2 = 1,227.6$ MHz.
P_2	Pseudorange observation based on the precision code P modulated on the L2 carrier signal.

Ground receivers can be classified into different groups depending on the implemented technology and, according to the observables listed in Table 3.2, their signal tracking capability. Although the categorization of receiver types plays a secondary role for ionosphere modeling it is worth mentioning at this point, that the code measurements are affected by different instrumental signal delays but it is henceforth assumed that the code pseudoranges are consistently based on P_1 and P_2 . For ground receivers only capable of tracking C/A code, C_1 is therefore converted to P_1 . The required biases are for instance provided by CODE at <ftp://ftp.unibe.ch/aiub/CODE/P1C1.DCB>.

An important component of the GNSS user segment is the International GNSS Service (IGS) contributing to the civilian usage of GNSS data with different services based on a world-wide network of GNSS tracking stations. The data become available through the IGS ionosphere analysis centers, specifically by the

¹²RINEX-3 format description: <http://igsb.jpl.nasa.gov/igsb/data/format/rinex301.pdf>;
RINEX-2 format description: <http://igsb.jpl.nasa.gov/igsb/data/format/rinex211.txt>

- Center for Orbit Determination Europe (CODE),
- Universitat Politècnica de Catalunya (UPC),
- Jet Propulsion Laboratory (JPL) and
- European Space Agency (ESA)

and by the IGS itself via <http://www.igs.org> or <http://igs.cb.jpl.nasa.gov>. The data product and service specifications can be found on the IGS websites or, for instance, in Hernández-Pajares et al. (2009) or Dow et al. (2009) and shall not be discussed here. As an example, the IPPs related to 164 IGS receiver sites are depicted in Fig. 3.2 for specific hourly intervals 06:00-07:00 UT (top-left), 10:00-11:00 UT (top-right), 14:00-15:00 UT (bottom-left) and 18:00-19:00 UT (bottom-right) on 8 January 2015. The satellite orbits are based on the ultra-rapid (predicted-half) IGS product provided in Standard Product 3 Orbit Format (SP3)¹³. An elevation cut-off with 10° has been considered. The plots show an excellent data distribution over most parts of the continents, but gaps in the southern regions of the Pacific, Atlantic and North Africa. The IPP colors are related to signal delays expressed in TECU as induced by the ionosphere and instrumental hardware delays. The westwards-movement of the ionospheric anomaly along the geomagnetic equator is nevertheless visible from increased values.

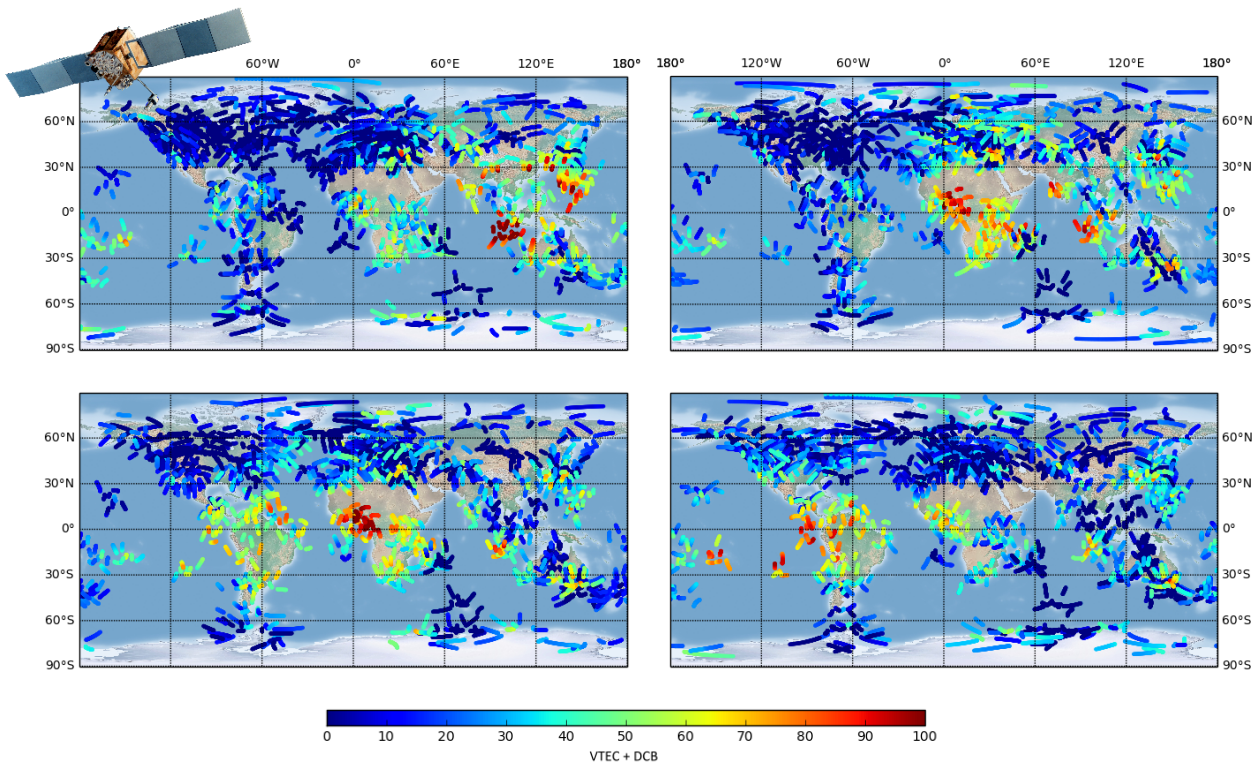


Figure 3.2: Distribution of ionospheric pierce points for specific hourly intervals 06:00-07:00 UT (top-left), 10:00-11:00 UT (top-right), 14:00-15:00 UT (bottom-left) and 18:00-19:00 UT (bottom-right) on 8 January 2015. The data is based on hourly GPS data and ultra-rapid orbits (predicted-half) provided by the IGS, available at <http://igs.cb.jpl.nasa.gov>. The IPP colors reflect signal delays induced by the ionosphere and instrumental hardware biases. A draft of a GPS-IIIF spacecraft is depicted in the top-left corner.

GLONASS

GLONASS is the Russian Federation's GNSS that is like GPS, owned and operated by the military. The system is operational since 1993 and follows concepts similar to GPS in terms of a differentiation in ground-, space- and user-segment as well as signal usage for positioning and navigation. The signal

¹³SP3 format description: http://igs.cb.jpl.nasa.gov/igs/data/format/sp3_docu.txt

transmission design, however, implies the usage of different frequencies for different satellites related to the constellation slot.

Constellation specifications

GLONASS has been designed for a nominal constellation with three orbital planes and 24 spacecraft slots. At an altitude of 19,100 km above Earth, the orbits are separated by 120° and got an inclination of 64.8° as shown in Fig. 3.3. The eight satellites on a specific plane are separated by a displacement of 45° in argument of latitude. Due to the slightly lower orbital altitude as compared to GPS, the nominal orbit period yields approximately 11 hours and 16 minutes.

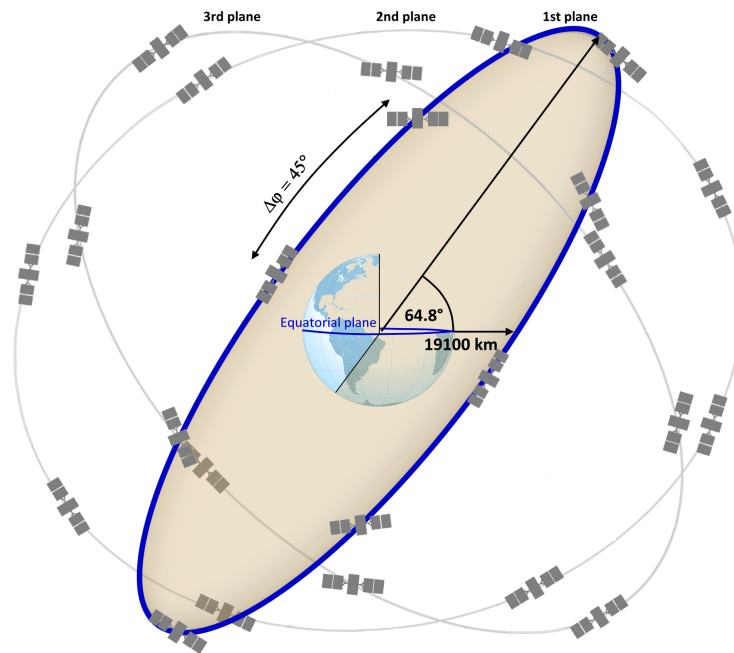


Figure 3.3: GLONASS core constellation with totally 24 spacecraft slots on three different orbital planes, i.e., eight satellites per orbit. The satellites on each plane are separated by 45° in argument of latitude.

Various generations of GLONASS satellites have been developed including Block-I, Block-IIa, Block-IIb and Block-IIv vehicles in the early years (first generation 1982-2001) and GLONASS-M or GLONASS-K spacecrafts in the modernization period (second generation since 2001). By 8 December 2011, GLONASS reached FOC.

As terrestrial reference system, GLONASS uses the PZ-90 ECEF frame. The reference ellipsoid definitions can be found in the Interface Control Document (ICD)¹⁴ of the current 2008 version. According to the GLONASS modernization plan, the PZ-90 reference system has been updated lately at 31 December 2013 to PZ-90.11 and coincides now with the latest ITRF by a maximum deviation of three centimeter in the x-component.

The time reference in GLONASS is related to GLONASS Time (GLNT) that matches to the Universal Time Coordinated of Russia UTC(SU) + 3 h better than one millisecond. Three hours is the difference between Moscow and the Greenwich Mean Time (GMT). Unlike GPST, GLNT contains leap seconds and is not continuous.

Signals

Similar to GPS, the GLONASS signals are transmitted on three signal links by modern GLONASS-K spacecrafts. The links will henceforth be identified by G1, G2 and G3 to distinguish them from

¹⁴GLONASS PZ-90 specifications: <http://www.spacecorp.ru/upload/iblock/1c4/cgs-aaixymyt205.120ENG20v202014.02.18w.pdf>

the GPS links. As for GPS, the G3 link has been designed for SoL applications and currently plays a minor role for ionosphere modeling. The carriers are right-hand circularly polarized in the L-band but differ with respect to a specific channel number $k \in \{-7, \dots, 6\}$ assigned to the individual satellites. Based on two fundamental frequencies with $f_{0,G1} = 1,602$ MHz and $f_{0,G2} = 1,246$ MHz, the channel dependent carrier frequencies for the G1 and G2 links can be derived as

- G1: $f_1(k) = f_{0,G1} + 9k/16$ MHz = 1,602 + 9k/16 MHz
- G2: $f_2(k) = f_{0,G2} + 7k/16$ MHz = 1,246 + 7k/16 MHz.

The GLONASS constellation status including information about the channel allocation is provided, e.g., by the GLONASS System Control Center (SCC)¹⁵ of the Russian Federal Space Agency. A summary of the allocation between slots and channels is given by Table 3.3

Table 3.3: GLONASS channel allocation to the spacecraft slots (28 November 2014).

Plane 1								
Slot	01	02	03	04	05	06	07	08
Channel	1	-4	5	6	1	-4	5	6

Plane 2								
Slot	09	10	11	12	13	14	15	16
Channel	-2	-7	0	-1	-2	-7	0	-1

Plane 3								
Slot	17	18	19	20	21	22	23	24
Channel	4	-3	3	2	4	-3	3	2

It shall be noticed, that the channel numbers show a systematic pattern with a repeating sequence for each plane where the channel number has been reduced to totally 12 channels. In this setup, satellites with same channel numbers are located on antipodal orbit positions to guarantee that a ground receiver never tracks signals transmitted on the same carrier frequency. Here, the slot 01 satellite orbits for instance antipodal to slot 05 on plane one.

Originally, the civil C/A code was modulated on the G1 link in terms of the SPS, but with the deployment of GLONASS-M satellites, C/A is now modulated on both the G1 and G2 link. Related to the PPS, military P code is modulated on G1 and G2 as for GPS. Since the GLONASS spacecrafts are identified by the carrier frequency, the PRN sequence of modulated codes is common for all satellites.

As an example, the distribution of GLONASS IPPs between 14:00 UT and 15:00 UT is depicted in Fig. 3.4 where an 10° elevation cut-off has been taken into account. Minor differences regarding a poorer coverage compared to GPS can be detected in South America, Greenland and some isolated regions due to fewer GLONASS tracking stations.

Galileo

The project Galileo yields an European global navigation satellite system inter-operable with GPS and GLONASS. Galileo is extended by the European Geostationary Navigation Overlay System (EGNOS) which serves as a Satellite Based Augmentation System (SBAS) for satellite navigation. The

¹⁵GLONASS channel allocation: <https://glonass-iac.ru/en/CUSGLONASS>

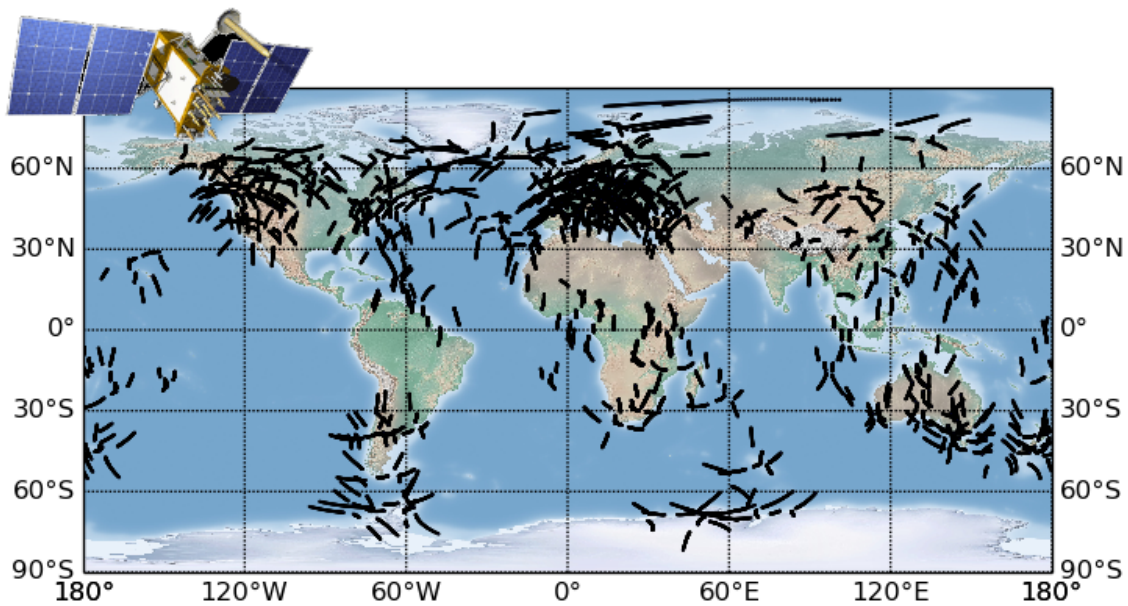


Figure 3.4: Distribution of ionospheric pierce points during an one-hour timeslice between 14:00 UT and 15:00 UT at 8 January 2015 related to tracked GLONASS passes. The data is based on hourly IGS data and ultra-rapid orbits (predicted-half) available at <http://igs.cb.jpl.nasa.gov>. A draft of a GLONASS-K spacecraft is depicted in the top-left corner.

definition phase, development and In Orbit Validation (IOV) are carried out by the European Space Agency (ESA) and co-funded by ESA and the European Union (EU). The FOC phase is funded by the EU and managed by the European Commission (EC).

Constellation Specifications

For FOC, the Galileo space segment requires a minimum of 24 satellites where it is planned to deploy totally 30 including 3 spares. Three orbital planes with inclination angles of 56° and ascending nodes separated by 120° in argument of longitude are designated with a nominal orbit altitude of 23,222 km. For each orbit, 10 slots with 9 operational satellites and one spare are planned.

The Galileo IOV phase started with the launch of the two experimental Galileo In-Orbit Validation Elements (GIOVE) on 28 December 2005 and 27 April 2008. With GIOVE-A and -B, the Galileo signal links have been secured in terms of reserving the frequencies at the International Telecommunications Union (ITU). GIOVE-A and -B are not intended to belong to the fully developed constellation. By now, six FOC satellites have already been placed into orbit (status at March 2015). Amongst other payload, each satellite is equipped with passive hydrogen maser and rubidium atomic frequency standard clocks¹⁶. The planned date to reach FOC has already been postponed numerous times and is currently scheduled for 2020.

A Galileo consortium, namely the Galileo Geodetic Reference Service Provider (GRSP)¹⁷, are responsible for the realization of a Galileo Terrestrial Reference Frame (GTRF) that shall include all Galileo Sensor Stations (GSS). Due to the fact, that GSS are not part of the IGS, selected IGS stations are included to align GTRF to the ITRF and at the same time improve the accuracy through additional data and network densification. The computation steps include a free network adjustment by means of all stations and afterwards an ITRF alignment using the selected IGS stations. Hence, the GTRF is planned as an independent realization of the ITRS including the requirement that the three-dimensional differences of the position compared to the most recent ITRF should not exceed three centimeter.

¹⁶Galileo status documents: http://www.esa.int/Our_Activities/Navigation/Galileo_satellites_status_update

¹⁷Galileo Geodetic Reference Service Provider: <http://www.ggsp.eu>

The Galileo time reference is defined as Galileo System Time (GST) and synchronized with TAI including a tolerance of 50 ns. GST is a continuous time scale starting from 22 August 1999 00:00 UTC.

Signals

Galileo is designed to offer a variety of services in the frequency bands E1 (1,575.42 MHz), E5a (1,176.45 MHz), E5b (1,207.14 MHz) and E6 (1,278.75 MHz) where it can be noticed that the E1 frequency is identical to the GPS L1-band. Ranging codes are modulated on the carrier signals by using the Binary Offset Carrier (BOC, applied for the E1 and E6-A modulation) or Binary Phase Shift Keying (BPSK, applied for the E6-B, E6-C, E5a and E5b modulation) technique. Four modulations serve as pilot (or secondary) channels, meaning that they are supporting the tracking of weak signals.

The meaning and definition of the different services with the corresponding signal support can be briefly summarized as

- **Open Service (OS):** Free of charge and intended to be used by civil users based on unencrypted, open signals. The single-frequency performance shall be slightly improved compared to GPS C/A due to the combined processing of GPS and Galileo signals. OS is supported by E1 (unencrypted E1-B and E1-C ranging codes) and also by the modulated E5a and E5b codes.
- **Public Regulated Service (PRS):** Intended to be used by security applications (police, military, etc.) where regulated access is obligatory. This service can be used with E1 (encrypted E1-A ranging code) and E6 (E6-A).
- **Commercial Service (CS):** This service is secured with a commercial encryption and supported by E1 (E1-A), E6 (E6-B and E6-C) and E5b frequency bands.
- **Search and Rescue (SaR):** Designed for emergency cases with signal forwarding to the Rescue Coordination Center. Additionally, the user in distress will be informed by Galileo through the SaR service that the location has been transmitted.

BeiDou

The Chinese BeiDou navigation satellite system consists of two constellations - the BeiDou Satellite Navigation Experimental System (BeiDou-1) and the BeiDou Satellite Navigation System (BeiDou-2 or Compass). BeiDou-1 is a test system in operation since 2000 with limited coverage and therefore mainly used by customers from China. BeiDou-2/Compass will serve as a GNSS and is currently under construction.

Constellation Specifications

It can be distinguished between three types of BeiDou satellites, namely the geostationary BeiDou-G, geosynchronous BeiDou-IGSO and Medium Earth Orbiter (MEO) BeiDou-M satellites. The space segment of BeiDou-2/Compass yields a constellation of 35 spacecrafts including 5 BeiDou-G securing the compatibility with BeiDou-1, 27 BeiDou-M and 3 BeiDou-IGSO satellites and offers the complete coverage of the globe. As for Galileo, the completion of BeiDou-2/Compass is planned for 2020.

BeiDou-2/Compass considers the China Geodetic Coordinate System 2000 (CGCS2000) referring to the ITRF 1997 at the epoch 2000. The maintenance of CGCS2000 is based on GNSS Continuously Operating Reference Stations (CORS) as a part of Chinas geodetic infrastructure. The ellipsoidal parameters of CGCS2000 are defined in the BeiDou ICD¹⁸ of December 2013.

¹⁸BeiDou Interface Control Document: http://www2.unb.ca/gge/Resources/beidou_icd_english_ver2.0.pdf

The BeiDou Time (BDT) starts as a continuous time scale from 1 January 2006 00:00 UTC and is aligned to UTC with a tolerance of 100 ns.

Signals

As for GPS, Galileo and GLONASS, also BeiDou transmits right-hand circularly polarized signals. Three frequency bands indicated as B1, B2 and B3 serve as carrier signals with modulations based on Quadrature Phase Shifted Keying (QPSK) or BPSK. Similar to GPS, BeiDou differentiates between the SPS as an open, free of charge service and an authorize service satisfying in particular the demand for a high reliability. It should however be noticed, that the BeiDou signal transmission concept is related to the current deployment stage and not all technical aspects are defined for the final FOC phase¹⁹.

3.2 Acquiring the ionospheric refraction from dual-frequency microwave signals

For electromagnetic waves, the ionosphere is a dispersive medium, meaning that the ionospheric delay on the signal depends on its frequency. After Seeber (2003) and Hofmann-Wellenhof et al. (2008), the phase refraction index for a given radio signal frequency can be approximated by the power series

$$\eta_{\Phi} = 1 + \frac{c_2}{f^2} + \frac{c_3}{f^3} + \dots \quad \text{with the frequency derivative} \quad \frac{d\eta_{\Phi}}{df} = -\frac{2c_2}{f^3} - \frac{3c_3}{f^4} - \dots \quad (3.1)$$

The series coefficients c_{fi} depend on the electron density along the signal propagation path. Furthermore, the relation between the group (P) and phase (Φ) refractive index as a function of the frequency have been found many years ago by Rayleigh and Lindsay (1945)²⁰ and can be expressed as

$$\eta_P = \eta_{\Phi} + f \frac{d\eta_{\Phi}}{df}. \quad (3.2)$$

Substituting Eq. (3.1) into Eq. (3.2) yields

$$\eta_P = 1 + \frac{c_2}{f^2} + \frac{c_3}{f^3} + \dots - \frac{2c_2}{f^2} - \frac{3c_3}{f^3} - \dots \quad (3.3)$$

Based on the formula of dispersion (Davies, 1990), defined with

$$\eta = 1 - \frac{cN_e}{f^2}, \quad (3.4)$$

the approximation $c_2 = -40.3N_e$ can be found (Seeber, 2003). Under negligence of higher order terms $O(c_3)$, Eq. (3.3) can thus be reformulated as

$$\eta_P = 1 + \frac{c_2}{f^2} - \frac{2c_2}{f^2} = 1 + \frac{40.3N_e}{f^2} \quad (3.5)$$

and it follows from Eq. (3.1), that

$$\eta_{\Phi} = 1 - \frac{40.3N_e}{f^2}. \quad (3.6)$$

For a radio signal passing a planetary atmosphere, the refractive index can generally also be obtained from $\eta = c/v$ where c is the speed of light in vacuum and v the medium dependent propagation speed.

¹⁹BeiDou signal structure: http://www.navipedia.net/index.php/BeiDou_Signal_Plan

²⁰John William Strutt, 3rd Baron Rayleigh (12.11.1842 - 30.06.1919) was an English physicist.

Therefore, it can be concluded that the ionosphere causes with $\eta_P > \eta_\Phi$ and $v_P < v_\Phi$ a group delay and phase advance of the signal. From the Eqs. (3.6) and (3.5) it can further be interpreted that the following applies: The higher the frequency number, the smaller the ionospheric impact. For the GPS carrier frequencies f_1 and f_2 it follows for the group delay that $P_{r,1}^t < P_{r,2}^t$ and for the phase advance that $\lambda_1 \Phi_{r,1}^t > \lambda_2 \Phi_{r,2}^t$.

The basic observation equations for code pseudorange and carrier phase measurements between a transmitter $t \in \{1, \dots, T\}$ and a receiver $r \in \{1, \dots, R\}$ are given by

$$P_r^t = \rho_r^t + c (\Delta t_r - \Delta t^t) + \Delta_{r,\text{NTR}}^t + \left[\Delta_{r,\text{ION}}^t + c (b_r + b^t) + \epsilon_P \right]_f \quad (3.7)$$

and

$$\Phi_r^t = \rho_r^t + c (\Delta t_r - \Delta t^t) + \Delta_{r,\text{NTR}}^t + \left[-\Delta_{r,\text{ION}}^t + \text{CPB}_r^t + \epsilon_\Phi \right]_f \quad (3.8)$$

where the frequency dependent terms have been collected in cornered brackets. Concerning the frequency independent parameters, ρ_r^t is the geometric LOS distance between the satellite transmitter t and receiver r , Δt_r and Δt^t are clock offsets and Δ_{NTR} identifies the impact of the neutral atmosphere (mainly the troposphere).

The frequency dependent terms are defined by the ionospheric signal delay Δ_{ION} , hardware specific code biases or instrumental delays b_r and b^t for receiver and satellite as well as a Carrier Phase Bias (CPB). Additional frequency dependent effects may be induced by multipath, Phase Center Offsets (PCOs) or Phase Center Variations (PCVs). Code multipath can cause pseudorange errors in the decimeter level whereas the phase impact is usually less than a few centimeters (Yang et al., 2004). Impacts due to PCVs can reach up to few centimeters (El-Rabbany, 2006). Such terms have not been explicitly considered here but it can be expected that the errors are partially absorbed in ρ_r^t or the bias parameters b_r , b^t and CPB_r^t . The CPB parameter contains in particular the carrier phase ambiguity λN and phase variations due to circular polarization of the electromagnetic signal, known as Phase Wind-Up (PWU), caused by continuous rotation of the satellite relatively to the receiver for aligning its solar panels towards the sun. N designates a frequency dependent ambiguity parameter in cycles that remains constant during a satellite pass where a pass is defined as an uninterrupted, continuous data arc linked between a specific satellite and a specific receiver. ϵ_P and ϵ_Φ are unmodeled measurement noise terms. It shall further be noted, that ρ may contain additional effects such as antenna environment influences and relativistic effects on the satellite orbit due to the Earth's gravity field and the satellite's velocity.

The ionospheric information is contained in the signal delay Δ_{ION} where the sign indicates the group delay and phase advance according to Eq. (3.5) and Eq. (3.6). A common procedure is the determination of the ionospheric impact for the correction of single frequency receivers working only with L_1 (1 TECU corresponds to 0.163 m range error in C_1). Therefore, the ionospheric delay can be related to the first frequency by consideration of the carrier phase frequency ratio

$$\xi = f_1^2 / f_2^2. \quad (3.9)$$

The Eqs. (3.7) and (3.8) can thus be modified to

$$P_r^t = \rho_r^t + c (\Delta t_r - \Delta t^t) + \Delta_{r,\text{NTR}}^t \begin{cases} +\Delta_{r,\text{ION}}^t + [c (b_r + b^t) + \epsilon_P]_{f_1} \\ +\xi \Delta_{r,\text{ION}}^t + [c (b_r + b^t) + \epsilon_P]_{f_2} \end{cases} \quad (3.10)$$

for the code pseudoranges and

$$\Phi_r^t = \rho_r^t + c (\Delta t_r - \Delta t^t) + \Delta_{r,\text{NTR}}^t \begin{cases} -\Delta_{r,\text{ION}}^t + [\text{CPB}_r^t + \epsilon_\Phi]_{f_1} \\ -\xi \Delta_{r,\text{ION}}^t + [\text{CPB}_r^t + \epsilon_\Phi]_{f_2} \end{cases} \quad (3.11)$$

for the carrier phases. At this point, it is important to note, that the formula with fixed carrier frequencies on both signal links is valid for GPS, Galileo and also BeiDou, but requires a PRN or channel k dependent modification by

$$\xi = \xi(k) = f_1^2(k)/f_2^2(k) \quad (3.12)$$

for the processing of GLONASS signals. The channel distribution, based on the status of 28 November 2014, is provided by Table 3.3.

The availability of multi-frequency signals plays an important role allowing to compute linear data combinations in the form of

$$P_{LC} = a_1 P_1 + a_2 P_2 \quad \text{or} \quad \Phi_{LC} = a_1 \lambda_1 \Phi_1 + a_2 \lambda_2 \Phi_2 \quad (3.13)$$

in case of dual-frequency measurements, where a_1 and a_2 are arbitrary numbers. With respect to Eq. (3.10) and Eq. (3.11), the selection of $a_1 = 1$ and $a_2 = -1$ allows to eliminate the geometry dependent terms, i.e., the non-dispersive parameters. The so-called geometry-free linear or ionosphere combination, denoted as P_4 and L_4 , is then defined with

$$P_{r,4}^t = P_{r,1}^t - P_{r,2}^t = (1 - \xi) \Delta_{r,\text{ION}}^t + \text{DCB} + \epsilon_{P_4} \quad (3.14)$$

$$L_{r,4}^t = \lambda_1 \Phi_{r,1}^t - \lambda_2 \Phi_{r,2}^t = (\xi - 1) \Delta_{r,\text{ION}}^t + \text{CPB}_{4,r}^t + \epsilon_{L_4}. \quad (3.15)$$

The remaining unknowns in this equations are the bias terms for code and phase measurements. $\text{DCB} = c(\Delta b_r + \Delta b^t)$ is denoted as inter-frequency Differential Code Bias (DCB) and $\text{CPB}_{4,r}^t$ contains the merged carrier phase biases, in particular the ambiguity differences $\lambda_1 N_1 - \lambda_2 N_2$. The ionospheric signal is contained in the target parameter $\Delta_{r,\text{ION}}^t$ which is defined here in range units.

In Section 1.5, the STEC [TECU] has been introduced as a characteristic ionospheric parameter that is defined by the integral

$$\text{STEC} = \int N_e ds \quad (3.16)$$

over the electron density along the signal propagation path. The conversion between the ionospheric delay $\Delta_{r,\text{ION}}^t$ in range units to TECU will be derived in the following.

It has been previously shown by means of Eq. (3.5) and Eq. (3.6), that the refraction indices for phase η_Φ and group η_P of first order can be expressed as

$$\eta_\Phi = 1 - \frac{40.3N_e}{f^2} \quad \text{and} \quad \eta_P = 1 + \frac{40.3N_e}{f^2}. \quad (3.17)$$

According to Fermat's²¹ principle a measured range s can be described with

$$s = \int \eta ds \quad (3.18)$$

where the refractive index η is integrated along the signal path. The LOS distance s_0 can therefore be obtained by setting $\eta = 1$ and consequently the signal delay as the difference between curved and straight path can be computed from

$$\Delta s = \int \eta ds - \int ds_0. \quad (3.19)$$

Taking into account that the signal delay is mainly caused by ionospheric refraction, leads to $\Delta s = \Delta_{r,\text{ION}}^t$. Furthermore, the substitution of Eq. (3.17) into Eq. (3.19) yields

$$\Delta_{r,\text{ION}}^t = \int \left(1 + \nu \frac{40.3N_e}{f^2} \right) ds - \int ds_0 \quad (3.20)$$

²¹Pierre de Fermat (second half of 1607 - 12.01.1665) was a French mathematician and lawyer.

with $\nu = 1$ for group and $\nu = -1$ for phase signals. A simplification is introduced at this point, where the integration is performed along the LOS instead of the curvature signal. It follows that $s = s_0$, i.e., the integrals appearing in Eq. (3.20) can be merged in the reformulation

$$\Delta_{r,\text{ION}}^t = \nu \frac{40.3}{f^2} \int N_e ds_0 \quad (3.21)$$

which can also be written as

$$\Delta_{r,\text{ION}}^t = \nu \frac{40.3}{f^2} \text{STEC}_r^t. \quad (3.22)$$

Equation (3.22) can now be considered in Eq. (3.15) to obtain a formulation including the ionospheric refraction on the first carrier signal in TECU. With the frequency dependent factors summarized in

$$\alpha = (\xi - 1) \frac{40.3}{f_1^2} = 40.3 \frac{f_1^2 - f_2^2}{f_1^2 f_2^2} \quad (3.23)$$

the geometry-free linear combinations for code and phase can be written as

$$P_{r,4}^t = P_{r,1}^t - P_{r,2}^t = -\alpha \text{STEC}_r^t + \text{DCB} + \epsilon_{P_4} \quad (3.24)$$

$$L_{r,4}^t = \lambda_1 \Phi_{r,1}^t - \lambda_2 \Phi_{r,2}^t = \alpha \text{STEC}_r^t + \text{CPB}_{4,r}^t + \epsilon_{L_4}. \quad (3.25)$$

For GLONASS signal processing, this formulation yields accordingly

$$\alpha = \alpha(k) = (\xi(k) - 1) \frac{40.3}{f_1^2(k)} = 40.3 \frac{f_1^2(k) - f_2^2(k)}{f_1^2(k) f_2^2(k)}. \quad (3.26)$$

The Eqs. (3.24) and (3.25) can finally be solved as

$$\text{STEC}_r^t = \alpha^{-1} \begin{cases} P_{r,2}^t - P_{r,1}^t + \text{DCB} + \epsilon_{P_4} & \text{(code)} \\ \lambda_1 \Phi_{r,1}^t - \lambda_2 \Phi_{r,2}^t - \text{CPB}_{4,r}^t + \epsilon_{L_4} & \text{(phase)} \end{cases} \quad (3.27)$$

for the determination of STEC.

Further details about ionospheric influences on GNSS signals can for instance be found in Hofmann-Wellenhof et al. (2008), Xu (2010) or Hoque and Jakowski (2012) and many other literature.

According to Eq. (3.17), this formulation considers only ionospheric influences of first order. Second order terms can be expressed through

$$\text{STEC}_{r,2nd}^t = \alpha^{-1} \left(-\frac{7,527c}{2f_1 f_2 (f_1 + f_2)} \right) \int N_e B \cos \Theta ds \quad (3.28)$$

taking the Earth's magnetic field B and the angle Θ between the signal path and B into account (Hernández-Pajares et al., 2007). The consideration of $\text{STEC}_{r,2nd}^t$ is mainly relevant for clock and orbit modeling but contributes less than 0.1% to the total ionospheric delay in GNSS signals why it is mostly neglected.

Carrier phase leveling and code smoothing

Pseudorange measurements are noisy but unambiguous while the carrier phase data is precise but biased. For this reason, algorithms for smoothing the code or leveling the phase data, respectively, are applied to reduce the noise (roughly by a factor of \sqrt{N} , where N is the number of data samples of the data arc) while maintaining the precision of the phase measurements.

A simple but efficient approach to determine leveled geometry-free phase observations $\widetilde{L}_{r,4}^t$ is based on the calculation of an offset

$$C_j \approx \text{CPB} \approx \frac{1}{N} \sum_{i=1}^N \left((P_{r,2}^t - P_{r,1}^t) - (\lambda_1 \Phi_{r,1}^t - \lambda_2 \Phi_{r,2}^t) \right)_i \quad (3.29)$$

for each pass j where absolute measurements are derived as

$$\widetilde{L}_{r,4}^t = L_{r,4}^t + C_j. \quad (3.30)$$

Another method is published in Schaer (1999) where the smoothed code $\overline{P}_{r,4}^t$ for both frequencies is computed from

$$\overline{P}_{r,4}^t = \begin{cases} \lambda_1 \Phi_{r,1}^t + \overline{P}_{r,1}^t - \overline{\lambda_1 \Phi_{r,1}^t} + \frac{2f_2^2}{f_1^2 - f_2^2} \left(L_{r,4}^t + \overline{\lambda_2 \Phi_{r,2}^t} - \overline{\lambda_1 \Phi_{r,1}^t} \right) & \text{for } f_1 \\ \lambda_2 \Phi_{r,2}^t + \overline{P}_{r,2}^t - \overline{\lambda_2 \Phi_{r,2}^t} + \frac{2f_1^2}{f_1^2 - f_2^2} \left(L_{r,4}^t + \overline{\lambda_2 \Phi_{r,2}^t} - \overline{\lambda_1 \Phi_{r,1}^t} \right) & \text{for } f_2 \end{cases} \quad (3.31)$$

with $\overline{P}_{r,1}^t$ and $\overline{P}_{r,2}^t$ designating the mean code and $\overline{\lambda_1 \Phi_{r,1}^t}$ as well as $\overline{\lambda_2 \Phi_{r,2}^t}$ identifying the mean phase measurements referring to an uninterrupted data arc.

It shall be noticed that the Differential Code Biases (DCBs) are still contained in the geometry-free observables $\overline{P}_{r,4}^t$ and $\widetilde{L}_{r,4}^t$.

3.3 Doppler Orbitography and Radiopositioning Integrated by Satellite

The DORIS system has been developed for Precise Orbit Determination (POD), in particular for Low Earth Orbiter (LEO) satellites, based on the principle of the Doppler²² effect. For the reason that DORIS beacons serve as transmitters that only require power supplies without any data transfer connections, several stations are deployed in isolated regions. This advantage can be seen in the site distribution depicted in Fig. 3.5 showing a rather homogeneous pattern where plenty beacons are located on islands.



Figure 3.5: Map of current DORIS ground beacon distribution. Source: International DORIS Service (IDS), International DORIS Service: <http://ids-doris.org>, last update on 25 November 2014.

The system measures on two frequencies $f_1 = 2,036.25$ MHz and $f_2 = 401.25$ MHz in the L-band with modulated codes on the carrier signals, similar to GPS. Modern DORIS DGXX (Jayles, 2009)

²²Christian Andreas Doppler (29.11.1803 - 17.03.1853) was an Austrian mathematician and physicist.

receivers hold the capability to track synchronous phase measurements and thus expand the horizon of DORIS usage in geodetic applications. DGXX receivers can presently be found in the payload of Jason-2 (also known as Ocean Surface Topography Mission (OSTM)), Cryogenic Satellite 2 (Cryosat-2), Satellite with Argos and AltiKa (SARAL) as well as Hy-2a and will be installed on future missions, e.g., Sentinel-3A (scheduled for second quarter 2015) followed by Sentinel-3B, Jason-3 (scheduled for the end of 2015), Jason-CS (scheduled for 2017) and Swot (scheduled for 2019). The observations are released in RINEX DORIS 3.0²³ with a similar formatting as for GNSS RINEX. With the availability of DGXX signal tracking, the systematic differences between DORIS and GPS may be found in (1) the inverted signal propagation direction where terrestrial DORIS beacons transmit the signal and LEO satellites carry the receiver antennas and (2) the frequency bands with $f_1 = 2,036.25$ MHz (wavelength $\lambda_1 = 14.7$ cm) and $f_2 = 401.25$ MHz (wavelength $\lambda_2 = 74.7$ cm).

Due to the large frequency spacing, the ionospheric delays differ strongly between both channels with $[\Delta_{t,ION}^r]_2 > [\Delta_{t,ION}^r]_1$. Because of the similar signal structure with respect to GPS, the steps to derive the ionospheric refraction from DORIS measurements basically follow the sequence described in Section 3.2, at least for the carrier phase observations. Leveling the phase observations is limited though due to an increased code pseudorange noise in the order of magnitude 1 km as compared to approximately 1 m for GPS (Mercier et al., 2010). Therefore, P-IV: Dettmering et al. (2014b) de-biased the TEC, e.g., by means of GIMs provided by the IGS for the drawback of being dependent on external information.

Furthermore, clock corrections which are included in the RINEX file, shall be taken into account for DORIS to refer the DORIS system time to TAI. The clock offsets for selected satellite missions carrying a DGXX receiver are provided in Table 3.4 where Saral exhibits, for instance, a significant clock bias of 200 s.

Table 3.4: DORIS receiver clock biases for selected satellite missions with DGXX instrument.

Mission	Clock bias [s]	Mission	Clock bias [s]
Jason-2	1.38	Cryosat-2	-4.28
HY-2A	-2.08	Saral	212.65

The observation equation for DORIS phase measurements finally reads

$$\text{STEC} = \alpha^{-1} \left(\lambda_1 \Phi_{r,1}^t - \lambda_2 \Phi_{r,2}^t - \text{CPB}_{4,r}^t + \Delta D + \epsilon_{L_4} \right) \quad (3.32)$$

where Eq. (3.27) has been extended by a geometry correction term ΔD accounting for the PCOs in the transmitter and receiver antenna. Higher order effects are not considered in this equation, but may be necessary due to the low second frequency of DORIS. According to Fig. 3.6, the path length difference under the assumption of a straight line propagation between satellite and beacon can be approximated as

$$\Delta d_t = \sin(el) d_t \quad \text{and} \quad \Delta d^r = \sin(el) d^r \quad (3.33)$$

depending on the elevation angle el . Here, d_t and d^r indicate the zenith and nadir correction at the beacon transmitter and satellite receiver, respectively. The total correction to be considered in the geometry-free combination consequently yields

$$\Delta D = \Delta d_t + \Delta d^r = \sin(el) (d_t + d^r). \quad (3.34)$$

²³ ftp://ftp.ids-doris.org/pub/ids/data/RINEX_DORIS.pdf

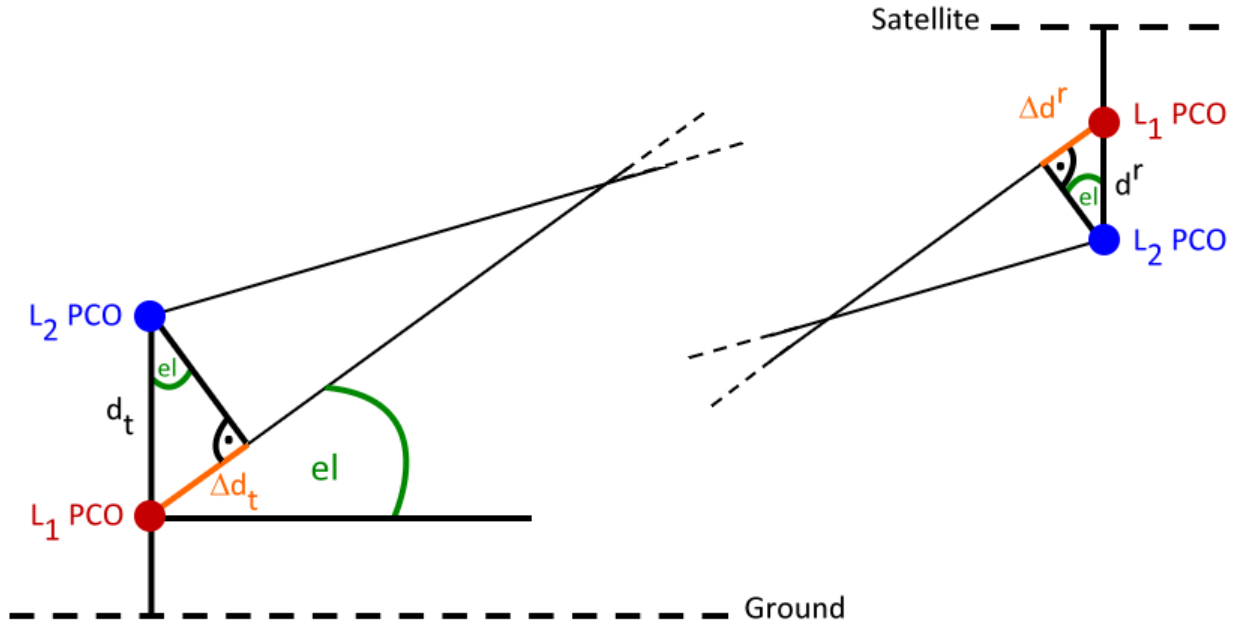


Figure 3.6: Geometrical consequence of DORIS transmitter and receiver phase offsets.

It shall be noted, that the curvature of the orbit has been neglected in this approximation for the geometry correction. Absolute phase center locations in $x/y/z$ for various satellite antennas are published in Cerri and Ferrage (2014) and PCOs for the beacons, specifically for Starec and Alcatel antennas, can be found in the IDS (2012). A summary including selected satellite missions is provided by Table 3.5. The range error due to PCOs can amount up to 0.65 cm for Jason-2 in L_1 , i.e., on the 400 MHz signal link (Mercier, 2010). Furthermore, the phase wind-up in case of Jason-2 can reach a maximum of 0.30 m, but is much smaller for almost all passes.

Table 3.5: Overview on zenith and nadir antenna corrections due to PCOs for currently active missions with DGXX receiver payload. The values have been calculated from the phase center locations published in Cerri and Ferrage (2014) under consideration of the antenna orientation.

Mission	Nadir offset [m]	Mission	Nadir offset [m]
Jason-2	0.164	Cryosat-2	0.153
HY-2A	0.162	Saral	0.158
Beacon antenna	Zenith offset [m]	Beacon antenna	Zenith offset [m]
Alcatel	0.175	Starec	0.487

The daily distribution of ionospheric piece points for the missions Jason-2 (top-left), SARAL (top-right), Cryosat-2 (bottom-left) and Hy-2a (bottom-right) is shown in Fig. 3.7. The passes are colored to indicate the observed VTEC signal where ascending and descending passes, i.e., day and nighttime passages, become visible from increased and very low VTEC, respectively. The elevation mask has been chosen with 10° cut-off and the absolute VTEC has been derived here by means of IGS data.

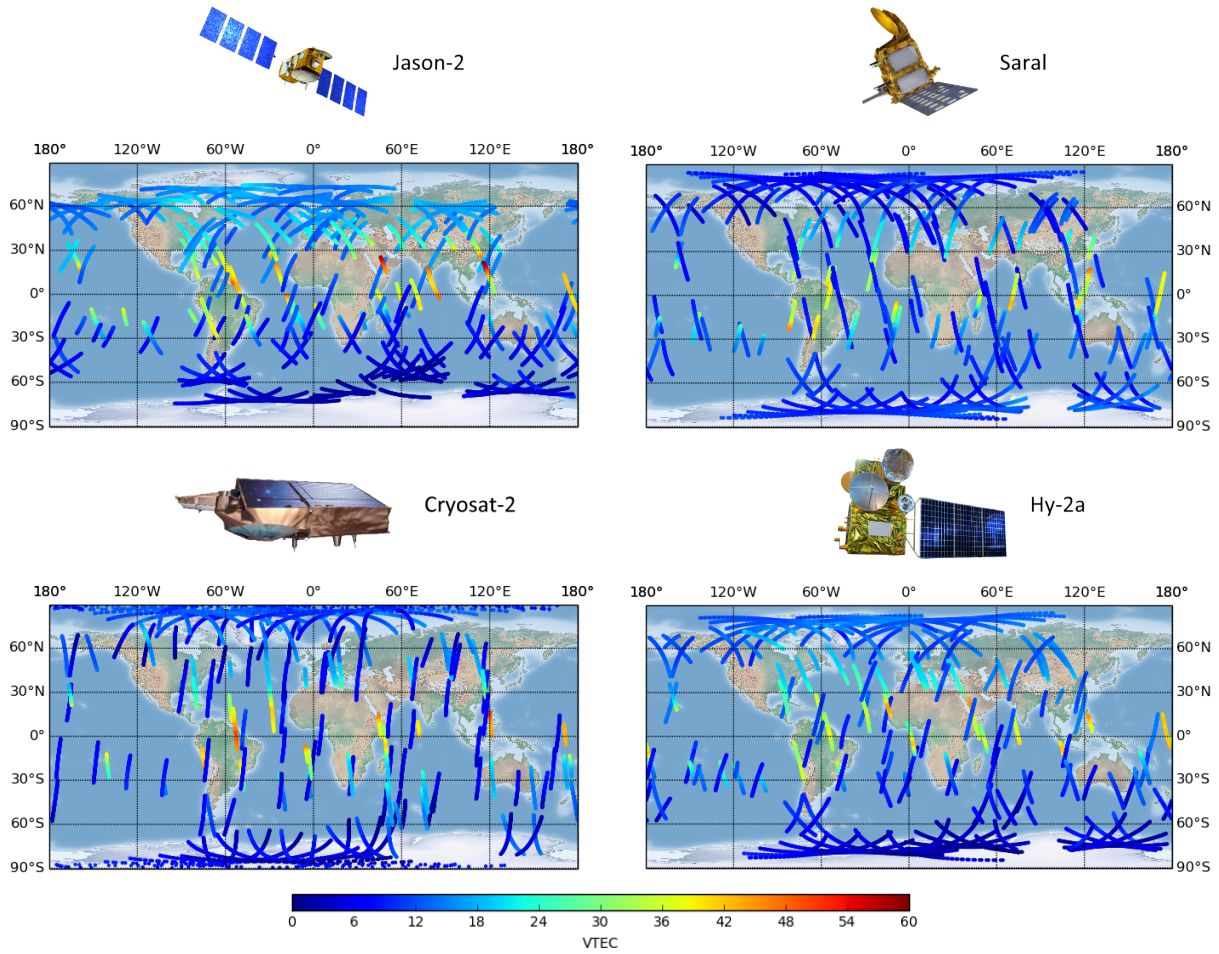


Figure 3.7: Daily distribution of ionospheric piece points at 15 September 2013 computed for DORIS carrier-phase measurements of different satellite missions with DGXX instrument, specifically Jason-2 (top-left), Saral (top-right), Cryosat-2 (bottom-left) and Hy-2a (bottom-right). For the mapping, a single layer model with MSLM has been taken into account. The observation leveling is based on TEC derived from IGS GIMs.

3.4 Dual-frequency radar altimetry

Satellite altimetry missions carry a radar instrument that emits a radio wave beam in nadir direction and receives its reflection from the ground, specifically from Earth water surfaces. Measuring the emission and reception time yields the (double) range between surface and antenna. Thus, RA provides vertical observations over oceans, lakes and rivers. The true range ρ can be calculated from

$$\rho = [P - \Delta_{\text{ION}} + \epsilon]_{f_i} + \epsilon_{\text{nd}} \quad (3.35)$$

where P represents the measured range, Δ_{ION} the ionospheric range error and ϵ the measurement noise, each depending on the frequency f_i (Fu and Cazenave, 2001). Non-dispersive errors such as the tropospheric delay, tidal influences and electromagnetic biases are merged in the parameter ϵ_{nd} .

Diverse frequencies are used for radar altimeters. The choice depends upon regulations, mission objectives, constraints and technical (im-)possibilities. It can generally be distinguished between the following frequency bands:

- Ku-band (13.6 GHz):** The Ku-band provides the best compromise between technology capability and atmospheric sensitivity including ionospheric perturbations. It is the most common frequency band in altimeter missions and has been realized, for instance, for the radar instruments of Topex/Poseidon, Jason-1, Jason-2, Envisat, Cryosat-2, Hy-2a and ERS.

C-band (5.3 GHz): The C-band is highly sensitive to ionospheric refraction and robust against water vapor in the atmosphere. Together with the Ku-band it is considered for the retrieval of the ionospheric delay. Jason-2 and Hy-2a measure, e.g., in the Ku- and C-band.

S-band (3.2 GHz): The S-band is also used in combination with the Ku-band measurements, for the same reasons as the C-band.

More details on RA frequencies are published at <http://www.altimetry.info>.

Active altimeter instruments working in dual-frequency mode are currently deployed onboard Jason-2 and SARAL allowing for the retrieval of the ionospheric range error by means of the geometry-free linear combination. According to Eq. (3.14), it follows that

$$P_4 = P_1 - P_2 = (1 - \xi) \Delta_{\text{ION}} + \epsilon_{P_4} \quad (3.36)$$

where ξ has been defined by Eq. (3.9). VTEC is then computed from

$$\text{VTEC} = \alpha^{-1} (P_2 - P_1 + \epsilon_{P_4}) \quad (3.37)$$

by means of the frequency dependent factor α which was introduced in Eq. (3.23). The altimetry products of most missions are published with different latencies, identified by Geophysical Data Record (GDR) (delayed), Interim Geophysical Data Record (IGDR) (near real-time) and Operational Geophysical Data Record (OGDR) (real time) as described by Archiving, Validation and Interpretation of Satellites Oceanographic data (AVISO)²⁴.

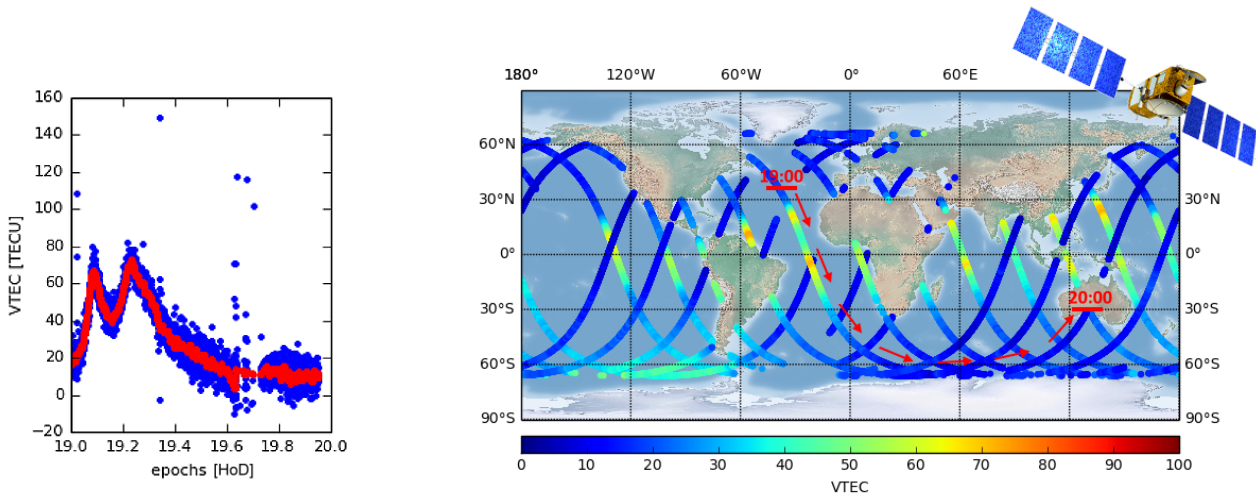


Figure 3.8: Raw (blue) and filtered (red) VTEC series computed from OGDR data.

Figure 3.9: Daily distribution of Jason-2 altimetry VTEC at 1 January 2015, computed from OGDR data. The pass plotted in Fig. 3.8 has been highlighted by red arrows with start and end time. A draft of Jason-2 has been depicted in the top-right corner.

The raw ionosphere RA measurements contain strong noise and therefore, a median filter should be applied. For Jason-2, a filter length of 20-25 samples for 1 Hz data is recommended in the products handbook²⁵.

Figure 3.8 shows a series of OGDR Jason-2 VTEC measurements, raw (blue) and filtered (red) referring to a timespan between 19:00 and 20:00 UT on 1 January 2015. A filter length of 25 samples has been taken into account. The data is provided by National Oceanic and Atmospheric Administration (NOAA) via File Transfer Protocol (FTP)²⁶. Epochs are related to Hours of Day (HoD). The double

²⁴Product overview of GDR, IGDR and OGDR data sets:

<http://www.aviso.altimetry.fr/en/data/products/sea-surface-height-products/global/gdr-igdr-and-ogdr.html>

²⁵OSTM/Jason-2 products handbook: http://www.aviso.oceanobs.com/fileadmin/documents/data/tools/hdbk_j2.pdf

²⁶NOAA Jason-2 OGDR: <ftp://ftp.nodc.noaa.gov/pub/data.nodc/jason-2/ogdr/>

peaks at the beginning of the arc are caused by the equatorial anomaly as can be seen from Fig. 3.9. This plot shows the daily distribution of Jason-2 OGDR VTEC tracks where the pass of Fig. 3.8 is emphasized by means of red arrows including start and end time of the interval. Due to the nearly sun-synchronous orbit of Jason-2, the local times of the ground tracks are changing very slowly with a rate of around -2 hours in 10 days referring to the local time of the ascending node (P-IV: Dettmering et al., 2014b).

When comparing the GPS and GLONASS measurement distribution depicted in Fig. 3.2 and Fig. 3.4 with the altimetry ground tracks visible in Fig. 3.9, it is obvious that the number of RA measurements from only few dual-frequency missions is limited. The strength of altimetry arises rather from the contribution of observations over water surfaces. In geodetic ionosphere modeling, altimetry is therefore mostly considered alongside with GNSS as a supporting technique to bridge data gaps over the oceans.

4 Ionospheric GNSS radio occultations for observing the electron density

The common scope of application for GNSS receivers can primarily be found in PNT, on Earth and in space. As introduced in Section 3.1, the travel time of the transmitted microwave signals is influenced by the ionosphere as a dispersive medium leading to an advance of the signal carrier phase and a delay of the modulated code pseudorange. The affected signal travel time and consequently biased distance contains information about atmospheric properties such as the ionospheric electron density.

From terrestrial GNSS tracking, the signal travel paths are given mostly in the radial direction helping in particular to determine for horizontal ionospheric variations. Measurements from low elevations may contribute to observe vertical structures, but the risk of interpreting additional signal noise, induced by multipath or signal deflection due to objects in the near receiver environment, increases. An excellent geometrical scenario to resolve for the vertical stratification is found when the signal is passing the atmosphere rather horizontally while the receiver is located behind the limb. This favorable situation can be achieved in radio occultation geometry where the GNSS receiver is carried by a LEO satellite. In this case, the signal source, e.g., the GNSS transmitter, can reach an elevation angle below zero from the LEO receiver perspective. It is distinguished between setting and rising occultations as defined by increasing or decreasing signal elevations. Depending on the LEO orbit height, the signal then passes the whole or partial ionospheric halo. This geometrical situation is schematically depicted in Fig. 4.1 where Formosat-3/COSMIC (F-3/C) has been chosen as the LEO mission tracking the signals.

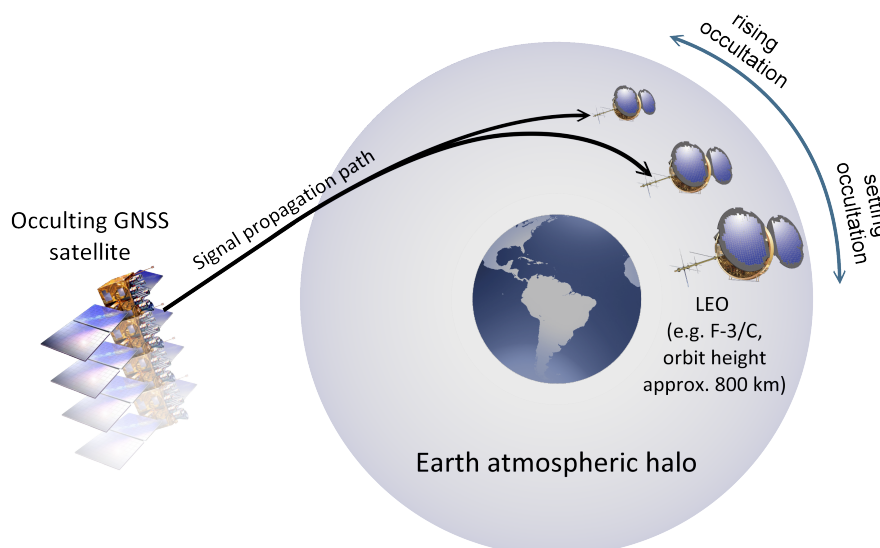


Figure 4.1: Schematic representation of the radio occultation geometry between a GNSS transmitter and F-3/C receiver.

The first successful proof-of-concept on limb sounding the Earth atmosphere was carried out in 1993 by the University Corporation for Atmospheric Research (UCAR) by means of the GPS/Meteorology (GPS/MET) experiment with the Microlab-1 satellite (Ware et al., 1996). The studies with GPS/MET were mainly focused on numerical weather predictions but besides, the radio occultation technique has been exploited for profiling the ionosphere and derive EDPs (Hajj and Romans, 1998). Due to

Table 4.1: Chronology of LEO research missions carrying radio occultation instruments as published by Mannucci et al. (2014).

LEO mission	Acronym	RO instrument heritage	Data collection period
GPS Meteorological Satellite	GPS/MET	NASA	1995-1997
Oersted	-	NASA	1995-2001
Stellenbosch University Satellite	Sunsat	NASA	1999-2001
Ionospheric Occultation Experiment on board PicoSat	IOX	NASA	2001-2004
Challenging Minisatellite Payload	CHAMP	NASA	2001-2008
Satélite de Aplicaciones Cientificas-C	SAC-C	NASA	2001-2013
Federaton Satellite	Fesat	NASA	2002-2007
Gravity Recovery and Climate Experiment	GRACE	NASA	2006-
Meteorological Operational Satellite Program	Metop-A, B	European Organization for the Exploitation of Meteorological Satellites	2006-
Formosa Satellite 3/Constellation Observing System for Meteorology, Ionosphere and Climate	Formosat-3/COSMIC	NASA	2006-
Communications/Navigation Outage Forecasting System	C/NOFS	NASA	2008-2013
Terra-Synthetic Aperture Radar X-band	TerraSAR-X	NASA	2008-
Ocean Satellite 2	Oceansat-2	Italian Space Agency	2009-
TerraSAR-X Add-on for Digital Elevation Measurement at X-band	TanDEM-X	NASA	2010-
Megha-Tropiques		Italian Space Agency	2011-
Satélite de Aplicaciones Cientificas-D	SAC-D	Italian Space Agency	2011-
Korean Multipurpose Satellite-5	KOMPSAT-5	NASA	2013-
FengYun-3		Center for Space Science and Applied Research, Chinese Academy of Sciences	2013-

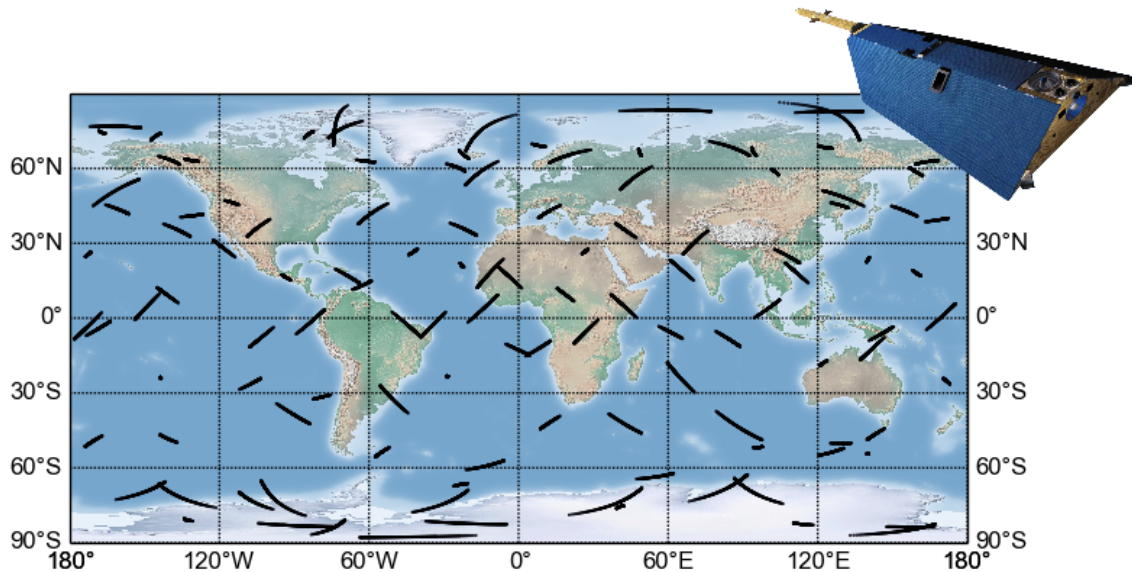


Figure 4.2: Global distribution of 116 electron density profiles computed from CHAMP occultations as collected during 8 January 2007. The map shows clearly the horizontal extent of the profiles. Data source: COSMIC Data Analysis and Archive Center (CDAAC), <http://cdaac-www.cosmic.ucar.edu>.

the rapidly increasing number of LEO satellites, presently in particular thanks to the F-3/C mission, a global measurement coverage can be obtained. The spatio-temporal distribution of data is rather inhomogeneous though. For empirical electron density modeling, IRO play an outstanding role allowing to derive electron density profiles from carrier-phase measurements as a non-integrated data type in contrast to GNSS, satellite altimetry or DORIS. Electron density profiles have been considered as input data for ionosphere modeling by P-I: Limberger et al. (2013); P-II: Limberger et al. (2014) where data have been combined from different LEO missions. P-V: Liang et al. (2014); P-VI: Liang et al. (2015) extended the data base with GPS TEC measurements. Besides, this chapter has a strong connection to the publication P-III: Limberger et al. (2015) where an improved electron density retrieval method has been studied and the resulting electron density profiles have been considered to assess the quality of F2 Chapman peak parameters from the validation with ionosonde measurements.

An overview of LEO missions that have been launched in the past with radio occultation instruments on-board has recently been published by Mannucci et al. (2014) and is provided by Table 4.1. The entries are chronologically ordered by the start of tracking occultations where some missions are already decommissioned and others are still ongoing. This chapter starts with descriptions for selected LEO constellations capable of tracking occultations. Particularly, the missions Challenging Minisatellite Payload (CHAMP), Gravity Recovery And Climate Experiment (GRACE) and F-3/C (highlighted by blue colored cells in Table 4.1) significantly contributed to the development of the occultation technique during the last decade and have been considered in several publications belonging to this thesis. Afterwards the retrieval fundamentals, in particular the Abel inversion algorithms, are derived. The chapter closes with the derivation of an improved Abel transform inversion algorithm for the retrieval of electron density profiles as a partial recapitulation of P-III: Limberger et al. (2015).

4.1 CHAMP, GRACE and Formosat-3/COSMIC

CHAMP: The CHAMP mission was designed mainly to detect precise gravitational and magnetic field variations in space and time (Reigber et al., 2005). CHAMP was a German mission managed by the German Research Centre for Geosciences at the Helmholtz Centre Potsdam (GFZ) and has been launched on 15 July 2000. After more than 10 years in orbit it was decommissioned at 19 September 2010. With the near polar orbit (inclination of 87°) and altitude just above the ionospheric

peak in approximately 450 km, CHAMP was very suitable to be used for the tracking of IRO. For that reason, the mission became a significant contributor not only for geopotential research, but also for sounding the troposphere and ionosphere. An overview of the daily distribution of CHAMP electron density profiles is depicted in Fig. 4.2. The data has been re-processed by the University Corporation for Atmospheric Research (UCAR) and is provided through the CDAAC data base at <http://cdaac-www.cosmic.ucar.edu>.

GRACE: The GRACE consists of a satellite pair aiming to observe the Earth gravitational field from a low orbit at around 450-500 km (Tapley et al., 2004). The mission has been developed by a cooperation of the National Aeronautics and Space Administration (NASA), JPL and the German Aerospace Center (DLR). As for CHAMP, the orbit is nearly circular with an inclination angle of 89° . The measurement principle is based on precise distance monitoring between the satellites where gravitational anomalies can be observed from the relative acceleration of the two satellites. For ionospheric sounding through radio occultations, GRACE shows similar characteristics as CHAMP capable of providing profiles including the main ionospheric layers. Figure 4.3 shows the distribution of GRACE profiles provided by CDAAC during 8 January 2009.

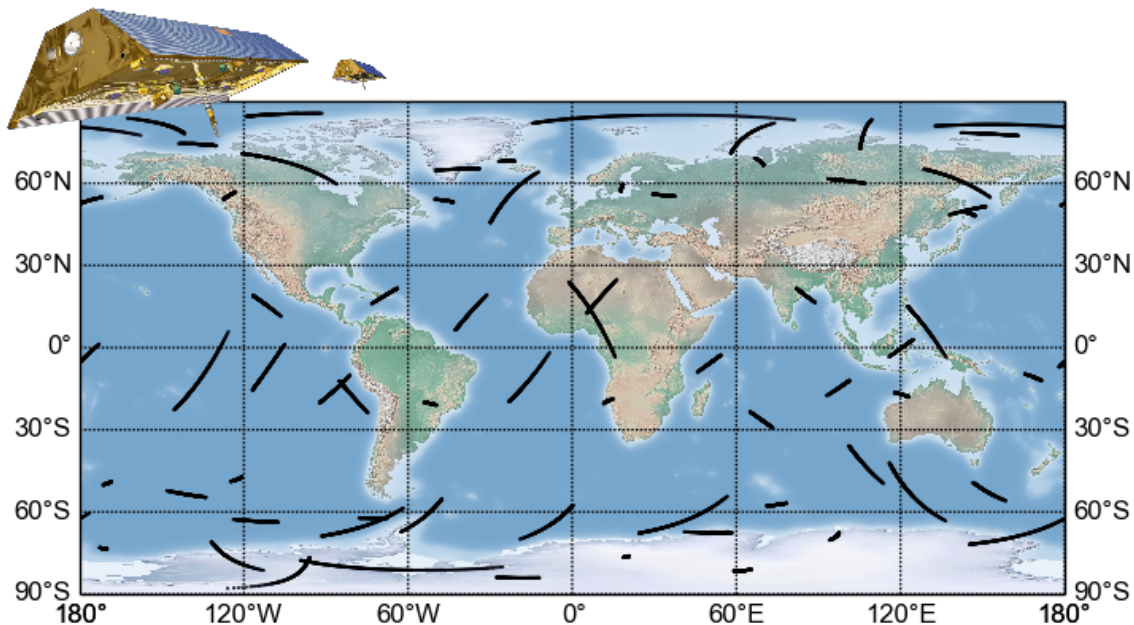


Figure 4.3: Global distribution of 66 electron density profiles computed from GRACE occultations as collected on 8 January 2009. The map shows clearly the horizontal extent of the profiles. Data source: CDAAC, <http://cdaac-www.cosmic.ucar.edu>.

Formosat-3/COSMIC: A key component in the provision of IRO plays the F-3/C mission contributing observations by means of six mini-satellites orbiting on six individual planes at around 800 km altitude. The constellation is a joint U.S.-Taiwanese project with major participants including UCAR, the National Science Foundation (NSF), the Naval Research Laboratory (NRL), the Air Force Research Laboratory (AFRL) on the U.S. side and the National Space Organization (NSPO) on the Taiwanese side. The six orbital planes are inclined by 72° with ascending nodes separated by 60° in argument of longitude. Thus the constellation allows up to 2,500 occultations per day. After performing a sophisticated data screening, a significant amount of data is however rejected—mostly due to high noise. Figure 4.4 shows the profile distribution for 8 January 2015. In this case, 391 profiles have been stored in the database of CDAAC. However, it is obvious that the number of profiles from F-3/C significantly outperforms the contribution of GRACE and CHAMP. In the three first-author publications P-I: Limberger et al. (2013), P-II: Limberger et al. (2014) and P-III: Limberger et al. (2015), F-3/C has been considered as the main or even only data contributor for studies and analysis.

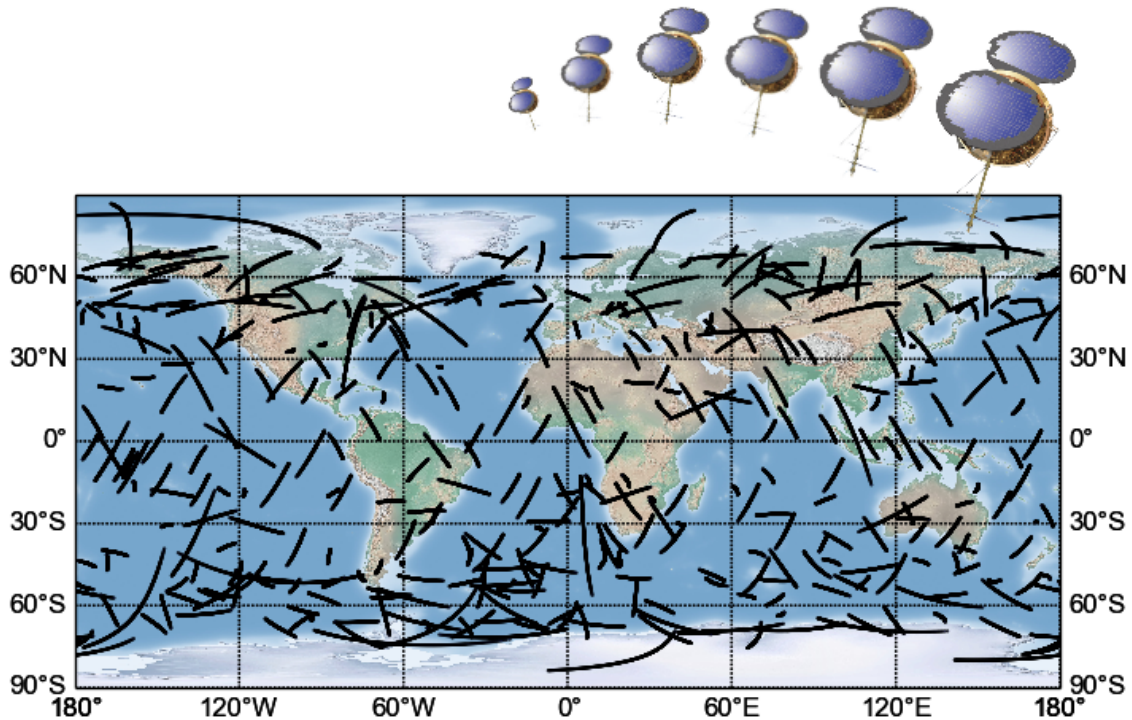


Figure 4.4: Global distribution of 391 electron density profiles computed from F-3/C occultations as collected on 8 January 2015. The map shows clearly the horizontal extent of the profiles. Data source: CDAAC, <http://cdaac-www.cosmic.ucar.edu>.

4.2 The Abelian inversion

The propagation of electromagnetic waves can be treated as rays which are connecting transmitter and receiver (Ge, 2006). When passing through the atmosphere, the ray trajectory is affected by varying refractivity indices according to Fermat's principle. A straight forward solution for the ray bending angle may be found by means of the Abelian integral equation taking the radial variations of refractivity into account. The principles of this equation together with its inversion play a key role in the electron density retrieval of ionospheric radio occultations and will be derived in the following. At this point it is important to note, that the determination of the three-dimensional refractivity from one-dimensional measurements as they are tracked by a GNSS receiver is usually impossible. However, it is assumed, that the bending is primarily caused by vertical refractivity gradients and the problem can be projected on a vertically oriented plane, henceforth the occultation plane.

The Abelian integral equation

In 1823, the Norwegian mathematician Niels Henrik Abel²⁷ studied as a pioneer integral equations related to mechanical problems. He investigated an integral transform, the Abelian integral equation or Abel transform, that is often used in the analysis of spherically symmetric or axially symmetric functions. In particular in the field of image analysis, his methods found intensive application. For instance, axially symmetric emission functions can be projected onto a plane by means of the forward Abel transform while the inversion allows to retrieve the emission function from a given projection such as a scan or photography. More recent developments include variants of the inverse Abel transformation applied with onion peeling methods in the fields of photoelectron and photoion image analysis. Details about the mathematical background are provided, for instance, by Gorenflo and Vessella (2009).

²⁷Niels Henrik Abel (5 August 1802 – 6 April 1829) was a Norwegian mathematician.

Relevant papers dealing with the retrieval of refractivity index profiles for planetary atmospheres from satellite occultation measurements have, for instance, been published by Phinney and Anderson (1968) and Fjeldbo et al. (1971). As mentioned previously, the problem is simplified by projecting the signal propagation onto a plane and additionally, a symmetrical refractivity field is taken into account. Under the assumption that the Earth's center of mass is the origin of the refractivity field, a polar coordinate system can be defined where the refractivity index η is a function of the radius r .

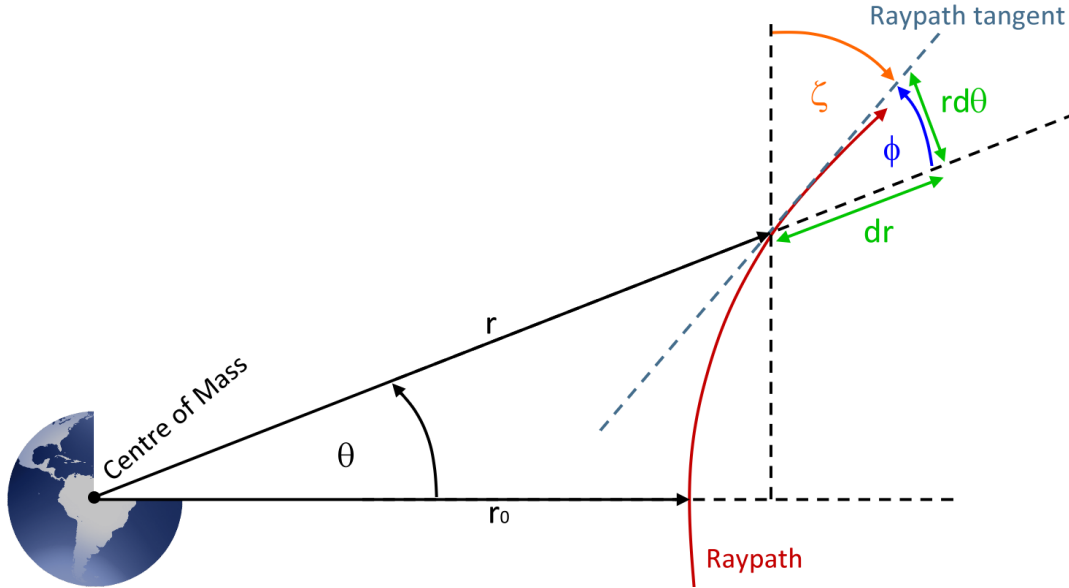


Figure 4.5: Schematics for the geometry of refraction on a plane (design inspired by Fjeldbo et al. (1971)).

According to Fig. 4.5, the angle between the ray path and the current radial direction can be formulated as

$$\tan \phi = \frac{r d\Theta}{dr} \quad (4.1)$$

and the angles sum yields

$$\zeta + \Theta + \phi = \pi/2 = 90^\circ. \quad (4.2)$$

It can furthermore be concluded that the integration of $d\zeta$ along the ray path yields the total bending angle of the ray α ²⁸. Under consideration of the angle orientations as indicated by arrows in Fig. 4.5, the differential expression

$$d\zeta = -d\Theta - d\phi \quad (4.3)$$

follows from Eq. (4.2). At this point it is obvious, that a solution for $d\Theta$ and $d\phi$ is required to solve for α .

1.) Solving for ϕ

Taking into account, that the index of refraction is a continuous function of r , Bouguer's²⁹ rule with

$$\eta r \sin \phi = a = \text{constant} \quad (4.4)$$

can be found (Born and Wolf, 1999). a is the so-called impact parameter³⁰ that is defined with range units and constant along a ray trajectory. Rearranging Eq. (4.4) and taking into account that

²⁸Also known as the angular deflection of the beam (Fjeldbo et al., 1971).

²⁹Pierre Bouguer (16.02.1698-15.08.1758) was a French astronomer, geodesist and physician.

³⁰Also known as impact factor or, as in Fjeldbo et al. (1971), the ray asymptote miss distance.

$\cos^2 \phi = 1 - \sin^2 \phi$ leads to

$$\sin \phi = \frac{a}{\eta r} \quad \text{and} \quad \cos \phi = \frac{\sqrt{\eta^2 r^2 - a^2}}{\eta r}. \quad (4.5)$$

Substituting these expressions into the derivative of Eq. (4.4)

$$r \sin \phi d\eta + \eta \sin \phi dr + \eta r \cos \phi d\phi = 0 \quad (4.6)$$

and solving for $d\phi$ yields

$$d\phi = -\frac{adr}{\sqrt{\eta^2 r^2 - a^2}} \left(\frac{d\eta}{dr} \frac{1}{\eta} + \frac{1}{r} \right). \quad (4.7)$$

2.) Solving for Θ

Applying the trigonometric relation $\tan \phi = \sin \phi / \cos \phi$ to Eq. (4.1) under consideration of the dependencies from Eq. (4.5) leads to a solution for $d\Theta$ with

$$d\Theta = \frac{adr}{r \sqrt{\eta^2 r^2 - a^2}}. \quad (4.8)$$

3.) Solving for $d\zeta$

The solution for $d\zeta$ results from the substitution of Eq. (4.7) and Eq. (4.8) into Eq. (4.3). After merging the terms, a compact solution for $d\zeta$ is derived as

$$d\zeta = \frac{a}{\eta \sqrt{\eta^2 r^2 - a^2}} \frac{d\eta}{dr} dr. \quad (4.9)$$

The forward **Abelian integral equation** results from the integration of $d\zeta$ along the entire ray path under the assumption of spherical symmetry, i.e., a symmetric ray curvature about the Tangent Point (TP) at r_0 is taken into account. The total bending angle of the ray can thus be computed with

$$\alpha = 2a \int_{r=r_0}^{r=\infty} \frac{1}{\eta \sqrt{\eta^2 r^2 - a^2}} \frac{d\eta}{dr} dr \quad (4.10)$$

as a function of the refractivity η along the ray path.

The integral inversion

In order to retrieve the refractive index η as a function of the bending angle α and the impact factor a , Eq. (4.10) needs to be inverted. The analytical inversion has, for instance, been described by Tricomi (1985).

In the first step, the variable $x = \eta r$ is introduced (Fjeldbo et al., 1971; Ge, 2006) which simplifies Eq. (4.10) to

$$\alpha = 2a \int_{x=a}^{x=\infty} \frac{1}{\eta \sqrt{x^2 - a^2}} \frac{d\eta}{dx} dx. \quad (4.11)$$

The lower integration limit is adjusted by $x = a$ which is, according to Eq. (4.4), valid in r_0 with $\phi = 90^\circ$. In other words, the integration of the refractivity index along a specific ray is replaced by

the integration along the impact parameter of multiple rays.

Dividing both sides by $\sqrt{a^2 - a_1^2}$ gives

$$\frac{\alpha}{\sqrt{a^2 - a_1^2}} = \frac{2a}{\sqrt{a^2 - a_1^2}} \int_{x=a}^{x=\infty} \frac{1}{\eta \sqrt{x^2 - a^2}} \frac{d\eta}{dx} dx \quad (4.12)$$

where a_1 denotes the impact parameter that corresponds to the first ray $j = 1$ with the radius of closest approach $r_{0,1}$ at the tangent point. The integration of both sides between a_1 to ∞ yields

$$\int_{a=a_1}^{a=\infty} \frac{\alpha}{\sqrt{a^2 - a_1^2}} da = \int_{a=a_1}^{a=\infty} \frac{2a}{\sqrt{a^2 - a_1^2}} \left(\int_{x=a}^{x=\infty} \frac{1}{\eta \sqrt{x^2 - a^2}} \frac{d\eta}{dx} dx \right) da. \quad (4.13)$$

It follows that the lower limit of the inner integral on the right hand side can be replaced by $x = a_1$ and both integrals can be swapped under consideration that all a dependent terms must be collected in the inner integral. Applying these changes gives

$$\int_{a=a_1}^{a=\infty} \frac{\alpha}{\sqrt{a^2 - a_1^2}} da = \int_{x=a_1}^{x=\infty} \frac{d\eta}{\eta dx} \left(\int_{a=a_1}^{a=x} \frac{2a}{\sqrt{a^2 - a_1^2} \sqrt{x^2 - a^2}} da \right) dx. \quad (4.14)$$

The integrals can now be solved as

$$\begin{aligned} \int_{a=a_1}^{a=\infty} \frac{\alpha}{\sqrt{a^2 - a_1^2}} da &= \int_{x=a_1}^{x=\infty} \frac{d\eta}{\eta dx} 2 \left[\arcsin \left(\frac{a^2 - a_1^2}{x^2 - a_1^2} \right)^{\frac{1}{2}} \right]_{a=a_1}^{a=x} dx \\ &= \pi \int_{x=a_1}^{x=\infty} \frac{d\eta}{\eta dx} dx = \pi [\ln \eta]_{x=a_1}^{x=\infty} = \pi \left(\underbrace{0}_{\eta=1(\text{vacuum})} - \ln \eta(r_0) \right) \\ &= -\pi \ln \eta(r_0). \end{aligned} \quad (4.15)$$

Rearranging Eq. (4.15) leads to the **classical Abelian inversion**

$$\ln \eta(r_0) = -\frac{1}{\pi} \int_{a=a_1}^{a=\infty} \frac{\alpha}{\sqrt{a^2 - a_1^2}} da \quad (4.16)$$

as an expression for the refractivity index at r_0 depending on the bending angle α and the impact parameters a and a_1 . It shall be noted here, that the negative sign refers to a signal curvature as provided in Fig. 4.5 according to Fjeldbo et al. (1971) which is true for phase data ($\eta_\Phi < 1$) but may be inverted with respect to code measurements ($\eta_P > 1$) according to Eq. (3.17).

4.3 Electron density retrieval from GNSS data

It can generally be distinguished between two types of GNSS input observables that are suitable for the electron density retrieval process (García-Fernández, 2004), namely the Doppler shift and STEC. Electron density retrieval approaches for both observation types are described in the following sections.

4.3.1 Based on the Doppler shift

Electromagnetic signals experience a bending effect due to refractivity while passing the Earth's atmosphere. The refractivity index depends on pressure, humidity and temperature in the neutral atmospheric layers and on the electron density in the ionosphere. The bending angle of a signal can be derived from the Doppler shift as will be described in the following. Based on the Abel transform, the bending information can then be used to compute the refractivity and subsequently the ionospheric electron density. In this approach, precise orbits and clocks for the GNSS transmitter and LEO receiver are required to derive the range from L_1 or the ionosphere-free combination.

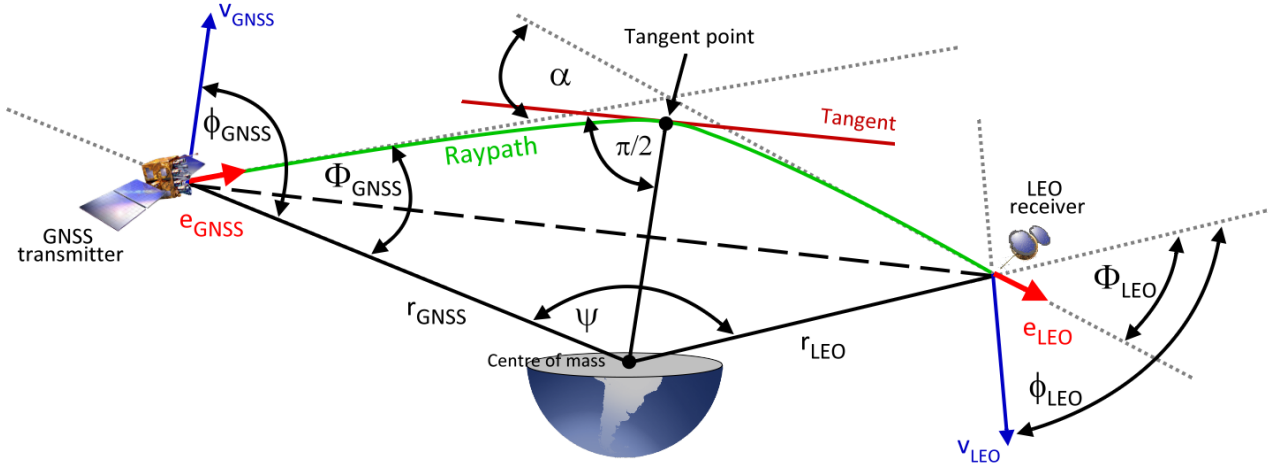


Figure 4.6: Occultation geometry for bending angle computation (design inspired by García-Fernández (2004)).

Following Fig. 4.6 and taking into account, that the sum of the inner angles in a quadrilateral yields always 2π , the expression

$$2\pi = \pi - \alpha + \Phi_{\text{LEO}} + \Phi_{\text{GNSS}} + \psi \quad (4.17)$$

allows to derive the bending angle α in case that Φ_{GNSS} , Φ_{LEO} and ψ are known. ψ can directly be obtained from the scalar product of the satellite positions. For the determination of Φ_{GNSS} and Φ_{LEO} , the Doppler shift D as a function of the radial velocity between the GNSS transmitter and LEO receiver is considered (García-Fernández, 2004). The frequency change Δf due to D can generally be computed from

$$\Delta f = -\frac{\Delta v}{c} f_0 \quad (4.18)$$

where f_0 is the frequency of the transmitted signal, c the speed of light and $\Delta v = v_{\text{LEO}} - v_{\text{GNSS}}$ the velocity of the receiver relative to the source. Equation (4.18) is valid if source and receiver move apart but the sign changes if they approach each other. With \mathbf{e}_{GNSS} and \mathbf{e}_{LEO} being unit vectors tangential to the ray path and located in the transmitter and receiver position, respectively, the Doppler shift can be expressed as

$$\Delta f = \frac{f_0}{c} (\mathbf{v}_{\text{GNSS}}^T \mathbf{e}_{\text{GNSS}} - \mathbf{v}_{\text{LEO}}^T \mathbf{e}_{\text{LEO}}). \quad (4.19)$$

Using the angle notations of Fig. 4.6, the scalar products in Eq. (4.19) can be rewritten as

$$\begin{aligned} \mathbf{v}_{\text{GNSS}}^T \mathbf{e}_{\text{GNSS}} &= v_{\text{GNSS}} \cos(\phi_{\text{GNSS}} - \Phi_{\text{GNSS}}) \\ \text{and } \mathbf{v}_{\text{LEO}}^T \mathbf{e}_{\text{LEO}} &= v_{\text{LEO}} \cos(\phi_{\text{LEO}} - \Phi_{\text{LEO}}) \end{aligned} \quad (4.20)$$

leading to

$$\Delta f = \frac{f_0}{c} (v_{\text{GNSS}} \cos(\phi_{\text{GNSS}} - \Phi_{\text{GNSS}}) - v_{\text{LEO}} \cos(\phi_{\text{LEO}} - \Phi_{\text{LEO}})). \quad (4.21)$$

The angles ϕ_{GNSS} and ϕ_{LEO} can be calculated from the scalar product of the satellite position and velocity vectors. Values for Φ_{GNSS} and Φ_{LEO} can then be derived from Eq. (4.21) together with Bouger's rule (Born and Wolf, 1999)

$$\text{constant} = \eta_{\text{GNSS}} r_{\text{GNSS}} \sin \Phi_{\text{GNSS}} = \eta_{\text{LEO}} r_{\text{LEO}} \sin \Phi_{\text{LEO}} \quad (4.22)$$

that implies a spherical symmetry assumption as one drawback of this approach. Thus, values for the refractive indices η_{LEO} and η_{GNSS} at the LEO and GNSS satellite positions are required. A common approach is the consideration of constrains $\eta_{\text{GNSS}} = \eta_{\text{LEO}} = 1$ implying that the plausibility of the assumption increases with rising orbit altitudes as η is approaching to one for an electromagnetic wave propagating in vacuum. Hajj and Romans (1998) stated that this assumption affects the final electron density retrieval by an overestimation of not more than 0.5%. Finally, the total bending angle can be solved by means of Eq. (4.17) from the computed angles Φ_{GNSS} , Φ_{LEO} and ψ .

Bending angle inversion

With the Abel integral equations, Eq. (4.10) and Eq. (4.16), a relationship between the total bending angle and the refractivity index has been derived. Equation (3.6) reads

$$\eta_{\Phi} = 1 - 40.3 \frac{N_e}{f^2} \quad (4.23)$$

and provides the definition of the refractivity as a function of the electron density in el/m^3 and signal frequency in Hz (Schreiner et al., 1999). Substituting Eq. (4.23) into Eq. (4.16) leads to the relation

$$N_e(r_0) = \frac{f^2}{40.3} \left(1 - \exp \left(-\frac{1}{\pi} \int_{a=a_1}^{a=\infty} \frac{\alpha}{\sqrt{a^2 - a_1^2}} da \right) \right) \quad (4.24)$$

allowing for the derivation of the electron density through the inverse Abel transform based on Doppler shift measurements. Equation (4.23) is valid to approximate only the first order ionospheric effects on the bending angle as already discussed in Subsection 3.2. However, errors due to the inversion in the retrieval process mask the degradations induced by no consideration of higher order influences (Hardy et al., 1993; Schreiner et al., 1999).

4.3.2 Based on STEC

The retrieval procedure under consideration of STEC input observations is based on the assumption, that the absolute bending angle due to ionospheric refraction is rather small. Following Hajj and Romans (1998), even during daytime and during high solar activity the bending angle of the L1 signal in ionospheric heights, in particular the F region, does not exceed 0.03° . A mismodeling of lower ionospheric layers such as the E layer cannot be excluded but the impact is significantly smaller than degradations originating from the spherical symmetry assumption. As depicted in Fig. 4.7, a straight line propagation of the signal between transmitter and receiver is assumed for the electron density retrieval from STEC data.

The geocentric distance at the TP on the LOS can be computed from

$$a = r_{\text{LEO}} \sin(90 - el) = r_{\text{LEO}} \cos(el) \quad (4.25)$$

as a function of the geocentric distance r_{LEO} of the LEO and the current signal elevation angle el . The definition of STEC as the integral of the electron density along the signal path s can generally be written as

$$\text{STEC}(TP) = \int_{x_{\text{TP}}}^{x_{\text{LEO}}} N_e(r) ds_{\text{LEO}} + \int_{x_{\text{TP}}}^{x_{\text{GNSS}}} N_e(r) ds_{\text{GNSS}} \quad (4.26)$$

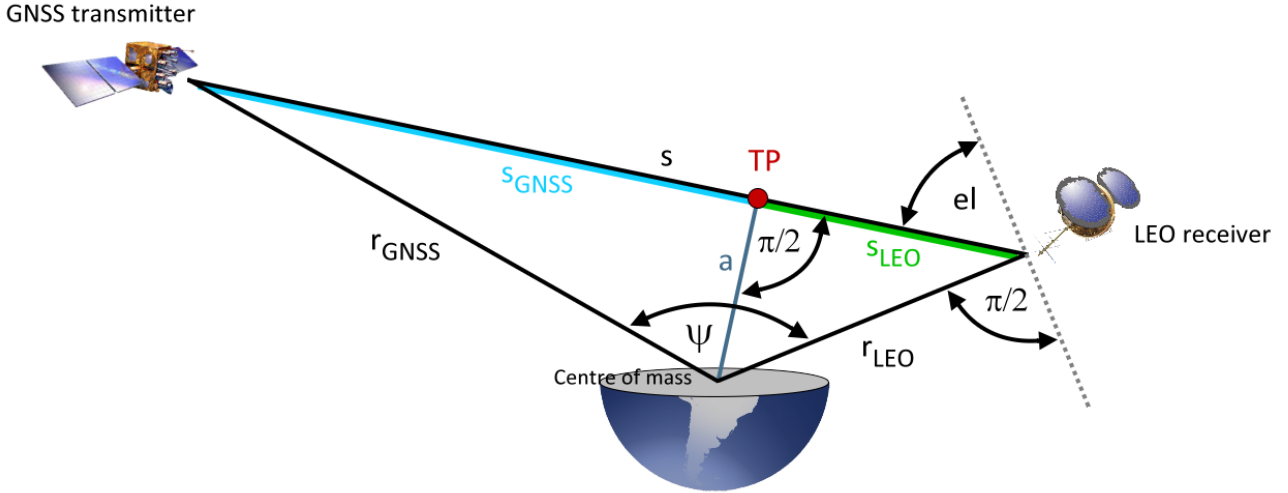


Figure 4.7: Occultation geometry under the assumption of straight line propagation.

with s indicating the LOS between transmitter and receiver. The integral limits x_{TP} , x_{LEO} and x_{GNSS} denote the TP, GNSS and LEO locations, respectively. Taking into account that a and r_{LEO} as well as a and r_{GNSS} are part of a right-angled triangle as visible from Fig. 4.7, the distances s_{LEO} and s_{GNSS} can be computed as

$$s_{LEO} = \sqrt{r_{LEO}^2 - a^2} \quad \text{and} \quad s_{GNSS} = \sqrt{r_{GNSS}^2 - a^2} \quad (4.27)$$

with the derivations

$$ds_{LEO} = \frac{r_{LEO}}{\sqrt{r_{LEO}^2 - a^2}} dr_{LEO} \quad \text{and} \quad ds_{GNSS} = \frac{r_{GNSS}}{\sqrt{r_{GNSS}^2 - a^2}} dr_{GNSS}. \quad (4.28)$$

With s_{LEO} and s_{GNSS} being partitions of s as the LOS connection between the GNSS and LEO satellite, Eq. (4.26) can be rewritten as

$$\text{STEC}(TP) = \int_{x_{TP}}^{x_{LEO}} \frac{N_e(r)r_{LEO}}{\sqrt{r_{LEO}^2 - a^2}} dr_{LEO} + \int_{x_{TP}}^{x_{GNSS}} \frac{N_e(r)r_{GNSS}}{\sqrt{r_{GNSS}^2 - a^2}} dr_{GNSS}. \quad (4.29)$$

Under consideration of spherical symmetry, Eq. (4.29) can then be simplified to

$$\text{STEC}(TP) = 2 \int_{x_{TP}}^{x_{LEO}} \frac{N_e(r)r_{LEO}}{\sqrt{r_{LEO}^2 - a^2}} dr_{LEO} + \text{STEC}_{TOP} \quad (4.30)$$

where STEC_{TOP} has been introduced to account for the ionospheric contribution above the LEO orbit, i.e., the partition of s between the LEO orbit height and the GNSS transmitter.

Recursive STEC inversion

The subsequent derivation of the STEC inversion method follows the description of P-III: Limberger et al. (2015) with similar nomenclature and is originally based on the developments presented in Hernández-Pajares et al. (2000).

For Eq. (4.30), the fundamentals of the classical Abel transform including the plane projection and spherical symmetry assumption have been taken into account. $\text{STEC}(TP)$ are input measurements derived from GNSS registrations. In order to solve Eq. (4.30), an onion shell structure depending

on the height of successive TPs as mean radii can be established for the discretization of the integral equation. It is assumed here, that the electron density within a specific shell is constant, parametrized only by the radius r . Thus, the thicknesses of different shells depend on the measurement sampling. It follows, that with a decrease of the sampling, the assumption of density constancy increasingly deviates from the truth. The geometrical setup is depicted in Fig. 4.8 as an example for two observation epochs. Green and blue arrows highlight the intervals between layer intersections and the

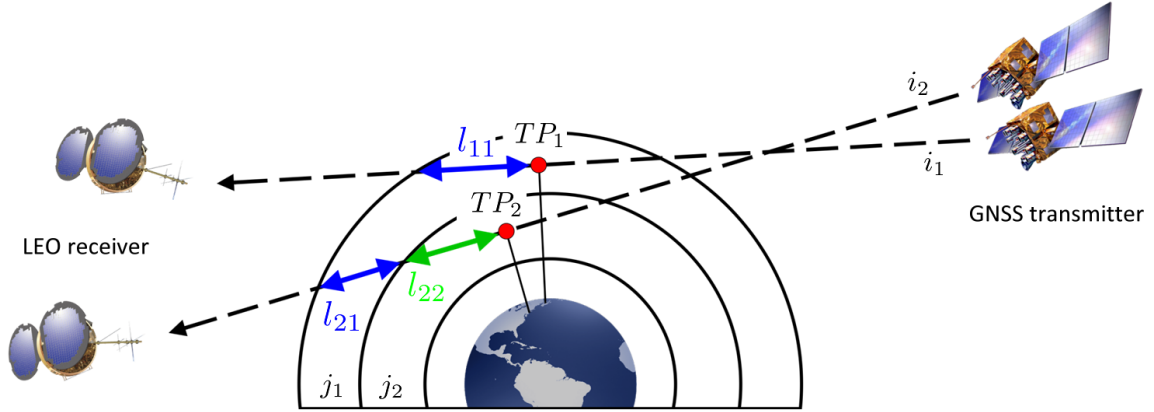


Figure 4.8: Integral discretization by means of the onion shell structure. Colored arrows illustrate the discretized integration steps between consecutive layers. This scheme shows the composition with measurements at two epochs i_1 and i_2 yielding the corresponding tangent points TP_1 and TP_2 that are located within the layers j_1 and j_2 .

tangent points are drawn as red dots. l_{ii} is the distance along the LOS between the TP_i at epoch i to the nearest layer boundary. l_{ij} are the pass lengths of the GNSS-LEO LOS at epoch i in shell j . It follows from Fig. 4.8 that $l_{ii} = l_{11}$ for the first epoch, $l_{ii} = l_{22}$ for the second epoch and j is counting from the outer towards the innermost shell where $j \leq i$. The full set of layers with $j \in \{j_1, j_2, \dots, j_N\}$ is consequently defined after collecting all measurements of a specific occultation pass. A solution of Eq. (4.30) can thus be approximated in discretized form with

$$\text{STEC}(TP_i) = 2l_{ii}N_e(TP_i) + \sum_{j=1}^{j=i-1} 2 \cdot l_{ij} \cdot N_e(TP_j) + \text{STEC}_{\text{TOP}}. \quad (4.31)$$

After collecting all data of an occultation pass, Eq. (4.31) can be solved recursively, starting from the outermost shell towards the innermost shell for the determination of electron density values along the tangent points.

Improved STEC inversion

The main drawback of the previously described inversion methods is the spherical symmetry assumption. Naturally, the horizontal extent between the impact parameters or TP can vary up to 10° in geographical longitude and latitude which corresponds to around 1,000 km. It is well known that the spherical symmetry assumption is one of the most significant error sources of the classical Abel inversion transform that degrades the N_e accuracy in particular in the presence of the EIA. This deficiency led to the situation that various facilities developed their own modified retrieval algorithms with different concepts to account for horizontal electron density variations in the data processing. Research facilities such as the UPC in Spain (Hernández-Pajares et al., 2000) or the Center for Space and Remote Sensing Research (CSRSR) in Taiwan (Tsai and Tsai, 2004) perform an independent retrieval based on improved Abel inversion techniques under consideration of horizontal ionospheric gradients.

The improved inversion developed by the Research Group of Astronomy and Geomatics (gAGE) of UPC is an efficient approach that allows for a relatively simple implementation into software applications. The method has already been described by different authors. Details about the mathematical fundamentals and validations have been published, for instance, by Hernández-Pajares et al. (2000), García-Fernandez et al. (2003) and Aragón-Ángel (2010). An assessment of the retrieved electron density profiles has been carried out by Aragón-Ángel et al. (2011). Since the method description is also contained in P-III: Limberger et al. (2015) as part of this thesis, it shall only briefly be described here.

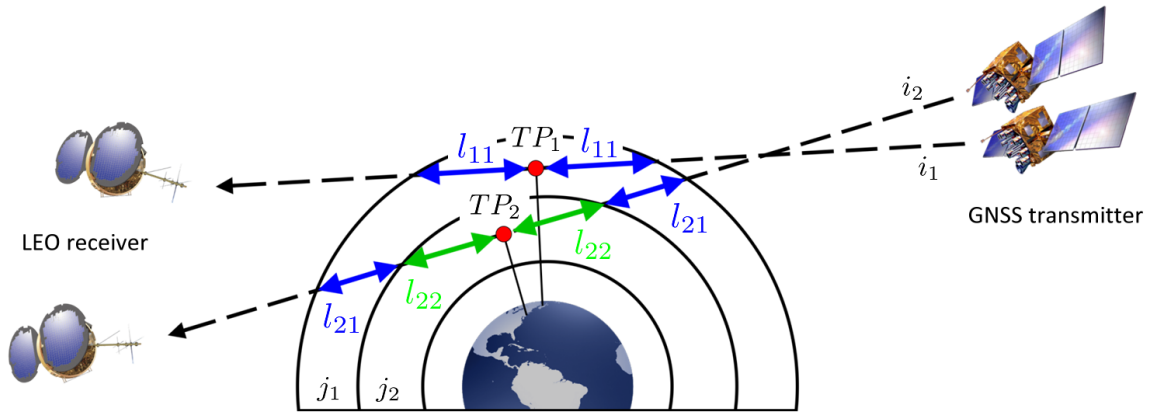


Figure 4.9: Improved setup for recursive STEC inversion under consideration of the separability hypothesis. Labels and notations are similar to Fig. 4.8.

To account for the drawback of spherical symmetry the separability hypothesis can be introduced with

$$N_e(\varphi, \lambda, h, t) = \text{VTEC}(\varphi, \lambda, t) \text{SF}(h). \quad (4.32)$$

It describes the N_e distribution as a function of VTEC and a shape function $\text{SF}(h)$ to account for horizontal and vertical gradients, respectively.

The substitution of $N_e(TP)$ by $\text{VTEC}(\varphi, \lambda, t) \text{SF}(TP)$ in Eq. (4.31) then leads to

$$\begin{aligned} \text{STEC}(TP_i) &= 2l_{ii}^{\text{TP}} \text{VTEC}_i^{\text{TP}} \text{SF}(TP_i) + \sum_{j=1}^{j=i-1} l_{ij} \left(\text{VTEC}_{ij}^{\text{LEO}} + \text{VTEC}_{ij}^{\text{GNSS}} \right) \text{SF}(TP_j) + \text{STEC}_{\text{TOP}} \end{aligned} \quad (4.33)$$

where $\text{SF}(TP_i)$ and $\text{SF}(TP_j)$ indicate the affiliation of the shape function to a specific TP. The VTEC values are specified by the different annotations TP, LEO and GNSS denoting the position to which the VTEC refers to. For instance, $\text{VTEC}_i^{\text{TP}}$ is related to the VTEC observed at the TP position while $\text{VTEC}_{ij}^{\text{LEO}}$ and $\text{VTEC}_{ij}^{\text{GNSS}}$ are the VTEC values at the layer intersection points in LEO and GNSS direction, respectively. It should be kept in mind that VTEC with

$$\text{VTEC}_{ij}^{\text{LEO}} = \text{VTEC}(\varphi_{ij}, \lambda_{ij}, t_i), \quad (4.34)$$

$$\text{VTEC}_{ij}^{\text{GNSS}} = \text{VTEC}(\varphi_{ij}, \lambda_{ij}, t_i) \quad (4.35)$$

$$\text{VTEC}_i^{\text{TP}} = \text{VTEC}(\varphi_i, \lambda_i, t_i) \quad (4.36)$$

refers to different horizontal positions such as the geographical latitude φ and longitude λ . This modified setup is depicted in Fig. 4.9 as an update of Fig. 4.8 by separating the LOS into a TP-LEO and TP-GNSS directed part. The unknown parameters of Eq. (4.33) are the SF values related to the different shells and tangent points, respectively. VTEC is assumed to be given and can be obtained from a background data set, e.g., based on GIMs provided by the IGS or its individual analysis centers.

The input observables are GNSS carrier-phase measurements allowing for the derivation of the geometry-free linear combination L_4 as described in Eq. (3.15) of the previous section. To eliminate the phase bias CPB_4 , differential STEC to a reference observation $L_{4,R}$ belonging to the same occultation pass are introduced. Thus, Eq. (4.33) can be rewritten as

$$\alpha^{-1}(L_{4j} - L_{4,R}) = 2l_{ii}^{\text{TP}} \text{VTEC}_i \text{SF}(TP_i) + \sum_{j=1}^{j=i-1} \left[l_{ij} \left(\text{VTEC}_{ij}^{\text{LEO}} + \text{VTEC}_{ij}^{\text{GNSS}} \right) \text{SF}(TP_j) \right] + \text{STEC}_{\text{TOP}} - \text{STEC}_R \quad (4.37)$$

where STEC differences are considered as input observables and CPB_4 cancels. Under the supposition that $L_{4,R}$ is affected only by a minor ionospheric refraction, the difference $\text{STEC}_{\text{TOP}} - \text{STEC}_R$ is negligibly. This assumption is acceptable in case that the LEO orbit altitude is high enough and the reference observation is chosen with an elevation angle, e.g., larger than 0° . For the F-3/C constellation with an orbit at approximately 800 km altitude this assumption can be applied but probably fails for other satellite missions like CHAMP or GRACE. Other strategies are the consideration of calibrated STEC or the iterative extrapolation of the shape function (Hernández-Pajares et al., 2000).

After collecting all measurements of an occultation pass, a triangular linear equation system can be established from Eq. (4.37) which is recursively solvable for the shape function. A least squares fit is not required. Finally, a vector containing shape function values of distinct heights related to the tangent points is determined. According to Eq. (4.32), electron density values can then be reconstructed under consideration of given VTEC information to account for horizontal gradients in the ionosphere. It shall be noted, that this approach even allows to generate electron density profiles in the nearby region of the occultation event under the assumption that the shape function maintains its validity.

5 Modeling the ionosphere

For the development of an ionosphere model, aiming the representation of key quantities on multidimensional scales, various criteria have to be taken into account. Amongst others, the choice for input data and the formulation of mathematical or physical descriptions for the parameter state and variations. Many aspects are addressed in the previous Chapters accounting for the processing of input measurements (Chapters 3 and 4) or the spatio-temporal representation (Chapter 2) of ionospheric target parameters (Chapter 1). The model approach considered for this dissertation will be described in the following Sections.

5.1 Categorization of models

A majority of established ionosphere models can, in principle, be categorized as climatological representations reflecting the regular variability of the ionosphere depending on the geographical location and solar activity or seasonal as well as diurnal trends. Ionospheric irregularities such as TIDs or solar storms are hardly taken into account by most models. A main reason is the trade-off that needs to be found between computational load and physical depth of the model. In abstract words, it follows that models are either of empirical nature driven by ionospheric sounding measurements or they include advanced physical mechanisms capable to describe ionospheric process interactions at the expense of an increased processing effort. Besides, there exist hybrid models aiming a compromise between profound physics and the processing of measurements.

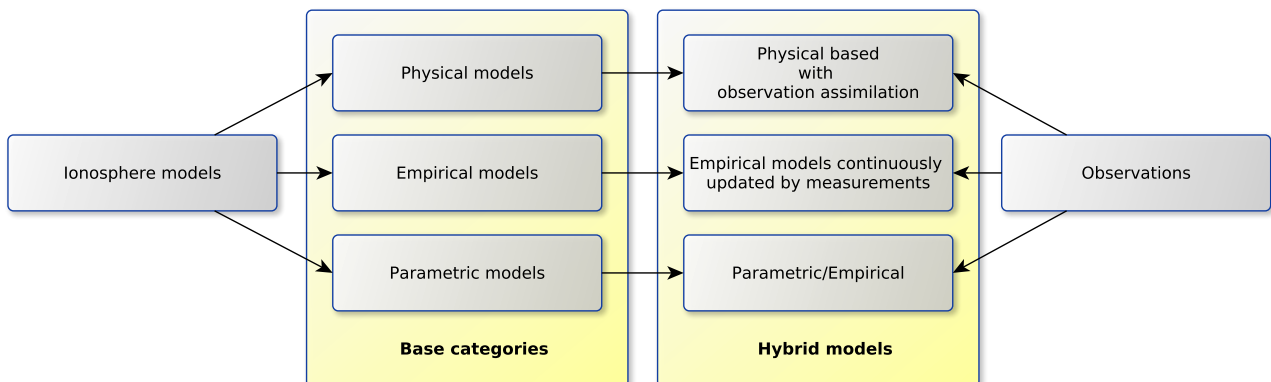


Figure 5.1: Categorization of ionosphere models.

In this work, a classification of three fundamental model types as base categories is defined by the differentiation into physical, empirical and parametric models as depicted in Fig. 5.1. Based on these model classes, the strategy of involving measurements, e.g., through assimilation techniques, gains importance and popularity in the last decades. The transition of a model from the physical or specifically empirical class into the assimilative state can be very smooth and the assimilation is rather a result of the model development progress and modernization.

The different data sets can, for instance, be assimilated into a background model, mostly a physical or empirical model, by the use of Kalman³¹ filter or sequential least squares techniques with Tikhonov³²

³¹Rudolf Emil Kálmán (born 19.05.1930) was a Hungarian-US-mathematician.

³²Andrey Nikolayevich Tikhonov (30.10.1906 - 07.10.1993) was a Russian mathematician.

regularization (Phillips, 1962; Tikhonov, 1963; Hansen, 1996). If the datasets are dense enough for resolving at least the ionospheric climatology and the model is able to properly handle the data gaps, a background model can possibly be omitted. For these models, usually rather simple but robust analytical base functions (e.g. related to the model parametrization as described in Chapter 2) are considered to derive a continuous spatio-temporal representation of the ionospheric state. In accordance to Fig. 5.1, these sort of models are henceforth denoted as hybrid models. Based on the identified categories, selected ionosphere models will be described briefly in the following.

Physical models

In physical models, physical laws and principles such as continuity, energy and momentum equations are taken into account and partial differential equations need to be solved. Such kind of models theoretically allow to detect ionospheric irregularities and follow the way of a consistent solution to describe Sun-Earth interactions. The processing effort is however significantly high, in particular for global modeling, making physical models rather unsuitable for operational applications and most geodetic purposes.

Physical models with extensive history of development and validation are, for instance,

- the **Time Dependent Ionospheric Model (TDIM)** (Schunk et al., 1986) developed at the Utah State University (USU),
- the **Coupled Thermosphere-Ionosphere Model (CTIM)** (Fuller et al., 1987) of the University College London and Sheffield University,
- the **Thermosphere Ionosphere General Circulation Model (TIGCM)** (Robble et al., 1988) of the National Center for Atmospheric Research (NCAR),
- the **Field Line Interhemispheric Plasma Model (FLIP)** (Richards and Torr, 1988) or
- the **Global Theoretical Ionospheric Model (GTIM)** (Anderson, 1971, 1973) that has been developed at the Geophysics Directorate of Phillips Laboratory.

A comparison of different physical models has e.g. been performed by Anderson et al. (1998).

Empirical models

In contrast to physical models, empirical models are driven by actual measurements as provided from one or even multiple observation systems during a long time period in the past that should at least cover a solar minimum and maximum. The aspect of having a sufficient data sensitivity, coverage and sampling to capture at least regular ionospheric structures plays a central role for empirical models. Typically, a set of model coefficients for describing the spatio-temporal ionospheric climatology are determined from the input data set.

Typical representative empirical models are

- the **Bent model** (Bent et al., 1972a,b) and
- the **International Reference Ionosphere (IRI)** (Bilitza, 2001; Bilitza and Reinisch, 2008; Bilitza et al., 2011).

Parametric models

A third class of models is characterized by the adaption of rather simple analytical functions to the results of extensive physical computations. This type is denoted as analytical or parametric model and

can be interpreted as a simplification of the physical models for the benefit of an increased processing efficiency.

Examples for parametric models are

- the **Fully Analytical Ionospheric Model (FAIM)** (Anderson et al., 1989) and
- the **Parameterized Ionospheric Model (PIM)** (Daniell et al., 1995).

Hybrid models

Hybrid models are able to represent at least the regular ionospheric structures and have the potential to resolve irregularities in case that they are detected by the assimilated observations. The time delay depends mainly on the measurement availability and the processing effort which is relatively low compared to physical models.

Empirical models with continuous measurement updates

- CODE is one of the IGS analysis centers and routinely processes GPS and GLONASS data to model GIMs with two hour and more recently with one hour sampling. The spatial resolution of the GIMs is fixed at 2.5° latitude and 5° according to the IGS standards. This model can be denoted as **CODE ionosphere model**. Its spatial representation is based on a spherical harmonic expansion of degree and order 15 resulting in 256 model coefficients determined in a solar-magnetic reference frame. The time domain is considered through piecewise linearity. In case of 2 hour sampling, the time vertices are ± 1 hour around the snapshot time. No background model is taken into account. Daily instrumental biases are determined under consideration of a zero mean condition for the satellite DCBs. Furthermore, CODE provides 1-day, 2-day and 5-day predictions resulting from a trend analysis as described in Schaer (1999).
- The **Tomographic Ionosphere Model (TOMIOM)** (Juan et al., 1997; Hernández-Pajares et al., 1999) has been developed at the UPC and bases upon a grid approach as described in Section 2.2 with double layered voxel shells. The model resolution is based on the voxel size and can be increased, e.g. by means of a Kriging³³ interpolation. In the current state, TOMIOM includes the feasibility to process GNSS, radio occultations and ionosonde data. UPC belongs to the ionospheric analysis centres for the IGS contributing GIMs of different temporal sampling generated with TOMIOM (Hernández-Pajares et al., 2009).
- ESA, in particular the European Space Operation Center (ESOC), is also an IGS analysis center and has developed the **Ionosphere Monitoring Facility (IONMON)** to describe ionospheric structures by means of vertical electron density profiles with varying scale heights based on the Chapman function (Feltens, 1998) in combination with horizontal surface functions (Feltens, 2007; Feltens et al., 2011). The model is feasible to process GNSS data in combination with electron density profiles derived from radio occultations and thus includes a TEC integrator. IONMON does not consider a background model and consequently the quality suffers in regions of poor data coverage.
- The JPL completes the four analysis center of the IGS. The model developed at JPL, henceforth **JPL model**, provides TEC at the vertices of an almost uniform grid where the temporal TEC evolution at each vertex is stochastically considered (Mannucci et al., 1998). The spatial data representation is carried out by means of locally supported functions based on the interpolation of TEC within uniformly distributed triangular tiles (Mannucci et al., 1999). Another representation method, that is used by JPL for an operational global mapping system, considers bicubic splines as spatially smoother functions.

³³Danie Gerhardus Krige (26.08.1919-03.03.2013) was a South African engineer for geostatic

Additionally, the **New Ionosphere Climatology 09 (NIC09)** has been developed as another climatological TEC model intended mainly to derive ionospheric corrections for altimetry processing. NIC09 originates from a fit to the JPL maps that matches at the level of 4.5 TECU (Scharoo and Smith, 2010).

- By means of Epstein functions for different ionospheric layers (E, F1, F2), the **NeQuick model** models the global electron density (Di Giovanni and Radicella, 1990; Nava et al., 2008; Radicella, 2009). The model has been developed at the Aeronomy and Radiopropagation Laboratory (now T/ICT4D Laboratory) of the Abdus Salam International Center for Theoretical Physics (ICTP) in Trieste, Italy, in collaboration with the Institute for Geophysics, Astrophysics and Meteorology of the University of Graz, Austria. The model uses monthly sets of coefficients provided by the International Telecommunication Union - Radiocommunication (ITU-R) reflecting seasonal and solar cycle variations of the maximum electron density. NeQuick will be incorporated as the correction model for the European GALILEO system where daily model coefficients will be broadcasted with the satellite navigation message.
- The **Neustrelitz TEC Model (NTCM)** of the Institute of Communications and Navigation at the DLR in Neustrelitz has particularly been developed for operational usage and takes only 12 model coefficients into account to describe the main ionospheric features (Jakowski et al., 2011). Diurnal, semidiurnal, annual, semiannual, latitude, solar zenith angle and solar activity dependence are modeled in terms of a polynomial. Originally, input data of the European IGS stations were processed to establish a TEC database covering more than a solar cycle. However, the model has recently been updated for the global operation where CODE GIMs have been used to estimate the NTCM model coefficients.
- The **Electron Density Assimilative Model (EDAM)** of QinetiQ (UK) aims the assimilation of measurements into the IRI 2007 background model, in particular GNSS data from the IGS network and more recently also occultation data (Angling, 2004; Angling and Khattatov, 2006; Angling, 2008). The combination strategy is based on a weighted least squares estimation taking the differences of the initial state (the background data) to the actual observations into account.

Physical models with observation assimilation

- Following a physics-based assimilative procedure, the **Utah State University Global Assimilation of Ionospheric Measurements (USU-GAIM)** model includes a Gauß-Markov³⁴ Kalman filter (Thompson et al., 2006) to incorporate a set of diverse Near Real Time (NRT) measurements. The physical component is realized by means of the Ionosphere Forecast Model (IFM) that globally covers the E- and F-region. Input parameters are, e.g., the solar radio flux F10.7, geomagnetic KP and AP indices as well as empirical parameters for the neutral wind, electric field, auroral precipitation, solar Extreme Ultraviolet (EUV) and resonantly scattered radiation. Details on USU-GAIM can be found in Schunk et al. (2004).

Parametric/Empirical models

- **FAIM** is based on the formalism of the ionosphere model published by Ching and Chiu (1973), expresses the time variation by means of a Fourier³⁵ series up to order six and has been extended in 1997 by the empirical **Gallagher plasmasphere model** (Gallagher et al., 1988). Due to the synergy of parametric and empirical modeling, the extended FAIM can be classified as a hybrid model.

The modeling procedure presented in this thesis aims at the combination of various satellite-based observation techniques to determine the electron density distribution by means of a least squares

³⁴ Andrei Andrejewitsch Markov (02.06.1856 - 20.07.1922) was a Russian mathematician.

³⁵ Jean Baptiste Joseph Fourier (21.03.1768 - 16.05.1830) was a French mathematician and physician.

adjustment or Variance Component Estimation (VCE), i.e., the base character of the model can be identified as empirical or assimilative. The vertical electron density distribution is approximated by an α -Chapman function as introduced in Section 1.5 and for the spatio-temporal interpolation, B-spline base functions as described in Section 2.3 are taken into account. The method has been described in P-I: Limberger et al. (2013) with first comparative validations of the model against CODE GIMs. Further studies have been performed by P-II: Limberger et al. (2014), P-V: Liang et al. (2014) and P-VI: Liang et al. (2015). Complementary to these publications, the model approach will be described in detail now.

5.2 Observation equations for the discrete and integrated electron density

Selected ionospheric key quantities have been introduced in Chapter 1, specifically the

- Chapman parameters ($N_{e_{\max}}, h_{\max}, H$),
- electron density (N_e) and
- integrated electron density as the total electron content (TEC)

with their interrelation defined in Section 1.6. It was concluded that the Chapman parameters can be used to describe the N_e distribution and TEC results from the integration of the N_e .

Furthermore, different satellite based measurement techniques have been introduced in the Chapters 3 and 4 allowing for the observation of TEC (GNSS, DORIS, Altimetry) and N_e (radio occultations) and thus, a functional relation between the input measurements and the Chapman parameters can be defined.

A common representation of the vertical electron density N_e distribution for specific ionospheric layers is provided through the α -Chapman function as introduced in Eq. (1.26) of Chapter 1. It is defined by the three descriptive parameters $N_{e_{\max}}$ as the maximum density, h_{\max} identifying the corresponding peak height and H as the layer scale height. With respect to the F2 layer as the most prominent region of the ionosphere, the formulation

$$N_e = NmF2 \exp\left(\frac{1}{2} \left(1 - \frac{h - hmF2}{HF2} - \exp\left(-\frac{h - hmF2}{HF2}\right)\right)\right) \quad (5.1)$$

according to Eq. (1.27) is obtained. As can be seen from the top right panel of Fig. 1.8, a narrow and vertically rather localized layer can be described by a small scale height while a large scale height opens the profile function for a smoother transition of the layer at the lower and upper boundaries. In reality, the bottom (below h_{\max}) and topside (above h_{\max}) profiles may differ naturally. Regarding the F2 representation, in particular the transition from ionosphere into the plasmasphere in the topside region plays a central role. Therefore, different scale heights with respect to the bottom and topside representation or even an altitude-dependent scale height may be introduced. Improved descriptions have, for instance, been published by Reinisch et al. (2007) and Nsumei (2012) as vary-chap profiles including a height-dependent scale height for the topside representation. Another method was published by Di Giovanni and Radicella (1990) and Leitinger et al. (2005) where the sum of so-called semi-Epstein³⁶ layers is considered to model the E, F1 and F2 layers. The use of Epstein functions (Epstein, 1906) has firstly been proposed by Rawer (1963) and is integrated in the NeQuick electron density model that will operationally be implemented in the GALILEO system.

Stankov and Jakowski (2005) and Jakowski (2005) proposed an alternative method where a transition function between the F2 layer and plasmasphere is considered as an extension of the α -Chapman

³⁶Paul Epstein (24. Juli 1871 - 11. August 1939) was a German mathematician.

profile. Equation (5.1) can then be reformulated to

$$N_e = \underbrace{NmF2 \exp \left(0.5 \left(1 - \frac{h - hmF2}{HF2} - \exp \left(-\frac{h - hmF2}{HF2} \right) \right) \right)}_{\alpha\text{-Chapman for F2 layer description}} + \underbrace{NOP \exp \left(-\frac{|h - hmF2|}{HP} \right)}_{\text{Transition between F2 layer and plasmasphere}}. \quad (5.2)$$

The set of original Chapman parameters is extended by two more quantities only: the plasmasphere basis density NOP and the plasmasphere scale height parameter HP . The extended Chapman profile is a simple but efficient formulation to indirectly account for the necessity of a second or altitude dependent scale height, although the physical meaning of the plasmasphere parameters is rather questionable. Following Jakowski (2005), reasonable values for HP and NOP can be introduced with $HP = 10^4$ km and $NOP = \gamma NmF2$ where proportionality between $NmF2$ and N_0^P , controlled by the scaling factor γ , is supposed. Here, the F2 scale height is still invariant with height but the function shape nevertheless benefits from the slowly decaying plasmaspheric exponential term.

From ionospheric radio occultations, discrete electron density observations can be retrieved as described in Chapter 4. Consequently, the Chapman equation can directly be considered to formulate the relation between measurements and unknowns. GNSS, DORIS and altimetry on the contrary provide TEC, i.e., the integrated electron density as introduced with Eq. (1.28), leading to the demand for an integration function to solve

$$\text{STEC} = \int_{x_r}^{x^s} N_e ds = \int_{x_r}^{x^s} \left(NmF2 \exp \left(\frac{1}{2} \left(1 - \frac{h - hmF2}{HF2} - \exp \left(-\frac{h - hmF2}{HF2} \right) \right) \right) + NOP \exp \left(-\frac{|h - hmF2|}{HP} \right) \right) ds. \quad (5.3)$$

The integral boundaries are defined by the satellite transmitter x^s and receiver x_r and the integration has to be performed along the (curved) raypath. For altimetric VTEC, x_r identifies the water surface

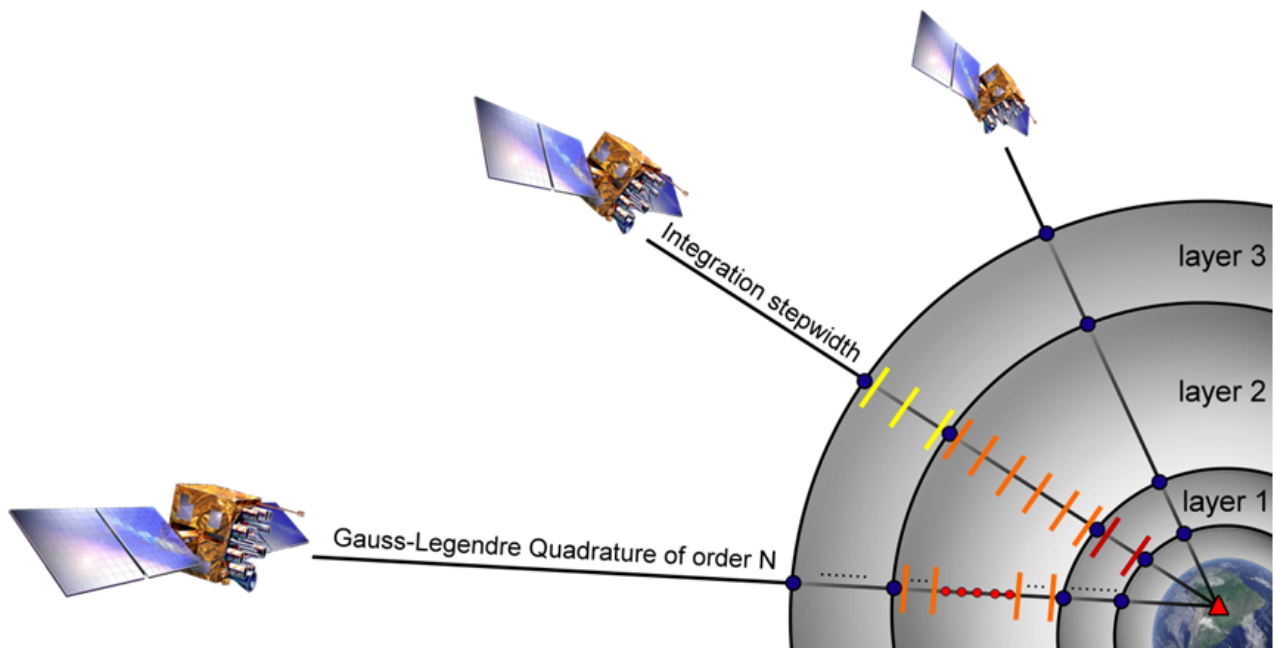


Figure 5.2: Layer composition for the extended Gauß-Legendre integration of the electron density for the computation of TEC.

point on Earth in nadir direction of the satellite. To integrate numerically in the 3-D space, an extended Gauß³⁷-Legendre³⁸ Quadrature is applied. A similar approach has been considered by Zeilhofer et al. (2008).

Therefore, the Earth ionosphere is firstly approximated by three different layers as depicted in Fig. 5.2. The layer boundaries are chosen to separate the lower atmosphere with less ionization (e.g. between 80 km and 200 km) from the F2 and plasmasphere transition region (e.g. 200 km - 1,000 km) and the upper atmosphere including mainly the less ionized plasmaspheric layers (e.g. 1,000 km - 2,000 km). The lowermost and uppermost boundaries are chosen at heights where the electron content is negligible for the TEC derivation. Afterwards, each synthetic layer is decomposed into a set of integration intervals defined by a given integration step width. The selection of an adequate step width orients on the ionospheric gradients that are expected within the three synthetic layers, i.e., typically a small step width for layer 2 and larger ones for layer 1 and 3 are chosen. In this work, the input step width refers to a vertical integration path and is transformed to the slant by

$$SW_s = \begin{cases} SW_v / \sin el & \text{if } 30^\circ \leq el < 90^\circ \\ SW_v / \sin 30 & \text{if } el < 30^\circ \end{cases} \quad (5.4)$$

where SW_s and SW_v are the slant and vertical stepwidth, respectively, and el is the elevation angle of the ray. Each integration interval is finally integrated by the classical Gauß-Legendre method of order N . This method yields the approximation of the integration interval as a sum of given sample values at N so-called knot points (or nodal points) $n_i \in \{n_1, \dots, n_N\}$ with positive-valued weights $w \in \{w_1, \dots, w_N\}$. The knot points are derived from the zeros of the Legendre polynomials L_N . With the given knot points, the individual weights are then calculated from

$$w_i = \int_{-1}^1 \prod_{j=1, j \neq i}^N \frac{n - n_j}{n_i - n_j} dn \quad \text{for } 1 \leq i \leq N \quad (5.5)$$

leading to the approximation of the integral as

$$I_f = \int_{P1}^{P2} f(n)w(n)dn \approx \sum_{i=1}^N f(n_i)w_i \quad (5.6)$$

where P1 and P2 are the boundaries defined by the integration interval.

In order to assess the performance of this integration method at varying step widths and quadrature orders, different test scenarios have been analyzed. For instance, the positions of GPS satellites together with five GPS tracking stations in South America belonging to the SIRGAS network have been

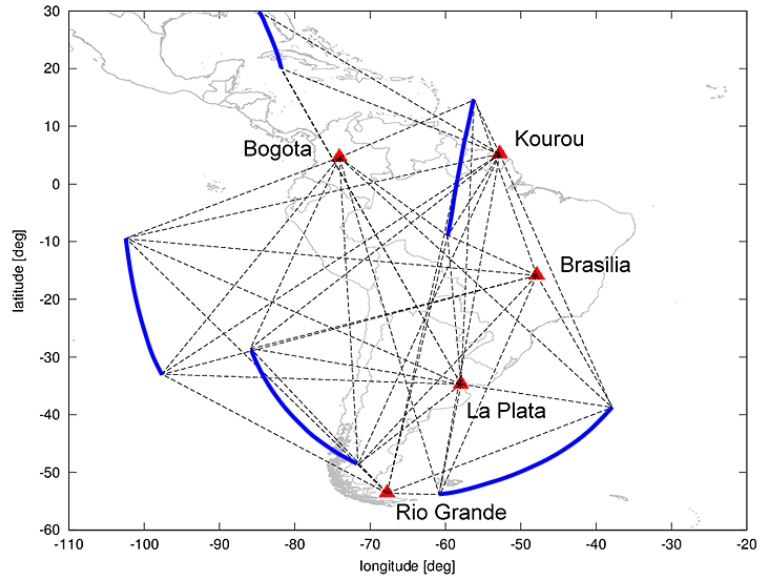


Figure 5.3: Geometrical ray path distribution including five Sistema de Referencia Geocéntrico para Las Américas (SIRGAS) network stations (red triangles) tracking five GPS satellites passes (blue).

³⁷Johann Carl Friedrich Gauß (30.04.1777 - 23.02.1855) was a German mathematician, astronomer, geodesist and physicist.

³⁸Adrien-Marie Legendre (18.09.1752 - 10.01.1833) was a French mathematician.

considered to simulate a realistic geometrical ray path distribution. For one hour data between 06:00 UT and 07:00 UT at 1 July 2002, the geometry of five GPS satellite passes is shown by Fig. 5.3. Satellite passes are depicted as blue lines and receivers as red triangles where pass start- and end-points are connected by dashed lines. From these stations, totally 2,404 synthetic TEC observations according to the epochs provided by their RINEX data are generated with 30 s sampling according to Eq. (5.3). The Chapman parameters are derived from IRI data while the integration is adjusted with $N = 9$ and 1 km step width fixed for all three layers to obtain a synthetic reference solution for the validation of the internal accuracy. The Root Mean Square (RMS) of the reference solution for this selected testbed yields 21.85 TECU.

Afterwards, integrations are performed with varying vertical step widths of 20 km, 40 km, 60 km and 80 km and different quadrature order $N \in \{3, 5, 7, 9\}$. Figure 5.4 depicts the comparison of the RMS values related to the TEC differences (green bars) and the processing time (blue bars). The darker the color, the smaller the step width and consequently, the computation time decreases with decreasing quadrature order and increased step width. The RMS on the contrary increases with the step width and decreasing order. In this internal validation, it can be seen that the RMS values are permanently small while the processing time must be considered as the limiting factor, in particular since the results here are based on only 2,404 observations. Typically, a maximum quadrature level of $N = 6$ was considered in this work. A vertical step width of 20 km was assigned for the second layer to account for increased ionospheric gradient and larger step widths between 60 km and 80 km are commonly chosen for the first and third layer.

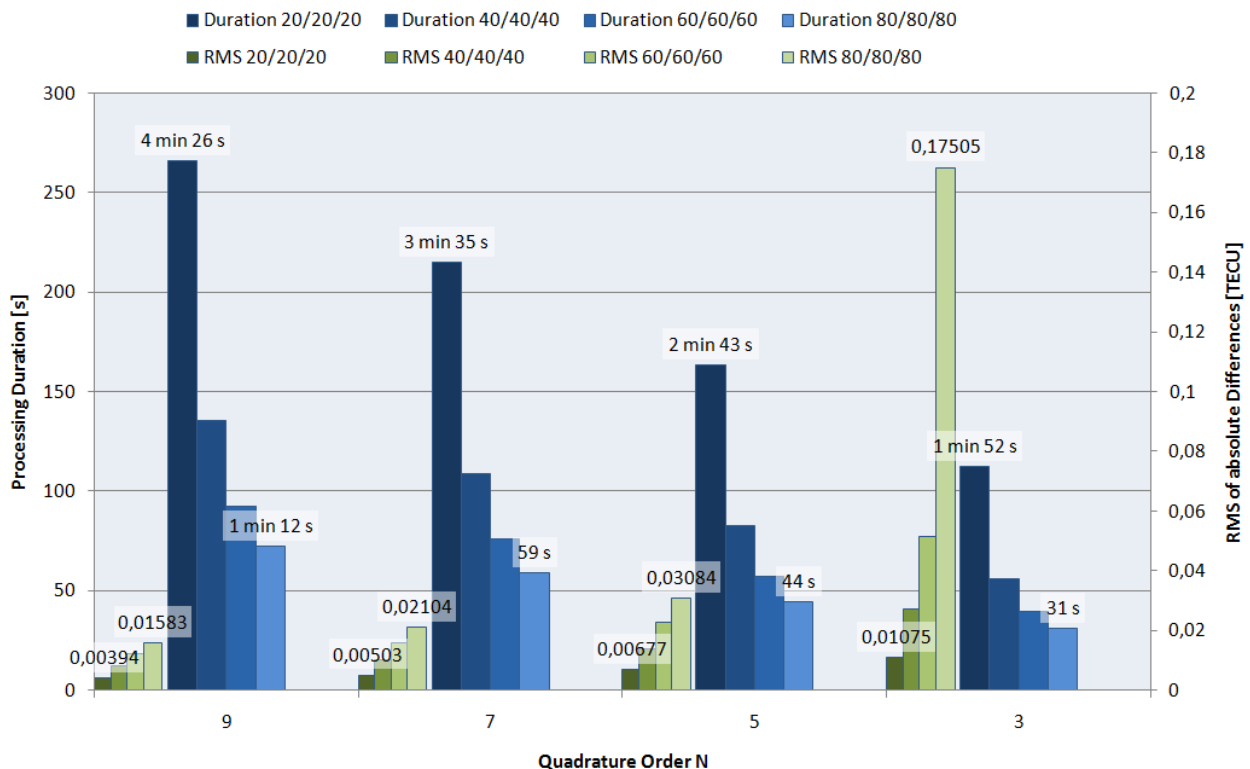


Figure 5.4: Comparison of processing effort in computation time (blue bars) with the RMS of TEC differences (green bars) for different quadrature orders and integration step widths in a simulated scenario.

5.3 Parameter estimation

The adjustment procedure aiming the estimation of key parameters is based on the method of least-squares to solve an overdetermined linear equation system following the Gauß-Markov theory (Koch,

1999; Niemeier, 2008). The linear deterministic model describing the functional relation between the observations and unknown target parameters is defined by

$$\underset{(N \times 1)}{\mathbf{l}} + \underset{(N \times 1)}{\mathbf{e}} = \underset{(N \times U)(U \times 1)}{\mathbf{A}} \underset{(N \times 1)}{\mathbf{x}} \quad (5.7)$$

where $\mathbf{l} = [l_1, l_2, \dots, l_N]^T$ contains the input observations, $\mathbf{e} = [e_1, e_2, \dots, e_N]^T$ denotes randomly distributed measurement errors and \mathbf{A} is the real-numbered coefficient or design matrix. The unknown target parameters are collected in the vector $\mathbf{x} = [x_1, x_2, \dots, x_U]^T$. N and U are introduced here as the number of observations and unknowns, respectively. In case that the dependencies $\mathbf{f}(\mathbf{x}) = \mathbf{l} + \mathbf{e}$ are given as non-linear functions, a Taylor³⁹ series expansion must be applied to linearize each equation f_i around the point \mathbf{x}_0 of initial values with

$$f_i(\mathbf{x}_0 + \Delta\mathbf{x}) = f_i(\mathbf{x}_0) + \left| \frac{\partial f_i(\mathbf{x})}{\partial \mathbf{x}} \right| \Delta\mathbf{x} \quad (5.8)$$

under negligence of second $O((\Delta\mathbf{x})^2)$ and higher order terms. The partial derivatives are collected in the Jacobian⁴⁰ matrix \mathbf{A} .

Associated with Eq. (5.7), the stochastic part of the Gauß-Markov model is defined as

$$\underset{(N \times N)}{\boldsymbol{\Sigma}_{ll}} = \sigma_0^2 \underset{(N \times N)}{\mathbf{P}_{ll}}^{-1} = \sigma_0^2 \underset{(N \times N)}{\mathbf{Q}_{ll}} \quad (5.9)$$

where \mathbf{P}_{ll} is the positive-definite observation weight matrix and σ_0^2 the initially unknown variance factor. $\boldsymbol{\Sigma}_{ll}$ identifies the covariance matrix that contains the standard deviations σ_i and correlation coefficients ρ of the observations such that

$$\boldsymbol{\Sigma}_{ll} = \begin{bmatrix} \sigma_1^2 & \rho_{12}\sigma_1\sigma_2 & \cdots & \rho_{1N}\sigma_1\sigma_N \\ \rho_{21}\sigma_2\sigma_1 & \sigma_2^2 & & \vdots \\ \vdots & & \ddots & \\ \rho_{N1}\sigma_N\sigma_1 & \cdots & & \sigma_N^2 \end{bmatrix}. \quad (5.10)$$

The inverse of \mathbf{P}_{ll} is often denoted as cofactor matrix \mathbf{Q}_{ll} . In case that no correlations between observations are taken into account, the matrices \mathbf{P}_{ll} , \mathbf{Q}_{ll} and consequently also $\boldsymbol{\Sigma}_{ll}$ have a diagonal structure including only the individual observation variances along the diagonal. For equally weighted, uncorrelated observations it follows that \mathbf{P}_{ll} can be set to the unit matrix \mathbf{I} .

In Section 5.2, the fundamental observation equations for the electron density and TEC have been introduced by means of the Eqs. (5.2) and (5.3). Due to the exponential term contained in the Chapman function, the dependencies are non-linear and need to be linearized to comply with the conditions of the Gauß-Markov model. According to the system of linear relations of Eq. (5.7), each measurement can be described by means of Eq. (5.8) with

$$l_i + e_i = f_i(\mathbf{x}_0 + \Delta\mathbf{x}) = f_i(\mathbf{x}_0) + \sum_{j=1}^U \left(\frac{\partial f_i}{\partial x_j} \right)_{\mathbf{x}_0} \Delta x_j \quad (5.11)$$

where \mathbf{x}_0 indicates the linearization point that is defined by a priori information. Now, a linear system of equations with

$$\mathbf{L} + \mathbf{e} = \mathbf{A}\Delta\mathbf{x} \quad (5.12)$$

³⁹ Brook Taylor (18.08.1685-29.12.1731) was a British mathematician and member of the royal society.

⁴⁰ After Carl Gustav Jacob Jacobi (10.12.1804-18.02.1851), a German mathematician.

can be established including the reduced observation vector $\mathbf{L} = \mathbf{l} - \mathbf{f}(\mathbf{x}_0)$ and the design matrix

$$\mathbf{A}_{(N \times U)} = \begin{bmatrix} a_{11} & a_{12} & \cdots & a_{1U} \\ a_{21} & \ddots & & \vdots \\ \vdots & & & \\ a_{N1} & \cdots & & a_{NU} \end{bmatrix} \quad \text{where} \quad a_{ij} = \left(\frac{\partial f_i}{\partial x_j} \right)_{\mathbf{x}_0}. \quad (5.13)$$

Following the principle of minimum as postulated by the method of least squares, the errors

$$\mathbf{e} = \mathbf{A}\Delta\mathbf{x} - \mathbf{L} \quad \text{shall satisfy the minimum condition for} \quad \mathbf{e}^T \mathbf{P}_{ll} \mathbf{e}. \quad (5.14)$$

A minimum can be found at the zeros of the first derivative of $\mathbf{e}^T \mathbf{P}_{ll} \mathbf{e}$ which is true for $\mathbf{A}^T \mathbf{P}_{ll} \mathbf{A} \Delta\hat{\mathbf{x}} \stackrel{!}{=} \mathbf{A}^T \mathbf{P}_{ll} \mathbf{L}$. The product $\mathbf{A}^T \mathbf{P}_{ll} \mathbf{A}$ is commonly identified as normal equation matrix, henceforth denoted as **NEQ**. If **NEQ** is of full rank and thus invertible, a solution for the unknown parameters can be found with

$$\Delta\hat{\mathbf{x}} = (\mathbf{A}^T \mathbf{P}_{ll} \mathbf{A})^{-1} \mathbf{A}^T \mathbf{P}_{ll} \mathbf{L} \quad (5.15)$$

as the Best Linear Unbiased Estimation (BLUE) (Koch, 1999).

Observation equation

The theory shall now be applied to determine the electron density or TEC, respectively. The emphasis is on the modeling of the F2 layer by estimating the F2 Chapman parameters. The Eqs. (5.2) and (5.3) describe the relation between the Chapman parameters and the observations. The plasmasphere parameters have been approximated by constant values with physical meaning. Following Jakowski (2005), a reasonable value of 10^4 km for HP (in the case of $h > hmF2$, otherwise 10 km) and the assumption of proportionality between $N0P$ and $NmF2$ can be taken into account. The following steps can of course also be applied for other ionospheric layers and the parameter basis may be extended by additional unknowns.

With

$$f_i(\mathbf{x}) = N_e(NmF2, hmF2, HF2) \quad \text{or} \quad f_i(\mathbf{x}) = \int_{x_r}^{x^s} N_e(NmF2, hmF2, HF2) ds, \quad (5.16)$$

the observation vector \mathbf{l} contains electron density or TEC measurements depending on the input data of the ionospheric sounding technique.

Under consideration of the linearization point $\mathbf{x}_0 = (NmF2|_0, hmF2|_0, HF2|_0)^T$, the electron density can be modeled as

$$\underbrace{l_i + e_i - N_{e,i}(\mathbf{x}_0)}_{L_i} = \left[\frac{\partial N_{e,i}}{\partial NmF2} \Big|_{\mathbf{x}_0} \right] \Delta NmF2 + \left[\frac{\partial N_{e,i}}{\partial hmF2} \Big|_{\mathbf{x}_0} \right] \Delta hmF2 + \left[\frac{\partial N_{e,i}}{\partial HF2} \Big|_{\mathbf{x}_0} \right] \Delta HF2 \quad (5.17)$$

taking the Chapman profile function into account to represent the vertical distribution. For modeling the horizontal and temporal variation, a B-spline parametrization as specified in Section 2.3 is applied. Polynomial B-splines have, for instance, been considered by Schmidt et al. (2008) and Zeilhofer et al. (2008) for modeling the regional GPS TEC. P-I: Limberger et al. (2013) incorporated the Chapman profile into the approach to represent regional electron density from occultation data. Furthermore, Schmidt et al. (2011) and P-IV: Dettmering et al. (2014b) applied a combination of trigonometric and polynomial B-splines for modeling the global TEC distribution based on GPS and DORIS measurements, respectively.

Each Chapman key parameter is decomposed into tensor products of three one-dimensional B-splines with respect to latitude φ , longitude λ and time t . The reference systems are typically defined in an Earth- or Sun-fixed frame and therefore φ identifies the geographical or geomagnetic latitude and λ the geographical or Sun-fixed longitude (= local time). Based on the general notation κ_h with $h \in \{1, 2, \dots, H\}$ which is henceforth used to identify the key parameters, the B-spline representation yields

$$\kappa_h(\lambda, \varphi, t) = \begin{cases} \sum_{k_1=1}^{K_1} \sum_{k_2=1}^{K_2} \sum_{k_3=1}^{K_3} d_{k_1, k_2, k_3}^{J_1, J_2, J_3} \phi_{k_1}^{J_1}(\varphi) \phi_{k_2}^{J_2}(\lambda) \phi_{k_3}^{J_3}(t) & \text{regional} \\ \sum_{k_1=1}^{K_1} \sum_{k_2=1}^{K_2} \sum_{k_3=1}^{K_3} d_{k_1, k_2, k_3}^{J_1, J_2, J_3} \phi_{k_1}^{J_1}(\varphi) T_{k_2}^{J_2}(\lambda) \phi_{k_3}^{J_3}(t) & \text{global} \end{cases}. \quad (5.18)$$

For regional applications, the F2 Chapman parameters, $NmF2$, $hmF2$ and $HF2$, are thus represented as

$$\kappa_1(\varphi, \lambda, t)_R = NmF2(\varphi, \lambda, t)_R = \sum_{k_1=1}^{K_1} \sum_{k_2=1}^{K_2} \sum_{k_3=1}^{K_3} (d_{k_1, k_2, k_3}^{J_1, J_2, J_3})_{NmF2} \phi_{k_1}^{J_1}(\lambda) \phi_{k_2}^{J_2}(\varphi) \phi_{k_3}^{J_3}(t) \quad (5.19)$$

$$\kappa_2(\varphi, \lambda, t)_R = hmF2(\varphi, \lambda, t)_R = \sum_{k_1=1}^{K_1} \sum_{k_2=1}^{K_2} \sum_{k_3=1}^{K_3} (d_{k_1, k_2, k_3}^{J_1, J_2, J_3})_{hmF2} \phi_{k_1}^{J_1}(\lambda) \phi_{k_2}^{J_2}(\varphi) \phi_{k_3}^{J_3}(t) \quad (5.20)$$

$$\kappa_3(\varphi, \lambda, t)_R = HF2(\varphi, \lambda, t)_R = \sum_{k_1=1}^{K_1} \sum_{k_2=1}^{K_2} \sum_{k_3=1}^{K_3} (d_{k_1, k_2, k_3}^{J_1, J_2, J_3})_{HF2} \phi_{k_1}^{J_1}(\lambda) \phi_{k_2}^{J_2}(\varphi) \phi_{k_3}^{J_3}(t) \quad (5.21)$$

where $d_{k_1, k_2, k_3}^{J_1, J_2, J_3}$ are the unknown scaling coefficients that need to be determined. For global modeling, $\phi_{k_2}^{J_2}(\varphi)$ may be replaced by trigonometric B-splines $T_{k_2}^{J_2}(\varphi)$. Further details about the application of B-splines for ionosphere modeling can be found in Section 2.3. It shall however be noted once more, that the number of unknowns depends on the number K of spline functions and therefore on the model resolution defined by the level J . It follows that the unknowns collected in \mathbf{x} are $U = \prod_{j=1}^J K_j$ B-spline series coefficients.

Under consideration of the same B-spline levels for the longitude and time ($J_2 = J_3 = 2$) but a different level for the latitude ($J_1 = 3$), the number of unknowns for the regional model with polynomial B-splines yields, for instance, $U = 360$ coefficients per key parameter.

To account for B-spline coefficients as target parameters, Eq. (5.17) needs to be adapted. The modification leads to

$$\underbrace{l_i + e_i - N_{e,i}(\boldsymbol{\kappa}(\mathbf{x}_0))}_{L_i} = \sum_{h=1}^H \left(\left[\frac{\partial N_e}{\partial \kappa_h} \Big|_{\boldsymbol{\kappa}(\mathbf{x}_0)} \right] \left[\frac{\partial \kappa_h}{\partial \mathbf{d}_{\kappa_h}} \Big|_{\mathbf{x}_0} \right] \right)_i^T \Delta \mathbf{d}_{\kappa_h} \quad (5.22)$$

where $\mathbf{x}_0 = [d_{0, \kappa_1}, d_{0, \kappa_2}, \dots, d_{0, \kappa_H}]^T$ contains initial values of the series coefficients related to the Chapman key parameters. All key parameters are contained in the vector $\boldsymbol{\kappa}$.

The model equation for the integrated electron density along the ray path between transmitter and receiver follows instantly from Eq. (5.3) and according to Eq. (5.22) can be obtained as

$$\underbrace{l_i + e_i - \int_{x_r}^{x_s} N_{e,i}(\boldsymbol{\kappa}(\mathbf{x}_0)) ds}_{L_i} = \int_{x_r}^{x_s} \left(\sum_{h=1}^H \left(\left[\frac{\partial N_e}{\partial \kappa_h} \Big|_{\boldsymbol{\kappa}(\mathbf{x}_0)} \right] \left[\frac{\partial \kappa_h}{\partial \mathbf{d}_{\kappa_h}} \Big|_{\mathbf{x}_0} \right] \right)_i^T \Delta \mathbf{d}_{\kappa_h} \right) ds. \quad (5.23)$$

Partial derivatives of F2 model parameters

The partial derivatives of Eq. (5.2) with respect to the F2 Chapman parameters are part of the right-hand sides in Eq. (5.22) and Eq. (5.23) and will be placed in the design matrix A . Therefore, the corresponding terms for $NmF2$, $hmF2$ and $HF2$ are summarized in the following.

1. Partial derivatives of the α -Chapman function for $NmF2$ and the B-spline coefficients:

$$\frac{\partial N_{e,i}}{\partial NmF2} = \exp\left(\frac{1}{2}\left(1 - \frac{h - hmF2}{HF2} - \exp\left(-\frac{h - hmF2}{HF2}\right)\right)\right) \quad (5.24)$$

$$\frac{\partial N_{e,i}}{\partial NmF2} \frac{\partial NmF2}{\partial (d_{k_1, k_2, k_3}^{J_1, J_2, J_3})_{NmF2}} = \frac{\partial N_{e,i}}{\partial NmF2} \cdot \phi_{k_1}^{J_1}(\lambda) \phi_{k_3}^{J_3}(t) \begin{cases} \phi_{k_2}^{J_2}(\varphi) & \text{regional} \\ T_{k_2}^{J_2}(\varphi) & \text{global} \end{cases} \quad (5.25)$$

2. Partial derivatives of the α -Chapman function for $hmF2$ and the B-spline coefficients:

$$\frac{\partial N_{e,i}}{\partial hmF2} = \begin{cases} \frac{NmF2}{2HF2} \frac{\partial N_{e,i}}{\partial NmF2} \left(1 - \exp\left(-\frac{h - hmF2}{HF2}\right)\right) + \frac{NOP}{HP} \frac{\partial N_{e,i}}{\partial NOP} & \text{if } h \geq hmF2 \\ \frac{NmF2}{2HF2} \frac{\partial N_{e,i}}{\partial NmF2} \left(1 - \exp\left(-\frac{h - hmF2}{HF2}\right)\right) - \frac{NOP}{HP} \frac{\partial N_{e,i}}{\partial NOP} & \text{else} \end{cases} \quad (5.26)$$

$$\frac{\partial N_{e,i}}{\partial hmF2} \frac{\partial hmF2}{\partial (d_{k_1, k_2, k_3}^{J_1, J_2, J_3})_{hmF2}} = \frac{\partial N_{e,i}}{\partial hmF2} \phi_{k_1}^{J_1}(\lambda) \phi_{k_3}^{J_3}(t) \begin{cases} \phi_{k_2}^{J_2}(\varphi) & \text{regional} \\ T_{k_2}^{J_2}(\varphi) & \text{global} \end{cases} \quad (5.27)$$

3. Partial derivatives of the α -Chapman function for $HF2$ and the B-spline coefficients:

$$\frac{\partial N_{e,i}}{\partial HF2} = NmF2 \frac{\partial N_{e,i}}{\partial NmF2} \frac{h - hmF2}{2(HF2)^2} \left(1 - \exp\left(-\frac{h - hmF2}{HF2}\right)\right) \quad (5.28)$$

$$\frac{\partial N_{e,i}}{\partial HF2} \frac{\partial HF2}{\partial (d_{k_1, k_2, k_3}^{J_1, J_2, J_3})_{HF2}} = \frac{\partial N_{e,i}}{\partial HF2} \phi_{k_1}^{J_1}(\lambda) \phi_{k_3}^{J_3}(t) \begin{cases} \phi_{k_2}^{J_2}(\varphi) & \text{regional} \\ T_{k_2}^{J_2}(\varphi) & \text{global} \end{cases} \quad (5.29)$$

The functional dependencies between measurements and model parameters define the basis of the adjustment system including the unknown parameters that will be estimated. Therefore, the observation equations for those techniques presented in the Chapters 3 and 4 are summarized in the following and the structure of the associated design matrix is provided. It should be noticed, that the unknowns introduced here are only the very essential ones to be considered for regional modeling. For global modeling, additional B-spline constraints as described in Section 2.4 may be taken into account. Besides, the estimation of bias parameters with respect to a reference technique are recommended to absorb relative biases between different missions and observation techniques.

Ionospheric GNSS radio occultations

The electron density retrieval procedure described in Chapter 4 allows to obtain electron density profiles including discrete N_e values derived from STEC observations between a GNSS transmitter

and a LEO receiver. After a relatively complex preprocessing and data retrieval, the retrieved electron density values can be modeled by

$$N_e + e = NmF2 \exp \left(0.5 \left(1 - \frac{h - hmF2}{HF2} - \exp \left(-\frac{h - hmF2}{HF2} \right) \right) \right) + N0P \left(-\frac{|h - hmF2|}{HP} \right) \quad (5.30)$$

resulting directly from Eq. (5.2) under consideration of the extended α -Chapman layer. As aforementioned, the design matrix \mathbf{A} contains the partial derivatives and the vector of unknowns the corrections of the B-spline series coefficients. It follows that

$$\mathbf{A}_{\text{IRO}} = \begin{bmatrix} \frac{\partial N_{e,1}}{\partial \kappa_1} \frac{\partial \kappa_1}{\partial d} & \dots & \frac{\partial N_{e,1}}{\partial \kappa_H} \frac{\partial \kappa_H}{\partial d} \\ \frac{\partial N_{e,2}}{\partial \kappa_1} \frac{\partial \kappa_1}{\partial d} & \dots & \frac{\partial N_{e,2}}{\partial \kappa_H} \frac{\partial \kappa_H}{\partial d} \\ \vdots & \ddots & \vdots \\ \frac{\partial N_{e,N}}{\partial \kappa_1} \frac{\partial \kappa_1}{\partial d} & \dots & \frac{\partial N_{e,N}}{\partial \kappa_H} \frac{\partial \kappa_H}{\partial d} \end{bmatrix} \quad (5.31)$$

and

$$\Delta \widehat{\mathbf{x}}_{\text{IRO}} = \left[\Delta \widehat{d}_{\kappa_1,1}, \Delta \widehat{d}_{\kappa_1,2}, \dots, \Delta \widehat{d}_{\kappa_2,1}, \Delta \widehat{d}_{\kappa_2,2}, \dots, \Delta \widehat{d}_{\kappa_H,1}, \Delta \widehat{d}_{\kappa_H,2}, \dots \right]^T. \quad (5.32)$$

GNSS

In case of GNSS, the integrated electron density along a slant ray path as described in Section 3.2 is observed by means of leveled carrier phase observations, i.e., Eq. (5.3) must be taken into account where additional instrumental biases, the DCBs, for the satellites and receivers need to be considered. The observation equation yields

$$\begin{aligned} \text{STEC} + e &= \int_{x_r}^{x_s} N_e ds + \text{DCB}_r + \text{DCB}^s \\ &= \int_{x_r}^{x_s} NmF2 \exp \left(0.5 \left(1 - \frac{h - hmF2}{HF2} - \exp \left(-\frac{h - hmF2}{HF2} \right) \right) \right) + N0P \left(-\frac{|h - hmF2|}{HP} \right) ds \\ &\quad + \text{DCB}_r + \text{DCB}^s. \end{aligned} \quad (5.33)$$

It is assumed, that an approximation for the carrier phase bias has already been determined by means of a suitable leveling procedure. With the DCBs as additional unknowns, the system blows up where \mathbf{A} and $\Delta \widehat{\mathbf{x}}$ are expanded to

$$\mathbf{A}_{\text{GNSS}} = \left[\begin{array}{ccc|ccc} \frac{\partial N_{e,1}}{\partial \kappa_1} \frac{\partial \kappa_1}{\partial d} & \dots & \frac{\partial N_{e,1}}{\partial \kappa_H} \frac{\partial \kappa_H}{\partial d} & \frac{\partial N_e}{\partial \text{DCB}_{r_1}} & \dots & \frac{\partial N_e}{\partial \text{DCB}_{r_{N_r}}} & \frac{\partial N_e}{\partial \text{DCB}^{s_1}} & \dots & \frac{\partial N_e}{\partial \text{DCB}^{s_{N_s}}} \\ \frac{\partial N_{e,2}}{\partial \kappa_1} \frac{\partial \kappa_1}{\partial d} & \dots & \frac{\partial N_{e,2}}{\partial \kappa_H} \frac{\partial \kappa_H}{\partial d} & \frac{\partial N_e}{\partial \text{DCB}_{r_1}} & \dots & \frac{\partial N_e}{\partial \text{DCB}_{r_{N_r}}} & \frac{\partial N_e}{\partial \text{DCB}^{s_1}} & \dots & \frac{\partial N_e}{\partial \text{DCB}^{s_{N_s}}} \\ \vdots & \ddots & \vdots & \vdots & \ddots & \vdots & \vdots & \ddots & \vdots \\ \frac{\partial N_{e,N}}{\partial \kappa_1} \frac{\partial \kappa_1}{\partial d} & \dots & \frac{\partial N_{e,N}}{\partial \kappa_H} \frac{\partial \kappa_H}{\partial d} & \frac{\partial N_e}{\partial \text{DCB}_{r_1}} & \dots & \frac{\partial N_e}{\partial \text{DCB}_{r_{N_r}}} & \frac{\partial N_e}{\partial \text{DCB}^{s_1}} & \dots & \frac{\partial N_e}{\partial \text{DCB}^{s_{N_s}}} \end{array} \right] \quad (5.34)$$

and

$$\Delta \widehat{\mathbf{x}}_{\text{GNSS}} = \left[\begin{array}{c} \Delta \widehat{d} \\ \widehat{dcb} \end{array} \right] \quad (5.35)$$

with

$$\Delta \widehat{\mathbf{d}} = \left[\Delta \widehat{d}_{\kappa_1,1}, \Delta \widehat{d}_{\kappa_1,2}, \dots, \Delta \widehat{d}_{\kappa_2,1}, \Delta \widehat{d}_{\kappa_2,2}, \dots, \Delta \widehat{d}_{\kappa_H,1}, \Delta \widehat{d}_{\kappa_H,2}, \dots \right]^T \quad (5.36)$$

$$\widehat{\mathbf{dcb}} = \left[\widehat{\text{DCB}}_{r_1}, \dots, \widehat{\text{DCB}}_{r_{N_r}}, \widehat{\text{DCB}}^{s_1}, \dots, \widehat{\text{DCB}}^{s_{N_s}} \right]^T. \quad (5.37)$$

N_r and N_s indicate the number of distinct receivers and satellites considered in the system. The partial derivatives for the DCBs of a specific observation are one for the satellite-receiver pair and otherwise zero. For the reason, that all DCBs may be shifted by a common offset, a zero-mean assumption for relative constraining is commonly introduced for the satellite DCBs with

$$\sum_{i=s_1}^{N_s} \text{DCB}_i \stackrel{!}{=} 0. \quad (5.38)$$

This constraint can, for instance, be considered by means of an additional observation equation included at the normal equations level.

DORIS

The derivation of ionospheric signals from DORIS measurements has been described in Section 3.3. A strong drawback of DORIS data is the high noise level in the pseudorange observations causing that standard procedures for the carrier phase leveling cannot be applied. Thus, the observation equation

$$\begin{aligned} \text{STEC} + e &= \int_{x_r}^{x_s} N_e ds + \text{CPB} \\ &= \int_{x_r}^{x_s} NmF2 \exp \left(0.5 \left(1 - \frac{h - hmF2}{HF2} - \exp \left(-\frac{h - hmF2}{HF2} \right) \right) \right) + N0P \left(-\frac{|h - hmF2|}{HP} \right) ds + \text{CPB} \end{aligned} \quad (5.39)$$

is related to unlevelled data and still contains a CPB term including, e.g., the PWU and in particular the phase ambiguities. As a preliminary strategy to account for the CPB, the TEC data of IGS GIMs have been exploited by Dettmering et al. (2014a); P-IV: Dettmering et al. (2014b) as a reference to level the DORIS STEC. The entries of \mathbf{A} and $\hat{\mathbf{x}}$ are basically related to the series coefficients as shown in Eq. (5.31) and Eq. (5.32). However, the consideration of an additional offset with respect to other techniques and missions is recommended to account for systematic biases.

Altimetry

From altimetry, vertical range errors are provided that can directly be converted into VTEC. Thus, the observation equation reads

$$\begin{aligned} \text{VTEC} + e &= \int_{x_r}^{x_s} N_e dh \\ &= \int_{x_r}^{x_s} NmF2 \exp \left(0.5 \left(1 - \frac{h - hmF2}{HF2} - \exp \left(-\frac{h - hmF2}{HF2} \right) \right) \right) + N0P \left(-\frac{|h - hmF2|}{HP} \right) dh. \end{aligned} \quad (5.40)$$

As for occultations and DORIS, the minimum unknowns are defined with the B-spline coefficients. The existence of biases with few TECU between altimetry and GNSS is well known. The relative leveling between the techniques and also altimetry missions is therefore highly recommended.

5.4 Handling data gaps

The model approach presented here considers localizing B-spline functions that imply, in contrast to globally defined functions, that data gaps need to be handled properly. In case of a sparse observation distribution the system may even become singular or ill-conditioned. There are basically two ways to bridge the data gaps:

(1) The B-spline level is conservatively adapted to the typically sparse data distribution. In this case, the system is thoroughly defined and resolvable but the model resolution in those regions with enough observations will suffer by strong smoothing effects. For scenarios where data gaps cannot be excluded, e.g., in the absence of GNSS data over the oceans, it can be expected that only the ionospheric climatology will be resolved.

(2) The B-spline level is fixed to achieve the desired resolution wherever possible. This method also includes compromises as, for instance, the adaption of the level to the mean measurement distribution. In this case, data gaps need to be bridged, e.g., by prior information from a background model. This strategy thus relies on external data that will be improved in those regions where enough measurements are available.

When considering the second method, a data grid for the Chapman key parameters needs to be extracted from a given background model. Applying a Gauß-Markov model allows then for the estimation of initial B-spline scaling coefficients that can be exploited (1) as initials in the Taylor linearization and (2) as a priori information to bridge data gaps. In P-I: Limberger et al. (2013) and P-II: Limberger et al. (2014) as well as P-V: Liang et al. (2014) and P-VI: Liang et al. (2015), IRI 2007 data have been taken into account to extract the a priori information as

$$\mathbf{x}_0 = \left[\mathbf{d}_{\text{IRI},N_mF2}^T, \mathbf{d}_{\text{IRI},hmF2}^T, \mathbf{d}_{\text{IRI},HF2}^T \right]^T. \quad (5.41)$$

The linear dependencies between the IRI background information and initial scaling coefficients can be formulated in the B-spline domain where the level must be adapted to the resolution of the gridded IRI data.

The functional relation of a specific key parameter κ_h in B-spline notation for regional modeling has been defined by Eq. (5.19) - Eq. (5.21). Such expression as

$$\left(\kappa_h(\varphi, \lambda, t) + e = \sum_{k_1=1}^{K_1} \sum_{k_2=1}^{K_2} \sum_{k_3=1}^{K_3} \left(d_{k_1, k_2, k_3}^{J_1, J_2, J_3} \right)_{0, \kappa_h} \phi_{k_1}^{J_1}(\lambda) \phi_{k_2}^{J_2}(\varphi) \phi_{k_3}^{J_3}(t) \right)_i \quad (5.42)$$

can accordingly be applied here for each grid point $i = 1, \dots, N_G$ where N_G indicates the total number of background data samples. As a matter of course, the B-spline level must be consistent during this preprocessing step and the subsequent parameter estimation to maintain the number of series coefficients. Furthermore, the density of IRI data should consequently satisfy the model resolution, here defined by the levels J_1 , J_2 and J_3 in latitude, longitude and time. As introduced with Eq. (2.19), a relation between the level and the observation density can be found for regional modeling by means of polynomial B-splines with

$$J < \log_2 \left(\frac{s_{\text{imax}} - s_{\text{imin}} - \Delta s_i}{\Delta s_i} \right). \quad (5.43)$$

This equation also applies here since Δs_i can be derived from the gridded data with homogeneous distribution.

The deterministic and stochastic parts of the Gauß-Markov model are defined according to the Eqs. (5.7) and (5.9) as

$$\mathbf{l}_{\kappa_h} + \mathbf{e} = \mathbf{A} \mathbf{d}_{0, \kappa_h} \quad \text{and} \quad \boldsymbol{\Sigma}_{ll} = \sigma_0^2 \mathbf{P}_{ll}^{-1} \quad (5.44)$$

where the observation vector \mathbf{l}_{κ_h} contains the background data of a specific key parameter, \mathbf{e} are truncation errors, \mathbf{A} identifies the coefficient matrix and \mathbf{d}_{0,κ_h} contains the unknown B-spline coefficients to be determined. From Eq. (5.42) it is instantly obvious, that the partial derivatives of the coefficient collected in \mathbf{A} are the tensor products of the polynomial B-splines, i.e.,

$$\frac{\partial \kappa_h(\varphi, \lambda, t)}{\partial (d_{k_1, k_2, k_3}^{J_1, J_2, J_3})_{\kappa_h}} = \phi_{k_1}^{J_1}(\lambda) \phi_{k_2}^{J_2}(\varphi) \phi_{k_3}^{J_3}(t). \quad (5.45)$$

Since the target coefficients will serve only as prior information, uncorrelated and equally weighted data with $\mathbf{P} = \mathbf{I}$ are taken into account. The initials then are estimated with

$$\widehat{\mathbf{d}}_{0,\kappa_h} = (\mathbf{A}^T \mathbf{A})^{-1} \mathbf{A}^T \mathbf{l}_{\kappa_h} = \mathbf{d}_{\text{init}}. \quad (5.46)$$

It shall be noted, that the entries \mathbf{A} only depend on the position of the grid points as can be seen from Eq. (5.45) but not on the values of the background model parameters. While maintaining the grid and B-spline resolution, the model is multivariate and allows for a shared usage of the same \mathbf{A} to estimate series coefficient related to different key parameters.

5.5 Combination of techniques or satellite missions

Different measurement techniques providing ionospheric signals have been introduced in the Chapters 3 and 4 which shall be considered now for a combined adjustment. The conjunction of observation blocks regarding different satellite missions or measurement techniques is based on the stacking of normal equations. The approach orientates on the regularization method presented by Koch and Kusche (2002). Therefore, individual normal equation systems with respect to each observation group $g \in \{1, \dots, G\}$ are established as

$$\mathbf{l}_g + \mathbf{e}_g = \mathbf{A}_g \mathbf{x} \quad \text{with} \quad \Sigma_g = \sigma_g^2 \mathbf{P}_g^{-1} = \sigma_g^2 \mathbf{Q}_g. \quad (5.47)$$

In Section 5.4, the methodology to derive prior information from a background model has been described. The estimated background coefficients are taken into account here as a priori values and will be involved as an additional observation group to bridge data gaps. Thus, an associated prior information model is defined by

$$\boldsymbol{\mu} + \mathbf{e}_\mu = \mathbf{I} \mathbf{x} \quad \text{with} \quad \Sigma_\mu = \sigma_\mu^2 \mathbf{P}_\mu^{-1} = \sigma_\mu^2 \mathbf{Q}_\mu. \quad (5.48)$$

The vector $\boldsymbol{\mu}$ contains a priori values for the B-spline series coefficients, σ_μ^2 is the variance factor of the prior information and \mathbf{P}_μ the weight matrix. σ_g^2 and σ_μ^2 are assumed as initially unknown variance factors and account for a system regularization where large factors decrease the weight of the assigned observation group and vice versa. The combined linear equation system follows from

$$\begin{bmatrix} \mathbf{l}_1 + \mathbf{e}_1 \\ \vdots \\ \mathbf{l}_G + \mathbf{e}_G \\ \boldsymbol{\mu} + \mathbf{e}_\mu \end{bmatrix} = \begin{bmatrix} \mathbf{A}_1 \\ \vdots \\ \mathbf{A}_G \\ \mathbf{I} \end{bmatrix} \mathbf{x} \quad \text{with} \quad \Sigma_{ll} = \mathbf{Q}_{ll} = \sum_{g=1}^G (\sigma_g^2 \mathbf{V}_g) + \sigma_\mu^2 \mathbf{V}_\mu \quad (5.49)$$

and

$$\mathbf{V}_1 = \begin{bmatrix} \mathbf{P}_1^{-1} & \cdots & \mathbf{0} & \mathbf{0} \\ \vdots & \ddots & \vdots & \vdots \\ \mathbf{0} & \cdots & \mathbf{0} & \mathbf{0} \\ \mathbf{0} & \cdots & \mathbf{0} & \mathbf{0} \end{bmatrix}, \dots, \mathbf{V}_G = \begin{bmatrix} \mathbf{0} & \cdots & \mathbf{0} & \mathbf{0} \\ \vdots & \ddots & \vdots & \vdots \\ \mathbf{0} & \cdots & \mathbf{P}_G^{-1} & \mathbf{0} \\ \mathbf{0} & \cdots & \mathbf{0} & \mathbf{0} \end{bmatrix} \quad \text{and} \quad \mathbf{V}_\mu = \begin{bmatrix} \mathbf{0} & \cdots & \mathbf{0} & \mathbf{0} \\ \vdots & \ddots & \vdots & \vdots \\ \mathbf{0} & \cdots & \mathbf{0} & \mathbf{0} \\ \mathbf{0} & \cdots & \mathbf{0} & \mathbf{P}_\mu^{-1} \end{bmatrix}. \quad (5.50)$$

It shall be noticed, that the matrix \mathbf{Q}_{ll} (or \mathbf{P}_{ll}^{-1}) equals the merged covariance matrix Σ_{ll} as it includes the variance information.

It follows for the linearized model as introduced with Eq. (5.15), that the estimated unknowns are corrections for the B-spline coefficients collected in the vector $\mathbf{x} = \Delta\hat{\mathbf{d}}$ and \mathbf{l} is replaced by the reduced observation vector \mathbf{L} . The consideration of different observation techniques in a combined equation system by means of normal equation stacking is thus defined with

$$\underbrace{\left(\sum_{g=1}^G \frac{1}{\sigma_g^2} \mathbf{A}_g^T \mathbf{P}_g \mathbf{A}_g + \frac{1}{\sigma_\mu^2} \mathbf{P}_\mu \right)}_{\text{NEQ}} \Delta\hat{\mathbf{d}} = \left(\sum_{g=1}^G \frac{1}{\sigma_g^2} \mathbf{A}_g^T \mathbf{P}_g \mathbf{L}_g + \frac{1}{\sigma_\mu^2} \mathbf{P}_\mu \boldsymbol{\mu} \right). \quad (5.51)$$

Substituting the prior information term $\frac{1}{\sigma_\mu^2} \mathbf{P}_\mu$ by the extended weight matrix \mathbf{W} with block diagonal structure

$$\mathbf{W} = \Sigma_\mu^{-1} = \text{diag} \left(\frac{\mathbf{P}_{\kappa_1}}{\sigma_{\kappa_1}^2}, \frac{\mathbf{P}_{\kappa_2}}{\sigma_{\kappa_2}^2}, \dots, \frac{\mathbf{P}_{\kappa_R}}{\sigma_{\kappa_H}^2} \right) \quad (5.52)$$

yields the solution for the B-spline coefficient corrections

$$\Delta\hat{\mathbf{d}} = \left(\sum_{g=1}^G \frac{1}{\sigma_g^2} \mathbf{A}_g^T \mathbf{P}_g \mathbf{A}_g + \mathbf{W} \right)^{-1} \left(\sum_{g=1}^G \frac{1}{\sigma_g^2} \mathbf{A}_g^T \mathbf{P}_g \mathbf{L}_g + \mathbf{W} \boldsymbol{\mu} \right). \quad (5.53)$$

In this notation, key parameter specific variance factors and weight matrices are contained in \mathbf{W} . It follows from the linearization, that Eq. (5.53) is solved iteratively. Therefore, $\boldsymbol{\mu}$ is replaced by the iteratively adapted vector \mathbf{M} which stabilizes the system and counteracts a possible ill-conditioning of the normal equations in the presence of data gaps.

Due to the inhomogeneous data distribution provided by almost every observation technique, the presence of large data gaps cannot be excluded. Or in other words, the selected uniform B-splines may not be able to represent the data distribution. As a consequence, the $N_g \times U$ Jacobi matrices \mathbf{A}_g may have a rank deficiency of $U - \text{rg}(N_g)$ with $\text{rg}(N_g) < U$ and the corresponding sub normal equation matrix $\text{NEQ}_g = \frac{1}{\sigma_g^2} \mathbf{A}_g^T \mathbf{P}_g \mathbf{A}_g$ will be singular. However, under consideration that the weight matrices of the observations \mathbf{P}_g are positive-definite, each NEQ_g is symmetric and at least positive-semidefinite. Thus, the eigenvalues of NEQ_g are real and ≥ 0 where it follows that the diagonal elements of NEQ_g are non-negative. The positive-definite prior information matrix \mathbf{W} is finally introduced to regularize the system leading to a stacked NEQ system that is of full rank, positive-definite and regular, i.e., invertible.

5.6 Adjustment sequence

The adjustment comprises a nested iteration sequence accounting for (1) the linearization of the model and (2) the estimation of variance factors for the observation techniques and the prior information. A schematic flowchart of the fundamental processing steps is provided by Fig. 5.5.

The data sources for the prior information and initial coefficients may coincide, i.e., both can also be obtained from the same background model. Based on these data, the model is linearized and the normal equations under consideration of weighted observation groups are established to solve for corrections of the B-spline series coefficients. Input data originate from the actual measurements, the background model (for the derivation of prior information) and optionally from additional external sources (for the provision of initial B-spline series coefficients).

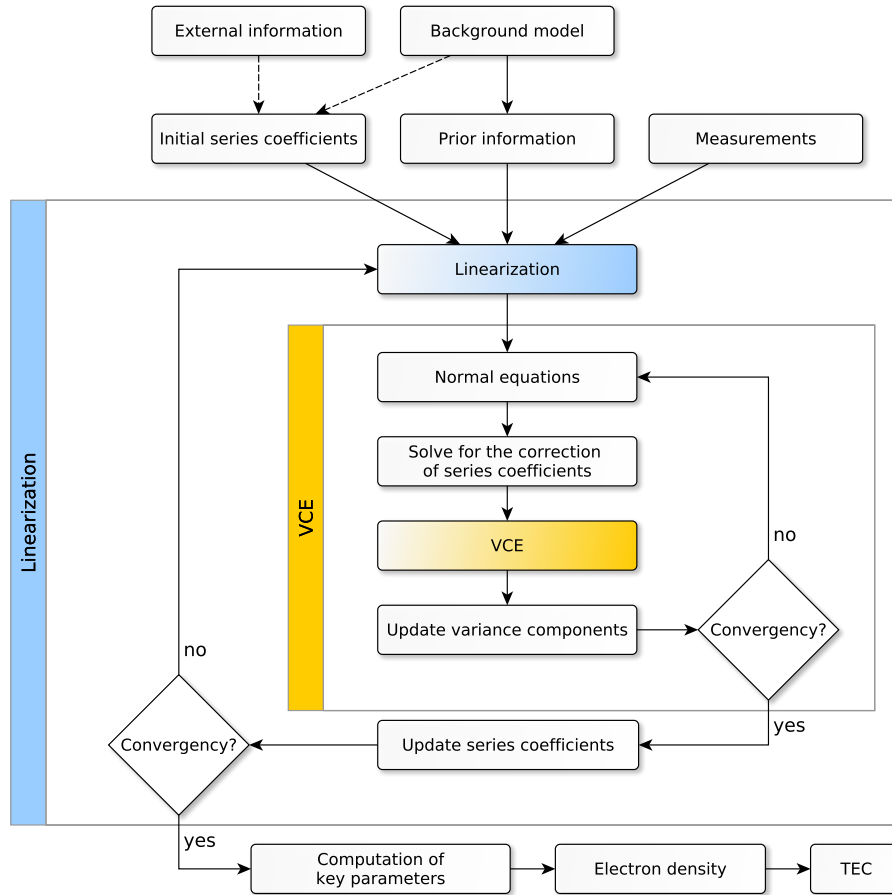


Figure 5.5: Flowchart of the iterative solving procedure with nested variance component estimation.

As the observation models are based on the non-linear Chapman function, the linearization by means of a Taylor series approximation is performed. Estimations for the target parameters follow from an iterative computation where the initial coefficients are iteratively improved. According to Fig. 5.5, the VCE is embedded into the solving procedure as a second iteration that is carried out for each linearization step. The sequences of both the linearization and VCE iterations will be described in the following.

5.6.1 Outer iteration: Linearization

The outer iteration loop, accounting for the linearization, will henceforth be denoted by the subscript L_{it} whereas the inner loop with respect to the VCE will be identified by the subscript V_{it} .

Initial iteration

For the 0^{th} iteration, denoted as $L_{it} = 0$, the prior information vector $\boldsymbol{\mu}$ is set to

$$\boldsymbol{\mu} = \begin{bmatrix} d_{0,\kappa_1} \\ d_{0,\kappa_2} \\ \vdots \\ d_{0,\kappa_H} \end{bmatrix} \quad (5.54)$$

and

$$\boldsymbol{M}_{L_{it}=0} = \boldsymbol{\mu} - \boldsymbol{d}_{L_{it}=0} \quad (5.55)$$

where $\boldsymbol{d}_{L_{it}=0}$ is a vector containing starting values for the coefficients. The closer the entries of $\boldsymbol{d}_{L_{it}=0}$ to the final values, the faster the convergence of the iterative solver. Such as for the prior information

$\boldsymbol{\mu}$, initial coefficients can be derived from a given background model according to Eq. (5.46). In case that $\boldsymbol{\mu}$ contains the initial coefficients $\boldsymbol{d}_{\text{Lit}=0}$, it follows that

$$\boldsymbol{M}_{\text{Lit}=0} = \boldsymbol{\mu} - \boldsymbol{d}_{\text{Lit}=0} \underset{\boldsymbol{d}_{\text{Lit}=0}=\boldsymbol{\mu}}{=} \mathbf{0}. \quad (5.56)$$

→ Run VCE (Section 5.6.2) → The 0^{th} iteration yields the solution for $\Delta\widehat{\boldsymbol{d}}_{\text{Lit}=0}$.

Iteration 1

The 1^{st} iteration starts with the definition of new initial coefficients

$$\boldsymbol{d}_{\text{Lit}=1} = \boldsymbol{d}_{\text{Lit}=0} + \Delta\widehat{\boldsymbol{d}}_{\text{Lit}=0} \quad (5.57)$$

and

$$\boldsymbol{M}_{\text{Lit}=1} = \boldsymbol{\mu} - \left(\boldsymbol{d}_{\text{Lit}=0} + \Delta\widehat{\boldsymbol{d}}_{\text{Lit}=0} \right) \underset{\boldsymbol{d}_{\text{Lit}=0}=\boldsymbol{\mu}}{=} -\Delta\widehat{\boldsymbol{d}}_{\text{Lit}=0} \quad (5.58)$$

where only those coefficients are updated, which fall into the support region of the given measurements. Coefficients which are located in data gaps remain untouched.

→ Run VCE (Section 5.6.2) → The 1^{st} iteration yields the solution for $\Delta\widehat{\boldsymbol{d}}_{\text{Lit}=1}$.

Iteration 2

In the 2^{nd} iteration, the prior information is derived as

$$\boldsymbol{d}_{\text{Lit}=2} = \boldsymbol{d}_{\text{Lit}=0} + \Delta\widehat{\boldsymbol{d}}_{\text{Lit}=0} + \Delta\widehat{\boldsymbol{d}}_{\text{Lit}=1} = \boldsymbol{d}_{\text{Lit}=1} + \Delta\widehat{\boldsymbol{d}}_{\text{Lit}=1} \quad (5.59)$$

and

$$\boldsymbol{M}_{\text{Lit}=2} = \boldsymbol{\mu} - \left(\boldsymbol{d}_{\text{Lit}=0} + \Delta\widehat{\boldsymbol{d}}_{\text{Lit}=0} + \Delta\widehat{\boldsymbol{d}}_{\text{Lit}=1} \right) \underset{\boldsymbol{d}_{\text{Lit}=0}=\boldsymbol{\mu}}{=} - \left(\Delta\widehat{\boldsymbol{d}}_{\text{Lit}=0} + \Delta\widehat{\boldsymbol{d}}_{\text{Lit}=1} \right). \quad (5.60)$$

→ Run VCE (Section 5.6.2) → The 2^{nd} iteration yields the solution for $\Delta\widehat{\boldsymbol{d}}_{\text{Lit}=2}$.

Iteration P-1

Assuming the convergence with a sufficient accuracy of the solution is reached after the P^{th} iteration, the initial scaling coefficient vector for the antecedent $(P-1)^{\text{th}}$ iteration is obtained from

$$\boldsymbol{d}_{\text{Lit}=P-1} = \boldsymbol{d}_{\text{Lit}=0} + \sum_{p=0}^{P-2} \Delta\widehat{\boldsymbol{d}}_{\text{Lit}=p} \quad (5.61)$$

with the adapted prior information vector

$$\boldsymbol{M}_{\text{Lit}=P-1} = \boldsymbol{\mu} - \left(\boldsymbol{d}_{\text{Lit}=0} + \sum_{p=0}^{P-2} \Delta\widehat{\boldsymbol{d}}_{\text{Lit}=p} \right) \underset{\boldsymbol{d}_{\text{Lit}=0}=\boldsymbol{\mu}}{=} - \left(\sum_{p=0}^{P-2} \Delta\widehat{\boldsymbol{d}}_{\text{Lit}=p} \right). \quad (5.62)$$

→ Run VCE (Section 5.6.2) → The $P-1^{\text{th}}$ iteration yields the solution for $\Delta\widehat{\boldsymbol{d}}_{\text{Lit}=P-1}$.

Iteration P

The final solution for the B-spline series coefficients in the P^{th} iteration is then obtained from

$$\boldsymbol{d}_{\text{Lit}=P} = \boldsymbol{d}_{\text{Lit}=0} + \sum_{p=0}^{P-1} \Delta\widehat{\boldsymbol{d}}_{\text{Lit}=p}. \quad (5.63)$$

Iteration B

It shall be noticed that the number of VCE iterations varies for each linearization step. Assuming the convergence of the variance components with a sufficient accuracy of the solution after the B^{th} iteration, the final steps are

1. Deployment of the system defined by Eq. (5.53) under consideration of the variance components $\sigma_{g, \text{Vit}=B}^2 = \widehat{\sigma}_{g, \text{Vit}=B-1}^2$, $\sigma_{\kappa_h, \text{Vit}=B}^2 = \widehat{\sigma}_{\kappa_h, \text{Vit}=B-1}^2$ and initial coefficients $d_{\text{Lit}=0}$
 2. Estimation of corrections $\Delta \widehat{d}_{\text{Vit}=B}$ (Eq. (5.53))
 3. Computation of residuals \widehat{e}_g , \widehat{e}_{κ_h} with $\Delta \widehat{d}_{\text{Vit}=B}$ (Eq. (5.65))
 4. Computation of partial redundancies r_g , r_{κ_h} with $\sigma_{g, \text{Vit}=B}^2$, $\sigma_{\kappa_h, \text{Vit}=B}^2$ (Eq. (5.66))
 5. Calculation of updated variance components $\widehat{\sigma}_{g, \text{Vit}=B}^2$, $\widehat{\sigma}_{\kappa_h, \text{Vit}=B}^2$ (Eq. (5.64))
-

Now the procedure continues with the linearization, i.e., the outer loop under consideration of the latest estimation for the coefficients $\Delta \widehat{d}_{\text{Vit}=B}$ and variances $\widehat{\sigma}_{g, \text{Vit}=B}^2$, $\widehat{\sigma}_{\kappa_h, \text{Vit}=B}^2$. The latest estimates for the variance components are introduced as a priori values into the next VCE iteration. As the number of VCE iterations varies between the linearization steps, the iteration number B generally depends on Lit with $B \in \{B_{\text{Lit}=0}, B_{\text{Lit}=1}, \dots, B_{\text{Lit}=P-1}\}$. The coefficients are updated after each terminated VCE, i.e, after the final VCE iterations $\text{Vit} = B_{\text{Lit}=0}, \text{Vit} = B_{\text{Lit}=1}, \dots, \text{Vit} = B_{\text{Lit}=P-1}$. The final set of coefficient is thus determined from

$$d_{\text{Lit}=P} = d_{\text{Lit}=0} + \Delta \widehat{d}_{\text{Lit}=0, \text{Vit}=B_{\text{Lit}=0}} + \Delta \widehat{d}_{\text{Lit}=1, \text{Vit}=B_{\text{Lit}=1}} + \dots + \Delta \widehat{d}_{\text{Lit}=P-1, \text{Vit}=B_{\text{Lit}=P-1}} \quad (5.68)$$

$$= d_{\text{Lit}=0} + \sum_{p=0}^{P-1} \Delta \widehat{d}_{\text{Lit}=p, \text{Vit}=B_{\text{Lit}=p}} \quad (5.69)$$

5.7 Parameter variances and correlations

The success of the parameter estimation, based on the presented adjustment system, strongly depends on the resolvability of the B-spline coefficients. Therefore, correlation studies have been performed by P-II: Limberger et al. (2014) for the regional model presented in P-I: Limberger et al. (2013). The correlations are related to mathematical dependencies and interpreted from correlation matrices that are computed for the B-spline coefficients and F2 Chapman parameters. In this sense, physical relations are only marginally reflected.

Based on the Variance Propagation Law (VPL) (Niemeier, 2008; Koch, 1999), a general relation between the cofactor matrices of the B-spline coefficients Q_{dd} and the stacked cofactor matrix of the observations Q_{ll} as introduced with Eq. (5.49) is given by

$$Q_{dd} = F Q_{ll} F^T \quad (5.70)$$

where F is designated as transformation matrix. It follows from Eq. (5.49), the variance components are already contained in Q_{ll} , i.e., $\Sigma_{ll} = Q_{ll}$ and accordingly $\Sigma_{dd} = Q_{dd}$. Furthermore, the cofactor matrix can be expressed as the inverse of the normal equations $Q_{dd} = N E Q^{-1}$. Thus, under consideration of the stacked normal equations inverse contained in Eq. (5.53), the relation

$$\Sigma_{dd} = N E Q^{-1} = \left(\sum_{g=1}^G \frac{1}{\sigma_g^2} A_g^T P_g A_g + W \right)^{-1} \quad (5.71)$$

is obtained. The diagonal elements of Σ_{dd} are the variances of the B-spline series coefficients

$$(\Sigma_{dd})_{i,i} \in \{\widehat{\sigma}_{d_1}^2, \widehat{\sigma}_{d_2}^2, \dots, \widehat{\sigma}_{d_U}^2\}. \quad (5.72)$$

Based on the solution for Σ_{dd} , the VPL can be applied to retrieve variances for the key parameters. Therefore, the transformation matrix Y is considered to derive the covariance matrix of key parameters as

$$\Sigma_{\kappa\kappa} = Y \Sigma_{dd} Y^T. \quad (5.73)$$

According to Eq. (5.72), $\Sigma_{\kappa\kappa}$ contains the variances of the target parameters

$$(\Sigma_{\kappa\kappa})_{i,i} \in \{\widehat{\sigma}_{\kappa_{1,1}}^2, \widehat{\sigma}_{\kappa_{1,2}}^2, \dots, \widehat{\sigma}_{\kappa_{2,1}}^2, \widehat{\sigma}_{\kappa_{2,2}}^2, \dots, \widehat{\sigma}_{\kappa_{H,1}}^2, \widehat{\sigma}_{\kappa_{H,2}}^2, \dots\} \quad (5.74)$$

The size of $\Sigma_{\kappa\kappa}$ is defined by the dimension of Y . Specifically, Y contains B-spline tensor products. Under consideration of polynomial B-splines for regional modeling with respect to latitude, longitude and time, the entries for the key parameter κ_h are then computed from

$$\frac{\partial \kappa_h}{\partial d_{k_1, k_2, k_3}^{J_1, J_2, J_3}} = \phi_{k_1}^{J_1}(\varphi) \phi_{k_2}^{J_2}(\lambda) \phi_{k_3}^{J_3}(t). \quad (5.75)$$

The column number of $\Sigma_{\kappa\kappa}$ depends therefore on the selected B-spline levels and the number of rows on the selected locations where key parameter correlations are calculated. The correlation matrices K_{dd} and $K_{\kappa\kappa}$ for series coefficients and key parameters are established from the element-wise division of the entries in Σ_{dd} and $\Sigma_{\kappa\kappa}$, respectively, by the product of the associated standard deviations. Thus, K_{dd} and $K_{\kappa\kappa}$ contain the correlations

$$\text{Cor}(d_i, d_j) = \frac{\sigma_{d_i d_j}}{\sigma_{d_i} \sigma_{d_j}} \quad \text{and} \quad \text{Cor}(\kappa_i, \kappa_j) = \frac{\sigma_{\kappa_i \kappa_j}}{\sigma_{\kappa_i} \sigma_{\kappa_j}} \quad (5.76)$$

identified by their corresponding row and column indices, i and j .

Correlation studies based on two different scenarios, one with synthetic observations and data distribution (dense, homogeneous) and a second under consideration of F-3/C measurements (sparse, inhomogeneous), have been performed by P-II: Limberger et al. (2014). From the simulated scenario, moderate positive correlations between $hmF2$ and $HF2$ as well as inverse correlation between $NmF2$ and $HF2$ are found. In the sparse real data scenario, the VCE leads to an increase of the prior information weight, i.e., a small $\widehat{\sigma}_\mu^2$ is estimated. However, the impact of the F-3/C observations has been still strong enough to correct the background information significantly, as shown by P-I: Limberger et al. (2013) and P-V: Liang et al. (2014). In combination with other observation techniques it can be assumed that the estimability benefits from the improved sensitivity for the model parameters, leading to a (desired) down-weighting of the prior information.

6 Summary and Synthesis

The combination of satellite measurement techniques for sounding the ionosphere is a highly topical subject that has been addressed in this thesis. Constellations with different characteristics regarding the orbit geometry, sensitivity and signal properties contribute to an improved global data coverage. With the step from describing the total electron content in a three-dimensional space (e.g. latitude, longitude, time) to four-dimensional electron density modeling (latitude, longitude, height, time), an additional spatial dimension comes into play and with it new challenges, in particular with respect to the description of the vertical electron distribution. In this regard, the selection of relevant ionospheric target parameters and the sensitivity of the input observations to resolve these model quantities are aspects of high importance. Essential questions related to these issues have been formulated in the preface of this thesis and shall be addressed in the following with focus on the primary results of the publications. The chapter closes with conclusions and an outlook regarding future works.

6.1 Primary results of the papers

Each category of questions is addressed by different parts of this thesis. Corresponding references are provided as blue colored responses and the relevant paper results are summarized in the following where particularly selected key findings of the first author publications are presented.

Electron density retrieval

- Which retrieval algorithms can be applied to derive the electron density from GNSS radio occultations?
- ▷ [References: Chapter 4, P-III: Limberger et al. \(2015\)](#)
- What accuracy can be expected from the electron density profiles, in particular for the ionospheric F2 layer?
- ▷ [References: P-III: Limberger et al. \(2015\)](#)

As part of this thesis, various investigations have been performed to analyze the sensitivity of satellite based observation techniques for ionospheric sounding, in particular with respect to ionospheric radio occultations (in Chapter 4), GNSS and DORIS (both in Chapter 3) measurements. The retrieval of electron density profiles from ionospheric radio occultations between GPS and F-3/C has for instance been studied in P-III: Limberger et al. (2015) aiming at the assessment of the F2 peak parameters $NmF2$ and $hmF2$. For this purpose, an improved Abel inversion algorithm that was developed at the UPC has been applied to overcome the spherical symmetry assumption on which the classical Abel inversion is based. The assessment was performed for a period of almost eight years between 2006 and 2014 exploiting the full F-3/C measurement availability. At first, climatological aspects have been studied from the temporal behavior of $NmF2$ and $hmF2$ derived from globally distributed F-3/C electron density profiles. Exemplarily, the time series of global averages together with daily standard deviations for both parameters are provided in Fig. 6.1 showing a clear correlation with the solar cycle, i.e., quiet conditions approximately between 2007-2010 and increased solar activity after 2012.

The comparison of these global trends with daily solar flux F10.7 indices and sunspot numbers as independent physical quantities shows a high agreement with correlation coefficients between 0.83

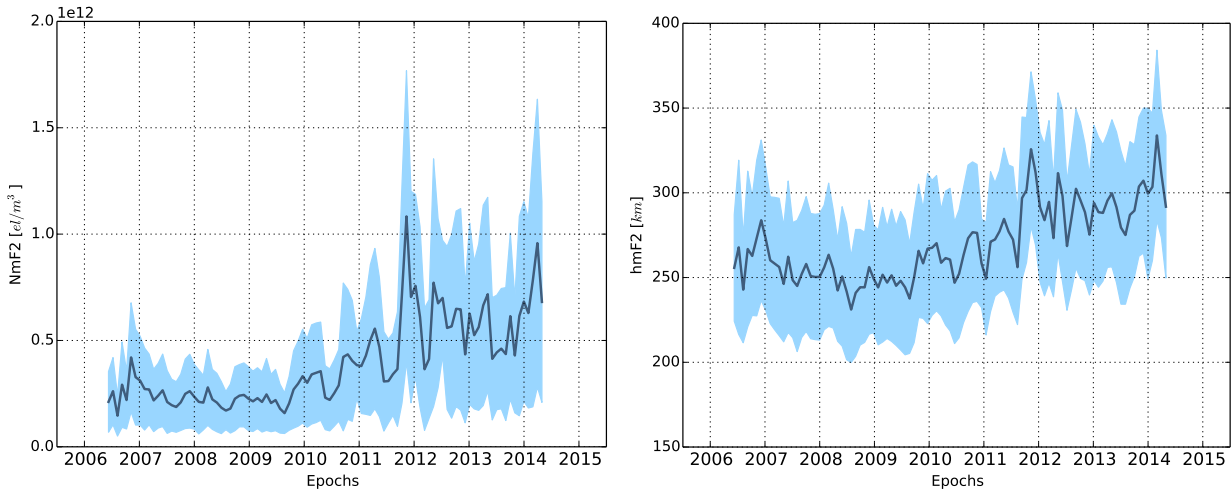


Figure 6.1: Climatology of $NmF2$ (left) and $hmF2$ (right) described by global averages of F2 peaks derived from F-3/C radio occultations between 2006 and 2014.

and 0.89 indicating the suitability of these parameters to characterize the solar activity. The main motivation of P-III: Limberger et al. (2015) can, however, be found in the assessment of the F2 peak parameter derived from occultations against reference data of ionosondes. Therefore, globally distributed data pairs of F-3/C profile peaks together with nearby ionosonde measurements provided by the Space Physics Interactive Data Resource (SPIDR) are considered to evaluate $NmF2$ and $hmF2$ in different magnetic latitude sectors ($\pm[0, 20^\circ]$, $\pm[20^\circ, 60^\circ]$ and $\pm[60^\circ, 90^\circ]$) and local times (LT) accounting for different ionospheric conditions at night ($02:00 \text{ LT} \pm 2 \text{ hours}$), dawn ($08:00 \text{ LT} \pm 2 \text{ hours}$) and day ($14:00 \text{ LT} \pm 2 \text{ hours}$). The results show generally a high correlation between the F2 peaks from F-3/C occultations and ionosondes with slightly better performance for $NmF2$.

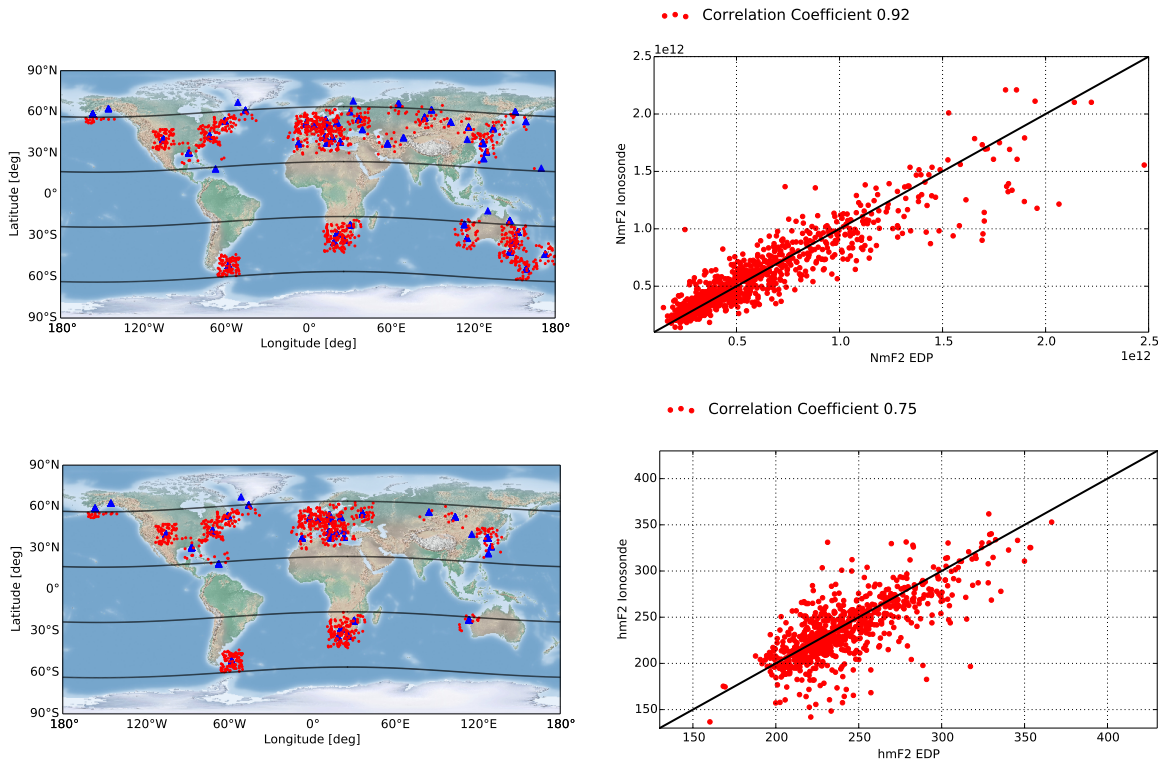


Figure 6.2: Left column: Collocated F2 peaks derived from ionosondes (blue triangles) and F-3/C occultations (red). Right column: Correlations between ionosonde and F-3/C $NmF2$ (top) and $hmF2$ (bottom) during daytime [$12:00 \text{ LT}, 16:00 \text{ LT}$] in the mid-latitude sector, i.e., between $\pm [20^\circ, 60^\circ]$ magnetic latitude.

The correlation plots for the daytime (14:00 LT \pm 2 hours) comparison in mid-latitudes are, for instance, depicted in Fig. 6.2 with $NmF2$ on the upper and $hmF2$ on the lower panel. Data distribution plots are given along the left column and represent ionosonde stations as blue triangles and locations of the observed peak as red dots. Exemplary, the separation of magnetic latitude sectors based on the magnetic North Pole of 2014 is depicted. It shall be noticed that not every ionosonde measurement contributes both, $NmF2$ as well as $hmF2$, and thus the number of red dots differs. Correlation plots of data pairs are shown in the right column with occultation based values referring to the x- and ionosonde measurements to the y-axis. In this case, correlations of 0.92 ($NmF2$) and 0.75 ($hmF2$) have been achieved.

Accordingly, the nighttime (2:00 LT \pm 2 hours) results for the mid-latitude sector are depicted in Fig. 6.3. The correlation coefficients, 0.83 for $NmF2$ and 0.64 for $hmF2$ indicate reduced correlations where particularly the $hmF2$ correlations are remarkably weaker.

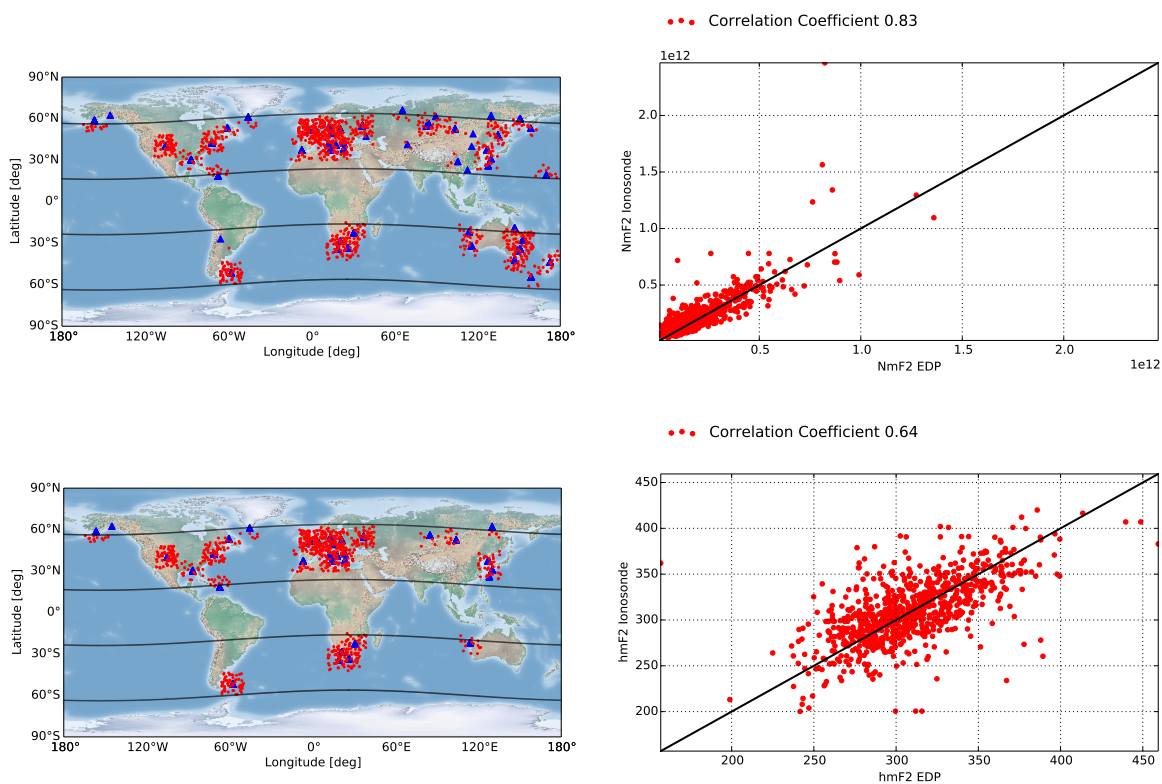


Figure 6.3: Left column: Collocated F2 peaks derived from ionosondes (blue triangles) and F-3/C occultations (red). Right column: Correlations between ionosonde and F-3/C $NmF2$ (top) and $hmF2$ (bottom) during nighttime [0:00 LT,4:00 LT] in the mid-latitude sector, i.e., between $\pm [20^\circ, 60^\circ]$ magnetic latitude.

From the result obtained by P-III: Limberger et al. (2015), the average differences of $NmF2$ and $hmF2$ between F-3/C peaks and ionosonde data are found to be insignificant. Relative variations of the peak differences are determined in the range of 20% to 30% for $NmF2$ and 10% to 15% for $hmF2$. For further details about the outcomes with respect to the climatological study and the comparisons for other latitude bands and time intervals, it shall be referenced to P-III: Limberger et al. (2015).

The capability to retrieve electron density profiles from ionospheric radio occultations is valuable for ionosphere modeling and therefore constitute a key part of this thesis. The assessment of the F2 peak as derived by means of the improved retrieval method yields a good agreement with ionosondes. However, the retrieval algorithms are based on various assumptions and the requirement of external TEC data. It is expected that the accuracy of the retrieved electron density is highly correlated with the spatio-temporal resolution of the GIM.

The extraction of ionospheric information from terrestrial dual-frequency GNSS observations has been described as part of Section 3.2 and considered in P-V: Liang et al. (2014) and P-VI: Liang et al. (2015) where GPS TEC was combined with electron density profiles for regional electron density modeling. The incorporation of integrated TEC data into the 4-D model was successfully carried out by means of a Gauß-Legendre quadrature integration. This integration approach was applied in P-I: Limberger et al. (2013) to obtain TEC maps for the comparison with CODE GIMs and by P-V: Liang et al. (2014) as well as P-VI: Liang et al. (2015) for modeling the electron density by GPS data and evaluating the results against ionosonde measurements. The Gauß-Legendre integration has been validated to be highly adequate as a trade-off between accuracy and computational performance.

Similar to GNSS, the processing of DORIS signals for ionosphere modeling was analyzed by P-IV: Dettmering et al. (2014b) where data of the satellite missions Jason-2, SARAL, Cryosat-2 and Hy-2a are taken into account. A significant improvement for global TEC model has been achieved by the combination of DORIS TEC with GPS, in particular due to the localization of DORIS transmitter beacons in isolated regions such as islands.

Data representation

- How could an adequate representation of the electron density distribution, in particular for the vertical direction, look like?
- ▷ References: Chapter 1, P-I: Limberger et al. (2013)
- What kind of basis functions are suitable and meet the model requirements?
- ▷ References: Chapter 2, P-I: Limberger et al. (2013), P-V: Liang et al. (2014)

In Chapter 1, ionospheric key quantities have been defined by means of the Chapman ion production law that is stimulated by photoionization processes. The F2 layer contains the highest concentration of charged particles and plays a key role in this context. For this region, the maximum production rate or maximum ionospheric electron density $NmF2$ of the F2 layer, the corresponding peak height $hmF2$ and the F2 scale height $HF2$ are fundamental parameters to describe the vertical electron density distribution. Although the Chapman profile is a rather simple approximation it is capable to describe the basic structure of ionospheric layers. As proposed by Jakowski (2005), the Chapman function together with a slowly decaying term allowing for a smooth transition into the plasmasphere was applied by P-I: Limberger et al. (2013), P-II: Limberger et al. (2014) and P-V: Liang et al. (2014) as well as P-VI: Liang et al. (2015) for modeling the electron density. $NmF2$, $hmF2$ and $HF2$ have been selected as model parameters whereas fixed approximations for NOF and HP were taken into account.

Spherical harmonics, voxels and B-spline base functions have been described in Chapter 2 as adequate parametrization methods for modeling ionospheric parameters. The consideration of spherical harmonics is the most common approach – proven for years and defined on the sphere, i.e., appropriate for global representations. Spherical harmonics suffer however from the drawback that every signal influences the solution on the entire globe.

To overcome this issue, localizing B-splines are applied in this work to facilitate the data support in finite intervals. Different B-spline tensor combinations can be introduced for regional and global modeling exploiting the features of endpoint-interpolation from polynomial splines and continuity from trigonometric splines, respectively. The parametrization based on polynomial B-splines has been applied by P-I: Limberger et al. (2013) and P-II: Limberger et al. (2014) for regional electron density modeling in the South American region within $\lambda = [250^\circ, 340^\circ]$ and $\varphi = [-60^\circ, 30^\circ]$. Therefore, tensor products of polynomial B-splines regarding longitude, latitude and time are taken into account. In accordance with P-I: Limberger et al. (2013), the function basis in the spatial domain with respect to longitude and latitude for the levels $J_\lambda = 2$ and $J_\varphi = 3$ is provided by Fig. 6.4. The figure includes a cuboid indicating the influence zone of an exemplary electron density profile. The utilization of tensor

products including a combination of polynomial and trigonometric B-spline intended for modeling in the global domain has been considered by P-IV: Dettmering et al. (2014b).

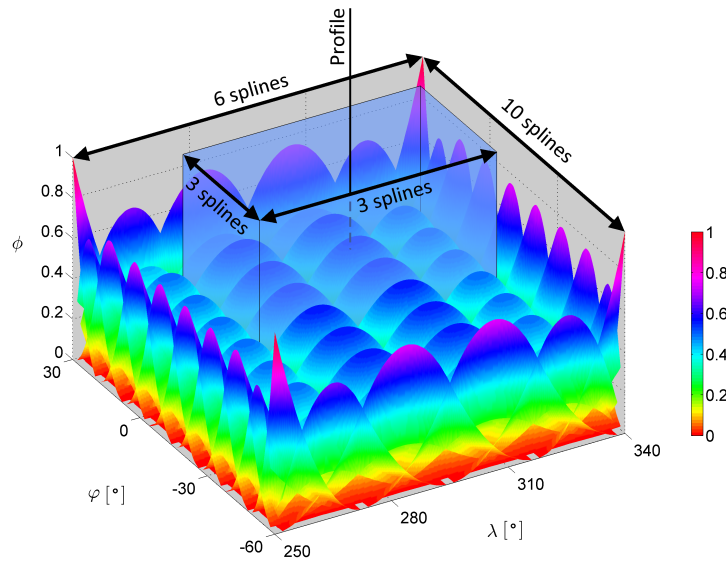


Figure 6.4: 2-D representation of polynomial B-splines defined by the levels $J_\lambda = 2$ and $J_\varphi = 3$ and distributed over an interval of $\lambda = [250^\circ, 340^\circ]$ and $\varphi = [-60^\circ, 30^\circ]$. The embedded transparent cuboid borders the influence zone of an exemplary vertical electron density profile that is indicated by the black solid line. In this example, altogether, $3 \times 3 = 9$ splines are affected.

Parameter estimation and combination of observation techniques

- Which model approach is adequate to comply with the general requirements for the localization of the observed signal, continuous data representation and proper handling of data gaps?
- ▷ References: Chapter 5, P-I: Limberger et al. (2013)
- How can observation groups be combined and individually weighted?
- ▷ References: Chapter 5, P-I: Limberger et al. (2013), P-IV: Dettmering et al. (2014b), P-V: Liang et al. (2014), P-VI: Liang et al. (2015)

P-I: Limberger et al. (2013) presented a 4-D B-spline model driven by CHAMP, GRACE and F-3/C electron density profiles. To stabilize the system and bridge data gaps, IRI 2007 was introduced to provide background information. Furthermore, the determination of relative weighting factors for the different LEO satellite missions and also the prior information was carried out by means of a VCE as described in Section 5.5. The electron density model is highly non-linear and therefore, nested iterations have been realized accounting for the estimation of variance components in the inner loop and the linearization of the model in the outer loop.

In Fig. 6.5, a selection of key parameter maps as computed from the B-spline model are depicted along the left column. The snapshots are related to 1 July 2008 at 12:00 UT. The plots refer to $\Delta hmF2$ (top), $\Delta HF2$ (middle) and $\Delta NmF2$ (bottom). Dark blue regions signalize significant reductions of the background information, i.e., IRI overestimates the key parameters in this case. Electron density profiles are depicted as font labels indicating the satellite mission as CH (CHAMP), GR (GRACE) and C1 - C6 (F-3/C 1-6) as well as the observed time. The spatio-temporal impact of the observations depends on the B-spline level which was chosen here with $J_\lambda = J_\varphi = 2$ and $J_t = 3$ for a region of $90^\circ \times 90^\circ$ in South America between 11:00 and 14:00 UT. Each plot contains an arrow pointing towards one profile with strong impact to the current estimation. The associated electron density

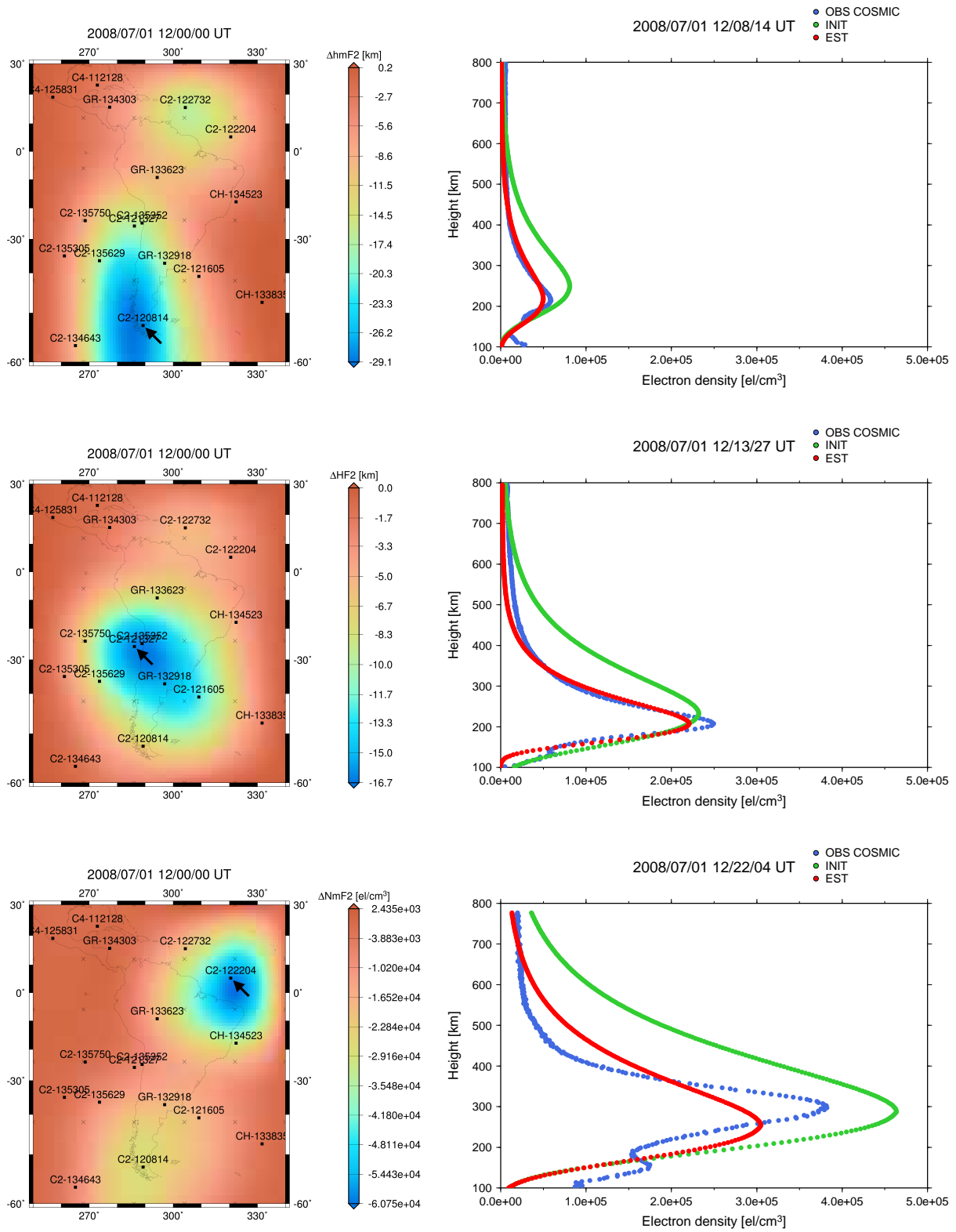


Figure 6.5: Key parameter corrections $\Delta hmF2$, $\Delta HF2$ and $\Delta NmF2$ for a fixed time moment at 12:00 UT on 1 July 2008 are depicted along the left column. Selected F-3/C profiles that have an impact on the key parameter estimation are plotted in the right column and indicated by arrows on the key parameter maps.

profiles are given in the right column. The Chapman profile based on a priori information is plotted in green, the observed profile in blue and the model estimation in red. The actual measurement times are provided in the title. Improvements are visible from the topmost plot where the estimated $hmF2$ is clearly below the IRI $hmF2$ and also the middle representation where the observed and estimated profiles are significantly more narrow, controlled by $HF2$, than the IRI profile. The bottom illustration shows a counterexample where the incidence of an E layer leads to the underestimation of $NmF2$.

After estimating the F2 Chapman parameters and modeling the electron density in the regional domain, a Gauß-Legendre integration following the method described in Section 5.2 was applied to compute VTEC maps. To evaluate the computed VTEC, GIMs provided by the IGS analysis center CODE (henceforth denoted by the subscript CODE) are taken into account as a reference. It shall be noticed that IRI is a climatological model initialized by ionosonde measurements whereas the CODE model is based on frequent updates by GNSS measurements, i.e., it can be expected that the model presented here approaches CODE.

Figure 6.6 shows VTEC snapshots provided by IRI 2007 and CODE as well as the differences $VTEC_{IRI} - VTEC_{CODE}$ (from left to right) for the time moment on 1 July 2008 at 13:55 UT.

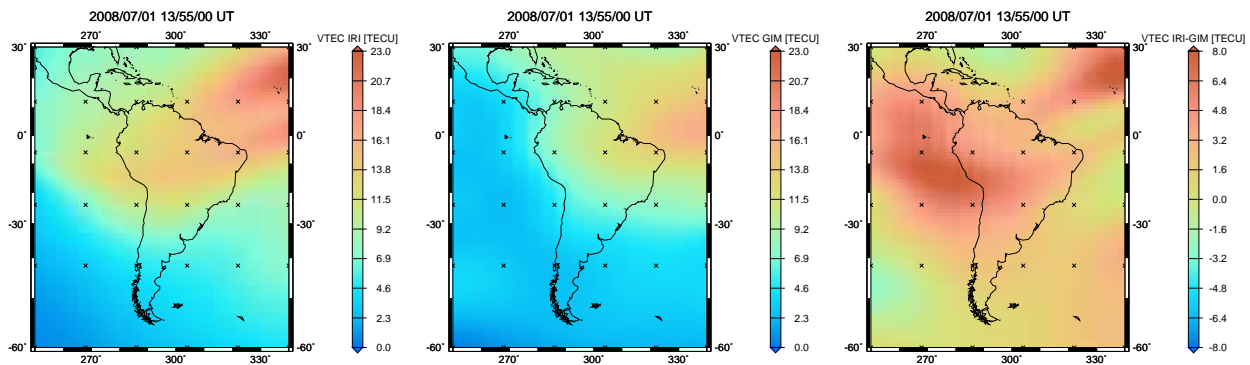


Figure 6.6: VTEC maps referring to IRI-2007 (left), IGS GIM (middle) and the difference between IRI-2007 and IGS GIM (right) for 1 July 2008 at 13:55 UT.

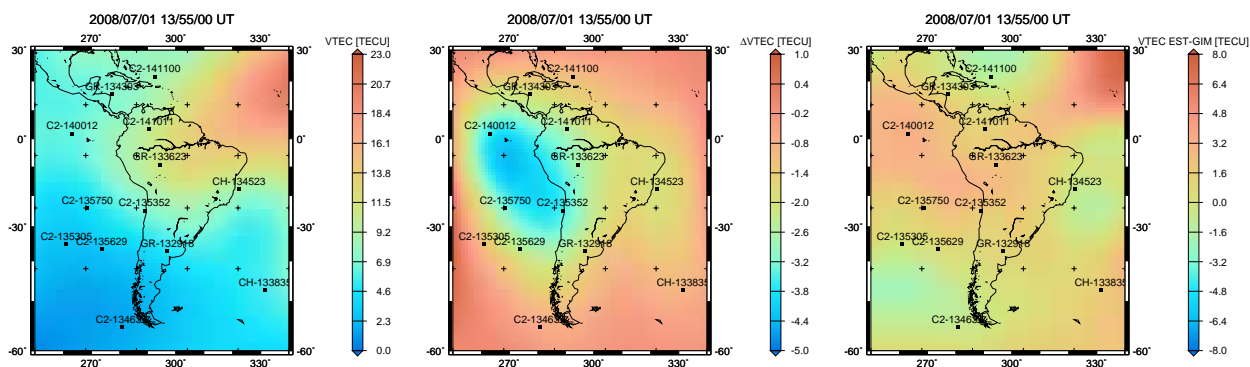


Figure 6.7: VTEC maps referring to the model estimation (left), $\Delta VTEC$ estimation (middle) and the difference between the model estimation and CODE GIM (right) for 1 July 2008 at 13:55 UT.

The main differences of both solutions at the magnitude of up to eight TECU can be found close to the EIA which enters from the North-East into the study region. The corresponding solution for the same time based on the model approach presented in this work, is depicted in Fig. 6.7. The illustrations refer to the modeled $VTEC_{MOD}$, associated corrections $VTEC_{MOD} - VTEC_{IRI}$ and the differences to CODE with $VTEC_{MOD} - VTEC_{CODE}$ (from left to right). The comparison of the differences $VTEC_{IRI} - VTEC_{CODE}$ (Fig. 6.6, right) and $VTEC_{MOD} - VTEC_{CODE}$ (Fig. 6.7, right) clearly shows that the model solution is a correction of IRI and approaches the CODE GIMs.

Aspects of stochastic modeling

- Which dependencies exist between the model parameters and base functions?

▷ References: Chapter 5, P-II: Limberger et al. (2014)

- What is the influence of variance components on the correlations?

▷ References: Chapter 5, P-II: Limberger et al. (2014)

Due to the overlapping feature of B-splines and the essential physical relations between Chapman key parameters, the existence of correlations between the model parameters can be expected. So far, correlations have not been considered in the adjustment system described in Section 5.3 but may cause convergence problems of the parameter estimation. Therefore P-II: Limberger et al. (2014) studied the mathematical correlations between $NmF2$, $hmF2$ and $HF2$ to evaluate the risk caused by the incomplete stochastic model.

Exemplarily, the key parameter correlations matrices for a simulated data ($K_{tt,sim}$) and a real data ($K_{tt,real}$) scenario are provided in Fig. 6.8. F-3/C electron density profiles provided by CDAAC are considered as input observations. For the simulation, synthetic measurements for real positions and epochs of the F-3/C profiles have been generated. The matrices are subdivided into diagonal block matrices regarding the different F2 parameters and off-diagonal blocks related to correlations between different parameters.

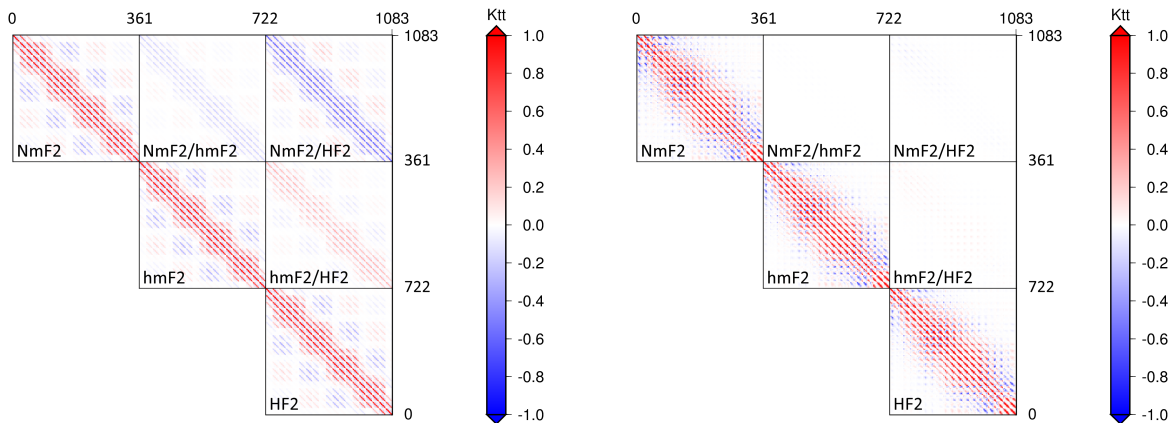


Figure 6.8: Correlation matrices of the key parameters K_{tt} at 12:00 UT on 1 July 2008 based on synthetic data (left) and F-3/C observations (right). Both matrices K_{tt} represent correlations for parameters related to a grid with $\Delta\varphi = 5^\circ \times \Delta\lambda = 5^\circ$ resolution.

From the left matrix $K_{tt,sim}$, reflecting dependencies of the simulated scenario, moderate model correlations between $hmF2$ and $HF2$, increased inverse correlations between $NmF2$ and $HF2$ and also weak inverse correlations between $NmF2$ and $hmF2$ have been determined. Additionally, the strong correlation between nearby parameters are reflected from the pattern along the diagonal which is mainly influenced by the overlapping B-splines characteristic. The main difference when comparing $K_{tt,sim}$ with the correlation matrix of the real data scenario $K_{tt,real}$, shown on the right hand side of Fig. 6.8, are the missing off-diagonal correlations. Based on the VCE, the relative weighting between observations and prior information strongly depends in the distribution of data. In scenarios of sparse observation distribution, correlations are even suppressed which is reflected from the results here.

In this study, the simulated scenario was vitiated by increased correlations but still was solvable. The implementation of an extended stochastic model is nevertheless recommended and in need for discussion in the near future. Possible improvements may be achieved from the consideration of correlations

between observations as well as key parameters. The results of P-II: Limberger et al. (2014) can be used as a basis for taking into account the correlations between Chapman key parameters. Regarding radio occultations, it is expected that particularly the consideration of height dependent correlations between the electron densities at the tangent points could have a significant impact.

6.2 Conclusions and Outlook

In this thesis, a regional 4-D electron density model that features the capability to account for the combination of different observation techniques has been developed and validated. The approach is based on the stacking of normal equations and enables the individual weighting of different observation groups by means of a VCE. To allow for the processing of TEC input observations, an integration technique based on the Gauß-Legendre quadrature method is applied. The modeling approach has been described and evaluated, e.g., by P-I: Limberger et al. (2013). Furthermore, the signal processing for different observation techniques has been studied as part of this work with emphasis on the retrieval and application of electron density profiles derived from IRO. The presented results highlight the significant contribution of IRO for 4-D modeling, in particular when used in combination with GPS.

The developed model has been tested particularly by the data combination of different radio occultation missions (CHAMP, GRACE, F-3/C) where the retrieved electron density profiles are considered for resolving the vertical ionospheric structure. The accuracy of the F2 peak derived from F-3/C occultations by means of an improved Abel inversion technique has been assessed by P-III: Limberger et al. (2015) from a long-term comparison with ionosonde observations. An open issue that needs further investigation concerns the treatment of the originally slant profiles. Based on the retrieval, electron density values are derived along so-called tangent points that vary in position and time during the occultation event. The horizontal discrepancy between the highest and lowest profile point can amount up to several degrees in latitude and longitude with a time difference of few minutes. In this work, the observed F2 peak is considered as the anchor point in which the profiles are assumed to be vertical – a temporary sufficient but nevertheless unsatisfying condition that requires further investigations.

In addition to radio occultations, signals of further satellite sounding techniques such as GNSS and DORIS were processed for the derivation of TEC. These data have been used by P-V: Liang et al. (2014), P-VI: Liang et al. (2015), Dettmering et al. (2014a) and P-IV: Dettmering et al. (2014b). A strong mutual support was achieved from the combination of GNSS with IRO. GNSS provide dense TEC data through terrestrial tracking networks mainly over the continents whereas IRO are more sensitive regarding the vertical direction and contribute electron density profiles that additionally support the bridging of data gaps over the oceans. Furthermore, improvements of global TEC solutions based on the processing of GPS were found by the incorporation of DORIS measurements. The terrestrial DORIS transmitters are part of a quite homogeneously distributed global network that, due to low infrastructure requirements, includes stations located even in isolated regions such as islands helping to cover gaps on the oceans. However, DORIS code pseudoranges are very noisy and only carrier phase observations are usable. The determination of the CPB is therefore an issue that needs to be considered when dealing with DORIS data. A preliminary solution is described in P-IV: Dettmering et al. (2014b) where external data of the IGS are taken into account to level the DORIS TEC.

A rather simple and limited stochastic model has been introduced in this thesis where correlations neither between the observations nor between the model parameters are considered. Related issues and resulting consequences have been discussed by P-II: Limberger et al. (2014) exposing the key role of the VCE in scenarios with sparse and dense data distributions but also the requirement for an improved stochastic model.

To describe the vertical electron density distribution, a simple but efficient Chapman layer has been chosen where the selected key parameters, $NmF2$, $hmF2$ and $HF2$, are expressed by series expansions

in tensor products of 1-D B-spline basis functions regarding latitude, longitude and time with initially unknown series coefficients. The estimation of B-spline coefficients for all three key parameters in a combined adjustment system has been successfully carried out with the developed model. The implemented Chapman model is however a rudimentary approximation and should be considered as a preliminary attempt. It can be expected, that a more sophisticated model for the vertical electron density distribution leads to significant improvements, in particular by the consideration of additional layers and parameters.

Quadratic, polynomial B-splines are selected for the regional modeling which offer excellent features in terms of local support and endpoint-interpolation. Periodic, trigonometric B-splines were introduced as another function type intended for the global modeling. The model resolution is controlled by the B-spline level and allows for the proper handling of data gaps by an individual level adjustment for each key parameter with respect to latitude, longitude and time. It is furthermore conceivable to exploit the developed approach for the modular computation of regional subsets with individual model resolutions to be embedded as densifications into a global solution.

The B-spline level has been adapted by P-I: Limberger et al. (2013) to the average distribution of the input observation. Thus, only a relatively low level could be taken into account due to the limited and mostly inhomogeneous distribution of electron density profiles based on radio occultations. It follows, that the model resolution in regions with high observation density cannot be fully exploited, i.e., the solution will be smoothed whereas data gaps in areas of low observation density are not properly bridged. Therefore, a background model has been introduced in this work to overcome data gaps and prevent a possible ill-conditioning or singularity of the stacked normal equation matrix. However, the B-spline parametrization allows for a MRR where the signal is split into a smooth approximation and a number of detail signals by successive low-pass filtering. The pyramidal algorithm of the MRR together with fusion techniques can then be applied to merge subregions of higher resolutions into a combined representation.

As an alternative to uniform B-splines with homogeneously distributed knot locations, non-uniform B-splines with adapted knot locations may be applied. In this case, the basis functions are adapted, for instance, to the distribution of the input observations. Thus, the model resolution in dense data areas is increased by narrow support of the splines and data gaps are bridged by wider extent, i.e., the need for prior information may even become unnecessary. It can also be imagined that the best solution follows from a compromise between the knot adaption (1) to the observations to overcome data gaps and (2) to the ionospheric structure for an improved resolution in high gradient regions, e.g., along the EIA.

Recommendations for future works are related to the development of a more sophisticated description for the vertical electron density distribution and the improvement of the stochastic model under consideration of correlations between key parameters as well as relations between observations, e.g., height dependent correlations between successive electron density profile values. It was shown furthermore, that the selection of B-spline basis functions provide essential advantages, specifically regarding the localization of signals and the opportunity for a MRR. However, the usage of adapted knot locations should be considered for upcoming works.

For this thesis, the F-3/C constellation played an essential role regarding the tracking of occultations and retrieval of electron density profiles. The developments for Formosat-7/COSMIC-2 (F-7/C-2), the follow-on mission of F-3/C, are under progress aiming an enhanced and, especially for ionospheric research, very promising mission design. The system will again be operated by a cooperation of US agencies under the lead of NOAA and the Taiwanese Space Organisation NSPO. The radio occultation instruments are developed at JPL. The constellation consists of six satellites in low inclined orbits (first space segment, launch scheduled for late 2015) plus six additional satellites in high inclined orbits (second space segment, launch scheduled for early 2018). An estimated distribution of electron density profiles during a time frame of three hours is depicted in Fig. 6.9. The distributions of profiles for F-3/C are represented as pink dots for comparison with F-7/C-2 profiles in green. Approximately

12,000 profiles per day are expected from the full F-7/C-2 constellation, a very large number with revolutionary benefit for ionosphere modeling.

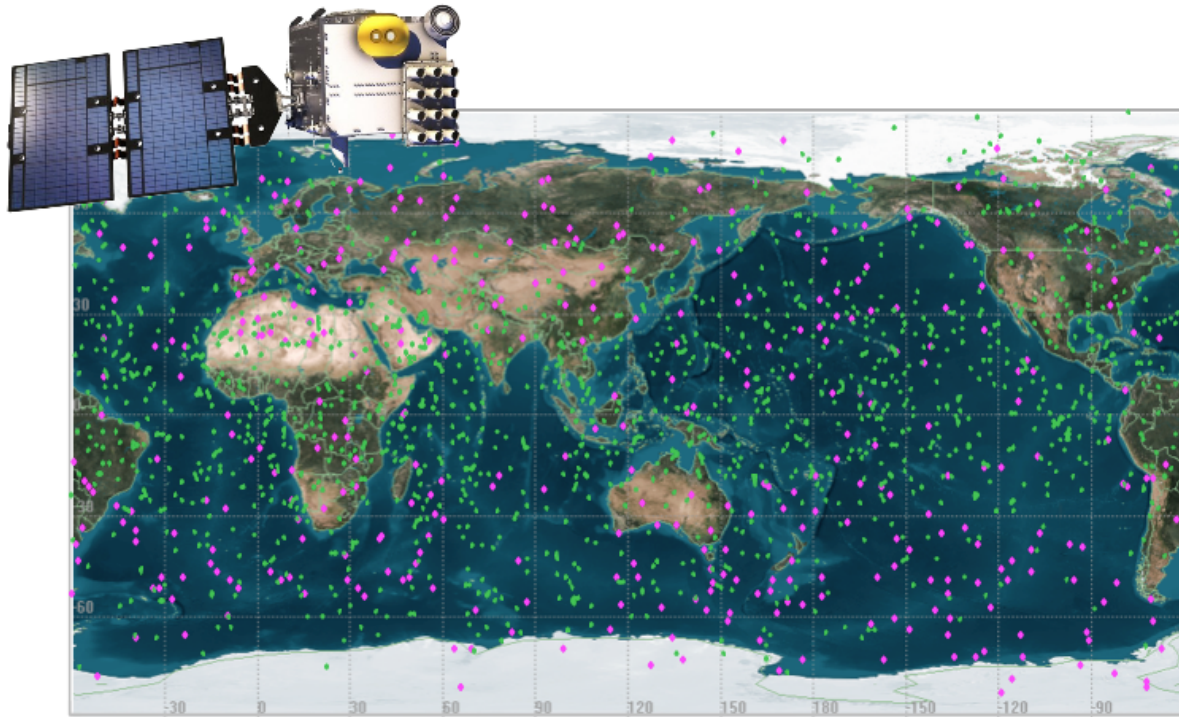


Figure 6.9: Example for the distribution of electron density profiles from F-3/C (pink dots) and F-7/C-2 (green dots) during a period of three hours, source: UCAR, <http://www.cosmic.ucar.edu/cosmic2/>. A F-7/C-2 satellite draft has been depicted in the top-left corner.

The number of LEO missions capable of tracking GNSS radio occultations has increased rapidly in recent years and continues to rise. The potential of occultation measurements for ionospheric sounding has been discovered but is far from being exhausted. In particular, 4-D electron density models will significantly benefit by an improved global coverage and diverse constellations sounding the ionosphere from different orbit altitudes and geometries.

7 Publications

This chapter summarizes those publications, that constitute the basis for this cumulative thesis. Specifically, P-I, P-II and P-III as first author publications and P-IV, P-V, P-VI as co-author publications. To estimate the own contribution regarding the realization process of each paper, percentage estimations with respect to different criteria are provided. It shall be noted that the percentages are just approximations and therefore have been rounded to tens. The following criteria have been taken into account:

1. Paper concept
2. Computations and software development
3. Data analysis and interpretation of results
4. Design and creation of figures
5. Manuscript structure and writing

For each paper, an overview containing a copyright paragraph, a brief summary and the declaration of own contribution including a table for the rating of the previously introduced criteria is provided. Besides, a percentage number rating the total own contribution to each publication has been roughly estimated and can be found as part of the declaration of own contribution. This overall approximation reflects the own contribution under consideration of the contribution significance.

7.1 P-I

Limberger, M., Liang, W., Schmidt, M., Dettmering, D., and Hugentobler, U. (2013): Regional representation of F2 Chapman parameters based on electron density profiles. *Ann. Geophys.*, 31(12), 2215-2227, European Geosciences Union, DOI 10.5194/angeo-31-2215-2013.

Copyright

This work is published in *Annales Geophysicae* under the license of Creative Commons. Copyrights are retained by the Authors. P-I is an open access publication and available at <http://www.ann-geophys.net/31/2215/2013/angeo-31-2215-2013.html>.

Summary

This paper has a strong impact to several aspects of this thesis as it contains the basic strategy and methodology for modeling the electron density from the combination of different observation techniques. Furthermore, P-I describes the nested iterations regarding the linearization and variance component estimation. Preprocessed electron density profiles of the occultation missions CHAMP, GRACE and F-3/C are taken into account for a regional electron density model in the South American sector. Therefore, polynomial B-splines are used for the representation of Chapman F2 key parameters in latitude, longitude and time for improving an IRI 2007 background model. For testing the model performance, a simulated and a real-data scenario covering a time frame of three hours under

low solar conditions have been analyzed.

P-I demonstrates the capability of the B-spline model approach to describe the 4-D electron density distribution exploiting the sensitivity of occultation data for resolving the vertical electron density structure. Through integration of the electron density by means of the Gauß-Legendre method, regional VTEC maps have been validated against CODE Global Ionosphere Map (GIM)s. It can be concluded that for those regions, where measurement have been available, our results approach the GIM and improve IRI.

Declaration of own contribution

This paper has been published as part of the Deutsche Forschungsgemeinschaft (DFG) project "Multi-scale model of the ionosphere from the combination of modern space-geodetic satellite techniques", initiated by Deutsches Geodätisches Forschungsinstitut (DGFI), Munich, Germany, the Institute of Communications and Navigation of the German Aerospace Center (DLR), Neustrelitz, Germany, and the Institute for Astronomical and Physical Geodesy (IAPG) of Technische Universität München (TUM), Germany. The paper conception has been proposed by M. Limberger and discussed with all co-authors. The computations are based on a C++ software application that has partially been developed by M. Limberger as part of the project. The variance component estimation as a significant component of this paper, has been implemented into the software by M. Limberger. Analysis and evaluations are carried out by M. Limberger under helpful assistance by the co-authors. The manuscript writing has been done by M. Limberger and reviewed by the co-authors.

The overall own contribution is estimated at 90 %.

Table 7.1: Apportionment of own contributions for P-I.

Criteria	Estimated own contribution
Paper concept	80 %
Computations and software development	80 %
Data analysis and interpretation of results	70 %
Design and creation of figures	90 %
Manuscript structure and writing	90 %

Confirmation by the authors

We hereby confirm the correctness of the declaration of own contribution for the publication

Limberger, M., Liang, W., Schmidt, M., Dettmering, D., and Hugentobler, U. (2013): Regional representation of F2 Chapman parameters based on electron density profiles. *Annales Geophysicae* 31(12), 2215-2227, European Geosciences Union, DOI: 10.5194/angeo-31-2215-2013.

Wenjing Liang

Deutsches Geodätisches Forschungsinstitut der
Technischen Universität München (DGFI-TUM),
München, Germany

Signature: 

Date: 1. 6. 2015

Prof. Michael Schmidt

Deutsches Geodätisches Forschungsinstitut der
Technischen Universität München (DGFI-TUM),
München, Germany

Signature: 

Date: 1. 6. 2015

Dr. Denise Dettmering

Deutsches Geodätisches Forschungsinstitut der
Technischen Universität München (DGFI-TUM),
München, Germany

Signature: 

Date: 20. 05. 2015

Prof. Urs Hugentobler

Technische Universität München (TUM),
Forschungseinrichtung Satellitengeodäsie (FESG),
München, Germany

Signature: 

Date: 18. May 2015



Regional representation of F2 Chapman parameters based on electron density profiles

M. Limberger¹, W. Liang², M. Schmidt², D. Dettmering², and U. Hugentobler¹

¹Technische Universität München – Institute of Astronomical and Physical Geodesy (IAPG), Arcisstr. 21, 80333 München, Germany

²Deutsches Geodätisches Forschungsinstitut (DGFI), Alfons-Goppel-Str. 11, 80539 München, Germany

Correspondence to: M. Limberger (marco.limberger@bv.tum.de)

Received: 23 August 2013 – Revised: 8 November 2013 – Accepted: 15 November 2013 – Published: 20 December 2013

Abstract. Understanding the physical processes within the ionosphere is a key requirement to improve and extend ionospheric modeling approaches. The determination of meaningful parameters to describe the vertical electron density distribution and how they are influenced by the solar activity is an important topic in ionospheric research. In this regard, the F2 layer of the ionosphere plays a key role as it contains the highest concentration of electrons and ions. In this contribution, the maximum electron density $NmF2$, peak height $hmF2$ and scale height $HF2$ of the F2 layer are determined by employing a model approach for regional applications realized by the combination of endpoint-interpolating polynomial B splines with an adapted physics-motivated Chapman layer. For this purpose, electron density profiles derived from ionospheric GPS radio occultation measurements of the satellite missions FORMOSAT-3/COSMIC, GRACE and CHAMP have been successfully exploited. Profiles contain electron density observations at discrete spots, in contrast to the commonly used integrated total electron content from GNSS, and therefore are highly sensitive to obtaining the required information of the vertical electron density structure. The spatio-temporal availability of profiles is indeed rather sparse, but the model approach meets all requirements to combine observation techniques implicating the mutual support of the measurements concerning accuracy, sensitivity and data resolution. For the model initialization and to bridge observation gaps, the International Reference Ionosphere 2007 is applied. Validations by means of simulations and selected real data scenarios show that this model approach has significant potential and the ability to yield reliable results.

Keywords. Ionosphere (equatorial ionosphere; modeling) – radio science (ionospheric physics)

1 Introduction

The steadily increasing number of appropriate measurements goes hand in hand with the availability of different observation techniques that may contribute individual sensitivities for resolving ionospheric key parameters. The majority of prevailing observation-driven ionosphere models consider the spatial and temporal variations of the total electron content (TEC) derived mainly or even only from GNSS measurements due to the availability of a dense data distribution. A widely used approach is the modeling of TEC variations in terms of a 3-D description with respect to longitude, latitude and time, while the vertical distribution of the electron density (N_e) is mostly not considered. Among other things, this is rooted in the fact that terrestrial GNSS measurements provide the TEC as an integral observable between the emitting satellite and the ground-based receiver, which is rather insensitive for the description of the electron density distribution with respect to height. Electron density profiles derived from radio occultation measurements may be used instead or in combination with other observation types to provide the required support for the determination of key parameters with height dependency. At its inception, the GPS radio occultation technique was tested by means of the Global Positioning System/Meteorology (GPS/MET) experiment, which was carried out between 1995 and 1997 by the University Corporation for Atmospheric Research (UCAR). Based on this pilot experiment, first promising results of limb sounding

of the Earth's atmosphere and ionosphere could be obtained (Ware et al., 1996; Hajj and Romans, 1998). Several low Earth orbiter (LEO) missions were launched afterwards, such as the German Challenging Minisatellite Payload (CHAMP) in July 2000, which was operated by the German Research Centre for Geosciences (GFZ) and ended in September 2010. The tandem satellite mission Gravity Recovery and Climate Experiment (GRACE) was launched in 2002 and is operated by a cooperation of NASA and the German Aerospace Center (DLR). Further improvements concerning the observation coverage have been achieved with the joint US–Taiwanese mission Formosa Satellite 3 and Constellation Observing System for Meteorology, Ionosphere, and Climate (FORMOSAT-3/COSMIC) as a result of the constellation of six satellites on six orbital planes with a 30° separation. The FORMOSAT-3/COSMIC satellites fly in an altitude of approximately 800 km, while for CHAMP and GRACE an initial orbit of around 450–500 km was chosen. All three missions are adequate for sounding the electron density peak region of the ionospheric F2 layer, which is typically located at an altitude of approximately 250–350 km in midlatitudes and under certain conditions up to 500 km in equatorial regions (Hoque and Jakowski, 2012).

The spaceborne atmospheric radio occultation technique allows for tracking of electromagnetic (EM) signals that have been modified by interactions with the atmospheric medium (Kirchengast et al., 2004). The geometry between the source transmitting the EM signal and the receiver is the key to ensure the propagation of the signal in limb-sounding geometry. In the case of GPS radio occultation, a receiver flown on a LEO satellite tracks the phase and amplitude of the GPS signal, while the GPS satellite sets or rises behind the Earth's atmosphere (= setting/rising occultation). The obtained observations contain information on the vertical refractivity below the LEO orbit and therefore enable the extraction of electron density profiles, which can be derived from the ionospheric index of refraction. Retrieval methods have been described in several publications such as Jakowski et al. (2002) or Tsai and Tsai (2004). The derived profiles contain discrete N_e observations that structurally describe the electron density distribution along the measured points. Relevant physical quantities such as the maximum electron density $NmF2$ or the corresponding peak height $hmF2$ become more or less directly visible. However, the data distribution given by retrieved electron density profiles is by far not as dense as for terrestrial GNSS, but the potential of profiles can be exploited in 4-D modeling. The vertical description of the electron density can be approximated by a Chapman function that has been successfully used in several applications for sounding the planetary ionosphere. The original Chapman layer was introduced in the 1960s by Rishbeth and Garriot (1969) for modeling the ionospheric electron density for a fixed atmospheric scale height. Variations of the original functions for an improved description of certain layers have been established over the years; for example, Reinisch et al.

(2007) introduced a modification of the original α -Chapman layer with a continuously varying scale height to model the F2 topside electron density. The model presented in this paper will take an adapted α -Chapman layer into account that was proposed by Jakowski (2005) and considers a F2 ionosphere layer for a fixed scale height plus a slowly decaying plasmasphere term. It can be described by a total of five key parameters where this contribution covers the determination of the F2 layer-related key parameters contained in the α -Chapman layer by means of exclusively electron density profiles. After the introduction of the mathematical and physics-motivated model (Sect. 2), the adjustment system, which forms the backbone of the parameter estimation, will be explained in detail (Sect. 3). The model validation will be carried out in several stages, comprising a closed-loop simulation (Sect. 4.1) and real data analysis (Sect. 4.2) with investigations on the key parameters (Sect. 4.2.1) and also TEC (Sect. 4.2.2).

2 Model

To model the vertical electron density, an adapted α -Chapman layer is introduced to allow for the consideration of the ionospheric F2 layer and the plasmasphere (Jakowski, 2005). It consists of a F2 Chapman function and a slowly decaying exponential term, which allow for a smooth transition between the topside electron density of ionosphere and plasmasphere. The model equation finally yields

$$\begin{aligned}
 N_e(h) &= \underbrace{N_e^{F2}(h, NmF2, hmF2, HF2)}_{\text{F2 layer}} + \underbrace{N_e^P(h, NOP, HP)}_{\text{Plasmasphere}} \\
 &= NmF2 \exp \left[\frac{1}{2} \left(1 - \frac{h - hmF2}{HF2} - \exp \left(\frac{hmF2 - h}{HF2} \right) \right) \right] \\
 &\quad + NOP \exp \left(\frac{-|h - hmF2|}{HP} \right) \quad (1)
 \end{aligned}$$

and contains five descriptive key parameters, namely the maximum electron density of the F2 layer $NmF2$, the corresponding F2 peak height $hmF2$, the F2 topside scale height $HF2$, the plasmasphere basis density NOP and the plasmasphere scale height HP . Following Jakowski (2005), a physically reasonable value of 10^4 km for HP (in the case of $h > hmF2$, otherwise 10 km) and the assumption of proportionality between NOP and $NmF2$ can be taken into account. It should be kept in mind that the F2 scale height differs with respect to bottomside and topside ionosphere but is assumed to be equal in the model approach presented here.

Each of the key parameters can be modeled in terms of three 1-D endpoint-interpolating polynomial B spline functions with regard to longitude λ , latitude φ and time t with initially unknown series coefficients d . The basic theory about B spline modeling is, for example, given by Schumaker (1981) and Lyche and Schumaker (2000), and discussions on the application of B splines to model the regional vertical total electron content (VTEC) have already been published by

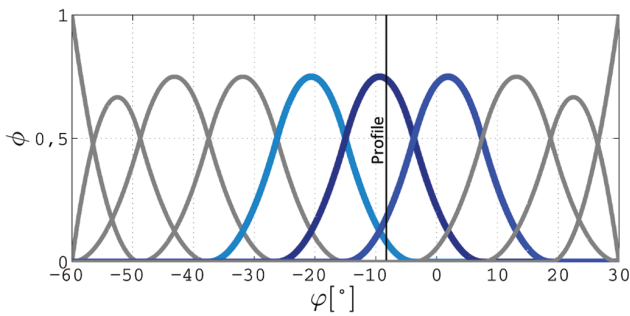


Fig. 1. Endpoint-interpolating polynomial B splines of level $J = 3 \rightarrow K = 10$ within $[-60^\circ, +30^\circ]$ latitude. The blue splines are influenced by the exemplary profile (black line) located at $\varphi = -8^\circ$.

Schmidt (2007), Zeilhofer et al. (2008) and Dettmering et al. (2011a). Polynomial B splines are chosen due to their advantage of the endpoint-interpolating and localizing characteristic for regional modeling, meaning that the spline values are constrained at the boundaries and generally are nonzero just within a compact interval. Results of the comparison between B splines and spherical harmonics and their different advantages with respect to regional and global modeling are given by Schmidt et al. (2011) and will not be further discussed at this point. Each measurement and vertical profile penetrates a certain number of B spline functions and consequently contributes to the determination of the corresponding series coefficients. Figure 1 shows a 1-D representation of endpoint-interpolating polynomial B splines based on level $J = 3$ within an area of $\varphi = [-60^\circ, +30^\circ]$. In the case of one dimension, the function values $f(\varphi)$ are computed from the scaling functions $\phi_k^{J_\varphi}(\varphi)$ by

$$f(\varphi) = \sum_{k=1}^{K(J_\varphi)} d_k^{J_\varphi} \phi_k^{J_\varphi}(\varphi) \quad (2)$$

and $d_k^{J_\varphi}$ are the series coefficients labeled with their affiliation to the corresponding $\phi_k^{J_\varphi}$. $K(J_\varphi)$ denotes the number of B spline functions calculated from

$$K(J_\varphi) = 2^J + 2 \quad (3)$$

according to the associated B spline level J_φ . Consequently $J_\varphi = 3$ defines 10 splines that are distributed over the given latitude sector. The endpoint-interpolating characteristic of polynomial B splines becomes clearly visible at the boundaries where only the first and last two scaling functions are modified. With regard to the use of electron density profiles, a black line has been depicted to indicate an exemplary profile and its influence zone. The profile is located at $\varphi = -8^\circ$ and solely penetrates the blue splines. Accordingly, each electron density observation supports exactly three spline functions in the case of modeling one dimension.

The transfer from one to n dimensions is achieved by the consideration of tensor products composed of n 1-D scaling

functions. Figure 2 shows an example for a 2-D representation based on

$$f(\lambda, \varphi) = \sum_{k_1=1}^{K(J_\lambda)} \sum_{k_2=1}^{K(J_\varphi)} d_{k_1, k_2}^{J_\lambda, J_\varphi} \phi_{k_1}^{J_\lambda}(\lambda) \phi_{k_2}^{J_\varphi}(\varphi), \quad (4)$$

where the situation refers to a two-dimensional scenario regarding latitude φ $[-60^\circ, +30^\circ]$ and longitude λ $[250^\circ, 340^\circ]$. The spline levels are defined as $J_\lambda = 2$ and $J_\varphi = 3$, and therefore the area is covered by $6(\lambda) \times 10(\varphi) = 60$ spline functions. An exemplary profile located at $\lambda = 304^\circ$ and $\varphi = 0^\circ$ is depicted as a solid black line where the cuboid covers all the splines that are located in the intersection zone of profile and splines. In this case, altogether $3(\lambda) \times 3(\varphi) = 9$ splines are affected by a single profile at a specific time. The modeling approach presented in this paper considers time as the third dimension to be modeled by polynomial B splines, and consequently $3(\lambda) \times 3(\varphi) \times 3(t) = 27$ splines are influenced by a single observation at a specific time. In terms of the B spline expression, the description of a specific key parameter yields

$$\kappa_r(\lambda, \varphi, t) = \sum_{k_1=1}^{K(J_\lambda)} \sum_{k_2=1}^{K(J_\varphi)} \sum_{k_3=1}^{K(J_t)} d_{k_1, k_2, k_3}^{J_\lambda, J_\varphi, J_t} \phi_{k_1}^{J_\lambda}(\lambda) \phi_{k_2}^{J_\varphi}(\varphi) \phi_{k_3}^{J_t}(t), \quad (5)$$

where κ_r denotes a specific key parameter identified by the subscript $r \in \{1, \dots, R\}$ with the total number R of key parameters intended to be determined, i.e., in the case of the three F2 Chapman parameters: $\kappa_1 = NmF2$, $\kappa_2 = hmF2$ and $\kappa_3 = HF2$. The unknown target quantities to be determined are B spline series coefficients with respect to each F2 key parameter, which henceforth are substituted with the coefficient vector \mathbf{d} . $K(J) \in \{K(J_\lambda), K(J_\varphi), K(J_t)\}$ and $J \in \{J_\lambda, J_\varphi, J_t\}$ are distinguished with respect to the given dimensions. The higher the level J , the sharper the spline functions and consequently the higher the detail resolution. Accordingly, J should be consistent with the given observation density. Under the assumption of a constant observation sampling Δsi on the interval $[si_{\min}, si_{\max}]$, the relation

$$\Delta si < \frac{si_{\max} - si_{\min}}{K(J) - 1} \quad (6)$$

will be taken into account (Schmidt et al., 2011). Rearrangements and the substitution of $K(J) = 2^J + 2$ based on Eq. (3) lead to

$$J < \log_2 \left(\frac{si_{\max} - si_{\min}}{\Delta si} - 1 \right) \quad (7)$$

and show the dependency between the defined B spline level J and data sampling Δsi . This formulation obviously has been developed for the case of a homogeneous data distribution. Although the distribution of electron density profiles is rather sparse and inhomogeneous, this definition can be used to find rough estimations for suitable B spline levels.

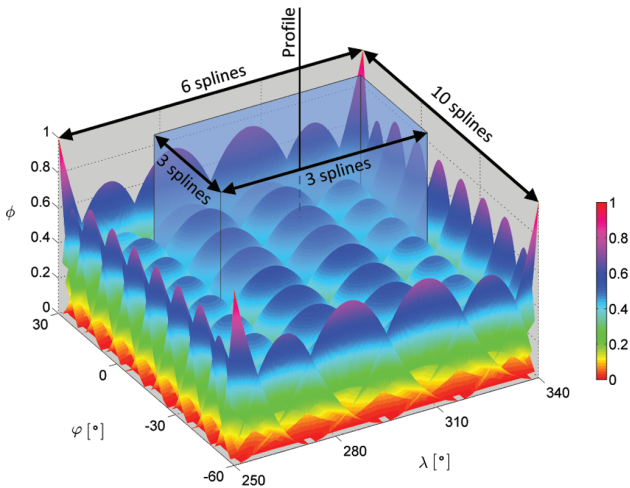


Fig. 2. 2-D B spline representation referring to $\lambda = [250^\circ, 340^\circ]$ and $\varphi = [-60^\circ, 30^\circ]$. The embedded transparent cuboid borders the influence zone of a profile that is indicated by the black solid line. Altogether, $3 \times 3 = 9$ splines are affected.

3 Determination of B spline series coefficients

For the determination of \mathbf{d} a Gauss–Markov model is established (Koch, 1999). A general expression for the functional and stochastic part is respectively given by

$$\mathbf{A}\mathbf{d} = \mathbf{l} + \mathbf{e}_l \quad \text{and} \quad \boldsymbol{\Sigma}_l = \sigma_l^2 \mathbf{P}_l^{-1}. \quad (8)$$

Here, \mathbf{A} is the $n \times u$ coefficient matrix with full column rank, the so-called design matrix, where n is the total number of observations and u is the number of unknowns, i.e., the total number of unknown B spline series coefficients collected in \mathbf{d} . In particular, \mathbf{d} is the $u \times 1$ vector that contains the unknown coefficients referring to the different key parameters $\mathbf{d} = (\mathbf{d}_{\kappa_1}^T, \dots, \mathbf{d}_{\kappa_R}^T)^T$. \mathbf{P}_l is the known positive definite $n \times n$ weight matrix of the observations collected in the $n \times 1$ vector \mathbf{l} and \mathbf{e}_l indicates observation noise. Furthermore, σ_l^2 identifies the unknown variance component of the observations and $\boldsymbol{\Sigma}_l$ is the corresponding $n \times n$ covariance matrix. Since the data distribution of electron density profiles is rather sparse, data gaps have to be bridged by prior information for the unknown series coefficients. The corresponding functional and stochastic model for the prior information can be found with

$$\mathbf{d} = \boldsymbol{\mu} + \mathbf{e}_\mu \quad \text{and} \quad \boldsymbol{\Sigma}_\mu, \quad (9)$$

where $\boldsymbol{\mu}$ indicates the $u \times 1$ vector of prior information with the $u \times u$ covariance matrix $\boldsymbol{\Sigma}_\mu$ and \mathbf{e}_μ denotes the prior information error. $\boldsymbol{\Sigma}_\mu$, in particular, contains the individual unknown variance components $\sigma_\mu^2 \in \{\sigma_{\kappa_1}^2, \sigma_{\kappa_2}^2, \dots, \sigma_{\kappa_R}^2\}$ as well as the known positive definite $u \times u$ weight matrices $\mathbf{P}_\mu \in \{\mathbf{P}_{\kappa_1}, \mathbf{P}_{\kappa_2}, \dots, \mathbf{P}_{\kappa_R}\}$ of the unknown key parameters and thus yields

$$\boldsymbol{\Sigma}_\mu = \text{diag} \left(\sigma_{\kappa_1}^2 \mathbf{P}_{\kappa_1}^{-1}, \sigma_{\kappa_2}^2 \mathbf{P}_{\kappa_2}^{-1}, \dots, \sigma_{\kappa_R}^2 \mathbf{P}_{\kappa_R}^{-1} \right). \quad (10)$$

In this paper, the weighting matrices \mathbf{P}_l and \mathbf{P}_μ for observations and prior information are applied as identity matrices; that is, equal weights without consideration of observation or prior information correlations are introduced. The observation model given by Eq. (1) is highly nonlinear and thus requires a linearization in order to apply the linear model defined on the left of Eq. (8). Therefore a Taylor series expansion based on a first-order approximation is performed. The linearized model for a specific observation i reads

$$N_e(h)_i = N_e(\kappa_1(\mathbf{d}_{\kappa_1,0}), \dots, \kappa_R(\mathbf{d}_{\kappa_R,0}))_i + \sum_{r=1}^R \left(\left[\frac{\partial N_e}{\partial \kappa_r} \right]_0 \left[\frac{\partial \kappa_r}{\partial \mathbf{d}_{\kappa_r}} \right]_0 \right)^T \Delta \mathbf{d}_{\kappa_r}, \quad (11)$$

where each key parameter κ_r is modeled by an appropriate set of corresponding series coefficients \mathbf{d}_{κ_r} according to Eq. (5). Afterwards, the normal equations for a single observation technique can be derived by

$$\left(\frac{1}{\sigma_l^2} \mathbf{A}^T \mathbf{P}_l \mathbf{A} + \mathbf{W} \right) \Delta \hat{\mathbf{d}} = \frac{1}{\sigma_l^2} \mathbf{A}^T \mathbf{P}_l \mathbf{L} + \mathbf{W} \mathbf{M}, \quad (12)$$

where \mathbf{W} substitutes an extended weight matrix with the block diagonal structure

$$\mathbf{W} = \boldsymbol{\Sigma}_\mu^{-1} = \text{diag} \left(\frac{\mathbf{P}_{\kappa_1}}{\sigma_{\kappa_1}^2}, \frac{\mathbf{P}_{\kappa_2}}{\sigma_{\kappa_2}^2}, \dots, \frac{\mathbf{P}_{\kappa_R}}{\sigma_{\kappa_R}^2} \right) \quad (13)$$

containing individual variance factors and weight matrices of the unknown key parameters. The observation vector, originally denoted as \mathbf{l} , is now replaced by the reduced observation vector \mathbf{L} that contains the differences between observed and computed initial electron densities

$$L_i = N_e(h)_i - N_e(\kappa_1(\mathbf{d}_{\kappa_1,0}), \dots, \kappa_R(\mathbf{d}_{\kappa_R,0}))_i \quad (14)$$

resulting from the linearization step in Eq. (11). The hat symbol used for $\Delta \hat{\mathbf{d}}$ symbolizes that the coefficient corrections are outcomes of the adjustment process and are identified as estimated quantities. \mathbf{M} stabilizes the system and counteracts a possible ill-conditioning of the normal equations in the case of data gaps where \mathbf{W} regularizes the proper weighting of the prior information. Since this approach is based on an iterative solving procedure, \mathbf{M} has to be adapted after each iteration step with respect to the linearization by

$$\mathbf{M}_{it} = \boldsymbol{\mu} - \left(\mathbf{d}_0 + \sum_{j=1}^{it} \Delta \hat{\mathbf{d}}_j \right), \quad (15)$$

where “it” denotes a specific iteration. Reliable prior information is inevitably required and can be extracted from a given background model such as the climatologically driven International Reference Ionosphere 2007 (IRI-2007), (Bilitza and Reinisch, 2008). In our paper we derived both the vector

of prior information μ and the initial values d_0 for the series coefficients from IRI-2007, but it should be kept in mind that the data sources for those coefficients that serve as prior and initial information may differ. In the case of $\mu = d_0$ the expression for the final iteration yields

$$M_{IT} = - \sum_{j=1}^{IT} \Delta \hat{d}_j \tag{16}$$

and “IT” substitutes the total number of required iterations until an appropriate threshold for the final solution is exceeded.

3.1 Initial and prior information

Naturally, the linearization introduced by Eq. (11) brings along the requirement for initial values of the unknown parameters. This means specifically that initial series coefficient vectors $d_{k_1,0}, \dots, d_{k_R,0}$ have to be introduced where, in the ideal case, initial values are derived in a preprocessing step from an external model. Additionally, by using electron density profiles exclusively, the observation coverage is rather sparse and leads to the presence of data gaps that have to be bridged by prior information. The basic principles of the prior information model have been explained previously in terms of Eqs. (9) and (15). The selection of a suitable background model for providing prior information is in any case quite important and some trust should be placed in it since the corresponding information is used to overcome data gaps and can only be improved in those regions where observations are given. IRI-2007 is considered here as the only data source used for the derivation of initial and prior information since it complies with the criterion to provide data of all three key parameters where *NmF2* and *hmF2* as well as *VTEC* are directly available. The derivation of initial values and prior information for *HF2* follows from the computation of the slab thickness τ , which is defined as the ratio between *VTEC* and *NmF2*, as introduced by Davies (1990). Moreover, Wright (1960) showed the equality of τ with $4.13 \cdot HF2$ for an α -Chapman layer. This relation is generally accepted and has been adopted in other publications such as Jayachandran et al. (2004). Initial values for *HF2* result from these relations in

$$\tau = \frac{VTEC}{NmF2} = 4.13 \cdot HF2 \rightarrow HF2 = \frac{VTEC}{4.13 \cdot NmF2}. \tag{17}$$

The availability of a suitable background model thus allows for the derivation of initial grid-based key parameters basically without data gaps, and subsequently the determination of initial B spline series coefficients $d_{k_r,0}$ resulting from a general Gauss–Markov least-squares estimation by

$$d_{k_r,0} = (A_{k_r}^T P_l^{back} A_{k_r})^{-1} A_{k_r}^T P_l^{back} l_{k_r}^{back}. \tag{18}$$

P_l^{back} is considered as an identity matrix; that is, the same observation weights are considered and no relative weightings

are introduced. A_{k_r} contains the partial derivatives for the initially unknown coefficients based on Eq. (5) and consequently its entries equal the tensor products of the spline values $\phi_{k_1}^{J_\lambda}(\lambda)\phi_{k_2}^{J_\varphi}(\varphi)\phi_{k_3}^{J_t}(t)$ depending on the defined B spline levels J_λ, J_φ and J_t . Values of the initial key parameters provided by the background model are introduced as observations collected in $l_{k_r}^{back}$. It has to be kept in mind that the detail resolution is controlled by the B spline levels, and accordingly the representation of the background model eventually becomes smoothed if the defined levels are low.

3.2 Combination of different observation techniques and missions

In order to account for the combination of various observation techniques, the system of normal equations in consideration of multiple observation groups has to be adapted and yields

$$\left(\sum_{q=1}^Q \frac{1}{\sigma_q^2} A_q^T P_q A_q + W \right) \Delta \hat{d} = \sum_{q=1}^Q \frac{1}{\sigma_q^2} A_q^T P_q L_q + WM, \tag{19}$$

where $q \in \{1, \dots, Q\}$ has been introduced to indicate specific observation techniques. Individual variance components, i.e., weighting factors for all observation techniques σ_q^2 including the prior information $\sigma_{k_r}^2$, are determined by an iterative maximum-likelihood variance component estimation (VCE) to account for the different accuracies. These variance factors are estimated iteratively taking approximate starting values into account. The approach is described in Koch and Kusche (2002) and applied to ionosphere modeling in Dettmering et al. (2011b). Here, the VCE is realized in a similar manner but has been extended to take different groups of unknowns into account. The computation of variance factors then follows from

$$\hat{\sigma}_q^2 = \frac{\hat{e}_q^T P_q \hat{e}_q}{r_q} \quad \text{and} \quad \hat{\sigma}_{k_r}^2 = \frac{\hat{e}_{k_r}^T P_{k_r} \hat{e}_{k_r}}{r_{k_r}} \tag{20}$$

for the different observation techniques and prior information groups, respectively. The vectors of residuals, \hat{e}_q and \hat{e}_{k_r} , are obtained with

$$\hat{e}_q = A_q \Delta \hat{d} - L_q \quad \text{and} \quad \hat{e}_{k_r} = \Delta \hat{d}_{k_r} - M_{k_r}. \tag{21}$$

The partial redundancies, r_q and r_{k_r} , yield

$$r_q = n_q - \text{Tr} \left(\frac{1}{\sigma_q^2} A_q^T P_q A_q N^{-1} \right) \tag{22}$$

and

$$r_{k_r} = u_{k_r} - \text{Tr} \left(\frac{1}{\sigma_{k_r}^2} P_{k_r} S_{k_r} \right), \tag{23}$$

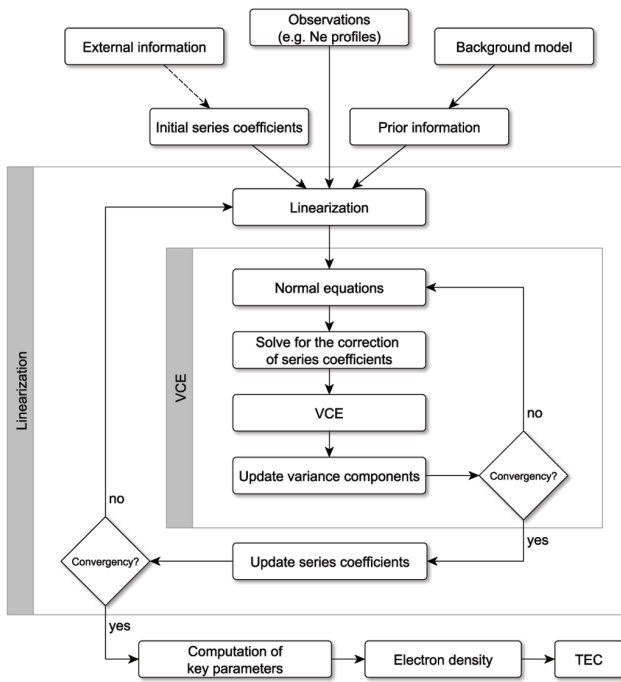


Fig. 3. Flowchart of the main processing steps.

where \mathbf{N} substitutes the $u \times u$ normal equations matrix, i.e., the left-hand side of Eq. (19),

$$\mathbf{N} = \sum_{q=1}^Q \frac{1}{\sigma_q^2} \mathbf{A}_q^T \mathbf{P}_q \mathbf{A}_q + \mathbf{W}, \quad (24)$$

and \mathbf{S}_{κ_r} denotes the key parameter specific submatrices along the diagonal of \mathbf{N}^{-1} . The realization of the described approach for the parameter estimation comprises now two iterations according to the linearization and the VCE implemented as a nested loop that considers the VCE as the inner iteration and the linearization as the outer. A flowchart of the most relevant processing steps is depicted in Fig. 3. After estimating the final sets of series coefficients, key parameters with respect to λ , φ and t may be constructed. Afterwards, the 4-D electron density distribution can be calculated from the adapted Chapman function and even allows for reconstruction of TEC values in consideration of an appropriate integration function. A possible reconstruction sequence hence covers the estimation of B spline series coefficients (Eq. 19) and subsequently the determination of F2 Chapman key parameters (Eq. 5), followed by the computation of the electron density (Eq. 1) and TEC.

4 Numerical investigations

For the study of the modeling approach described above, a selected region covering mainly South America within $\lambda \in [250^\circ, 350^\circ]$ and $\varphi \in [-60^\circ, +30^\circ]$ has been considered. Electron density profiles composed of discrete N_e

observations derived from ionospheric GPS radio occultation are used as the input data. In particular, measurements of the FORMOSAT-3/COSMIC (Taiwan–US), GRACE (US–Germany) and CHAMP (Germany) LEO satellite missions have been taken into account. Mission specifications are provided by the operating organizations and can be found on the corresponding websites at <http://www.cosmic.ucar.edu/>, <http://www.csr.utexas.edu/grace/> and <http://op.gfz-potsdam.de/champ/>. The processing of scientific data for the FORMOSAT-3/COSMIC mission is done by the UCAR. The Center for Space Research (CSR) at the University of Texas at Austin and the GFZ in Potsdam perform the data processing of the GRACE mission. The GFZ was also responsible for the data processing of CHAMP until it was decommissioned. Here we consider preprocessed CHAMP and GRACE electron density profiles kindly provided by the Institute of Communications and Navigation of the DLR and preprocessed FORMOSAT-3/COSMIC data from the Center for Space and Remote Sensing Research (CSRSR) of the National Central University (NCU) in Taiwan. The applied profiles passed different preprocessing strategies. A typical method is the consideration of the Abel inversion technique based on bending-angle data or slant total electron content (STEC) to derive electron density profiles. The assumption of a spherical symmetry in the nearby area during an occultation event is one of the drawbacks considered in the classical Abel transform. To overcome this assumption, improved strategies have been developed. Aragon-Angel (2010) for instance proposes a strategy based on the separability concept, introduced by Hernández-Pajares et al. (2000), where horizontal VTEC gradients are taken into account and the excess phase rate is considered as the main observable. CSRSR provides routinely processed data based on an improved Abel inversion process through compensated TEC values under consideration of horizontal electron density gradients published by Tsai et al. (2009). DLR’s preprocessing strategy follows the concept of a tomographic voxel approach published by Jakowski et al. (2004) and Jakowski (2005).

4.1 Closed-loop simulation

In order to validate our modeling approach, a closed-loop simulation has been carried out in order to assess the ability of the adjustment system to solve for all three F2 Chapman parameters simultaneously.

For the simulation procedure we choose real geographical locations and epochs of the measurements meaning that λ , φ and t are taken from real data, but simulated electron density observations have been considered. A specific measurement is simulated by

$$\tilde{N}_e(h)_i = \left(\tilde{N}_e^{\text{F2}}(h, \tilde{\kappa}_1, \dots, \tilde{\kappa}_R) + N_e^{\text{P}}(h, \text{NOP}, \text{HP}) + \tilde{\epsilon}_q \right)_i \quad (25)$$

with

$$\tilde{\kappa}_r = \kappa_r(\mathbf{d}_{\kappa_r}, 0) + \tilde{C}_{\kappa_r}, \quad (26)$$

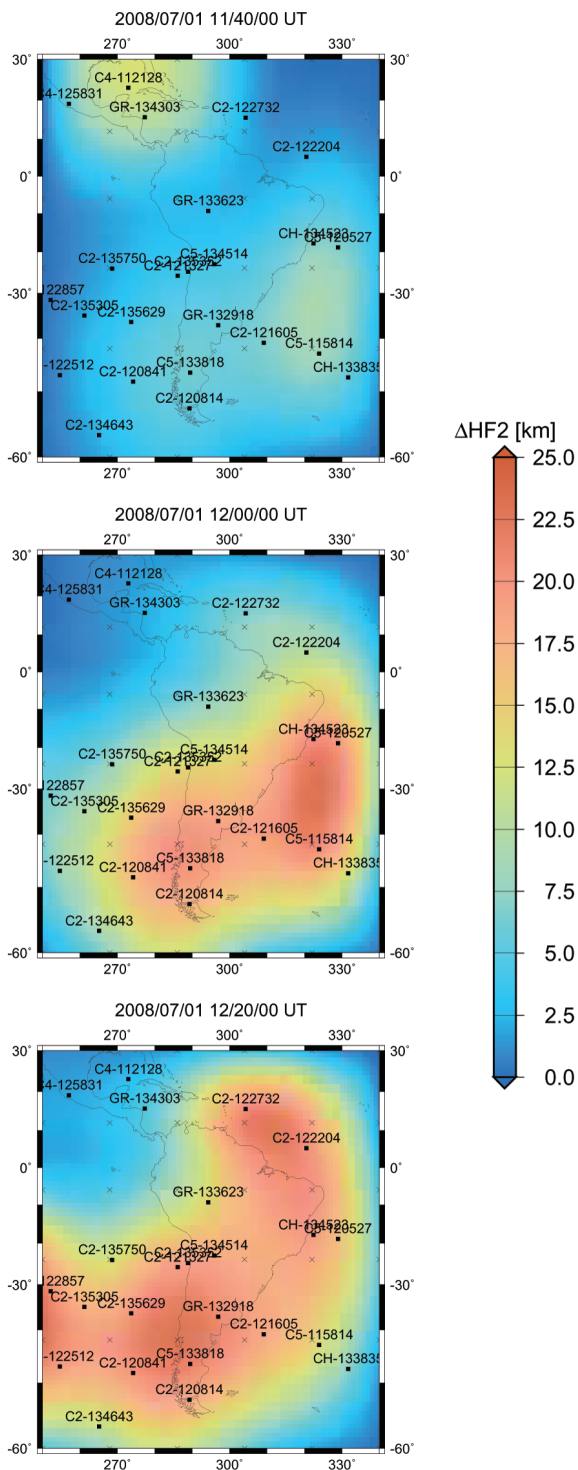


Fig. 4. Estimated scale height corrections $\Delta HF2 = HF2(\hat{d}_{HF2}) - HF2(d_{HF2,0})$ for 1 July 2008 at 11:40 UT (top), 12:00 UT (center) and 12:20 UT (bottom) based on the B spline levels $J_\lambda = 2$, $J_\varphi = 2$ and $J_t = 3$. Each electron density profile is labeled with a corresponding mission identifier: (C)osmic, (CH)amp or (GR)ace and the Universal Time of the observation.

where the tilde symbols indicate simulated quantities and \tilde{C}_{κ_r} are constants to simulate systematic biases referring to the different F2 key parameters. For the computation of $d_{\kappa_r,0}$ the IRI-2007 background model has been taken into account. $\tilde{\epsilon}_q$ is the mission-dependent simulated observation error based on random white noise with expectation value $E(\tilde{\epsilon}_q) = 0$ and standard deviation

$$\sigma_{\tilde{\epsilon}_q} = \left(\frac{0.02}{N_p} \cdot \sum_{p=1}^{N_p} \max(N_{e,p}) \right)_q. \quad (27)$$

This implies that 2 % of the averaged maximum electron density with respect to each profile $p \in \{1, \dots, N_{p,q}\}$ of a certain satellite mission q is adopted. Within a closed-loop simulation it is then possible to validate the approach in terms of reconstructing the introduced systematic discrepancies by means of the simulated \tilde{N}_e observations. This first validation is based on simulated data covering a time frame of three hours between 11:00 and 14:00 UT at 1 July 2008. In total, 19 FORMOSAT-3/COSMIC profiles (including 4871 discrete N_e observations), 3 GRACE profiles (including 63 N_e observations) and 2 CHAMP profiles (including 48 N_e observations) are taken into account. In the case of using exclusively electron density profiles, the data distribution is rather sparse. Additionally, one has to consider that the N_e profile reconstruction from ionospheric radio occultation implicates assumptions within the preprocessing where each pointwise electron density observation refers to a larger area with a diameter of up to 2000 km. Therefore, relatively low B spline levels of $J_\lambda = 2$, $J_\varphi = 2$ and $J_t = 3$ have been applied. In total, the B spline coverage then includes $6 \times 6 \times 10$ spline functions and hence, under the rough assumption of $1^\circ = 111$ km, there is a spline peak every 2000 km in λ and φ direction and every 20 min. The predefined systematic biases are listed in Table 1 and represent the “true” corrections considered within the simulated observations. The estimated corrections, determined within the closed-loop simulation, are depicted in Fig. 4 as an example of the F2 scale height with

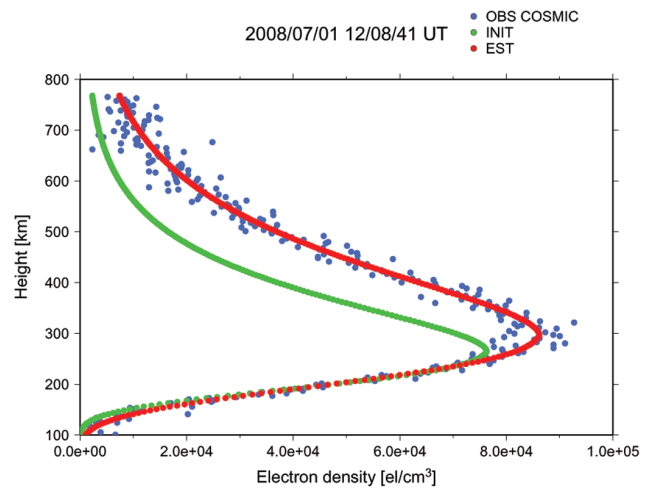
$$\Delta HF2 = HF2(\hat{d}_{HF2}) - HF2(d_{HF2,0}). \quad (28)$$

Consecutive time steps at 11:40, 12:00 and 12:20 UT are illustrated. B spline peaks are depicted as black crosses and profile locations are marked as black squares where the observed profiles are identified by an abbreviation that indicates the corresponding mission (GR=GRACE, CH=CHAMP, Cx=FORMOSAT-3/COSMIC with satellite identification number x) and Universal Time (UT) (e.g., 133818=13:38:18 UT). The key parameter maps demonstrate the impact of different profiles with respect to time and location. Corrections appear at those locations and times where measurements are given, while the adapted B spline levels control the degree of smoothing and consequently affect the extent of the correction zones. Due to the low

Table 1. Simulated systematic deviation.

C_{NmF2}	C_{hmF2}	C_{HF2}
10^4 el cm^{-3}	30 km	20 km

B spline levels, a strong smoothing effect is achieved. Blue areas indicate the presence of data gaps and consequently remain uncorrected; that is, the estimated scale height is defined by the prior information and thus shows a systematic deviance of 20 km from the “true” value. Other regions show good agreement between the estimation and the “truth”, indicated by corrections around $\Delta HF2 = 20$ km. The full correction can certainly only be obtained where the observation time of an illustrated profile correlates with the time moment represented by the image. The C2-122204 profile located at $\lambda = 320^\circ$ and $\varphi = 5^\circ$ in the northeast region provides a good example that demonstrates how the measurements influence the estimated correction in correlation with time and position. This profile has been observed around 12:20 UT and consequently shows a steadily increasing influence from 12:00 UT until its strongest impact on the bottom images related to 12:20 UT. The C4-112128 profile located at $\lambda = 273^\circ$, $\varphi = 23^\circ$ close to the northern boundary still has an influence at 11:40 UT, which completely vanishes afterwards. Some regions between profiles show an obvious overestimation of around 5–6 km for $\Delta HF2$. For example, on the 12:20 UT image, clearly visible by the intense red coloring. In these cases, two or more profiles are affecting the estimation of $\Delta \hat{d}_{HF2}$ at the same time. Since all profiles carry the information that the values of the initial parameters need to be increased (due to the simulated homogeneous systematic biases), the estimation procedure adjusts a surface through the measured values at the locations of the profiles and the surrounding a priori values, which causes a peak value between the profile locations. Whether such under- or overestimations are present thus depends on the spatial and temporal distribution of the profiles and on the measured values. To get an impression of the conformity between observed and estimated profiles, Fig. 5 shows the N_e values referring to the initial (green), simulated (blue) and estimated (red) electron density profiles with respect to height as an example for a selected C2 profile observed at 12:08:41 UT and located at $\lambda = 274^\circ$, $\varphi = -48^\circ$. The simulated electron density observations include the artificial input noise, defined by Eq. (27), which has been adapted differently with respect to the LEO missions. The difference between the observations and initial values is caused by the simulated systematic differences of the key parameters where the systematically increased $NmF2$ - and $hmF2$ -related offsets are visible right away and the higher $HF2$ causes an increase in the thickness of the profile. In the case of simulations, model errors do not appear, which allows for the comparison between the standard deviations of the simulated input noise $\sigma_{\hat{\epsilon}}$ and the

**Fig. 5.** Initial (green), simulated (blue) and estimated (red) electron density values referring to a simulated FORMOSAT-3/COSMIC profile observed at $\lambda = 274^\circ$, $\varphi = -48^\circ$ and 1 July 2008 12:08:41 UT

standard deviations of the outcome residuals $\sigma_{\hat{\epsilon}_q}$ related to the differences between observed and estimated electron density. Table 2 shows a comparison of $\sigma_{\hat{\epsilon}_q}$ and $\sigma_{\hat{\epsilon}_q}$ in relation to the considered LEO missions. The standard deviations of the residuals fit well together with the input noise levels and indicate a successful retrieval of the key parameters by the simulated electron density observations. Following Eq. (27), the noise is computed from the mean of the maximum electron densities of all profiles per mission. Therefore the magnitude of the input noise can naturally differ depending on whether the majority of profiles are located in regions with higher electron density (e.g., inside the crest region) or in quiet areas. The previous investigations were focused on the example of $HF2$ but also hold for $NmF2$ and $hmF2$. For the simulations, $HF2$ has been chosen as it is the most nonlinear and therefore weakest parameter in the system located in the denominator of the (twofold) exponential term; see Eq. (1).

4.2 Real data

The model assessment has been successfully carried out by means of simulated electron density data. In the next step, real data of FORMOSAT-3/COSMIC, GRACE and CHAMP are considered to obtain first results for the time frame between 11:00 and 14:00 UT on 1 July 2008. The year 2008 is characterized by low solar conditions and therefore offers a suitable basis for the evaluation of the modeling approach with real data. Again, B spline levels of $J_\lambda = 2$, $J_\varphi = 2$ and $J_t = 3$ have been accepted. In contrast to the closed-loop simulation, unusable profiles are removed here within a data-screening procedure to guarantee that the electron density structure around the peak can be described properly. Therefore, only profiles covering at least an altitude range of

Table 2. Standard deviations of simulated input noise and observation residuals.

	FORMOSAT-3/ COSMIC	CHAMP	GRACE
$\sigma_{\hat{\epsilon}_q}$ [el cm ⁻³]	3387.6	8541.5	7371.2
$\sigma_{\hat{\epsilon}_q}$ [el cm ⁻³]	3384.2	7924.8	7215.7

$hmF2 \pm 50$ km are considered where the detected $hmF2$ value of a specific profile must be located within an altitude region between 150 and 450 km as several erroneous profiles were found to show multiple electron density peaks in physically unrealistic altitudes. Other profiles are dominated by noise and have been eliminated. Figure 6 shows two examples related to a suitable electron density profile and to a profile that was detected as an outlier. The first profile clearly shows the peak region of the F2 layer and is only weakly influenced by lower layers such as the E region. The second profile shows large noise above 500 km, indicating data problems. From this profile, a reliable determination of $hmF2$ is not possible and thus it is rejected. Table 3 gives an overview on the data-screening statistics. The total number of available electron density profiles is reduced from 28 to 17 suitable profiles. In particular, the number of FORMOSAT-3/COSMIC profiles has been depleted from 22 to 12, while only 1 CHAMP profile has been rejected and all GRACE profiles remain. Accordingly, altogether 39% of the electron density profiles, mainly disturbed by high noise, are detected as outliers and have been rejected.

4.2.1 Key parameter evaluation

The representation of the F2 key parameters as a function of λ , φ and t based on the estimated B spline series coefficients is described by Eq. (5). It is important to note that the reconstruction does not depend on discrete grid points. The desired key parameters can be reconstructed at any location and time, while the detail resolution is controlled by the defined B spline levels. The spatial variations of the reconstructed key parameters for a specific epoch are depicted in Fig. 7 with a resolution of $\Delta\lambda = \Delta\varphi = 2.5^\circ$ and $\Delta t = 6$ min. In the left column the estimated corrections of the estimated key parameters $\kappa_r(\hat{\mathbf{d}})$ to the initial values $\kappa_r(\mathbf{d}_0)$ are shown for 12:00 UT, where

$$\Delta hmF2 = hmF2(\hat{\mathbf{d}}_{hmF2}) - hmF2(\mathbf{d}_{hmF2,0}),$$

$$\Delta HF2 = HF2(\hat{\mathbf{d}}_{HF2}) - HF2(\mathbf{d}_{HF2,0}),$$

and

$$\Delta NmF2 = NmF2(\hat{\mathbf{d}}_{NmF2}) - NmF2(\mathbf{d}_{NmF2,0}).$$

The colorbars are adapted to the minimum and maximum correction for the selected epoch. Again, key parameters are only corrected in areas where profiles support the estimation

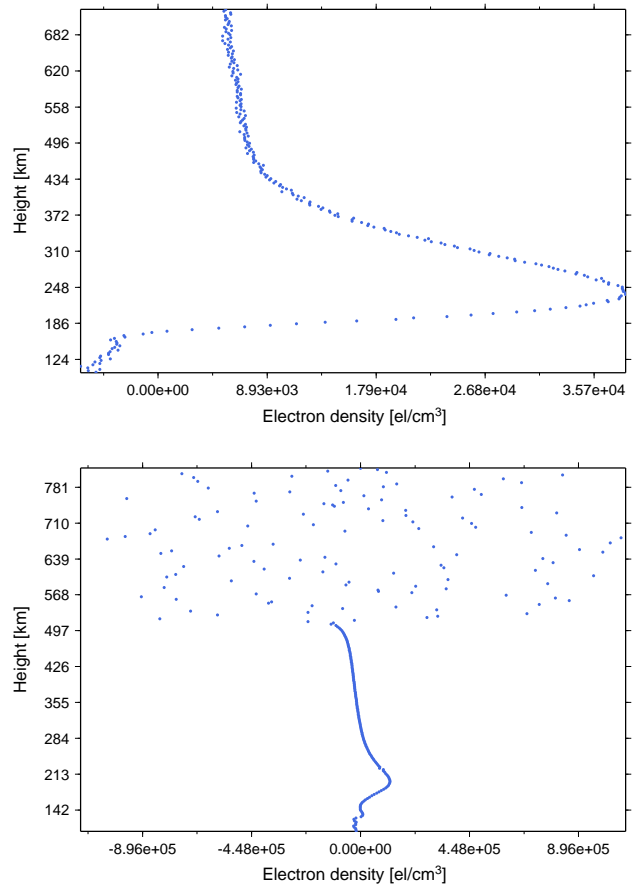


Fig. 6. Examples for a suitable (top) and an unusable (bottom) electron density profile observed by FORMOSAT-3/COSMIC

of the corresponding coefficients. Three selected profiles that have a strong impact on the estimated corrections are given along the right column, where observations (blue), initial values (green) and estimated values (red) are illustrated. These profiles are indicated by arrows on the key parameter correction maps. The image on top shows a profile that was observed at $\lambda = 289^\circ$, $\varphi = -52^\circ$ and mainly affects $hmF2$. Apart from that, $NmF2$ experiences a decrease, which becomes visible in the corresponding $\Delta NmF2$ correction map. The changes with respect to $HF2$ are clearly explainable by the middle profile, located at $\lambda = 286^\circ$ and $\varphi = -25^\circ$, where the observed curve, and consequently the estimated curve, is more narrow than the initial profile. The bottom profile is located at $\lambda = 320^\circ$, $\varphi = 5^\circ$ and obviously has a strong influence on the $NmF2$ estimation but also causes a slight decrease of $hmF2$. In particular, $NmF2$ is reduced by almost 2×10^5 el cm⁻³, which mainly roots from the impact of a lower atmospheric layer, possibly the E layer. The Chapman profile in this case is not able to approximate the observed profile correctly. Our model thus results in a systematic bias influencing the estimation of the key parameters, a situation that could be improved by rejecting

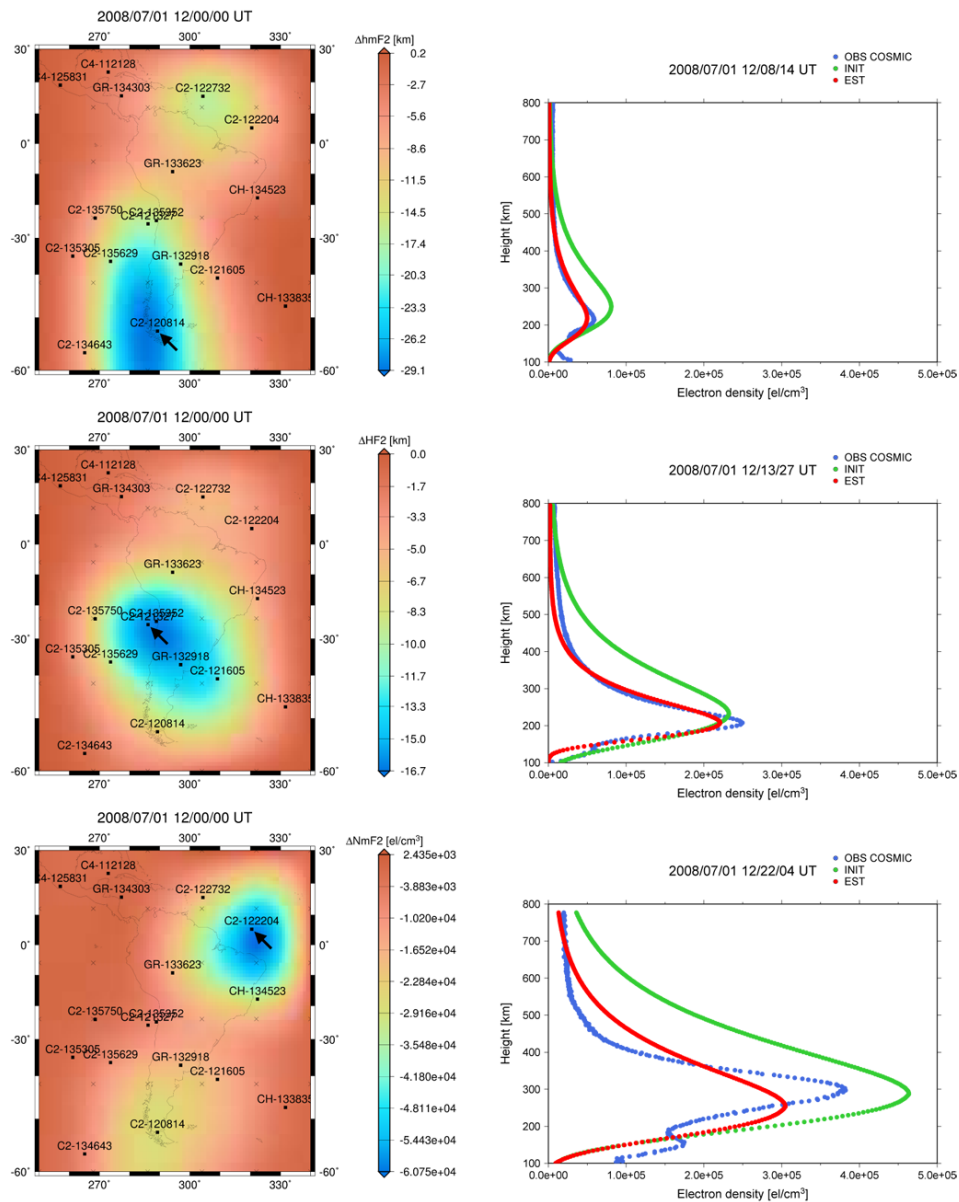


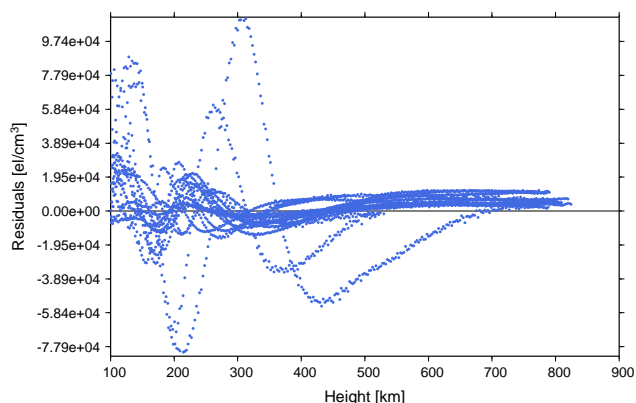
Fig. 7. Key parameter corrections $\Delta NmF2$, $\Delta hmF2$ and $\Delta HF2$ for a fixed time moment at 12:00 UT on 1 July 2008 (left column). Selected FORMOSAT-3/COSMIC profiles that have an impact on the key parameter estimation (right column). These profiles are indicated by arrows on the key parameter maps.

observations at lower atmospheric layers or by implementing an additional E layer into the model. The impact of the mismodeling can be seen in Fig. 8, where the residuals of all FORMOSAT-3/COSMIC profiles observed in the given time period are depicted. The mismodeling effect obviously increases towards lower altitudes and causes an oscillation of the estimated values around the observed values as a function of height. This oscillation effect can be expected from the bottom FORMOSAT-3/COSMIC profile in Fig. 7, where the E layer is very dominant and forces the model to adjust the Chapman layer as a compromise between the F2 and E layer. The estimated red curve consequently swings

around the blue observed curve. The standard deviation of the residuals, taking all FORMOSAT-3/COSMIC observations into account, is $\hat{\sigma}_{\text{COS}} = 18.3 \times 10^3 \text{ el cm}^{-3}$. Standard deviations of the residuals in Fig. 8 separated into two altitude regions, up to 400 km and above 400 km, yield $\hat{\sigma}_{\text{COS}}^{<400} = 24.1 \times 10^3 \text{ el cm}^{-3}$ and $\hat{\sigma}_{\text{COS}}^{\geq 400} = 10.2 \times 10^3 \text{ el cm}^{-3}$, respectively, and support the predication of larger mismodeling effects in the case of a dominant E layer. In general it can be noticed from Fig. 7 that all three key parameters are decreased with respect to the initial state, which allows for the implication that the IRI-2007 key parameter values are too high for the considered time period.

Table 3. Total, rejected and remaining electron density profiles before and after the data-screening process.

	Total	Rejected	Remaining
FORMOSAT-3/COSMIC	22	10	12
GRACE	3	0	3
CHAMP	3	1	2
Total	28	11	17

**Fig. 8.** Observation residuals related to all FORMOSAT-3/COSMIC electron density profiles observed on 1 July 2008 between 11:00 and 14:00 UT.

4.2.2 VTEC evaluation

In the following, reconstructed VTEC values computed with our model are validated by comparison with IRI-2007 data and global ionosphere maps (GIMs) provided by the International GNSS Service (IGS). Dow et al. (2009) and Hernández-Pajares et al. (2009) published detailed information on the IGS network structure and services including ionospheric products. IGS GIMs are computed with data from the IGS global GNSS tracking network and become publicly available in Ionosphere Map Exchange format (IONEX) with a resolution of 2 h and $\Delta\lambda = 5^\circ \times \Delta\varphi = 2.5^\circ$ in time and space, respectively. As based on observations, IGS GIMs represent a good reference for the validation of our model. In general, VTEC can be computed from

$$\text{VTEC} = \int_{h_{\text{bottom}}}^{h_{\text{top}}} \hat{N}_e(h) dh \quad (29)$$

as an integral of the estimated model electron density along a vertical path through the ionosphere between the altitude limits h_{bottom} and h_{top} with path element dh . The concept for the implemented numerical integration algorithm is described in Zeilhofer et al. (2008), where an integration layer covering the ionosphere with an upper and lower boundary is

defined. Here, an integration layer subdivided into three sublayers with intervals defined by [80 km, 200 km], [200 km, 1200 km] and [1200 km, 2000 km] has been applied. The integration within each of these sublayers is performed with individual integration step sizes to account for different characteristics of the ionospheric layers. Further, each integration step is carried out by means of a Gauss–Legendre quadrature of order N , where $N = 6$ has been found to be adequate as a compromise between accuracy and performance. VTEC maps for IRI-2007, IGS GIM and the difference between IRI-2007 and IGS GIM are depicted in Fig. 9. The investigated time moment refers to 13:55 UT on 1 July 2008. VTEC differences up to 9 TECU between IRI-2007 and IGS GIM appear in Fig. 9 (right panel) along the geomagnetic equator and the northeastern region although the time corresponds to quiet conditions outside of solar and local noon maxima. Both areas are a part of the border of the crest region that is moving westwards. In Fig. 10, the absolute VTEC computed with our model, estimated Δ VTEC and the difference between the model estimation and IGS GIM are shown. In this scenario, a group of FORMOSAT-3/COSMIC (C2) profiles has been observed close to the depicted time moment and is located in the equatorial region, where significant differences between IRI-2007 and IGS GIM appear. The estimated Δ VTEC in Fig. 10 (middle panel) yields a decrease of up to 4.5 TECU with respect to the initial IRI-2007 model in the region correlated with the positions of the FORMOSAT-3/COSMIC profiles. A closer look at Fig. 10 (right panel) shows that the eye-catching discrepancy between IRI-2007 and IGS GIM is extensively reduced by the measurements and that our model solution closely resembles the IGS GIM data. Other regions that do not benefit from the impact of measurements are dominated by prior information. One needs to keep in mind that the prior information has been derived from IRI-2007, which means specifically that the difference between our model estimation and IGS GIM equals the difference between IRI-2007 and IGS GIM in regions without measurements. This becomes obvious when comparing Figs. 9 (right panel) and 10 (right panel), where, among other things, the difference in the northeastern part remains due to the lack of profiles.

5 Summary and conclusions

In this paper, the advantage of using electron density profiles that are able to describe the vertical electron density structure has been exploited for the determination of the physically defined F2 Chapman key parameters $NmF2$, $hmF2$ and $HF2$. As a mathematical distribution function, the concept of determining series coefficients for polynomial B splines with respect to longitude, latitude and time has been successfully applied. The adapted Chapman function is introduced as a relatively simple mathematical formulation that considers, although rudimentary, a plasmasphere extension.

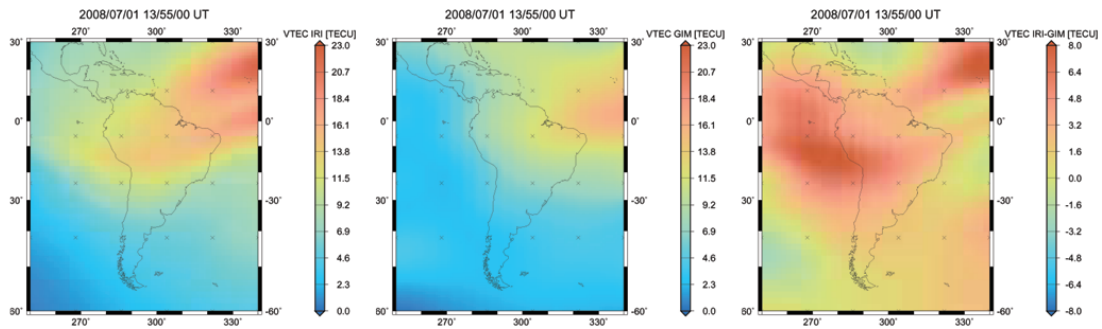


Fig. 9. VTEC maps referring to (left) IRI-2007, (middle) IGS GIM and (right) the difference between IRI-2007 and IGS GIM for 1 July 2008 at 13:55 UT (from left to right).

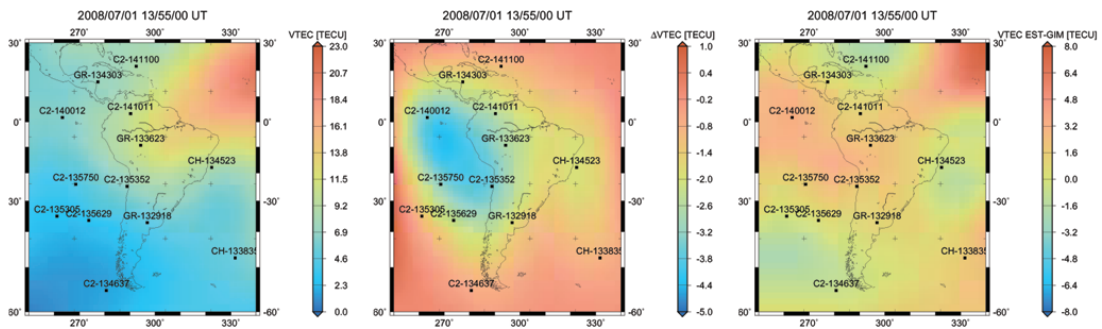


Fig. 10. VTEC maps referring to (left) the model estimation, (middle) estimated Δ VTEC and (right) the difference between the model estimation and IGS GIM for 1 July 2008 at 13:55 UT (from left to right).

E layer manifestations nevertheless cannot be intercepted by this model function, leading to mismodeling effects as soon as the E layer influence becomes prominent. Investigations on a more sophisticated model, including the consideration of lower atmospheric layers, are intended for upcoming studies. However, selected validation procedures on the basis of closed-loop simulations and profile evaluations with real data have demonstrated the functionality of the model. Although the results are based on a rather limited set of observations and short time frame during low solar activity, there is significant potential in the approach. Investigations on the estimated VTEC have been performed by comparisons with the climatological model IRI-2007 and the GNSS-driven VTEC solutions provided by the IGS. In general, the rather sparse distribution of electron density profiles considered as input observations results in few areas where the electron density parameters are adjusted. Corrections are computed at locations where profiles are available, and the results correspond well to the IGS GIMs, which demonstrates the potential of electron density profiles coupled with this model approach to improve existing solutions for appropriate key parameters. The determination system presented provides a basis for the combined usage of electron density profiles with other observation techniques to enable the mutual support concerning individual sensitivities with respect to different key parameters. Future work will include the combination of various

observation techniques. In particular, electron density profiles will be combined with ground- and space-based GNSS, DORIS and radar altimetry in order to benefit from the advantages of a higher spatio-temporal data resolution and the availability of measurements to bridge data gaps over the oceans.

Acknowledgements. The authors are very grateful to the ionospheric research group of the Institute of Communications and Navigation at DLR Neustrelitz for providing the preprocessed GRACE and CHAMP data and thank Lung-Chih Tsai from CSRSR at the NCU, Taiwan, for the FORMOSAT-3/COSMIC electron density profiles. Many thanks also go to Dieter Bilitza and one anonymous reviewer for the helpful comments. This work has been conducted as part of the project “Multi-scale model of the ionosphere from the combination of modern space-geodetic satellite techniques”, which is funded by the German Research Foundation (DFG), Bonn, Germany.

Topical Editor K. Hosokawa thanks D. Bilitza and one anonymous referee for their help in evaluating this paper.

References

- Aragon-Angel, A.: Contributions to ionospheric electron density retrieval, Ph.D. Thesis, Research Group of Astronomy and Geomatics (gAGE), Technical University of Catalonia (UPC), 53–63, 2010.
- Bilitza, D. and Reinisch, B.: International reference ionosphere 2007: Improvements and new parameters, *Adv. Space Res.*, 42, 599–609, doi:10.1016/j.asr.2007.07.048, 2008.
- Davies, K.: Ionospheric radio, Peter Peregrinus Ltd., London, 1990.
- Dettmering, D., Schmidt, M., Heinkelmann, R., and Seitz, M.: Combination of different space-geodetic observations for regional ionosphere modeling, *J. Geodesy*, 85, 989–998, doi:10.1007/s00190-010-0423-1, 2011a.
- Dettmering, D., Heinkelmann, R., and Schmidt, M.: Systematic differences between VTEC obtained by different space-geodetic techniques during CONT08, *J. Geodesy*, 85, 443–451, doi:10.1007/s00190-011-0473-z, 2011b.
- Dow, J. M., Neilan, R. E., and Rizos, C.: The International GNSS Service in a changing landscape of Global Navigation Satellite Systems, *J. Geodesy*, 83, 191–198, doi:10.1007/s00190-008-0300-3, 2009.
- Hajj, G. A. and Romans, J.: Ionospheric electron density profiles obtained with the Global Positioning System: Results from the GPS/MET experiment, *Radio Sci.*, 33, 175–190, doi:10.1029/97RS03183, 1998.
- Hernández-Pajares, M., Juan, J. M., and Sanz, J.: Improving the Abel inversion by adding ground data LEO radio occultations in the ionospheric sounding, *Geophys. Res. Lett.*, 27, 2743–2746, doi:10.1029/2000GL000032, 2000.
- Hernández-Pajares, M., Juan, J. M., Sanz, J., Orus, R., Garcia-Rigo, A., Feltens, J., Komjathy, A., Schaer, S. C., and Krankowski, A.: The IGS VTEC maps: a reliable source of ionospheric information since 1998, *J. Geodesy*, 83, 263–275, 2009.
- Hoque, M. M. and Jakowski, N.: A new global model for the ionospheric F2 peak height for radio wave propagation, *Ann. Geophys.*, 30, 797–809, doi:10.5194/angeo-30-797-2012, 2012.
- Jakowski, N.: Ionospheric GPS radio occultation measurements on board CHAMP, *GPS Solutions*, 9, 88–95, doi:10.1007/s10291-005-0137-7, 2005.
- Jakowski, N., Wehrenpfennig, A., Heise, S., Reigber, C., Lühr, H., Grunewaldt, L., and Meehan, T.: GPS radio occultation measurements of the ionosphere from CHAMP: Early results, *Geophys. Res. Lett.*, 29, doi:10.1029/2001GL014364, 2002.
- Jakowski, N., Leitinger, R., and Angling, M.: Radio occultation techniques for probing the ionosphere, *Ann. Geophys.*, 47, doi:10.4401/ag-3285, 2004.
- Jayachandran, B., Krishnankutty, T. N., and Gulyaeva, T. L.: Climatology of ionospheric slab thickness, *Ann. Geophys.*, 22, 25–33, doi:10.5194/angeo-22-25-2004, 2004.
- Kirchengast, G., Foelsche, U., and Steiner, A. K.: Occultations for probing atmosphere and climate, Springer Berlin Heidelberg, ISBN 3-540-22350-9, 2004.
- Koch, K. R.: Parameter estimation and hypothesis testing in linear models, Springer, Berlin, 1999.
- Koch, K.-R. and Kusche, J.: Regularization of geopotential determination from satellite data by variance components, *J. Geodesy*, 76, 259–268, doi:10.1007/s00190-002-0245-x, 2002.
- Lyche, T. and Schumaker, L. L.: A multiresolution tensor spline method for fitting functions on the sphere, *SIAM J. Sci. Comput.*, 22, 724–746, doi:10.1137/S1064827598344388, 2000.
- Reinisch, B. W., Nsumeima, P., Huang, X., and Bilitza, D. K.: Modeling the F2 topside and plasmasphere for IRI using IMAGE/RPI and ISIS data, *Adv. Space Res.*, 39, 731–738, doi:10.1016/j.asr.2006.05.032, 2007.
- Rishbeth, O. K. and Garriot, H.: Introduction to Ionospheric Physics, Academic Press, New York, 1969.
- Schmidt, M.: Wavelet modeling in support of IRI, *Adv. Space Res.*, 39, 932–940, doi:10.1016/j.asr.2006.09.030, 2007.
- Schmidt, M., Dettmering, D., Mößmer, M., Wang, Y., and Zhang, J.: Comparison of spherical harmonic and B spline models for vertical total electron content, *Radio Sci.*, 46, RS0D11, doi:10.1029/2010RS004609, 2011.
- Schumaker, L. L.: Spline functions basic theory, John Wiley and Sons Inc., New York, ISBN 0-471-76475-2, 1981.
- Tsai, L.-C. and Tsai, W.-H.: Improvement of GPS/MET ionospheric profiling and validation using the Chung-Li ionosonde measurements and the IRI model: Terrestrial, Atmospheric and Oceanic Sciences (TAO), 15, 589–607, doi:10.3319/TAO.2007.12.19.01(F3C), 2004.
- Tsai, L.-C., Liu, C. H., and Hsiao, T. Y.: Profiling of ionospheric electron density based on FormoSat-3/COSMIC data: results from the intense observation period experiment: Terrestrial, Atmospheric and Oceanic Sciences (TAO), 20, 181–191, 2009.
- Ware, R., Exner, M., Feng, D., Gorbunov, M., Hardy, K., Melbourne, W., Rocken, C., Schreiner, W., Sokolovsky, S., Solheim, F., Zou, X., Anthes, A. R., Businger, S., and Trenberth, K.: GPS Sounding of the Atmosphere from Low Earth Orbit: Preliminary Results, *B. Am. Meteorol. Soc.*, 77, 19–40, doi:10.1175/1520-0477(1996)077<0019:GSOTAF>2.0.CO;2, 1996.
- Wright, J. W.: A model of the F region above *hmF2*, *J. Geophys. Res.*, 65, 185–191, 1960.
- Zeilhofer, C., Schmidt, M., Bilitza, D., and Shum, C. K.: Regional 4-D modeling of the ionospheric electron density from satellite data and IRI, *Adv. Space Res.*, 43, 1669–1675, doi:10.1016/j.asr.2008.09.033, 2008.

7.2 P-II

Limberger, M., Liang, W., Schmidt, M., Dettmering, D., Hernández-Pajares, M., and Hugentobler, U. (2014): Correlation studies for B-spline modeled F2 Chapman parameters obtained from Formosat-3/COSMIC data. *Ann. Geophys.*, 32, 1533-1545, DOI 10.5194/angeo-32-1533-2014.

Copyright

This work is published in *Annales Geophysicae* under the license of Creative Commons. Copyrights are retained by the Authors. P-II is an open access publication and available at <http://www.ann-geophys.net/32/1533/2014/angeo-32-1533-2014.html>.

Summary

P-II extends P-I by the analysis of mathematical correlations between estimated F2 Chapman parameters, specifically the maximum density of the F2 layer $NmF2$, associated peak height $hmF2$ and scale height $HF2$. The data basis is established from F-3/C electron density profiles over the South American region during quiet and increased solar conditions on the 1 July 2008 and 1 July 2012, respectively. The evaluation has been performed through simulations and real-data studies. Moderate model correlations between $hmF2$ and $HF2$ and inverse correlations between $NmF2$ and $HF2$ are reflected from a scenario without data gaps taking synthetic measurements with homogeneous distribution into account. In case of applying real data, the estimation of variance components as relative weighting factors between observation groups leads to an increased weighting of the prior information and consequently the background data suppresses the correlations. Beside the assessment of the model correlations, the significant importance for a proper stochastic modeling has been demonstrated in P-II.

Declaration of own contribution

The idea for this publication originated from P-I, where a simplified, incomplete stochastic model is implemented that brought up the question for the parameter determinability. Thus, the idea and conception of the paper have its source in previous works of M. Limberger and has been developed from various discussions and meeting between the authors. The required software tools are based on the developments for P-I, partially realized by M. Limberger. The evaluation of the parameter correlations has been done by M. Limberger with input of the co-authors. The figure compilation as well as writing the manuscript has been done by M. Limberger.

The overall own contribution is estimated at 90 %.

Table 7.2: Apportionment of own contributions for P-II.

Criteria	Estimated own contribution
Paper concept	90 %
Computations and software development	80 %
Data analysis and interpretation of results	70 %
Design and creation of figures	100 %
Manuscript structure and writing	90 %

Confirmation by the authors

We hereby confirm the correctness of the declaration of own contribution for the publication

Limberger, M., Liang, W., Schmidt, M., Dettmering, D., Hernández-Pajares, M., and Hugentobler, U. (2014): Correlation studies for B-spline modeled F2 Chapman parameters obtained from Formosat-3/COSMIC data. *Annales Geophysicae*, 32, 1533-1545, DOI: 10.5194/angeo-32-1533-2014.

Wenjing Liang

Deutsches Geodätisches Forschungsinstitut der
Technischen Universität München (DGFI-TUM),
München, Germany

Signature: 

Date: 1.6.2015

Prof. Michael Schmidt

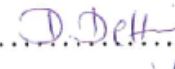
Deutsches Geodätisches Forschungsinstitut der
Technischen Universität München (DGFI-TUM),
München, Germany

Signature: 

Date: 1.6.2015

Dr. Denise Dettmering

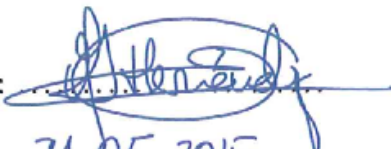
Deutsches Geodätisches Forschungsinstitut der
Technischen Universität München (DGFI-TUM),
München, Germany

Signature: 

Date: 20.05.2015

Prof. Manuel Hernández-Pajares

Universitat Politècnica de Catalunya (UPC),
Ionospheric determination and Navigation based on
Satellite And Terrestrial systems research (IONSAT),
Barcelona, Spain

Signature: 

Date: 21.05.2015

Prof. Urs Hugentobler

Technische Universität München (TUM),
Forschungseinrichtung Satellitengeodäsie (FESG),
München, Germany

Signature: 

Date: 18. May 2015



Correlation studies for B-spline modeled F2 Chapman parameters obtained from FORMOSAT-3/COSMIC data

M. Limberger^{1,2}, W. Liang², M. Schmidt², D. Dettmering², M. Hernández-Pajares³, and U. Hugentobler¹

¹Technische Universität München – Institute of Astronomical and Physical Geodesy (IAPG), Arcisstr. 21, 80333 Munich, Germany

²Deutsches Geodätisches Forschungsinstitut (DGFI), Alfons-Goppel-Str. 11, 80539 Munich, Germany

³UPC-IonSAT Research Group, Universitat Politècnica de Catalunya (UPC), Barcelona, Spain

Correspondence to: M. Limberger (marco.limberger@dgfi.badw.de)

Received: 9 June 2014 – Revised: 11 November 2014 – Accepted: 19 November 2014 – Published: 17 December 2014

Abstract. The determination of ionospheric key quantities such as the maximum electron density of the F2 layer $NmF2$, the corresponding F2 peak height $hmF2$ and the F2 scale height $HF2$ are of high relevance in 4-D ionosphere modeling to provide information on the vertical structure of the electron density (N_e). The N_e distribution with respect to height can, for instance, be modeled by the commonly accepted F2 Chapman layer. An adequate and observation driven description of the vertical N_e variation can be obtained from electron density profiles (EDPs) derived by ionospheric radio occultation measurements between GPS and low Earth orbiter (LEO) satellites. For these purposes, the six FORMOSAT-3/COSMIC (F3/C) satellites provide an excellent opportunity to collect EDPs that cover most of the ionospheric region, in particular the F2 layer. For the contents of this paper, F3/C EDPs have been exploited to determine $NmF2$, $hmF2$ and $HF2$ within a regional modeling approach. As mathematical base functions, endpoint-interpolating polynomial B-splines are considered to model the key parameters with respect to longitude, latitude and time. The description of deterministic processes and the verification of this modeling approach have been published previously in Limberger et al. (2013), whereas this paper should be considered as an extension dealing with related correlation studies, a topic to which less attention has been paid in the literature. Relations between the B-spline series coefficients regarding specific key parameters as well as dependencies between the three F2 Chapman key parameters are in the main focus. Dependencies are interpreted from the post-derived correlation matrices as a result of (1) a simulated scenario without data gaps by taking dense, homogeneously distributed profiles into account and (2) two real data scenarios on 1 July 2008 and 1 July 2012 including sparsely, inhomogeneously distributed F3/C EDPs. Moderate correlations between $hmF2$ and $HF2$ as well as inverse correlations between $NmF2$ and $HF2$ are reflected from the simulation. By means of the real data studies, it becomes obvious that the sparse measurement distribution leads to an increased weighting of the prior information and suppresses the parameter correlations which play an important role regarding the parameter estimability. The currently implemented stochastic model is in need of improvement and does not consider stochastic correlations which consequently cannot occur.

Keywords. Ionosphere (equatorial ionosphere; modeling and forecasting) – radio science (ionospheric physics)

1 Introduction

One of the major tasks in ionospheric research activities concerns the determination of physically relevant parameters from space geodetic observations. Exploiting the knowledge about the physical processes improves the description of the ionospheric behavior in time and space to monitor ionosphere phenomena and perform space weather studies. One of the most important parameters in this context is the electron density (N_e) distribution, which constitutes the focus in several current ionospheric modeling approaches and enables the study of ionospheric storms, ion composition and effects on radio communications between satellites and ground receivers. The ability to describe N_e variations in space and time is an important step along the way of understanding still

unsolved ionospheric phenomena affected by Sun–Earth interactions and to improve existing ionosphere models.

Various global (e.g., Hernández-Pajares et al., 1999; Azpilicueta et al., 2006; Todorova et al., 2007) and regional ionosphere models (e.g., Dettmering et al., 2011) describe the spatiotemporal distribution of the vertical total electron content (VTEC). Beside novelties in the application of different mathematical and physical modeling approaches, several modeling strategies nowadays are based on the combination of different measurement techniques to compensate for the diversity in the data resolution and to achieve the best possible measurement distribution. Terrestrial permanent networks, e.g., the International GNSS Service (IGS) tracking stations (Dow et al., 2009; Hernández-Pajares, 2004; Hernández-Pajares et al., 2009) and the Sistema de Referencia Geocéntrico para las Américas (SIRGAS) (Sánchez et al., 2013), have been deployed for the tracking of global navigation satellite systems (GNSS) and provide slant total electron content (STEC) data with a high spatial and temporal resolution over the continents.

Complementary, VTEC over the oceans can be derived from radar altimetry (RA) along the satellite orbits. On most of the current RA missions such as Jason-2, SARAL, Cyosat and HY-2A, a DORIS (Doppler Orbitography and Radiopositioning Integrated by Satellite) receiver that is active for orbit determination purposes can also be considered to derive STEC from the signals transmitted by DORIS ground beacons (Dettmering et al., 2014). The total electron content (TEC) is commonly considered as the backbone of ionosphere models, but its integral characteristic (TEC is defined as the integral of the N_e along any specific signal path) makes the TEC observable insensitive for the description of the N_e distribution, especially with respect to height.

However, empirical models such as NeQuick (Nava et al., 2008) and the International Reference Ionosphere (IRI) (Bilitza et al., 2011) provide global 4-D N_e descriptions, mainly driven by ionosonde parameters such as the layer-dependent critical frequencies f_0E (E layer), f_0F1 (F1 layer), f_0F2 (F2 layer) or the maximum usable frequency factor $M(3000)F2$ (ratio of maximum usable frequency at a distance of 3000 km and f_0F2). In addition to the provision of TEC data, the La Plata Ionospheric Model (LPIM) (Azpilicueta et al., 2006) incorporates space-based STEC measurements as tracked by satellites in low Earth orbit (LEO) to retrieve electron density information. In addition, several assimilation schemes of different complexity and relying on different kinds of data have been developed – for instance, GAIM (Schunk et al., 2001) and EDAM (Angling, 2008).

In order to obtain information of the N_e distribution from satellite measurements, ionospheric GPS radio occultations (IRO) (see, for example, Kirchengast et al. (2004) or Jakowski et al. (2004)), can be considered as an adequate observation type with height sensitivity. Relevant information of the N_e can be derived from GPS signal delay changes during an occultation event caused by atmospheric influences.

IRO can be used to derive electron density profiles (EDPs) and therefore allow for modeling of the N_e distribution with physically relevant key parameters with height dependence. For instance, the F2 peak height $hmF2$ and F2 scale height $HF2$ play an essential role in this context and contribute to the definition of the vertical N_e profile shape. Various model approaches have already been proposed, and recently published papers will be mentioned here: Altadill et al. (2012) modeled $hmF2$ from globally distributed ionosonde measurements by means of a spherical harmonic analytical model for quiet solar conditions, Hoque and Jakowski (2012) proposed the operational Neustrelitz peak height model based on 13 coefficients with only a few empirically fixed parameters and driven by ionosonde data plus IRO measurements, and Brunini et al. (2013) studied and compared different techniques to estimate $hmF2$. Moreover, Alizadeh (2013) used spherical harmonic expansions to model the N_e distribution globally from the combination of different satellite-based observation techniques and Limberger et al. (2013) dealt with the estimation of the three F2 Chapman parameters $NmF2$, $hmF2$ and $HF2$ in terms of a polynomial B-spline representation from IRO-derived electron density profiles (EDPs), which was further extended by Liang et al. (2014) for the usage of EDPs together with ground-based GPS data.

It stands to reason that, depending on the choice of key parameters, the question of parameter interdependencies arises and will form the emphasis of the investigations in this paper. Several studies dealing with the issue of correlations between ionospheric parameters are purely based on ionosonde measurements. To mention just a few of these, Zhang et al. (2006) and also Liu et al. (2006) studied correlations between the ionogram-derived Chapman scale height H_T (or H_m) and the F2 peak parameters f_0F2 and $hmF2$, the bottom-side F2 layer thickness parameter $B0$, and the slab thickness τ ; Lee and Reinisch (2007) investigated scale height variations from Jicamarca ionograms during quiet solar conditions and thereby analyzed appearing correlations with f_0F2 , $hmF2$ and $B0$. Instead of using ionosonde measurements, a data basis consisting of EDPs observed by the LEO mission Formosa Satellite 3 and Constellation Observing System for Meteorology, Ionosphere, and Climate (FORMOSAT-3/COSMIC, henceforth F3/C) (Rocken et al., 2000) has been established here. Investigations of parameter interdependencies on the regional scale are carried out for three F2 Chapman key parameters which are of fundamental importance in ionospheric research: the maximum electron density $NmF2$ of the F2 layer, the F2 peak height $hmF2$ and the F2 scale height $HF2$. These F2 Chapman parameters are required for the description of the F2 layer, which is, at least in large part, contained in the F3/C profiles – the six F3/C satellites fly at orbit heights of approximately 800 km. The modeling fundamentals leading to the determination of these key parameters have already been described in Limberger et al. (2013) and the intention of the subsequent investigations are supplementary with emphasis on correlation studies.

The basic principles of the modeling concept and parameter determination will therefore be repeated at the beginning of Sect. 2. Starting with a preliminary adjustment model (Sect. 3) that is applied to a simulation scenario (Sect. 4), first studies based on a dense, homogeneous measurement distribution without data gaps are performed. According to the subsequent real data scenario (Sect. 5), the adjustment system is extended (Sect. 6) and will be applied for studies during quiet solar conditions on 1 July 2008 (Sect. 7) and increased solar activity on 1 July 2012 (Sect. 8). Finally, some final conclusions will be given in Sect. 9.

2 Modeling the vertical N_e distribution

The description of the vertical N_e distribution follows from an adapted α -Chapman function proposed by Jakowski (2005) and considers a F2 Chapman layer with an additional plasmasphere expansion given by

$$N_e(h) = NmF2 \exp[0.5(1 - z - \exp(-z))] + NOP \exp(-|h - hmF2|/HP) \quad (1)$$

with $z = (h - hmF2)/HF2$.

Model parameters are the maximum electron density $NmF2$ of the ionospheric F2 layer, the corresponding F2 peak height $hmF2$ and a constant F2 topside scale height $HF2$, which constitute the key quantities for this study. The simplifying assumption in considering a constant scale height has been proposed by Reinisch et al. (2004) and, for instance, considered in Stankov and Jakowski (2005) as plasma scale height in the topside ionosphere. The description of the plasmasphere follows from the basis density NOP and plasmasphere scale height HP , where proportionality between $NmF2$ and NOP has been taken into account and HP is fixed at $HP = 10^4$ km ($h \geq hmF2$) and $HP = 10$ km ($h < hmF2$), respectively, to allow for a smooth transition between the F2- and plasmasphere layer.

The model approach presented here is in particular suited for regional applications since localizing endpoint-interpolating polynomial B-splines (Lyche and Schumaker, 2000; Schmidt, 2007) are exploited to model the target quantities. $NmF2$, $hmF2$ and $HF2$ are expressed as tensor products of three 1-D polynomial B-spline functions related to longitude λ , latitude φ and time t with unknown series coefficients. The formulation in terms of B-splines yields

$$hmF2(\lambda, \varphi, t) = \sum_{k_1=1}^{K(J_\lambda)} \sum_{k_2=1}^{K(J_\varphi)} \sum_{k_3=1}^{K(J_t)} d_{k_1, k_2, k_3}^{J_\lambda, J_\varphi, J_t} \phi_{k_1}^{J_\lambda}(\lambda) \phi_{k_2}^{J_\varphi}(\varphi) \phi_{k_3}^{J_t}(t) \quad (2)$$

for $hmF2$ and can be accordingly obtained for $NmF2$ and $HF2$. The validity of B-splines for ionospheric VTEC modeling, in particular when dealing with inhomogeneously distributed observations, has been successfully demonstrated in

Schmidt et al. (2011) through comparison with spherical harmonics series expansions. Moreover, an exemplary approach for regional VTEC modeling has been published by Dettmering et al. (2011) and later enhanced by Limberger et al. (2013) and Liang et al. (2014) to determine F2 Chapman key parameters, based on Eq. (1), aiming for regional 4-D N_e representation.

Thus, the target quantities to be determined are the B-spline series coefficients $d_{k_1, k_2, k_3}^{J_\lambda, J_\varphi, J_t}$ depending on the B-spline levels J_λ , J_φ and J_t , which are typically adapted to the average measurement density and finally define the degree of smoothing and model resolution. The number $K(J)$ of coefficients related to λ , φ and t can be calculated from $K = 2^J + 2$ and the total number of unknowns (for a specific key parameter) accordingly results from $N_u = 2^{J_\lambda} + 2^{J_\varphi} + 2^{J_t} + 6$. In general, all series coefficients are collected in the vector of unknowns $\mathbf{d} = [d_{NmF2}^T, d_{hmF2}^T, d_{HF2}^T]^T$ as defined in a Gauss–Markov model; it is important to note here that, due to the nonlinearity of Eq. (1), a linearization is required and no absolute coefficients apart from corrections $\Delta \hat{\mathbf{d}}$ for initial series coefficients \mathbf{d}_0 have to be estimated.

3 Preliminary adjustment system

Taking the linearized model into account, the estimated set of coefficients results from an iterative estimation procedure via

$$\hat{\mathbf{d}} = \mathbf{d}_0 + \Delta \hat{\mathbf{d}} = \mathbf{d}_0 + \mathbf{N}^{-1} \mathbf{A}^T \mathbf{P} \mathbf{L}, \quad (3)$$

with $\mathbf{N} = \mathbf{A}^T \mathbf{P} \mathbf{A}$

and includes the design matrix \mathbf{A} , positive definite observation weight matrix \mathbf{P} and reduced observation vector \mathbf{L} containing the differences between observed $N_{e,F3/C}$ and initial electron densities $N_e(\mathbf{d}_0)$. \mathbf{d}_0 contains initial values for the series coefficients and is adapted after each iteration step “it” by the outcome of the previous iteration it–1. Here, the initial coefficients \mathbf{d}_0 are derived in a pre-processing step from the International Reference Ionosphere 2007 (IRI07) (Bilitza, 2000; Bilitza et al., 2011). Values for $NmF2$ as well as $hmF2$ are directly accessible and, after Wright (1960) and Davies (1990), enable the derivation of $HF2 = \tau/4.13$ by taking the slab thickness $\tau = VTEC/NmF2$ into account (Jayachandran et al., 2004). Based on the initial IRI07 data set, a homogenous data grid can be established, allowing for the determination of initial coefficients \mathbf{d}_0 .

Concerning the parameter estimability, Limberger et al. (2013) showed that the presented modeling approach allows for a simultaneous determination of B-spline series coefficients regarding the three related F2 Chapman key parameters $NmF2$, $hmF2$ and $HF2$ by taking advantage of the sensitivity of EDPs.

In this paper, correlations between the B-spline series coefficients and also F2 Chapman key parameters are studied

in detail. A reliable separability of the key parameters is certainly required for obtaining realistic values and to ensure a safe convergency of the procedure. To discuss this question, the correlations between key parameters shall be analyzed on the basis of the correlation matrices \mathbf{K}_{xx} and \mathbf{K}_{tt} for coefficients and target key parameters, respectively, where the latter one results from the application of the error propagation law (EPL). The subscripts xx and tt will henceforth be used to identify the association of the matrices to the original unknowns, i.e., the B-spline series coefficients or target key parameters, respectively.

The covariance matrix of the unknown series coefficients $\Sigma_{xx} = \mathbf{N}^{-1}$ is the inverse of the normal equation matrix. The diagonal elements of Σ_{xx} are the variances $\hat{\sigma}_{d_j}^2$ for $j \in \{1, \dots, N_u\}$ of the series coefficients d_j . For the vector-valued function $\mathbf{f} = \mathbf{F}\mathbf{d}$, which is representing a set of key parameters as linear functions of the estimated B-spline series coefficients, the EPL can be applied to derive the corresponding covariance matrix Σ_{tt} of the key parameters as $\Sigma_{tt} = \mathbf{F}\Sigma_{xx}\mathbf{F}^T$. The transformation matrix \mathbf{F} consists of partial derivatives of the key parameters with respect to the series coefficients resulting from Eq. (2). This means particularly that \mathbf{F} contains the spline tensor products – for instance $\partial hmF2 / \partial d_{k_1, k_2, k_3}^{J_\lambda, J_\varphi, J_t} = \phi_{k_1}^{J_\lambda}(\lambda) \phi_{k_2}^{J_\varphi}(\varphi) \phi_{k_3}^{J_t}(t)$ in the case of $hmF2$. The correlation matrices \mathbf{K}_{xx} and \mathbf{K}_{tt} with $\mathbf{K}_{xx,rc} = \Sigma_{xx,rc} / \sigma_r \sigma_c$ and $\mathbf{K}_{tt,rc} = \Sigma_{tt,rc} / \sigma_r \sigma_c$ are defined as normalized covariance matrices, where r and c indicate the row and column indices here.

4 Simulation

A stable estimation of B-spline series coefficients applying the adjustment model presented in Eq. (3) requires a dense measurement distribution, i.e., a scenario without data gaps. This will not be the case for a real distribution of N_e profiles in the foreseeable future, but can be simulated to study the parameter correlations. Therefore, a 24 h timespan, 1 July 2008, and a region of $[250^\circ, 340^\circ]$ longitude and $[-60^\circ, 30^\circ]$ latitude (South America) have been selected. Homogeneously distributed EDPs with a resolution of $10^\circ(\lambda) \times 10^\circ(\varphi) \times 2\text{ h}$ are simulated, which is dense enough for the selected B-spline level of $J_\lambda = 2$, $J_\varphi = 2$ and $J_t = 3$ to allow for the estimation of all coefficients without any prior information required to bridge data gaps. According to these levels, the total number of unknown coefficients amounts here to 360 per key parameter and 1080 in total. Hence, the dimension of \mathbf{K}_{xx} is 1080×1080 . For the subsequent investigations, \mathbf{F} has been computed for fixed epochs and a geographical resolution of $5^\circ \times 5^\circ$ (see Sect. 3), leading to a matrix size of 1083×1080 . Consequently, \mathbf{K}_{tt} has a dimension of $3(\text{key parameters}) \times [90^\circ/5^\circ + 1](\varphi) \times [90^\circ/5^\circ + 1](\lambda)$ resulting in 1083×1083 elements for a specific epoch including all three key parameters.

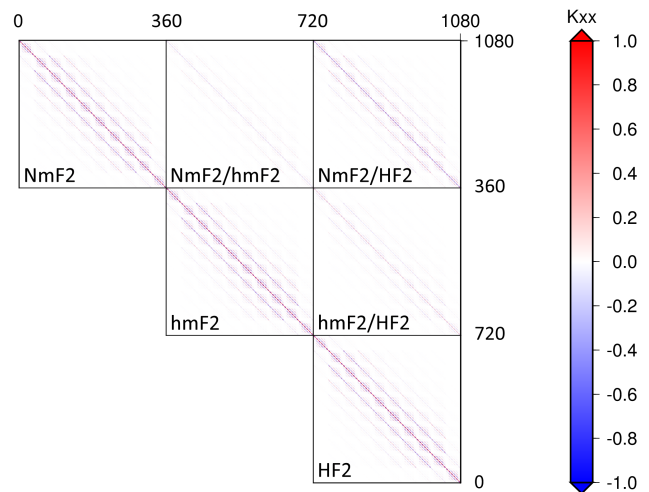


Figure 1. Correlation matrix of the coefficients \mathbf{K}_{xx} for the simulated scenario.

Each simulated profile contains synthetic N_e observations between 100 and 800 km height with an altitude sampling interval of 10 km. Each synthetic N_e observation is determined by means of Eq. (1), where the $NmF2$, $hmF2$ and also $HF2$ parameter values are computed from the initial coefficients $\mathbf{d}_{0, NmF2}$, $\mathbf{d}_{0, hmF2}$ and $\mathbf{d}_{0, HF2}$. For each of these key parameter vectors, an artificial systematic bias has been introduced that is contained in the simulated observations. Since IRI07 has been used to derive \mathbf{d}_0 , these offsets can be interpreted as corrections with respect to IRI07 that are reflected in the observations. The systematic biases are then retrieved within a closed-loop procedure. Two percent of the mean N_e per profile is considered to be the standard deviation to simulate a measurement error with zero mean. Thereby, the noise level is adapted to the current solar activity condition. The correlation matrices of the simulated scenario with respect to the coefficients and key parameters are depicted in Figs. 1 and 2.

\mathbf{K}_{xx} contains correlations between all coefficients (i.e., for all key parameters, geographical positions and epochs), where block submatrices are confined to black boxes and labeled with regard to whether referring to $NmF2$, $hmF2$, $HF2$ or an off-diagonal submatrix with interparameter-coefficient correlations. All coefficients are ordered by longitude (in the innermost loop) followed by latitude (in the second loop) and time (in the outer loop). The sorting scheme will be explained later in a separate subsection dealing with the matrix composition (see Sect. 7). Correlations are hardly visible in Fig. 1 along the diagonal, most probably related to B-spline dependencies, in particular between the $NmF2$ and $HF2$ coefficients. Although visible in both plots, the correlation structure is clearly enhanced for \mathbf{K}_{tt} in Fig. 2. The small blue off-diagonal patches within each key parameter block indicate a negative correlation of the scaling coefficients for neighboring B-splines, i.e., the increase of a series coefficient value for a specific spline leads to the de-

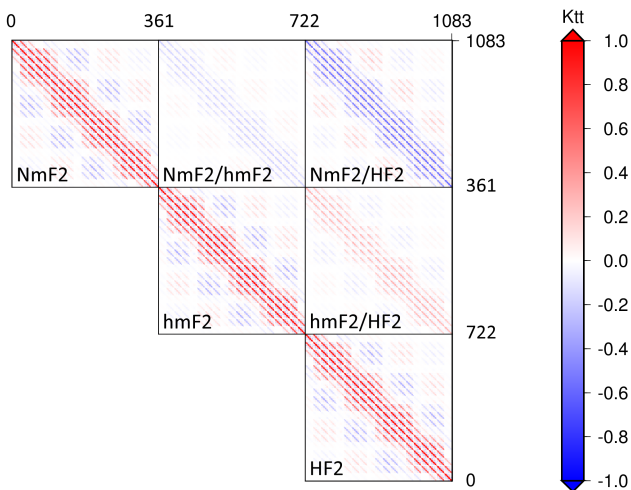


Figure 2. Correlation matrices of the key parameters K_{tt} for the fixed time moment 12:00 UT of the simulated scenario. K_{tt} represents correlations for parameters related to a grid with $\Delta\varphi = 5^\circ \times \Delta\lambda = 5^\circ$ resolution.

crease of another correlated coefficient. This can be anticipated since one key parameter is always defined by three overlapping splines. Furthermore, the colors indicate negative correlations between $NmF2$ and $HF2$ and, although slightly weaker, between $NmF2$ and $hmF2$. Moderate positive correlations become visible between $hmF2$ and $HF2$. Nevertheless, the correlations of nearby coefficients and parameters are the most prominent ones. The corresponding numerical values are given in Table 1 for the key parameters. Since the coefficient correlations are considerably weaker, a corresponding table for K_{xx} is not shown here.

In the first row, Table 1 provides the total minimum and maximum value of K_{tt} , followed by detailed information. Below, minimum and maximum values for the submatrices related to the specific key parameters are shown. Further, the correlations within the submatrices are binned into the intervals $[-1, -0.7]$, $] -0.7, -0.3]$, $] -0.3, 0[$, $[0, 0.3[$, $[0.3, 0.7[$ and $[0.7, 1]$ and are given as a percentage of the number of elements in the corresponding submatrix, excluding the matrix diagonals. The large percentages of correlations are shown in bold. Some cells in Table 1 include underlined numbers to highlight increased correlations beyond the $] -0.3, 0.3[$ interval.

As already claimed, those correlations originating from B-splines (appearing close to the diagonal of the K_{xx} and K_{tt} matrices) are particularly apparent as characteristic positive and negative dependencies due to the B-spline nature. Furthermore, the height-dependent parameters $hmF2$ and $HF2$ exhibit moderate positive correlations with a maximum of 0.63. 4.6% of the correlations between $hmF2$ and $HF2$ are located in the range of $[0.3, 0.7[$.

This output is based on a simulated scenario and purely shows the correlations between model parameters that are

Table 1. Key parameter correlations contained in K_{tt} for the simulated scenario for 1 July 2008. Minimum and maximum correlations of the whole matrix as well as for the key parameter-affiliated submatrices are depicted in the specific headlines (grey background). Percentage values related to different correlation intervals are listed beneath, where the dominant correlations are indicated by bold numbers. Increased correlations beyond the $] -0.3, 0.3[$ sector are underlined.

Total K_{tt}	Min	-0.62	Max	0.98	
<i>NmF2</i>	Min	-0.33	Max	0.97	
$[-1, -0.7]$	$] -0.7, -0.3]$	$] -0.3, 0[$	$[0, 0.3[$	$[0.3, 0.7[$	$[0.7, 1]$
0.0 %	0.2 %	47.8 %	44.8 %	<u>4.6 %</u>	2.6 %
<i>hmF2</i>	Min	-0.34	Max	0.98	
$[-1, -0.7]$	$] -0.7, -0.3]$	$] -0.3, 0[$	$[0, 0.3[$	$[0.3, 0.7[$	$[0.7, 1]$
0.0 %	0.3 %	47.2 %	45.5 %	<u>4.3 %</u>	2.7 %
<i>HF2</i>	Min	-0.34	Max	0.98	
$[-1, -0.7]$	$] -0.7, -0.3]$	$] -0.3, 0[$	$[0, 0.3[$	$[0.3, 0.7[$	$[0.7, 1]$
0.0 %	0.2 %	47.3 %	45.5 %	<u>4.3 %</u>	2.7 %
<i>NmF2, hmF2</i>	Min	-0.31	Max	0.11	
$[-1, -0.7]$	$] -0.7, -0.3]$	$] -0.3, 0[$	$[0, 0.3[$	$[0.3, 0.7[$	$[0.7, 1]$
0.0 %	0.0 %	52.4 %	47.6 %	0.0 %	0.0 %
<i>NmF2, HF2</i>	Min	-0.62	Max	0.23	
$[-1, -0.7]$	$] -0.7, -0.3]$	$] -0.3, 0[$	$[0, 0.3[$	$[0.3, 0.7[$	$[0.7, 1]$
0.0 %	<u>5.2 %</u>	47.4 %	47.5 %	0.0 %	0.0 %
<i>hmF2, HF2</i>	Min	-0.20	Max	0.63	
$[-1, -0.7]$	$] -0.7, -0.3]$	$] -0.3, 0[$	$[0, 0.3[$	$[0.3, 0.7[$	$[0.7, 1]$
0.0 %	0.0 %	47.3 %	48.1 %	<u>4.6 %</u>	0.0 %

indirectly obtained from IRI07 without input of F3/C measurements. However, the obtained results are in agreement with other correlation studies for the F2 key parameters that took ionosonde data into account: for instance, with Liu et al. (2006) and Zhang et al. (2006), who stated, based on ionogram studies at low-latitude regions, that the scale height around the F2 layer peak shows a moderate positive correlation with $hmF2$. It is important to note that $HF2$ is determined only from bottomside measurements below the peak in the case of using ionosonde data.

Furthermore, Lee and Reinisch (2007) studied $HF2$ variations from ionograms measured at the Jicamarca ionosonde station at $\lambda = 283.2^\circ$ and $\varphi = -12^\circ$ close to the dip equator and also located inside our study area during quiet solar conditions, and found high correlations between $hmF2$ and $HF2$. It should be kept in mind that these correlations are latitude dependent and following Lee and Reinisch (2007), they are more obvious close to the dip equator than in low latitudes. However, correlations between $hmF2$ and $HF2$ in general indicate the influence of the same physical processes on $hmF2$ and $HF2$ variations (Liu et al., 2006).

Negative correlations between $NmF2$ and $HF2$ appear in Fig. 2, where the minimum yields -0.62 . Of the corresponding correlations, 5.2 % can be found in the $] -0.7, -0.3]$ interval. Zhang et al. (2006) and Lee and Reinisch (2007) reported the existence of only marginal correlations between the critical frequency f_0F2 and $HF2$ in low latitudes. Based

on the relation $NmF2 [m^{-3}] = 1.24 \times 10^{10} \cdot (f_oF2)^2 [MHz]$ (Bilitza, 2002), the maximum electron density is linearly dependent on $(f_oF2)^2$. Poor correlations should consequently also exist between $NmF2$ and $HF2$.

In our model, approximate values for $HF2$ are directly retrieved from $HF2 = \tau/4.13$ including the slab thickness τ . Correlations between the plasma- or topside scale height and τ have been found in Stankov and Jakowski (2005) by analyzing CHAMP ionospheric radio occultation data. In addition, studies of Zhang et al. (2006) with ionosonde data showed very high correlations between τ and $HF2$, supporting the validity of the retrieval method. τ is obtained from $\tau = VTEC/NmF2$. Following Kouris et al. (2008), the correlation between VTEC and $NmF2$ is also certainly very high, i.e., more than 0.9 but not 1. This eventually causes the remaining negative correlations between $NmF2$ and $HF2$. Liu et al. (2006) found weak negative correlations between f_oF2 and $HF2$ with local time dependency from studies with ionosonde data of a station located in Wuhan, i.e., in low latitude at $\lambda = 114.4^\circ$, $\varphi = 30.6^\circ$.

In this simulation, the preliminary model of Eq. (3) with the ability to handle scenarios without gaps has been considered. However, reality looks different, showing a sparse and inhomogeneous distribution of measurements. Therefore, the investigation is continued in the following by applying F3/C EDPs.

5 Real data investigation

According to the simulated scenario described in Sect. 4, the South American region covering a study area between $[250^\circ, 340^\circ]$ longitude and $[-60^\circ, 30^\circ]$ latitude has also been selected for investigations with real F3/C data. Here, two time frames of 24 h, 1 July 2008 (Sect. 7) during quiet solar conditions and 1 July 2012 (Sect. 8) at increased solar activity, have been selected for studying correlations of B-spline coefficients and F2 Chapman parameters. The mean Kp index on 1 July 2008 is 1.1 with a sunspot number of 0, which indicates quiet conditions as a good starting point for these studies. For 1 July 2012 an increased solar activity with a mean Kp index of 3.3 and a sunspot number of 84 has been determined. The computation of the mean Kp here is based on indices and fractional parts provided in 3 h intervals by the National Geophysical Data Center of National Oceanic and Atmospheric Administration (NOAA, <http://www.noaa.gov>). The sunspot number refers to the Brussels International Sunspot Number.

The pre-processed F3/C electron density profiles kindly provided by the Center of Space and Remote Sensing Research (CSRSR, <http://www.csrsr.ncu.edu.tw>) of the National Taiwan University (NTU) (Tsai et al., 2001; Tsai and Tsai, 2004; Tsai et al., 2009) are considered as input data. The removal of outliers and corrupted profiles by means of a rather conservative data screening process has been accom-

plished within an additional pre-processing step. The process mainly comprises the following:

- the detection of larger jumps, here > 50 km, in the altitudes between consecutive N_e measurements of a specific EDP;
- the verification of data availability around the peak region within ± 50 km to guarantee a proper description of the profile shape in the peak region;
- the screening of $hmF2$ to be located within the physically reasonable altitude interval of $[150 \text{ km}, 500 \text{ km}]$.

Furthermore, only profiles that reach a minimum altitude below 250 km and maximum altitude above 500 km are taken into account to allow for a rather complete description of the vertical N_e distribution in the F2 region. One drawback of the simple mathematical model given by Eq. (1) is the neglect of an E layer which led in some cases to mismodeling effects (see Limberger et al., 2013). The E layer is typically located in an altitude interval between 90 and 130 km, and therefore only measurements above 150 km are taken into account. The consideration of the F1 layer has been neglected in this model. The F1 manifestation may arise during daytime at approximately 150–220 km above Earth and merges with the F2 layer at night. However, the intensity of ionization in the F1 region is generally less than in the E region, and significant features in the used EDPs due to F1 occurrence have not been monitored.

Based on the retrieval concept to derive EDPs from ionospheric radio occultation measurements, the position of each N_e value coincides with the closest point to Earth located on the line of sight between GPS and F3/C at the corresponding observation epoch. Therefore, the time and position of the measurements can vary during an occultation event by several minutes and up to about 10° in some cases. The derived profile describes the N_e distribution along a slant direction. The determination of F2 Chapman parameters in our model benefits primarily from observations in the peak region. In order to reference the observed profile to a fixed location and thus stabilize the parameter estimation, we assume the verticality of the profiles at latitude, longitude and time of the F2 peak measurement, i.e., the observed $NmF2$. Another characteristic of the retrieval concerns the availability of much denser observations at higher altitudes. These observations, however, contain only limited information about the F2 peak quantities. In order to reduce their influence, measurements above 650 km are neglected here.

Finally, a total of 123 F3/C profiles (52 % rejected) for 1 July 2008 and 96 F3/C profiles (38 % rejected) for 1 July 2012 remain above the target region in South America after the data screening. Most of the rejected profiles have been removed because of the high measurement noise, due to incompleteness or because they are affected by a dominant E layer. It thus becomes clear that a decreasing number of rejections can be expected if an E layer model is introduced.

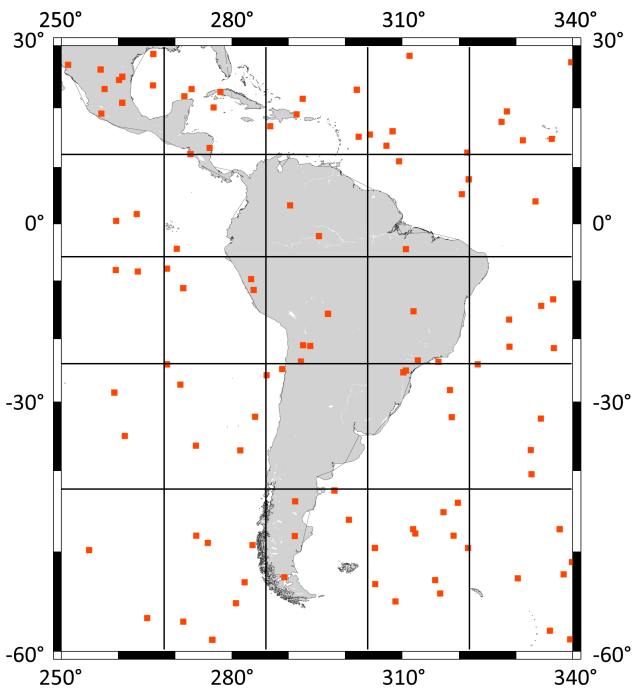


Figure 3. Spatial F3/C EDP distribution observed on 1 July 2008 over the study area in South America.

The distribution of all profiles for 1 July 2008, here independent of the corresponding measurement epoch, is depicted in Fig. 3, and gives a first impression of the sparsity and inhomogeneity of the data. The distribution of profiles for 2012 is comparable and not shown here.

It should be noted that the payload of each F3/C satellite includes two precise orbit determination (POD) and two occultation (OCC) antennas, all of which can be used for the retrieval of EDPs from radio occultations, i.e., different profiles from several antenna may be acquired for the same location and time. Hence, the number of profiles is larger than the number of orange squares in Fig. 3. Furthermore, although the number of input profiles in 2008 is slightly higher than 2012, the sparsity of the distribution is not significantly improved.

To derive a combined graphical relation between the localization of the EDPs with their corresponding measurement epoch, Fig. 3 has been firstly subdivided into $18^\circ \times 18^\circ$ wide cells. Afterwards, the 24 h investigation time frame has been divided into 2 h intervals and all profiles belonging to a specific spatiotemporal cell were counted. This situation is depicted in Fig. 4 as a combination of a graphical and numerical expression and gives a good impression of the data distribution.

Again, as also depicted in Fig. 3, the spatial $18^\circ \times 18^\circ$ cells are visible. Each cell contains a clock symbol, indicated by the centrally positioned black circle with a green background, that represents 12 h divided into 2 h segments. Two numerical values refer to each 2 h segment, the first one

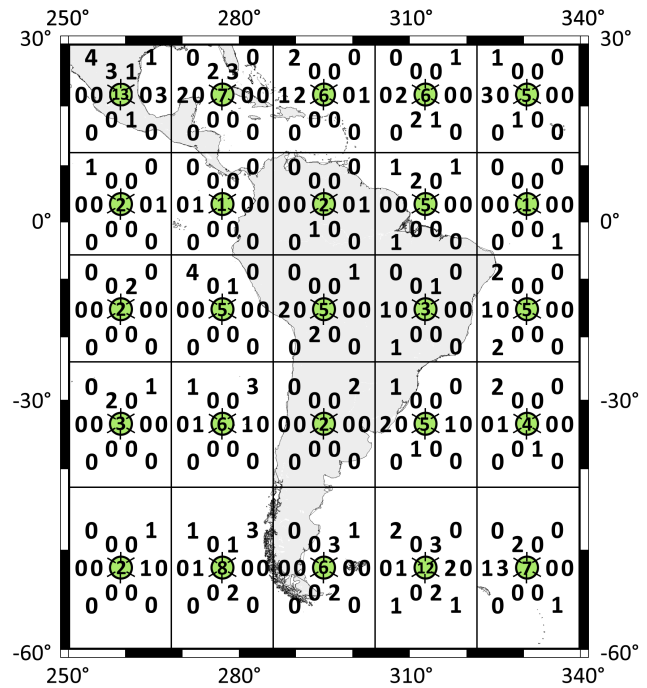


Figure 4. F3/C EDP distribution related to spatiotemporal grid cells observed on 1 July 2008 in the South America region.

on the inner ring and the second one on the outer ring. The inner value refers to the time between 00:00 and 12:00 UT, and numbers on the outer ring are related to a 2 h segment between 12:00 and 24:00 UT. Additionally, the number inside the clock denotes the total number of profiles observed in this specific cell, which equals the number of profiles in the corresponding cell of Fig. 3 (counting the numbers would consequently result in the total of 123 EDPs observed during this day). The first cell of the second row, for instance, covers the region of -6 to 12° latitude and 250 to 268° longitude. Altogether it contains two profiles: one which has been observed between 14:00 and 16:00 UT (outer circle, east side) and the second one between 22:00 and 24:00 UT (outer circle, northwest).

The total number of profiles measured within each cell spans from 1 to 13 and shows that the B-spline levels with respect to longitude and latitude have to be chosen rather low in order to bridge those regions without data. This situation is also visible from Fig. 3, where some cells are nearly empty or the profiles are at least located close to the cell border. Therefore we decided to adapt an average spatial distance between profiles of around 18° latitude and longitude according to the cell width. Depending on this assessment, the relation

$$J \leq \log_2 \left(\frac{s_{i_{\max}} - s_{i_{\min}}}{\Delta s_i} - 1 \right) \quad (4)$$

with the sampling Δs_i and boundaries $s_{i_{\min}}$ and $s_{i_{\max}}$ has been applied to estimate a suitable B-spline level. Equation (4) was proposed by Schmidt et al. (2011) and leads to

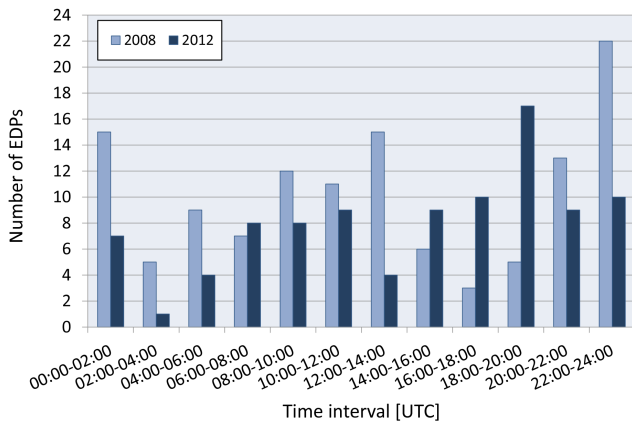


Figure 5. Temporal data distribution: EDPs are counted within 2 h intervals for 1 July 2008 (light blue) and 1 July 2012 (dark blue).

$J_\varphi \leq 2, J_\lambda \leq 2 \rightarrow J_\varphi = J_\lambda = 2$. Hence, the B-spline level has been adapted to the situation by selecting $J_\lambda = J_\varphi = 2$, meaning that the number of B-splines yields $K(J_\varphi) = K(J_\lambda) = 6$ in latitude and longitude directions.

To find an adequate level for the time, all profiles belonging to a specific time segment in Fig. 4, independent of the position, have been counted and plotted in Fig. 5, which demonstrates the sparsity of the data distribution in time.

For instance, there are only three profiles available between 16:00 and 18:00 UT in 2008 and just one between 02:00 and 04:00 UT in 2012. Based on this distribution, an approximate time sampling of 2.5 h has been chosen, and, according to Eq. (4), this leads to a B-spline level of $J_t \leq 3.1 \rightarrow J_t = 3$, resulting in $K(J_t) = 10$ splines with respect to time. The B-spline levels found here have also been considered for the studies of 2012.

6 Extended adjustment system

In order to process sparse and inhomogeneous data, the adjustment system introduced with Eq. (3) has to be extended to allow for the bridging of data gaps in a reliable way with prior information. The extended normal equations yield

$$\hat{\mathbf{d}} = \mathbf{d}_0 + \left(\frac{\mathbf{A}^T \mathbf{P} \mathbf{A}}{\hat{\sigma}_{F3/C}^2} + \mathbf{W} \right)^{-1} \left(\frac{\mathbf{A}^T \mathbf{P} \mathbf{L}}{\hat{\sigma}_{F3/C}^2} + \mathbf{W} \mathbf{M} \right), \quad (5)$$

where $\mathbf{M}_{it} = \boldsymbol{\mu} - \hat{\mathbf{d}}_{it-1}$ is computed from the difference between the prior information vector $\boldsymbol{\mu}$ and the coefficient solution of the previous iteration $it-1$ in order to constrain the solution in regions without observations to the prior information. Here, the prior information vector $\boldsymbol{\mu}$ (just like the initial coefficients \mathbf{d}_0) is derived in a pre-processing step from IRI07, which is considered as the background model, but it should be noted that the data sources for initial and prior information need not necessarily be the same. \mathbf{W} is an extended

weight matrix of the prior information defined by

$$\mathbf{W} = \text{diag} \left(\frac{\mathbf{P}_{NmF2}}{\hat{\sigma}_{NmF2}^2}, \frac{\mathbf{P}_{hmF2}}{\hat{\sigma}_{hmF2}^2}, \frac{\mathbf{P}_{HF2}}{\hat{\sigma}_{HF2}^2} \right) \quad (6)$$

with a block diagonal structure involving the individual weight matrices \mathbf{P}_{NmF2} , \mathbf{P}_{hmF2} and \mathbf{P}_{HF2} of the key parameter-related coefficients. Advanced information on dependencies between observations or key parameters, as well as knowledge allowing for an individual weighting, was not available, and therefore identity matrices were introduced.

Equation (5) considers variance factors for F3/C ($\sigma_{F3/C}^2$) and the prior information groups (σ_{NmF2}^2 , σ_{hmF2}^2 , σ_{HF2}^2) by means of \mathbf{W} . These variance components serve as relative weighting factors and are determined within a variance component estimation (VCE) (Koch, 1999; Koch and Kusche, 2002). The system does not account for covariance factors, meaning that no correlations between parameter groups or observations are taken into account. From the availability of a dense, homogenous measurement distribution – basically without data gaps – it can be expected that the VCE strongly decreases the influence of the prior information since no background data are required to solve for the unknown coefficient corrections. This in fact occurred for the simulation in Sect. 4, where increased correlations occurred while no prior information was involved. For a more realistic scenario the situation is typically dominated by an inhomogeneous, sparse measurement distribution and the system iteratively adapts the prior information weight in order to balance with the observation weight to bridge the data gaps. This should be kept in mind since possible information stemming from the observations may be suppressed in a scenario with a relatively high prior information weight. Especially concerning the covariance factors which have not been considered in the stochastic model so far, the relevant correlation information cannot be retrieved.

The resulting correlation matrices will still be denoted \mathbf{K}_{xx} and \mathbf{K}_{tt} . For further details on the estimation procedure for coefficients and variance components we refer the reader to Limberger et al. (2013). The modeling concept presented here is based on the idea of improving existing background information in regions where observations are available and bridging data gaps with prior information wherever necessary. The extent of the corrected regions depends on the chosen B-spline levels, which are typically adapted to the average measurement density.

7 1 July 2008: low solar activity

The studies on 1 July 2008 include a correlation analysis on the B-spline series coefficient level (\mathbf{K}_{xx}), followed by investigations on the key parameter correlations (\mathbf{K}_{tt}) and finally a section about the matrix composition structure.

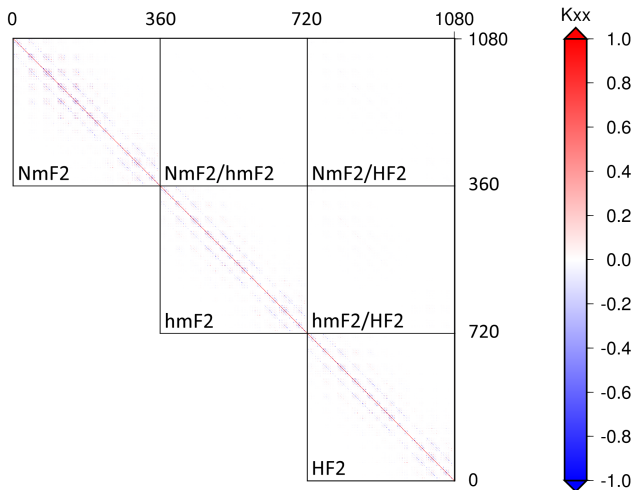


Figure 6. Correlation matrix of the coefficients \mathbf{K}_{xx} for 1 July 2008. Due to the symmetry of the matrices, only those block submatrices belonging to the upper triangular structure have been depicted.

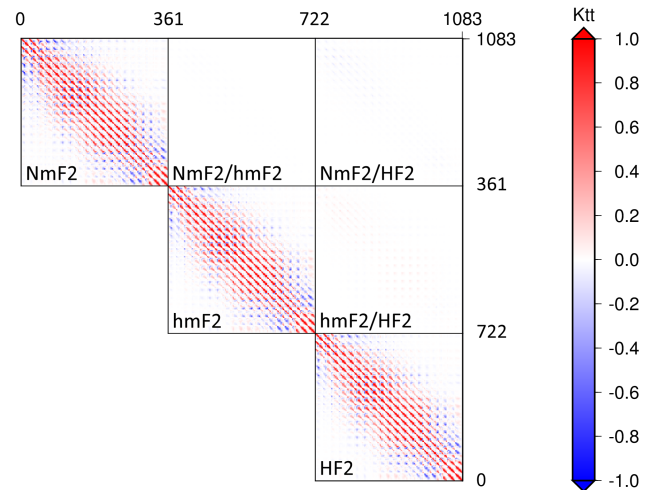


Figure 7. Correlation matrices of the key parameters \mathbf{K}_{tt} for the fixed time moment on 1 July 2008, 12:00 UT. \mathbf{K}_{tt} represents correlations for parameters related to a $\Delta\varphi = 5^\circ \times \Delta\lambda = 5^\circ$ grid.

7.1 Coefficient correlations, \mathbf{K}_{xx}

The correlation matrix of the coefficients \mathbf{K}_{xx} , computed for 1 July 2008, is given in Fig. 6.

It has previously been stated in Sect. 6 that key parameter covariances cannot be extracted from this system since they are not considered in the stochastic model and observation-based correlations may be suppressed because of strong prior information. This effect becomes obvious from the correlation matrix \mathbf{K}_{xx} in Fig. 6 with the absence of correlations between coefficients related to the different key parameters. The distribution of F3/C measurements is inhomogeneous and sparse, which consequently leads to an increased a priori information weighting and depression of interparameter correlations. It can be vaguely discerned that only correlations originating from adjacent B-splines appear close to the diagonal of \mathbf{K}_{xx} as a mixture of characteristic positive and negative dependencies due to the B-spline nature. According to the approach in Sect. 4, the correlation structure should be amplified by the step from \mathbf{K}_{xx} to \mathbf{K}_{tt} .

7.2 Key parameter correlations, \mathbf{K}_{tt}

As can be seen from Fig. 7, noticeable blue/red-colored patches along the diagonal become visible, identifying these correlations between nearby key parameters. The width of these patches depends on the resolution of the computed \mathbf{K}_{tt} matrix. Here, a spatial resolution of $5^\circ \times 5^\circ$ has been chosen.

The corresponding numerical information for \mathbf{K}_{tt} is provided in Table .

Total minimum and maximum correlations are close to ± 1 , reflecting, in particular, the linear dependencies between neighboring key parameters which are highly correlated due to the low B-spline level. This can also be interpreted from

Table 2. Key parameter correlations contained in \mathbf{K}_{tt} for 1 July 2008. Table is displayed in the same manner as Table 1.

Total \mathbf{K}_{tt}	Min	-0.89	Max	0.99	
<i>NmF2</i>	Min	-0.89	Max	0.99	
[-1, -0.7]]-0.7, -0.3]]-0.3, 0[[0, 0.3[[0.3, 0.7]	[0.7, 1]
0.0 %	1.6 %	43.9 %	42.9 %	<u>7.6 %</u>	<u>3.9 %</u>
<i>hmF2</i>	Min	-0.89	Max	0.99	
[-1, -0.7]]-0.7, -0.3]]-0.3, 0[[0, 0.3[[0.3, 0.7]	[0.7, 1]
0.0 %	1.0 %	44.7 %	42.6 %	<u>7.4 %</u>	<u>3.9 %</u>
<i>HF2</i>	Min	-0.89	Max	0.99	
[-1, -0.7]]-0.7, -0.3]]-0.3, 0[[0, 0.3[[0.3, 0.7]	[0.7, 1]
0.0 %	1.0 %	45.2 %	42.5 %	<u>7.3 %</u>	<u>3.9 %</u>
<i>NmF2, hmF2</i>	Min	-0.03	Max	0.01	
[-1, -0.7]]-0.7, -0.3]]-0.3, 0[[0, 0.3[[0.3, 0.7]	[0.7, 1]
0.0 %	0.0 %	60.8 %	39.2 %	0.0 %	0.0 %
<i>NmF2, HF2</i>	Min	-0.15	Max	0.04	
[-1, -0.7]]-0.7, -0.3]]-0.3, 0[[0, 0.3[[0.3, 0.7]	[0.7, 1]
0.0 %	0.0 %	60.8 %	39.2 %	0.0 %	0.0 %
<i>hmF2, HF2</i>	Min	-0.05	Max	0.18	
[-1, -0.7]]-0.7, -0.3]]-0.3, 0[[0, 0.3[[0.3, 0.7]	[0.7, 1]
0.0 %	0.0 %	43.5 %	56.5 %	0.0 %	0.0 %

those cells with underlined numbers which show significant positive correlations in the [0.3, 0.7[and [0.7, 1] intervals of *NmF2*, *hmF2* and *HF2*.

7.3 Matrix composition

Discussions about the correlation matrix structure have been neglected in the context of the simulation (Sect. 4) and will be explained in detail here. The upper triangle structure of the *hmF2* submatrix from Fig. 7 is depicted in Fig. 8. The submatrices for *NmF2* and *HF2* are structured in a similar way.

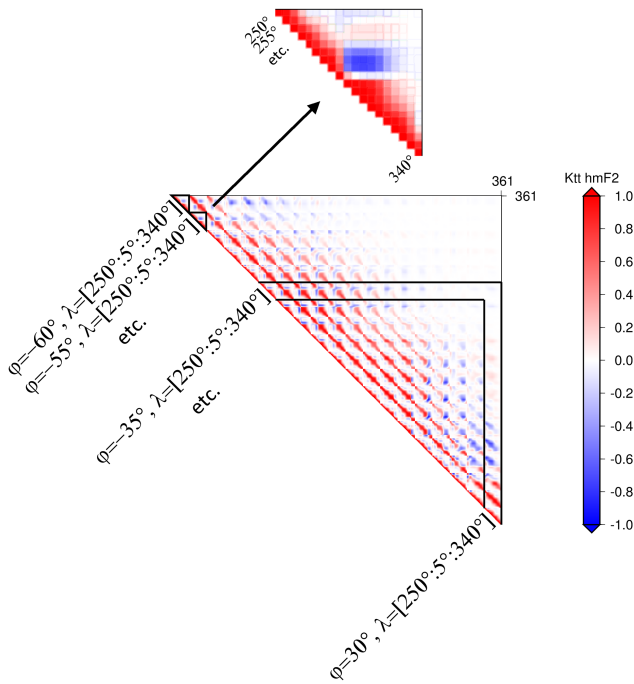


Figure 8. Upper triangular structure of the *hmF2* block submatrix located on the diagonal of Fig. 7 showing the internal *hmF2* key parameter correlations for the fixed time moment of 1 July 2008, 12:00 UT. The entries are related to a $\Delta\varphi = 5^\circ \times \Delta\lambda = 5^\circ$ grid.

The numbering of the matrix elements in \mathbf{K}_{tt} follows the order of longitude in the innermost loop and latitude in the outermost. Figure 7 is given as a snapshot at 12:00 UT, and therefore temporal correlations are not visible. For clarification, tags have been added in Fig. 8 to describe the arrangement of the diagonal elements, with each tag referring to a specific latitude position. Two small triangular-shaped areas have been framed to group all elements belonging to a specific latitude position. Consequently, pixels within such a triangle describe the longitude correlations of *hmF2*. As an example, the correlations between $\lambda = 250^\circ$ and $\lambda = 340^\circ$ at $\varphi = -55^\circ$ have been zoomed in on to give a detailed representation. Here, every pixel along the diagonal refers to a longitude position. It can be seen that, due to the 5° separation between key parameters, the diagonal consists of 19 elements. It becomes clear that the longitude correlations are very large for adjacent elements and that interior elements show a large negative correlation, indicated by the blue region. The same pattern appears multiple times in Fig. 8 and can be better explained by considering the spline distribution depicted in Fig. 9 as an example for latitude.

With regard to the investigation area covering $90^\circ \times 90^\circ$, it can be inferred that the distance between neighboring B-spline peaks is around 20° (≈ 2000 km) in latitude and longitude direction for the defined levels $J_\lambda = J_\varphi = 2$. This applies at least for the “regular” splines in the interior region and is different for the two first and two last endpoint-

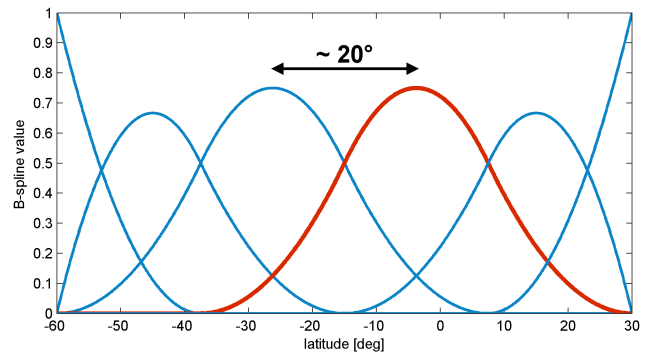


Figure 9. 1-D representation of endpoint-interpolating polynomial B-splines of level $J = 2$ ($K_J = 6$) with respect to a latitude interval between -60° and 30° . The distance between neighboring, “regular” spline peaks is approximately 20° .

interpolating splines. (For completeness, $K(J_t) = 10$ splines are distributed over time in the interval of 24 h and spline peaks are placed around every 160 min.) Figure 9 represents the spline distribution in the latitude direction with a peak separation of about 20° .

A single spline function, e.g., the red-colored spline ϕ_2^4 in Fig. 9, is again illustrated in Fig. 10a and shows that the nonzero interval for a regular interior spline based on level $J_\varphi = 2$ covers approximately 65° in a total interval of 90° . Again, it should be kept in mind that the boundary splines are exceptions. For this scenario, J_λ and J_φ are chosen equal and consequently the influence zone spanned by the latitude and longitude axis becomes circular (diameter yields around 65°), indicated by the bird’s eye view perspective in Fig. 10b.

Under consideration that the two interior splines together already cover the whole region, a negative correlation may appear between them and consequently also between key parameters located in the interior region. This relation can clearly be seen from the longitude correlations in Fig. 8. The effect, however, is not as obvious for the latitude correlations.

Additionally, two black bands related to $\varphi = -35^\circ$ and $\varphi = 30^\circ$ are depicted in relation to the knowledge that a single spline already covers more than two-thirds of the region and, following Fig. 10a (or also Fig. 10b), approximately 65° . The band therefore shows how the correlations evolve between directly neighboring and up to 65° separated parameters. A steadily decreasing trend is visible until the correlation converges to zero towards the intersection of both bands where the distance between the parameters reaches 65° in the latitude direction.

The appearance of internal correlations between the variables of a specific key parameter resulting from the B-spline modeling approach is expected and not surprising. The absence of interparameter dependencies in this scenario can be explained by studying the observation and parameter weighting resulting from the VCE. The normal equations are given by Eq. (5), where variance components for F3/C and the prior

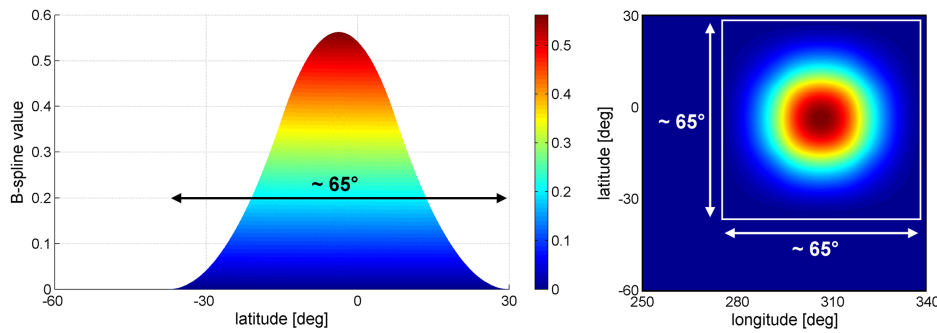


Figure 10. Representation of a single B-spline with nonzero interval of $\approx 65^\circ$ (a) and corresponding bird’s eye view perspective giving the extent of the spline function in latitude and longitude (b).

information, i.e., a global variance factor for each group of a priori coefficients with respect to $NmF2$, $hmF2$ and $HF2$, are included. All observations and the prior information are equally weighted, i.e., \mathbf{P} and \mathbf{P}_{NmF2} , \mathbf{P}_{hmF2} as well as \mathbf{P}_{HF2} are introduced as identity matrices, while the VCE controls the relative weighting between F3/C and the prior information. Following the investigations in Sect. 5, the EDP distribution is very sparse and the adjustment system has to deal with large data gaps. Hence, the ratio between COSMIC and the prior information weighting is rather small – due to a small σ_{hmF2} (or also σ_{NmF2} and σ_{HF2}) in comparison to $\sigma_{F3/C}$ – and consequently a relatively high prior information weighting is considered. In other words, the diagonal elements of the extended weight matrix \mathbf{W} , given by Eq. (6), contribute large values which are added to the diagonal of the normal equations matrix \mathbf{N} in Eq. (5). The influence of \mathbf{W} on the normal equations is therefore very strong and suppresses the occurrence of correlations originating from the observations. In addition, the stochastic model introduced here is incomplete and currently does not account for covariances between key parameters due to the fact that only diagonal weighting matrices have been introduced. Stochastic correlations therefore cannot appear. The absence of parameter correlations is confirmed by Figs. 6 and 7.

8 1 July 2012: Increased solar activity

To prove the general validity of the conclusions obtained for the 1 July 2008 scenario during quiet solar conditions, the same procedure has been conducted for 1 July 2012, a day with slightly higher solar activity.

All settings for the studies of 1 July 2012 are maintained as for 2008 – the configuration for the data screening, B-spline levels and computation sequence – as explained in Sects. 5 and 7. A detailed description of the matrix composition for the coefficient and key parameter correlation matrices \mathbf{K}_{xx} and \mathbf{K}_{tt} , respectively, has already been given in Sect. 7.

The results are comparable to the outcomes of 2008 and have not manifested any differences. Studies on the coef-

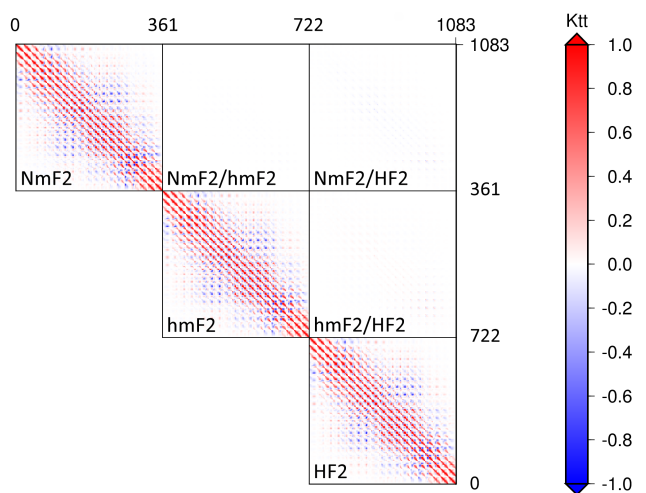


Figure 11. Correlation matrix of the key parameters \mathbf{K}_{tt} for the fixed time moment on 1 July 2012, 12:00 UT. \mathbf{K}_{tt} represents correlations for parameters related to a $\Delta\varphi = 5^\circ \times \Delta\lambda = 5^\circ$ grid.

ficient level are therefore neglected here and only \mathbf{K}_{tt} as well as the corresponding numerical values of the correlation distribution will be studied at this point. \mathbf{K}_{tt} is depicted in Fig. 11 and clearly shows a similar pattern to Fig. 7.

In accordance with Table , a numerical expression of the correlations is provided in Table . Again, the majority of correlations are located within the $] -0.3, 0[$ and $[0, 0.3[$ intervals. Around 9.3 and 4.7 % of the correlations for the single parameters have been detected in the $[0.3, 0.7[$ and $[0.7, 0.1]$ intervals, respectively. The results here again confirm the absence of correlations between key parameters resulting from the combination of the applied model approach with a sparse and inhomogeneous measurement distribution.

9 Conclusions

The investigations performed in this paper are provided as an extension of Limberger et al. (2013) and were strongly fo-

Table 3. Key parameter correlations contained in K_{tt} for 1 July 2012. Table is displayed in the same manner as Table 1.

Total K_{tt}		Min	−0.27	Max	0.99
$NmF2$		Min	−0.26	Max	0.99
[−1, 0.7]] − 0.7, −0.3]] − 0.3, 0[[0, 0.3[[0.3, 0.7[[0.7, 1]
0.0 %	0.0 %	35.0 %	51.1 %	<u>9.3 %</u>	<u>4.7 %</u>
$hmF2$		Min	−0.27	Max	0.99
[−1, 0.7]] − 0.7, −0.3]] − 0.3, 0[[0, 0.3[[0.3, 0.7[[0.7, 1]
0.0 %	0.0 %	35.6 %	50.5 %	<u>9.3 %</u>	<u>4.7 %</u>
$HF2$		Min	−0.26	Max	0.98
[−1, 0.7]] − 0.7, −0.3]] − 0.3, 0[[0, 0.3[[0.3, 0.7[[0.7, 1]
0.0 %	0.0 %	35.8 %	50.3 %	<u>9.3 %</u>	<u>4.7 %</u>
$NmF2, hmF2$		Min	−0.00	Max	0.00
[−1, 0.7]] − 0.7, −0.3]] − 0.3, 0[[0, 0.3[[0.3, 0.7[[0.7, 1]
0.0 %	0.0 %	77.2 %	22.8 %	0.0 %	0.0 %
$NmF2, HF2$		Min	−0.02	Max	0.00
[−1, 0.7]] − 0.7, −0.3]] − 0.3, 0[[0, 0.3[[0.3, 0.7[[0.7, 1]
0.0 %	0.0 %	74.6 %	25.4 %	0.0 %	0.0 %
$hmF2, HF2$		Min	−0.00	Max	0.02
[−1, 0.7]] − 0.7, −0.3]] − 0.3, 0[[0, 0.3[[0.3, 0.7[[0.7, 1]
0.0 %	0.0 %	31.9 %	68.1 %	0.0 %	0.0 %

cused on studies of correlations between F2 Chapman key parameters $NmF2$, $hmF2$ and $HF2$ based on the usage of endpoint-interpolating polynomial B-splines in a regional modeling approach. A simulated and a real data scenario were taken into account. One day during quiet solar conditions on 1 July 2008 and another one in the solar maximum period on 1 July 2012 have been considered. In addition to studies on the dependencies between the B-spline series coefficients referring to a specific key parameter, interdependencies between F2 Chapman key parameters have also been analyzed. After comparisons between the simulated scenario (dense, homogenous data grid) and the real data scenario (sparsely, inhomogeneously distributed F3/C EDPs), it can be concluded that the chosen preliminary stochastic model supports the separability of the different types of series coefficients regarding the use of sparse and inhomogeneously distributed input data. The stochastic model effectively causes a decorrelation by suppressing key parameter correlations and enables the reliable estimation of the key parameters by increasing the prior information weight by means of the VCE as a consequence of the sparse F3/C measurement distribution. However, there are enough F3/C input data to correct the background information, as shown by Limberger et al. (2013) and Liang et al. (2014). Another important point in this context concerns the incomplete stochastic model where no covariances between key parameters have been considered so far. In combination with other observation techniques it can be assumed that estimability benefits from the different sensitivities of the techniques, leading to a (desired) down-weighting of the prior information. Consequently, the importance of considering key parameter correlations goes along with the number and distribution of further observation tech-

niques. Since the simulated scenario with coefficient correlations reaching a minimum of -0.62 between $NmF2$ and $HF2$ (5.2 % of the correlations within the $] - 0.7, -0.3]$ interval) and a maximum of 0.63 between $hmF2$ and $HF2$ (4.6 % of the correlations within the $[0.3, 0.7[$ interval) was still solvable, the implementation of an extended stochastic model is not urgent but definitely an important task that is in need of discussion in the near future.

Acknowledgements. The authors would like to thank Lung-Chih Tsai from CSRSR at the NCU, Taiwan, for providing the FORMOSAT-3/COSMIC electron density profiles. This work was carried out as part of the project “Multi-scale model of the ionosphere from the combination of modern space-geodetic satellite techniques”, which is funded by the German Research Foundation (DFG), Bonn, Germany.

Topical Editor K. Hosokawa thanks J. F. Conte and M. M. Alizadeh for their help in evaluating this paper.

References

- Alizadeh, M. M.: Multi-Dimensional modeling of the ionospheric parameters, using space geodetic techniques, PhD Thesis, University of Technology, Vienna, Austria, February 2013.
- Altadill, D., Magdaleno, S., Torta, J. M., and Blanch, E.: Global empirical models of the density peak height and of the equivalent scale height for quiet conditions, *Adv. Space Res.*, 52: 1756–1769, 2012.
- Angling, M. J.: First assimilations of COSMIC radio occultation data into the Electron Density Assimilative Model (EDAM), *Ann. Geophys.*, 26, 353–359, doi:10.5194/angeo-26-353-2008, 2008.
- Azpilicueta, F., Brunini, C., and Radicella, S. M.: Global ionospheric maps from GPS observations using modip latitude, *Adv. Space Res.*, 38, 11, 2324–2331, doi:10.1016/j.asr.2005.07.069, 2006.
- Bilitza, D.: International Reference Ionosphere 2000, *Radio Sci.*, 36, 261–275, 2001.
- Bilitza, D.: Ionospheric models for radio propagation studies, *Review of Radio Science 1999–2002*, Oxford University Press, 625–679, 2002.
- Bilitza, D., Mckinnell, L. A., Reinisch, B., and Fuller-Rowell, T.: The international reference ionosphere today and in the future, *J. Geodesy*, 85, 909–920, 2011.
- Brunini, C., Conte, J. F., Azpilicueta, F., and Bilitza, D.: A different method to update monthly median $hmF2$ values, *Adv. Space Res.*, 51, 2322–2332, 2013.
- Davies, K.: Ionospheric radio, Peter Peregrinus Ltd., London, 1990.
- Dettmering, D., Schmidt, M., Heinkelmann, R., and Seitz, M.: Combination of different space-geodetic observations for regional ionosphere modeling, *J. Geodesy*, 85, 989–998, doi:10.1007/s00190-010-0423-1, 2011.
- Dettmering, D., Schmidt, M., Limberger, M.: Contributions of DORIS to ionosphere modeling, in: *Proceedings of “20 Years of Progress in Radar Altimetry”*, edited by: Ouwehand, L., IDS Workshop, Sept. 2012, Venice, Italy, ESA SP-710 (CD-ROM), ISBN 978-92-9221-274-2, ESA/ESTEC, 2013.

- Dow, J. M., Neilan, R. E., and Rizos, C.: The International GNSS Service in a changing landscape of Global Navigation Satellite Systems, *J. Geodesy*, 83, 191–198, doi:10.1007/s00190-008-0300-3, 2009.
- Feltens, J.: Chapman profile approach for 3-D global TEC representation, *Proceeding of the IGS AC Workshop*, 285–297, 1998.
- Hernández-Pajares, M., Juan, J. M., Sanz, J., Orus, R., Garcia-Rigo, A., Feltens, J., Komjathy, A., Schaer, S. C., and Krankowski, A.: The IGS VTEC maps: a reliable source of ionospheric information since 1998, *J. Geodesy*, 83, 263–275, 2009.
- Hernández-Pajares, M.: IGS Ionosphere WG Status Report: Performance of IGS Ionosphere TEC Maps, *IGS Workshop*, Bern, 2004.
- Hernández-Pajares, M., Juan, J. M., and Sanz, J.: New approaches in global ionospheric determination using ground GPS data, *J. Atmos. Sol.-Terr. Phys.*, 61, 1237–1247, doi:10.1016/S1364-6826(99)00054-1, 1999.
- Hoque, M. M. and Jakowski, N.: A new global model for the ionospheric F2 peak height for radio wave propagation, *Ann. Geophys.*, 30, 797–809, doi:10.5194/angeo-30-797-2012, 2012.
- Jakowski, N.: Ionospheric GPS radio occultation measurements on board CHAMP, *GPS Solutions*, 9, 88–95, doi:10.1007/s10291-005-0137-7, 2005.
- Jakowski, N., Leitinger, R., and Angling, M.: Radio occultation techniques for probing the ionosphere, *Ann. Geophys.*, 47, doi:10.4401/ag-3285, 2004.
- Jayachandran, B., Krishnankutty, T. N., and Gulyaeva, T. L.: Climatology of ionospheric slab thickness, *Ann. Geophys.*, 22, 25–33, doi:10.5194/angeo-22-25-2004, 2004.
- Kirchengast, G., Foelsche, U., and Steiner, A. K.: Occultations for probing atmosphere and climate, *Springer Berlin Heidelberg*, ISBN 3-540-22350-9, 2004.
- Koch, K. R.: Parameter estimation and hypothesis testing in linear models, *Springer*, Berlin, 1999.
- Koch, K.-R. and Kusche, J.: Regularization of geopotential determination from satellite data by variance components, *J. Geodesy*, 76, 259–268, doi:10.1007/s00190-002-0245-x, 2002.
- Kourisa, S. S., Polimerisa, K. V., Canderb, L. R., and Ciraoloc, L.: Solar and latitude dependence of TEC and SLAB thickness, *J. Atmos. Sol.-Terr. Phys.*, 70, 1351–1365, doi:10.1016/j.jastp.2008.03.009, 2008.
- Liang, W., Limberger, M., Schmidt, M., Dettmering, D., and Hugentobler, U.: Combination of ground- and space-based GPS data for the determination of a multi-scale regional 4-D ionosphere model, *International Association of Geodesy Symposia*, doi:10.1016/j.asr.2014.12.006, accepted, 2014.
- Limberger, M., Liang, W., Schmidt, M., Dettmering, D., and Hugentobler, U.: Regional representation of F2 Chapman parameters based on electron density profiles, *Ann. Geophys.*, 31, 2215–2227, doi:10.5194/angeo-31-2215-2013, 2013.
- Liu, L., Wan, W., and Ning, B.: A study of the ionogram derived effective scale height around the ionospheric hmF2, *Ann. Geophys.*, 24, 851–860, doi:10.5194/angeo-24-851-2006, 2006.
- Lee, C.-C. and Reinisch, B. W.: Quiet-condition variations in the scale height at F2-layer peak at Jicamarca during solar minimum and maximum, *Ann. Geophys.*, 25, 2541–2550, doi:10.5194/angeo-25-2541-2007, 2007.
- Lyche, T. and Schumaker, L. L.: A multiresolution tensor spline method for fitting functions on the sphere, *SIAM J. Sci. Comput.*, 22, 724–746, doi:10.1137/S1064827598344388, 2000.
- Nava, B., Coisson, P., and Radicella, S. M.: A new version of the NeQuick ionosphere electron density model, *J. Atmos. Sol.-Terr. Phys.*, 70, 1856–1862, 2008.
- Reinisch, B. W., Huang, X.-Q., Belehaki, A., Shi, J.-K., Zhang, M.-L., and Ilma, R.: Modeling the IRI topside profile using scale heights from ground-based ionosonde measurements, *Adv. Space Res.*, 34, 2026–2031, doi:10.1016/j.asr.2004.06.012, 2004.
- Rocken, C., Kuo, Y.-H., Schreiner, W. S., Hunt, D., Sokolovskiy, S., and McCormick, C.: COSMIC System Description, *Terr. Atmos. Ocean. Sci.*, 11, 21–52, 2000.
- Sánchez, L., Seemüller, W., Drewes, H., Mateo, L., González, G., Silva, A., Pampillón, J., Martínez, W., Cioce, V., Cisneros, D., and Cimbaro, S.: Long-Term Stability of the SIRGAS Reference Frame and Episodic Station Movements Caused by the Seismic Activity in the SIRGAS Region, *IAG Symposia*, 138, 153–161, Springer Berlin Heidelberg, 2013.
- Schmidt, M.: Wavelet modeling in support of IRI, *Adv. Space Res.*, 39, 932–940, doi:10.1016/j.asr.2006.09.030, 2007.
- Schmidt, M., Dettmering, D., Mößmer, M., Wang, Y., and Zhang, J.: Comparison of spherical harmonic and B-spline models for vertical total electron content, *Radio Sci.*, 46, RS0D11, doi:10.1029/2010RS004609, 2011.
- Schunk, R. W., Scherliess, L., Sojka, J. J., Thompson, D. C., Anderson, D. N., Codrescu, M., Minter, C., Fuller-Rowell, T. J., Heelis, R. A., Hairston, M., Howe B.: Global Assimilation of Ionospheric Measurements (GAIM), *Radio Sci.*, 39, RS1S02, doi:10.1029/2002RS002794, 2001.
- Stankov, S. M. and Jakowski, N.: Topside plasma scale height modelling based on CHAMP measurements: first results, *Earth Observation with CHAMP – Results from Three Years in Orbit*, Springer book, XVI, Springer, ISBN 3-540-22804-7, 2005.
- Todorova, S., Schuh, H., Hobiger, T., and Hernández-Parajes, M.: Global ionosphere models obtained by integration of GNSS and satellite altimetry data, *Österreichische Zeitschrift für Vermessung und Geoinformation (VGI)*, 2, 80–89, 2007.
- Tsai, L.-C., Tsai, W.-H., Schreiner, W. S., Berkey, F. T., and Liu, J. Y.: Comparisons of GPS/MET retrieved ionospheric electron density and ground based ionosonde data, *Earth Planet. Space*, 53, 193–205, 2001.
- Tsai, L.-C. and Tsai, W.-H.: Improvement of GPS/MET ionospheric profiling and validation using the Chung-Li ionosonde measurements and the IRI model: Terrestrial, *Atmos. Ocean. Sci.*, 15, 589–607, doi:10.3319/TAO.2007.12.19.01(F3C), 2004.
- Tsai, L.-C., Liu, C. H., and Hsiao, T. Y.: Profiling of ionospheric electron density based on FormoSat-3/COSMIC data: results from the intense observation period experiment: Terrestrial, *Atmos. Ocean. Sci.*, 20, 181–191, 2009.
- Wright, J. W.: A model of the F region above hmF2, *J. Geophys. Res.*, 65, 185–191, 1960.
- Zhang, M.-L., Reinisch, B. W., Shi, J.-K., Wu, S.-Z., and Wang, X.: Diurnal and seasonal variation of the ionogram-derived scale height at the F2 peak, *Adv. Space Res.*, 37, 967–971, doi:10.1016/j.asr.2006.02.0042, 2006.

7.3 P-III

Limberger, M., Hernández-Pajares, M., Aragón-Ángel, A., Altadill, D., and Dettmering, D. (2015): Long-term comparison of the ionospheric F2 layer electron density peak derived from ionosonde data and Formosat-3/COSMIC occultations. *J. Space Weather Space Clim.*, 5, A21, 2015, DOI 10.1051/swsc/2015023.

Copyright

This work is published in the *Journal of Space Weather and Space Climate* under the license of Creative Commons. Copyrights are retained by the Authors. P-III is an open access publication.

Summary

This publication was motivated by the requirement of an assessment for the electron density retrieval by means of the Abel transform approach. Specifically, the accuracy of F2 Chapman peak parameters have been estimated. Therefore the improved Abel inversion techniques extending the classical approach by the consideration of horizontal ionospheric gradient, developed at the UPC, has been applied as it is an efficient approach with manageable computational burden. The main innovation of P-III can be found in the exploitation of the F-3/C availability since 2006 for a long-term study of the F2 peak. The paper includes (1) climatological studies concerning the global trend of $NmF2$ and $hmF2$ as well as (2) the assessment of the observed F-3/C peak against ionosonde data provided by SPIDR.

At first, correlations between global $NmF2$ ($hmF2$) averages and sunspot numbers as well as F10.7 flux indices are computed where the studies identify the global F2 peak averages of F-3/C data as suitable parameters to characterize the solar conditions. In a second step, globally distributed data pairs of F-3/C profile peaks together with nearby ionosonde measurements provided by the SPIDR are considered to evaluate $NmF2$ and $hmF2$ in different geomagnetic latitude sectors ($\pm[0, 20^\circ]$, $\pm]20^\circ, 60^\circ]$ and $\pm]60^\circ, 90^\circ]$) and local times (LT) accounting for different ionospheric conditions at night (02:00 LT \pm 2 hours), dawn (08:00 LT \pm 2 hours) and day (14:00 LT \pm 2 hours). In general, high correlations between the F2 peaks derived from F-3/C occultations and ionosondes have been obtained with slightly better agreement for $NmF2$. An accuracy degrade was also observed during night, but could be related to outliers in the ionosonde data.

Beside numerous investigations regarding the F2 peak evaluation, an immense effort of preprocessing and data screening for the establishment of a reliable electron density database from occultation data turned out to be another important component in the studies of P-III.

Declaration of own contribution

The initiation of this paper is based on a research stay at the UPC, Barcelona, Spain. The conception and outline of the paper has been suggested by M. Limberger and discussed with all co-authors. Computations as well as analysis and evaluations are performed by M. Limberger. All co-authors supported the progress by intensive discussions on the result verification and through suggestions regarding the validation methods. All figures contained in the paper are designed and created by M. Limberger. The manuscript has been written by M. Limberger and reviewed by the co-authors.

The overall own contribution is estimated at 80 %.

Table 7.3: Apportionment of own contributions for P-III.

Criteria	Estimated own contribution
Paper concept	80 %
Computations and software development	80 %
Data analysis and interpretation of results	60 %
Design and creation of figures	90 %
Manuscript structure and writing	80 %

Confirmation by the authors

We hereby confirm the correctness of the declaration of own contribution for the publication

Limberger, M., Hernández-Pajares, M., Aragón-Angel, A., Altadill, D., and Dettmering, D. (2015):
Long-term assessment of the ionospheric F2 peak derived from Formosat-3/COSMIC occultations,
Journal of Space Weather and Space Climate, in review.

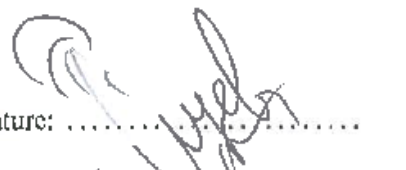
Prof. Manuel Hernández-Pajares

Universitat Politècnica de Catalunya (UPC),
Ionospheric determination and Navigation based on
Satellite And Terrestrial systems research (IONSAT),
Barcelona, Spain

Signature: 
Date: ... 24.05.2015

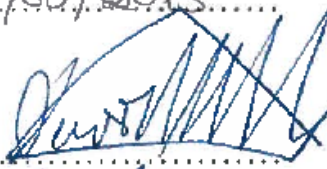
Dr. Angela Aragón-Angel

European Commission, Joint Research Centre (JRC),
Institute for the Protection and Security of the Citizen,
Ispra, Italy

Signature: 
Date: 26/05/2015

Dr. David Altadill

Director of the Ebro Observatory, Roquetes, Spain

Signature: 
Date: 22/05/2015

Dr. Denise Dettmering

Deutsches Geodätisches Forschungsinstitut der
Technischen Universität München (DGFI-TUM),
München, Germany

Signature: ... D. Dett. g.
Date: 20.05.2015

Long-term comparison of the ionospheric F2 layer electron density peak derived from ionosonde data and Formosat-3/COSMIC occultations

Marco Limberger^{1,*}, Manuel Hernández-Pajares², Angela Aragón-Ángel³, David Altadill⁴, and Denise Dettmering¹

¹ Deutsches Geodätisches Forschungsinstitut der Technischen Universität München (DGFI-TUM), Alfons-Goppel-Str. 11, 80539 München, Germany

*Corresponding author: marco.limberger@tum.de

² Universidad Politécnica de Cataluña, IonSAT research group, Jordi Girona, 1-3, Mod. C-3 Campus Nord, 08034 Barcelona, Spain

³ European Commission, Joint Research Centre (JRC), Institute for the Protection and Security of the Citizen, Ispra, Italy

⁴ Observatori de l'Ebre (OE), CSIC, Universitat Ramon Llull, Horta Alta 38, 43520 Roquetes, Spain

Received 27 April 2015 / Accepted 15 June 2015

ABSTRACT

Electron density profiles (EDPs) derived from GNSS radio occultation (RO) measurements provide valuable information on the vertical electron density structure of the ionosphere and, among others, allow the extraction of key parameters such as the maximum electron density $NmF2$ and the corresponding peak height $hmF2$ of the F2 layer. An efficient electron density retrieval method, developed at the UPC (Barcelona, Spain), has been applied in this work to assess the accuracy of $NmF2$ and $hmF2$ as determined from Formosat-3/COSMIC (F-3/C) radio occultation measurements for a period of more than half a solar cycle between 2006 and 2014. Ionosonde measurements of the Space Physics Interactive Data Resource (SPIDR) network serve as a reference. Investigations on the global trend as well as comparisons of the F2 layer electron density peaks derived from both occultations and ionosonde measurements are carried out. The studies are performed in the global domain and with the distinction of different latitude sectors around the magnetic equator ($\pm[0^\circ, 20^\circ]$, $\pm[20^\circ, 60^\circ]$ and $\pm[60^\circ, 90^\circ]$) and local times (LT) accounting for different ionospheric conditions at night (02:00 LT \pm 2 h), dawn (08:00 LT \pm 2 h), and day (14:00 LT \pm 2 h). The mean differences of F2 layer electron density peaks observed by F-3/C and ionosondes are found to be insignificant. Relative variations of the peak differences are determined in the range of 22%–30% for $NmF2$ and 10%–15% for $hmF2$. The consistency of observations is generally high for the equatorial and mid-latitude sectors at daytime and dawn whereas degradations have been detected in the polar regions and during night. It is shown, that the global averages of $NmF2$ and $hmF2$ derived from F-3/C occultations appear as excellent indicators for the solar activity.

Key words. Formosat-3/COSMIC – Radio occultations – Electron density retrieval

1. Introduction

The application of electron density profiles (EDPs) derived from radio occultation (RO) measurements for ionospheric electron density (N_e) modeling is widely accepted, helping to gain a global data coverage and increased sensitivity for the vertical structure of the N_e distribution. The ionospheric F2 layer peak, defined by the maximum electron density $NmF2$ and its corresponding peak altitude $hmF2$, can be directly accessed from the profiles' shape. The first successful proof-of-concept on limb sounding the Earth atmosphere was carried out in 1993 at the University Corporation for Atmospheric Research (UCAR) by means of the Global Positioning System/Meteorology (GPS/MET) experiment with the Micro-lab-1 satellite (Ware et al. 1996). The studies with GPS/MET were mainly focused on numerical weather predictions but besides, the RO technique has been exploited for profiling the ionosphere and deriving EDPs (Hajj & Romans 1998). The number of low earth orbit (LEO) satellites applicable for ionospheric sounding continuously rose in the last decade and radio occultations have become increasingly important. Among them, the Formosat-3/COSMIC (F-3/C) constellation

consisting of six satellites located on six individual orbital planes. F-3/C was launched on 15 April 2006 and contributes significantly towards a global coverage of ionospheric sounding data (Tsai et al. 2009).

One popular and probably the most widespread algorithm to derive EDPs from ionospheric RO measurements is the classical Abel transform inversion that can be driven by single-frequency bending angle data or directly by dual-frequency GNSS carrier-phase measurements. Hajj & Romans (1998) considered, for instance, the GPS single-frequency signal bending in the ionosphere and used the Abel inversion to derive EDPs to perform a validation between GPS/MET profiles with ionosonde measurements during low solar cycle conditions with a bending angle $<0.01^\circ$. It was concluded that the accuracy of $NmF2$ yields around 20% of its absolute level, which was later confirmed by Tsai et al. (2001). Furthermore, to estimate the absolute precision of the classical Abel inversion, Schreiner et al. (2007) studied the accuracy of N_e by co-located F-3/C EDPs and obtained a root-mean-square (RMS) difference of approximately 10^9 el/m³, a value which indicates already, that rough discrepancies cannot be ruled out by using the classical approach.

The use of GPS L1 frequency measurements for bending angle calculations is one possible method for the retrieval of EDPs but requires precise orbit and clock information. The processing of GNSS dual-frequency measurements on the contrary enables the elimination of geometry-dependent terms through forming the ionosphere (or geometry-free) linear combination L_4 , respectively. Various facilities provide EDPs routinely as preprocessed products mostly by exploitation of the carrier-phase excess. F-3/C EDPs are, for instance, processed and officially released by the COSMIC Data Analysis and Archival Center (CDAAC, US)¹ and the Taiwan Analysis Center for COSMIC (TACC, Taiwan)² as level 2 products. After registration, the data is freely available via http servers as daily tarballs. For the automatic real-data retrieval, CDAAC considers the classical Abel transform, most probably due to its simplicity and relatively low computational burden.

It is well known that the spherical symmetry assumption is one of the most significant error sources of the classical Abel inversion transform that degrades the N_e accuracy in particular in the presence of the equatorial ionization anomaly (EIA). This deficiency led to the situation that various facilities developed their own modified retrieval algorithms with different concepts to account for horizontal electron density variations in the data processing. Research facilities, such as the Universitat Politècnica de Catalunya (UPC, Spain) or the Center for Space and Remote Sensing Research (CSRSR, Taiwan), perform an independent retrieval based on improved Abel inversion techniques under consideration of horizontal ionospheric gradients. The CSRSR approach is based on the interpolation of information from nearby EDPs with a cubic spline fit (Tsai & Tsai 2004) while the UPC method considers the Vertical Total Electron Content (VTEC) derived from terrestrial GNSS observations (Hernández-Pajares et al. 2000). The latter approach is capable of improving the retrieval algorithm with relatively low implementation effort under support of global ionosphere maps (GIMs) as shown, for instance, by Hernández-Pajares et al. (2000), García-Fernández et al. (2003), and Aragon-Angel (2010). Therefore, the UPC approach has been applied in this work involving GIMs (Hernández-Pajares et al. 2009) provided by the International GNSS Service (IGS; Dow et al. 2009) in the Ionosphere Map Exchange (IONEX) format. Few potential drawbacks, however, remain. (1) Since the processing of IGS GIMs is driven by terrestrial GNSS data, it is a matter of fact that the improvement is limited over the oceans. (2) A single layer mapping is taken into account by most of the IGS data analysis centers, i.e., the accuracy of the GIMs partly depends on the quality of the associated mapping function. The accuracy improvement for the F2 layer peak achieved through the inclusion of horizontal VTEC gradients has for instance been studied by Yue et al. (2012) who obtained an enhancement of around 7% for the determination of $NmF2$ and a slightly weaker improvement for $hmF2$. From the comparison of EDPs against co-located Jicamarca ionosonde measurements during 2007, Aragon-Angel et al. (2011) obtained an error improvement of 10% by means of the UPC retrieval method.

Besides the evaluation of the GIM-aided improvement of the EDP retrieval, several authors published works focusing on the accuracy assessment of the F2 layer peak by using diverse evaluation methods with study periods of different lengths. For instance, Wu et al. (2009) compared $NmF2$ against ionosonde

observations during the period of 13 July 2006 and 31 December 2007 and Lei et al. (2007) evaluated correlations of maximum electron densities between F-3/C EDPs and ionosondes at the early stage of the constellation in July 2006. Krankowski et al. (2011) validated F2 peak parameters of F-3/C measurements in the European sector during 2008 and Yue et al. (2010) studied the retrieval accuracy by means of synthetic data driven by background information of the NeQuick model to determine absolute and relative accuracies for $NmF2$ and $hmF2$.

In contrast to the aforementioned publications, the study presented here deals with the global evaluation of $NmF2$ and $hmF2$ by exploitation of the long-term availability of F-3/C occultation measurements for a period of more than half a solar cycle. As a key innovation, the paper focuses on the monitoring and global accuracy assessment of the F2 layer peak against ionosonde measurements between 10 June 2006 and 29 April 2014, i.e., during a time frame of almost 8 years. The study interval thus includes a solar minimum and maximum period. Such a validation is based on an immense amount of data where the manual selection of reliable ionosonde data is no longer possible. Therefore, electron density peaks observed by the global SPIDR ionosonde network are considered as a reference. The SPIDR database provides automatically scaled measurements to be used as one of only few data sources for global long-term assessments. The evaluation presented here concentrates on the long-term aspect and less on the impact of diurnal and small-scale variations. For this purpose, a resolution of 30 days and consequently around one day per month has been chosen to account for the annual and seasonal trends of the ionosphere. As required for the electron density retrieval following the UPC strategy (García-Fernández et al. 2003; Aragon-Angel et al. 2011), horizontal VTEC gradients provided by the ionospheric IGS analysis facility CODE (Center of Orbit Determination in Europe) are considered in this study.

Starting with Section 2, the separability algorithms according to Hernández-Pajares et al. (2000), García-Fernández et al. (2003), and Aragon-Angel (2010) are briefly recapitulated as they constitute the fundamental methodology including the observation equation for the establishment of the EDP database containing the F2 layer peaks. The process chain as realized in this study is described in Section 3 together with the relevant data screening steps for the database generation. In Section 4, the global trends of $NmF2$ and $hmF2$ are investigated and compared with the solar activity. The assessment of ionospheric F2 layer peaks from the comparison between F-3/C and ionosonde observations for evaluating the accuracy level is presented in Section 5 in terms of a global evaluation and in Section 6 by distinction of local times and different magnetic latitude regions. Section 7 closes the paper with a summary and final remarks.

2. Electron density retrieval

The propagation of microwave signals is affected by the ionosphere in terms of a group delay and phase advance (or excess of phase). The ionosphere is a dispersive medium and the higher the signal frequency, the smaller the delay impact. Changes in the phase data are proportional to the Slant Total Electron Content (STEC) and can be exploited in dual-frequency measurements to extract information about the current N_e distribution. In terms of occultations, i.e., based on the condition that the signal transmitted by the GPS satellite reaches the LEO satellite from below the local horizon, N_e profiles below the LEO orbit can be derived. An occultation pass

¹ <http://cdaac-www.cosmic.ucar.edu/cdaac>

² <http://tacc.cwb.gov.tw>

is defined by a sequence of consecutive measurements in occultation geometry referring to the epochs $i \in \{1, \dots, M\}$. There are rising and setting occultations but due to the retrieval concept that will be described, all occultation passes in this work are treated as setting occultations starting from the highest to the lowest occultation. The so-called tangent point (TP) is defined as the closest point to Earth along the line-of-sight (LOS) between GPS and LEO satellite at a specific occultation epoch and defines the anchor point for the retrieved N_e . Consequently, each EDP is composed of a TP arc with associated N_e values at decreasing altitudes and also changing horizontal coordinates where each N_e observation corresponds to an individual occultation epoch. It is important to have in mind, that the whole occultation event can last up to several minutes and the distance between the first and last TP can differ in the magnitude of 20° – 30° (≈ 2000 – 3000 km) in latitude (φ) and longitude (λ).

The UPC retrieval approach is of particular importance for the following validation studies and the main steps for deriving the fundamental observation equation will therefore be recapitulated in accordance with [Hernández-Pajares et al. \(2000\)](#). The retrieval technique is based on the Abel transform inversion where each occultation is processed independently. From each dual-frequency occultation measurement, STEC can be derived as

$$\begin{aligned} \text{STEC} &= \int_{\text{GPS}}^{\text{LEO}} N_e(s) ds \\ &= 2 \cdot \int_{\text{TP}}^{\text{LEO}} N_e(s) ds + \text{STEC}^{\text{TOP}}, \end{aligned} \quad (1)$$

following the definition of the N_e integral along the signal path s from GPS to LEO satellite. Under the assumption of spherical symmetry as implied by the classical Abel retrieval, the integration can alternatively be performed between TP and LEO. The parameter STEC^{TOP} has been introduced in Eq. (1) to take the ionospheric contribution above the orbit into account. STEC can be obtained from phase geometry-free linear combinations L_4 as

$$L_4 = \lambda_1 \phi_1 - \lambda_2 \phi_2 = \alpha \text{STEC} + b_4 + \varepsilon, \quad (2)$$

where ϕ_1 and ϕ_2 are the dual-frequency carrier-phase measurements in cycles, λ_1 and λ_2 are the wavelengths of both carrier frequencies, b_4 is the carrier-phase bias on L_4 , and α is a frequency-dependent factor. ε denotes the unmodeled random measurement noise.

To solve Eq. (1) by means of integral discretization, an onion shell structure can be established with the heights of successive TPs as mean radii. This implies of course that the shell thicknesses depend on the given measurement sampling. The full set of layers $j \in \{1, \dots, N\}$ is consequently defined after collecting all measurements of a specific occultation pass. l_{ij} is the distance between the TP $_i$ at epoch i and the adjacent layer. l_{ij} are the pass lengths of the GPS-LEO LOS at epoch i in shell j . A solution of Eq. (1) at epoch i can then be determined from

$$\text{STEC}_i = 2l_{ii}N_e(\text{TP}_i) + \sum_{j=1}^{j=i-1} 2l_{ij}N_e(\text{TP}_j) + \text{STEC}_i^{\text{TOP}}. \quad (3)$$

Equation (3) is valid under the assumption of spherical symmetry, i.e., a constant density N_e in each shell, parameterized

only by the radius r . As a consequence, no horizontal gradients are considered in N_e . To account for this drawback, the separability hypothesis is introduced with

$$N_e(\varphi, \lambda, h, t) = \text{VTEC}(\varphi, \lambda, t) \times \text{SF}(h). \quad (4)$$

It describes the N_e distribution as a function of VTEC scaled by a shape function parameter $\text{SF}(h)$. The unknown parameters to be estimated are SF values located in the TP positions. VTEC is assumed to be given and can, for instance, be extracted from IGS GIMs. The consideration of Eq. (4) in Eq. (3) leads to the observation equation

$$\begin{aligned} y_i &= \Delta \text{STEC}_i = \alpha^{-1}(L_{4,i} - L_{4,R}) \\ &= 2l_{ii}\text{VTEC}_i^{\text{TP}}\text{SF}_i \\ &\quad + \sum_{j=1}^{j=i-1} \left[l_{ij} \left(\text{VTEC}_{ij}^{\text{F3C}} + \text{VTEC}_{ij}^{\text{GPS}} \right) \text{SF}_j \right] \\ &\quad + (\text{STEC}^{\text{TOP}} - \text{STEC}_R) + \varepsilon, \end{aligned} \quad (5)$$

where differences to a pass-specific reference observation STEC_R (or $L_{4,R}$ are taken into account. For simplicity, it is assumed that the b_4 term only contains the phase ambiguities whereas effects of secondary importance such as phase windup or antenna phase center variations, have been neglected and b_4 consequently cancels out. In the present work, the reference observation must satisfy the condition of being observed within the elevation interval $[0^\circ, -5^\circ]$. For the reason that the F-3/C satellites orbit in altitudes of approximately 800 km, the difference between STEC^{TOP} and STEC_R is expected to be negligibly small. This assumption should be considered with caution since it may be valid for F-3/C but typically not for LEO satellites in lower orbits. Regarding Eq. (5), it shall further be noticed that SF_i and SF_j indicate the affiliation of the shape function to the corresponding TP $_i$ and TP $_j$, respectively. The VTEC values are specified by different superscripts (TP, F3C, and GPS) denoting the position to which the VTEC refers to. For instance, VTEC^{TP} refers to the VTEC observed at the TP position while VTEC^{F3C} and VTEC^{GPS} are the VTEC values at the layer intersection points in LEO and GPS direction. This concept is depicted in [Figure 1](#) including the separation of the LOS into a TP-LEO and TP-GPS directed part.

After collecting all data of an occultation pass, Eq. (5) can be solved recursively starting from the outermost toward the innermost shell as a triangular linear equations system $\mathbf{x} = \mathbf{A}^{-1} \mathbf{y}$ that is established for each occultation pass. \mathbf{x} contains the set of shape function parameters, \mathbf{y} is the vector of STEC observations, and \mathbf{A} is the triangular coefficient matrix

$$\mathbf{A}_{(M=N)} = \begin{array}{c} \text{Outer to inner shell} \\ \downarrow \\ \begin{pmatrix} \frac{\partial y_1}{\partial \text{SF}_1} & & & & \mathbf{0} \\ \vdots & \ddots & & & \\ \frac{\partial y_j}{\partial \text{SF}_1} & \dots & \frac{\partial y_j}{\partial \text{SF}_j} & & \\ \vdots & & & \ddots & \\ \frac{\partial y_M}{\partial \text{SF}_1} & \dots & \dots & \dots & \frac{\partial y_M}{\partial \text{SF}_N} \end{pmatrix}, \end{array} \quad (6)$$

where rows represent the observations $i \in \{1, \dots, M\}$ with decreasing TP altitudes and the columns contain partial

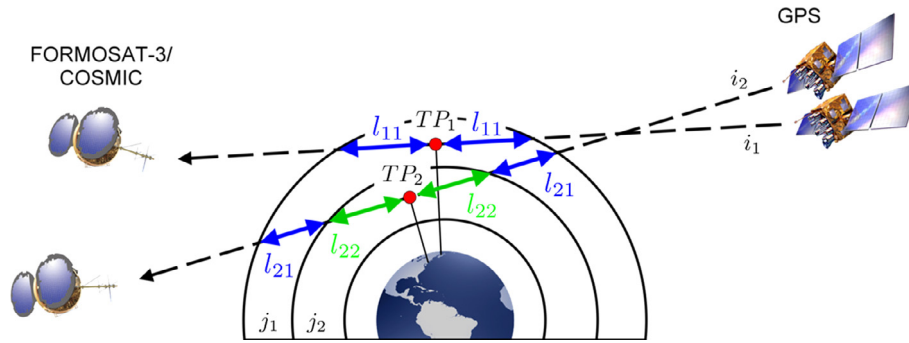


Fig. 1. Improved Abel inversion under consideration of the separability hypothesis with integral discretization by means of the onion shell structure. Colored arrows illustrate the discretized integration steps between adjacent layers. This draft shows the composition with measurements at two epochs i_1 and i_2 yielding the associated tangent points TP_1 and TP_2 that are located at the mean radii of the layers j_1 and j_2 .

derivatives of the shape function parameters starting from the outer toward the innermost shell $j \in \{1, \dots, N\}$.

3. Database of electron density profiles

The paper structure orients on the flowchart in Figure 2. Processing steps are distinguished by different colors: Green boxes are representing input data, yellow boxes indicate the retrieval computation steps, and blue boxes highlight the peak evaluation. To perform the retrieval, various data resources are incorporated. According to the topmost segment of Figure 2, observation data in the Receiver Independent Exchange (RINEX) Format and F-3/C orbits in the Standard Product 3 Orbit Format (SP3) are downloaded from the TACC or CDAAC data servers. Both data types are labeled with unique identifiers, podObs and leoOrb, as declared by CDAAC. For the podObs data, we used the re-processed products which are available since 22 April 2006, i.e., one week after the launch of F-3/C, until 20 April 2014 covering almost 8 years of measurements. GPS orbits³ as well as 2 h sampled GIMs⁴ are acquired from the network servers of the IGS Analysis Center CODE.

This study has been performed between 10 June 2006 and 29 April 2014 starting around 2 months after the launch of F-3/C due to missing data and orbits in the initial period of the constellation. A homogeneous sampling of 30 days has been chosen resulting in totally 97 days under investigation. For each day, the data sets depicted in Figure 2 are downloaded to perform the electron density retrieval as described in Section 2. Among others, the computation of geometry-free linear combinations from occultation measurements is performed in a pre-processing step. Occultation passes are composed of sequences of uninterrupted measurements between a specific GPS transmitter and LEO receiver in occultation geometry where various conditions have to be fulfilled. For instance, maximum thresholds for time gaps between adjacent measurements and for the STEC acceleration $d^2L/dt = L_{4,i+2} - 2L_{4,i+1} + L_{4,i}$ have been considered. Furthermore, a minimum number of observations per pass is mandatory. After performing the pre-processing, each retrieved profile is screened in a post-processing step including the

1. identification of *hmF2* within a defined altitude interval,
2. verification of the profile extending between given bottom and top height limits, and

³ <ftp://ftp.unibe.ch/aiub/CODE>

⁴ <ftp://cddis.gsfc.nasa.gov/pub/gps/products/ionex>

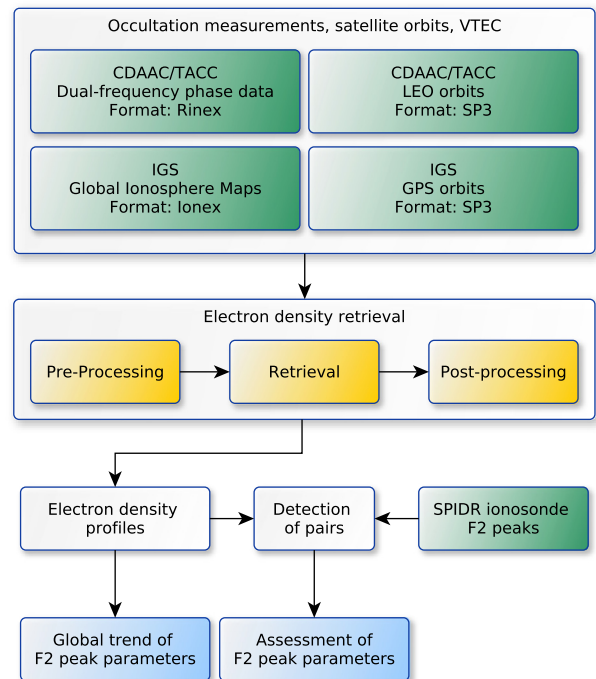


Fig. 2. Flowchart for the validation procedure providing an overview of data sources (green boxes), the retrieval (yellow boxes), and assessment steps (blue boxes).

3. exclusion of profiles with large electron density jumps between adjacent observations.

For each day included in this study, a database consisting of *NmF2* and *hmF2* observations derived from RO is finally established and checked for rough outliers by testing against a 3σ threshold. Those values, that exceed the interval of $\pm 3\sigma$ around the global average, are iteratively excluded. The daily numbers of profiles that passed the pre-processing and screening procedure are depicted in Figure 3.

In total, around 85,000 suitable EDPs have been stored for the validation. The minimum amount of 97 profiles has been obtained on the first investigation day, i.e., on 10 June 2006, where only FM-1 (or COSMIC-1) observations and orbit information between 00:00 UT and 05:59 UT were available. The maximum is reached on 5 June 2007 with 2301 profiles observed by all six F-3/C satellites. The distribution of the retrieved electron density peaks for both days, 10 June 2006

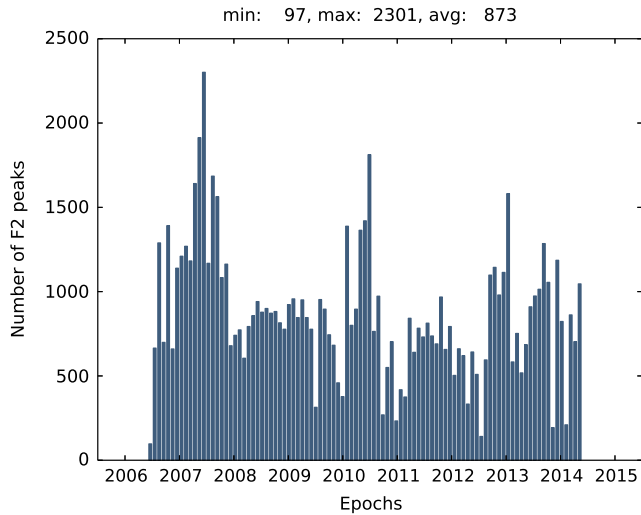


Fig. 3. Number of retrieved F2 layer peaks at each investigated day during the study period (10 June 2006–29 April 2014).

on the left and 5 June 2007 on the right, is shown in Figure 4. Different colors indicate the different F-3/C satellites (FM-1 = red, FM-2 = green, FM-3 = yellow, FM-4 = magenta, FM-5 = cyan, FM-6 = white).

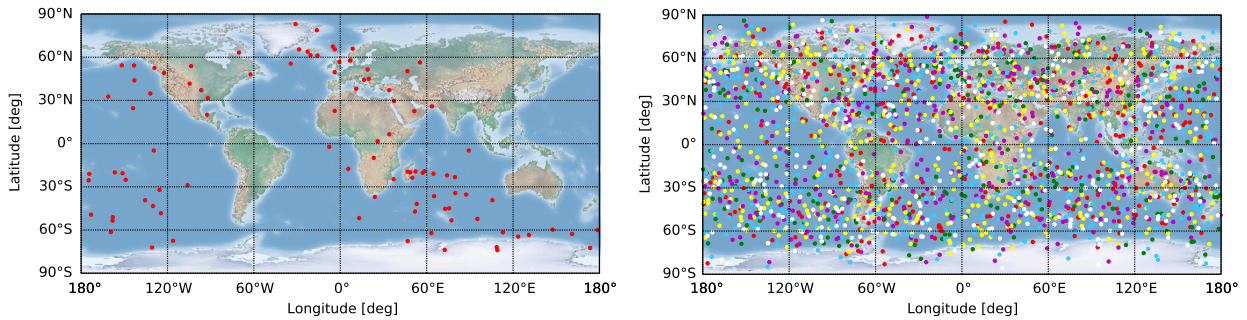


Fig. 4. Daily distribution of the electron density peaks derived from EDPs of FM-1 (left, 109 peaks) at 10 June 2006 vs. all F-3/C satellites FM-1 to FM-6 (right, 2447 peaks) at 5 June 2007.

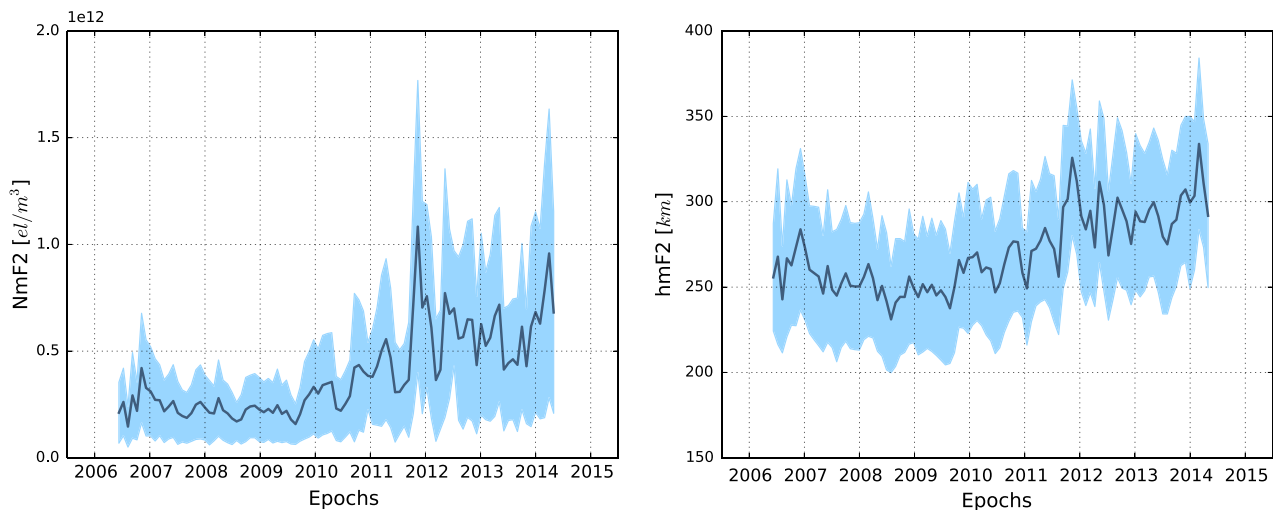


Fig. 5. Trend of the global $NmF2$ (left) and $hmF2$ (right) as derived from global averages and standard deviations of the retrieved F2 layer peak computed for the days under investigation. The data is plotted for the study period between 10 June 2006 and 29 April 2014.

4. Global trend of the F2 layer peak

The global trends of $NmF2$ and $hmF2$ have been evaluated in a first step. Therefore, all retrieved electron density profiles that passed the pre- and post screening steps as described in Section 3 are taken into account for the derivation of F2 layer electron density peaks and computation of global, daily averages. The time series of $NmF2$ and $hmF2$ are provided by Figure 5. As can be expected, an increase of the daily averages from low toward high solar activity becomes visible for both parameters, indicated by the dark blue line. Light blue bands represent the corresponding daily standard deviations, σ_{NmF2} as well as σ_{hmF2} , and characterize the variability of the parameters in the global domain. It is obvious, that σ_{NmF2} increases with the solar activity while the magnitude of σ_{hmF2} remains at a rather constant level and almost independent of the solar conditions. The effect may be interpreted as an increase of the global variations for $NmF2$ in correlation with the solar conditions while $hmF2$ likewise increases but with a consistent fluctuation magnitude.

Taking into account that the global mean may be a good representative for the solar conditions, comparisons with the daily sunspot number R and the solar radio flux parameter $F10.7$ as solar physical quantities have been performed. Both quantities are commonly accepted as indices for reflecting the solar condition, typically on a day-to-day basis, where R is determined from optical surveying and $F10.7$ is a measure of the solar radio flux per unit frequency at a wavelength of 10.7 cm. The data of R and

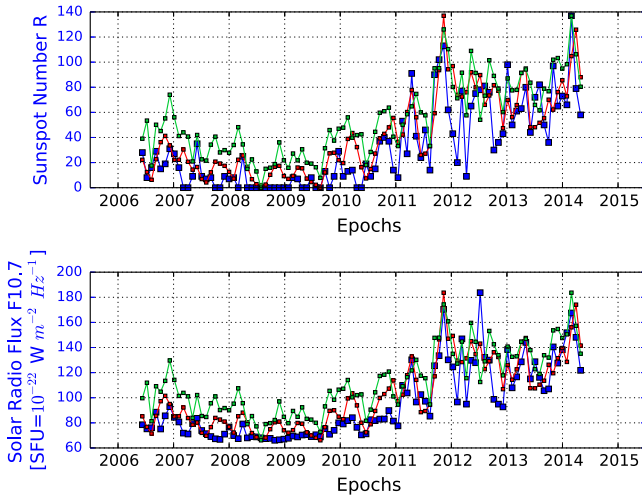


Fig. 6. Comparison of scaled daily $NmF2$ (red squares) and $hmF2$ (green squares) averages with the daily sunspot number R (top, blue squares) and daily solar flux $F10.7$ index (bottom, blue squares) during the study period (10 June 2006–29 April 2014). The unit of the y -axis units refers to the sunspot number and $F10.7$ and the $NmF2$ as well as $hmF2$ samples have been scaled.

$F10.7$ are downloaded via the NASA GSFC/SPDF OMNIWeb⁵ interface (King & Papitashvili 2005). With \mathbf{e} being a $N \times 1$ unit vector and $\mathbf{v}_{F10.7}$ as well as \mathbf{v}_{F2} being $N \times 1$ data vectors containing daily values of $F10.7$ and global averages of the $F2$ peak parameters observed by F-3/C, then the time series of $NmF2$ and $hmF2$ can be scaled by

$$\mathbf{v}_{F2, \text{scaled}} = \min(\mathbf{v}_{F10.7}) \cdot \mathbf{e} + (\mathbf{v}_{F2} - \min(\mathbf{v}_{F2}) \cdot \mathbf{e}) \cdot \frac{\max(\mathbf{v}_{F10.7}) - \min(\mathbf{v}_{F10.7})}{\max(\mathbf{v}_{F2}) - \min(\mathbf{v}_{F2})}, \quad (7)$$

to the units of $F10.7$ to enable a graphical comparison of the relative trends. This scaling procedure was accordingly carried out to scale $NmF2$ and $hmF2$ with respect to R .

The resulting time series are shown in Figure 6 where red squares represent the scaled averages of $NmF2$, green squares are the $hmF2$ samples, and the blue squares identify sunspot numbers (top) and $F10.7$ indices (bottom). According to the color of the y -axis labeling, its units thus refer to the blue squares. Figure 6 indicates that the retrieved averages, both for $NmF2$ and $hmF2$, characterize the solar conditions very well with a slightly better performance of $NmF2$ as can be expected due to its higher sensitivity with respect to solar variations. The individual correlation coefficients are provided in Table 1. A high correlation coefficient of 0.92 between $NmF2$ and $hmF2$ indicates the proportional increase of both parameters toward higher solar activity. R and $F10.7$ as established indicators for reflecting the solar conditions are as expected highly correlated with an index of 0.94. Furthermore, correlations between $NmF2$ ($hmF2$) and R as well as $F10.7$ are computed with 0.83 (0.87) and 0.89 (0.88), respectively. The equivalent calculations have been performed to obtain also correlations with $F2$ parameters observed by ionosondes of the SPIDR network (not depicted here). In this case, the correlations yield 0.83 ($NmF2$) and 0.80 ($hmF2$) as compared to $F10.7$ as well as 0.81 ($NmF2$) and 0.80 ($hmF2$) with respect to R . In this scenario, the global averages of electron density peaks derived from occultations seem to represent the purely

Table 1. Correlation coefficients between the time series of globally averaged $F2$ peak parameters derived from radio occultations, the sunspot number R , and the solar flux $F10.7$ as indicators for the solar activity.

	$NmF2_{F3C}$	$hmF2_{F3C}$	R	$F10.7$
$NmF2_{F3C}$	1.0	0.92	0.83	0.89
$hmF2_{F3C}$		1.0	0.87	0.88
R			1.0	0.94
$F10.7$				1.0

physical quantities R and $F10.7$ slightly better than the averages of those peaks observed by ionosondes. It can be assumed, that the better representation follows mainly from the improved global coverage of the occultation data. Global daily averages of RO-based $F2$ layer peaks can thus be identified as very suitable quantities to characterize the solar conditions.

5. Assessment of the global $F2$ layer peak

To assess the accuracy of the $F2$ layer peak retrieved from RO measurements, ionosonde data tracked by stations of the SPIDR network have been taken into account. The data is available via the National Geophysical Data Center (NGDC) website⁶ as a public service by the US Department of Commerce, National Oceanic and Atmospheric Administration (NOAA), National Environmental Satellite, Data and Information Service (NESDIS).

Initial investigations showed, that the ionosonde data set contained anomalous observations mostly located in critical regions with high ionospheric gradients, for instance while the EIA passes, or due to irregularities such as scintillations, sporadic E-layer or spread-F. To eliminate these outliers, additional ionosonde specific data screening steps have been implemented. Thresholds related to minimum and maximum peak heights as previously considered for the profile retrieval should of course also hold for the ionosonde measurements. Additional ionosonde-specific preprocessing algorithms reject single measurements that appear isolated with time gaps of more than 30 min difference to the previous and next observation and analyze the parameter variability for the rejection of observations that exceed a relative change of 30% ($NmF2$) and 20% ($hmF2$) within a time interval of 30 min.

After cleaning the peaks observed by the ionosondes, the vicinity of each EDP peak within $\pm 8^\circ$ and 20 min in space and time is scanned for co-located ionosonde measurements. The occultation peak together with the closest ionosonde observation is then considered as a value pair introduced into the assessment procedure. In total, 7780 ($NmF2$) and 5902 ($hmF2$) samples in co-location with ionosonde observations have been detected.

The magnitudes of $NmF2$ and $hmF2$ as determined from the EDPs are provided by daily RMS values in Figure 7. Two prominent peaks are contained in the $NmF2$ time series that may be caused by a large amount of profiles located in ionospheric active regions for the specific days. It is clearly visible how the trend is driven by the solar cycle. Total averages with variations of $4.34 \pm 2.19 \times 10^{11} \text{ el/m}^3$ and $270.27 \pm 22.18 \text{ km}$ are obtained for $NmF2$ and $hmF2$, respectively. Minimum RMS values during the solar minimum phase

⁵ <http://omniweb.gsfc.nasa.gov>

⁶ <http://spidr.ngdc.noaa.gov>

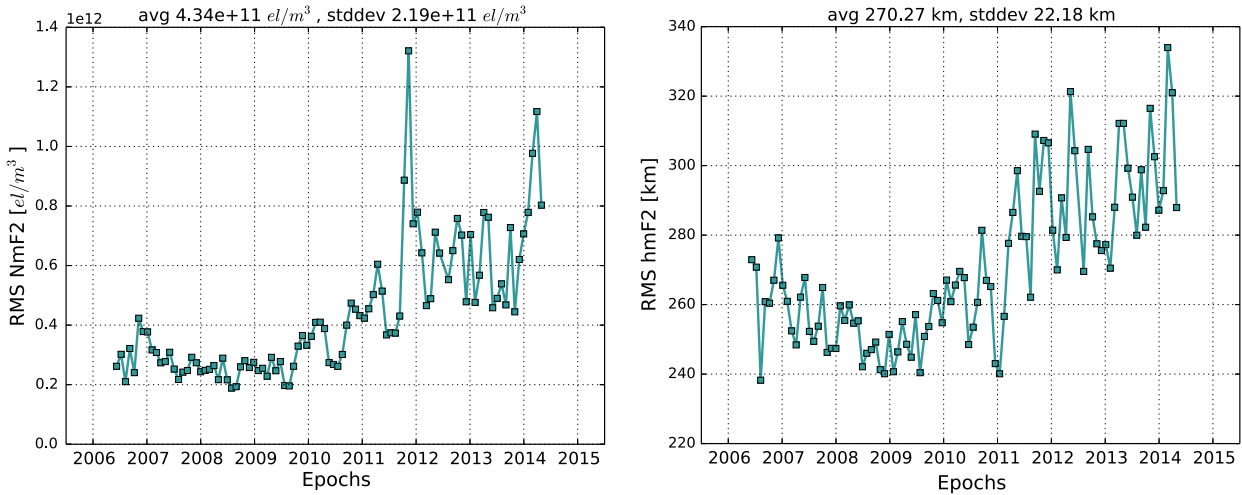


Fig. 7. Daily RMS of the retrieved peak density $NmF2$ (left) and corresponding height $hmF2$ (right) derived from radio occultations between 10 June 2006 and 29 April 2014.

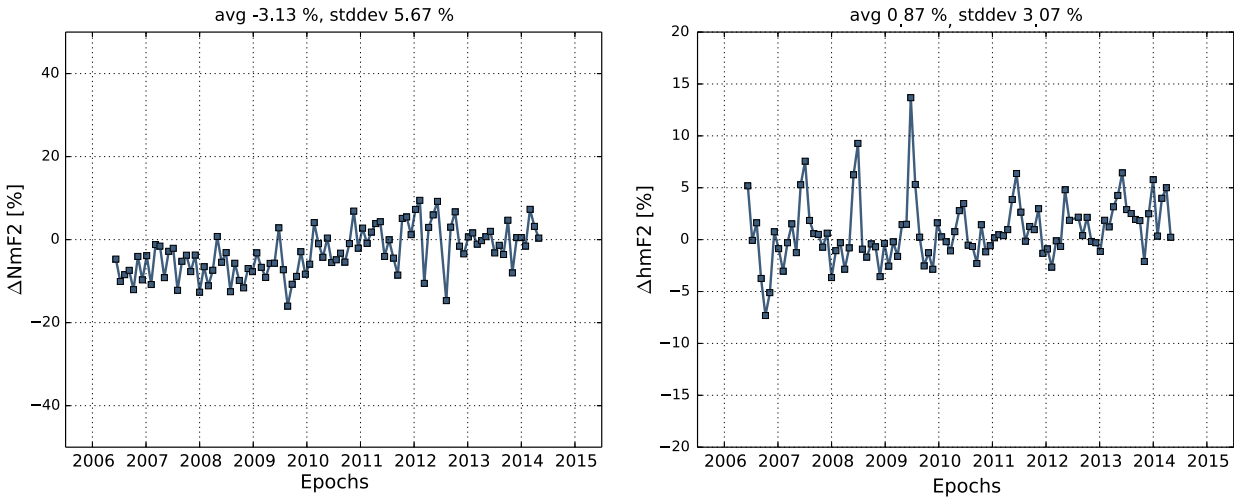


Fig. 8. Daily averaged relative differences between global $NmF2$ (left) and $hmF2$ (right) observations as measured by ionosondes and F-3/C radio occultations between 10 June 2006 and 29 April 2014.

(\approx between 2006 and 2010) are determined with around 2×10^{11} el/m^3 and 240 km. The maximum RMS values are analogously observed during the current solar maximum with up to 8×10^{11} el/m^3 for $NmF2$ under negligence of the peaks and 330 km for $hmF2$.

Relative differences to the nearby ionosonde measurements have been determined as

$$\Delta NmF2_{\%} = \frac{NmF2_{F3C} - NmF2_{IS}}{NmF2_{IS}} \times 100\% \quad (8)$$

and accordingly for $\Delta hmF2_{\%}$ where subscripts IS and F3C indicate the affiliation of the measurement to the ionosonde or RO and the subscript % identifies the relative differences given in percentage units. The results are depicted in Figure 8 for $\Delta NmF2_{\%}$ (left) and $\Delta hmF2_{\%}$ (right). Total averages with standard deviations of $\text{avg}(\Delta NmF2_{\%}) = -3.13 \pm 5.67\%$ and $\text{avg}(\Delta hmF2_{\%}) = 0.87 \pm 3.07\%$ indicate no significance for systematic biases. Few abnormal peaks are contained in the series of $\Delta hmF2_{\%}$ reaching 5%–14% which can be assigned to the middle of the years 2006–2009, i.e., during low

activity. The largest differences for these days are originating from significantly lower ionosonde $hmF2$ observations and clearly higher EDP peaks. Further investigation is required to locate the source of these discrepancies.

The trend of both series $\Delta NmF2_{\%}$ and $\Delta hmF2_{\%}$ features a slight increase correlated with the solar conditions over the years. The variations of $\Delta NmF2_{\%}$ and $\Delta hmF2_{\%}$ oscillate roughly in the range of 10% and 5%, respectively, under negligence of outliers. Compared to $\Delta hmF2_{\%}$, an increased variability is obtained for $\Delta NmF2_{\%}$.

In summary, the global evaluation showed a high agreement of the $NmF2$ and $hmF2$ trend with the sunspot number R and the F10.7 index. A rough approximate of the overall global accuracy of the F2 layer peak derived from RO measurements can be estimated from the global RMS together with the uncertainty computed from the relative differences to ionosondes. For $NmF2$, a standard deviation of around 5% together with a RMS varying with the solar activity between 2×10^{11} el/m^3 and 8×10^{11} el/m^3 yields an uncertainty of the retrieved peak density in the range of 1×10^{10} el/m^3 and

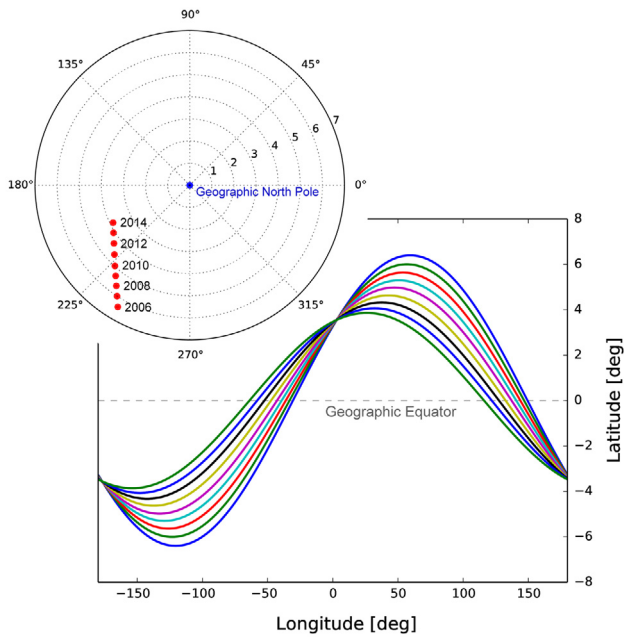


Fig. 9. Variation of the magnetic equator in geographic coordinates during 2006 (outermost blue curve) and 2014 (innermost green curve).

$4 \times 10^{10} \text{ el/m}^3$. Accordingly, the uncertainty of $hmF2$ with 3% and RMS between 240 km and 320 km leads to an approximation of the absolute difference in the range of 7 km and 10 km.

6. Peak evaluation under consideration of magnetic latitude and local time

With the outcomes of the Sections 4 and 5, initial estimates for the overall accuracy of $NmF2$ and $hmF2$ have been determined. In order to assess the accuracies under exclusion of strongly varying ionospheric conditions, different magnetic latitude sectors and local time intervals have been selected to account for daily ionospheric variations as well as the orientation of the structure (in particular the EIA) along the magnetic equator.

The time interval around the daily peak at 14:00 LT \pm 2 h has been selected to study the quality of the retrieval around the ionospheric day maximum and shifted by 12 h at 02:00 LT \pm 2 h to consider quiet conditions at night. Additionally, a timespan of moderate conditions at dawn between 8:00 LT \pm 2 h was investigated. Different magnetic latitude sectors $\Delta\varphi$ have been defined as $\Delta\varphi_{\text{EQU}} = \pm[0^\circ, 20^\circ]$, $\Delta\varphi_{\text{MID}} = \pm[20^\circ, 60^\circ]$, and $\Delta\varphi_{\text{POL}} = \pm[60^\circ, 90^\circ]$ to account for equatorial, mid-latitude, and polar regions. Due to the rather symmetric formation of the EIA along both sides of the magnetic equator, the latitude bands are defined with equal boundaries for the northern and southern hemisphere. The magnetic equator has been computed from yearly dependent North Pole coordinates as published by NOAA⁷ with annual Pole coordinates derived from the 10th generation of the International Geomagnetic Reference Field (IGRF). The variation of the magnetic equator in geographic coordinates as a consequence of the annual magnetic North Pole movement is depicted in Figure 9. The magnetic North Pole converged slowly from 2006 to 2014

toward the geographic Pole as can be seen from the polar plot in the top-left corner. The Pole latitudes vary approximately between $\varphi_{\text{NP}} = 83.5^\circ$ in 2006 and $\varphi_{\text{NP}} = 86^\circ$ in 2014. Consequently, the innermost and outermost curves of the main plot belong to 2014 and 2006, respectively. The magnetic equator varies within 2.5° latitude and exhibits a difference of up to 6.5° in 2006 with respect to the geographic equator that is depicted as a gray, dashed line.

Absolute differences $\Delta NmF2 = NmF2_{\text{F3C}} - NmF2_{\text{IS}}$ and $\Delta hmF2 = hmF2_{\text{F3C}} - hmF2_{\text{IS}}$ of both F2 peak parameters have been computed for each time interval and magnetic latitude sector. Exemplarily, the results of the daytime comparison in the interval 14:00 LT \pm 2 h are depicted in Figure 10 ($NmF2$) and Figure 11 ($hmF2$). Three plots on the right column include the data distribution with red circles for the peaks retrieved from F-3/C occultations and blue triangles as co-located ionosondes for the three magnetic latitude regions. It should be noticed that all electron density profiles within a specific latitude band are detected first and afterwards the search algorithm screens for co-located ionosondes. Thus, the ionosonde location must not mandatory lie within the same latitude band but may be located slightly outside of the bounds. The data has been collected and plotted for all days under investigation and therefore each ionosonde that contributes data at least once during the study time frame is contained in the plot. Furthermore, the magnetic latitude bands computed from the North Pole coordinates of the latest year 2014 are exemplary depicted. The parameter differences for each latitude interval are provided in the left columns of Figures 10 and 11. For each interval, the absolute averaged difference and standard deviation have been computed and included in the legends above the plots.

The increased presence of ionosondes in mid-latitudes in populated and urbanized regions is clearly visible from the figures. Consequently, the number of value pairs varies strongly with a majority in the mid-latitudes. For $\Delta NmF2$, averages and standard deviations of $1.22 \pm 1.91 \times 10^{11} \text{ el/m}^3$ in the equatorial region, $0.10 \pm 1.43 \times 10^{11} \text{ el/m}^3$ for the mid-latitude band and $-0.27 \pm 1.16 \times 10^{11} \text{ el/m}^3$ for the polar region, are determined. Since the differences are obtained during the daily ionospheric maximum, the standard deviation increase from the polar toward the equatorial band (or quiet toward active regions, respectively) can be related to the signal strength.

Accordingly, the averages and standard deviations of $\Delta hmF2$ are determined with $7.50 \pm 30.01 \text{ km}$ in the equatorial region, $5.43 \pm 23.81 \text{ km}$ for the mid-latitudes and $7.45 \pm 29.91 \text{ km}$ for the polar caps. Maximum differences of approximately 100 km for only few comparisons appear. All three plots related to $\Delta hmF2$ exhibit a positively biased mean, i.e., a possible overdetermination of the F2 layer peak height by the occultations. However, the significance of a systematic offset cannot be concluded as the variations of $\Delta hmF2$ in the range of 24 km–30 km are fairly high.

Furthermore, the correlations of the absolute measurements for $NmF2$ and $hmF2$ referring to the daytime interval during 14:00 \pm 2 h (according to the Figures 10 and 11) are depicted in Figure 12 for all detected pairs of F2 layer peaks. Those parameters derived from F-3/C are given along the x-axis and the associated ionosonde values refer to the y-axis. $NmF2$ is depicted in the left column and $hmF2$ on the right. Similar to the previous figures, the top subplots represent the equatorial band, the center plots refer to the mid-latitudes,

⁷ <http://www.ngdc.noaa.gov/geomag/data/poles>

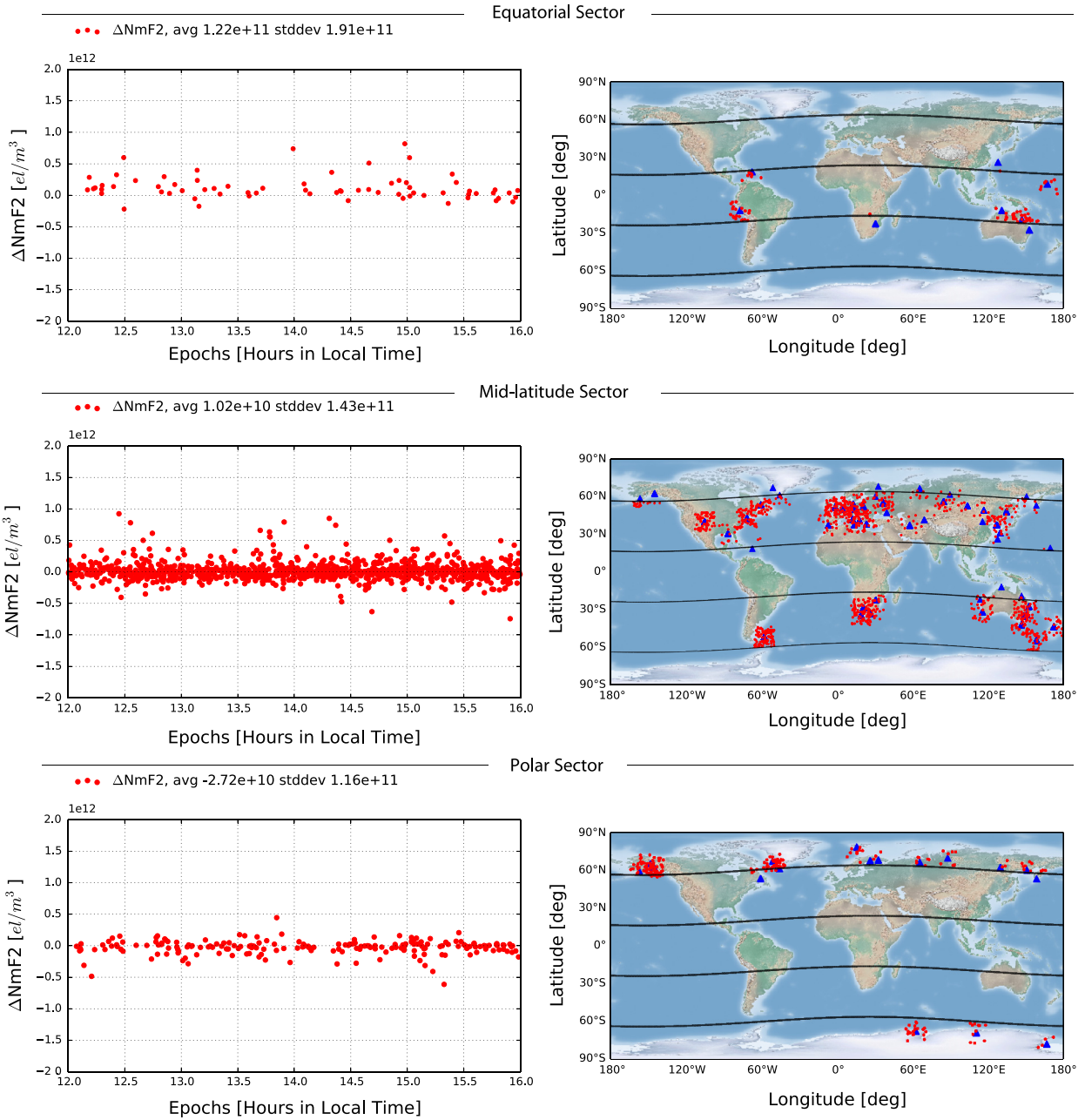


Fig. 10. Left column: Differences $\Delta NmF2$ between ionosonde observations and F2 layer peaks retrieved from F-3/C occultations collected during the days under investigation between 10 June 2006 and 29 April 2014 within 12:00 and 16:00 LT and magnetic latitude sectors $\Delta\phi_{\text{EQU}} = \pm[0^\circ, 20^\circ]$ (top), $\Delta\phi_{\text{MID}} = \pm[20^\circ, 60^\circ]$ (center) and $\Delta\phi_{\text{POL}} = \pm[60^\circ, 90^\circ]$ (bottom). Right column: Retrieved $NmF2$ positions (red circles) and co-located ionosondes (blue triangles) within the defined magnetic latitude bands. The latitude intervals are exemplary depicted here under consideration of the magnetic North Pole from 2014.

and the bottom plots show the results obtained for the polar areas. x - and y -axes of each plot are restricted to the same limits with edges connected by a black line indicating a 100% correlation.

Very good agreements have been obtained for $NmF2$ with correlation coefficients of 0.94 and 0.92 for the equatorial belt and mid-latitudes, respectively. A slightly weaker correlation coefficient of 0.84 was found at the polar caps. In the case of $hmF2$, the correlations are generally weaker compared to $NmF2$ but nevertheless reach 0.76 along the Equator and 0.75 in mid-latitudes. A moderate correlation of only 0.56 is obtained for the polar area. Results for the time periods at

dawn and night are not shown here, but included in the Tables 2 and 3, summarizing the outcomes of Section 6.

Absolute and relative averaged differences and standard deviations of $NmF2$ and $hmF2$ for all local time intervals and magnetic latitude sectors as well as correlation coefficients between ionosonde and EDP peaks are compared. Additionally, the number of samples (#) considered in the evaluation is provided.

For $\Delta NmF2$, mean differences in the magnitude of $-0.2 \times 10^{11} \text{ el}/\text{m}^3$ to $1.2 \times 10^{11} \text{ el}/\text{m}^3$ have been obtained together with standard deviations between $0.6 \times 10^{11} \text{ el}/\text{m}^3$ and $1.9 \times 10^{11} \text{ el}/\text{m}^3$. It can be noticed for the night interval,

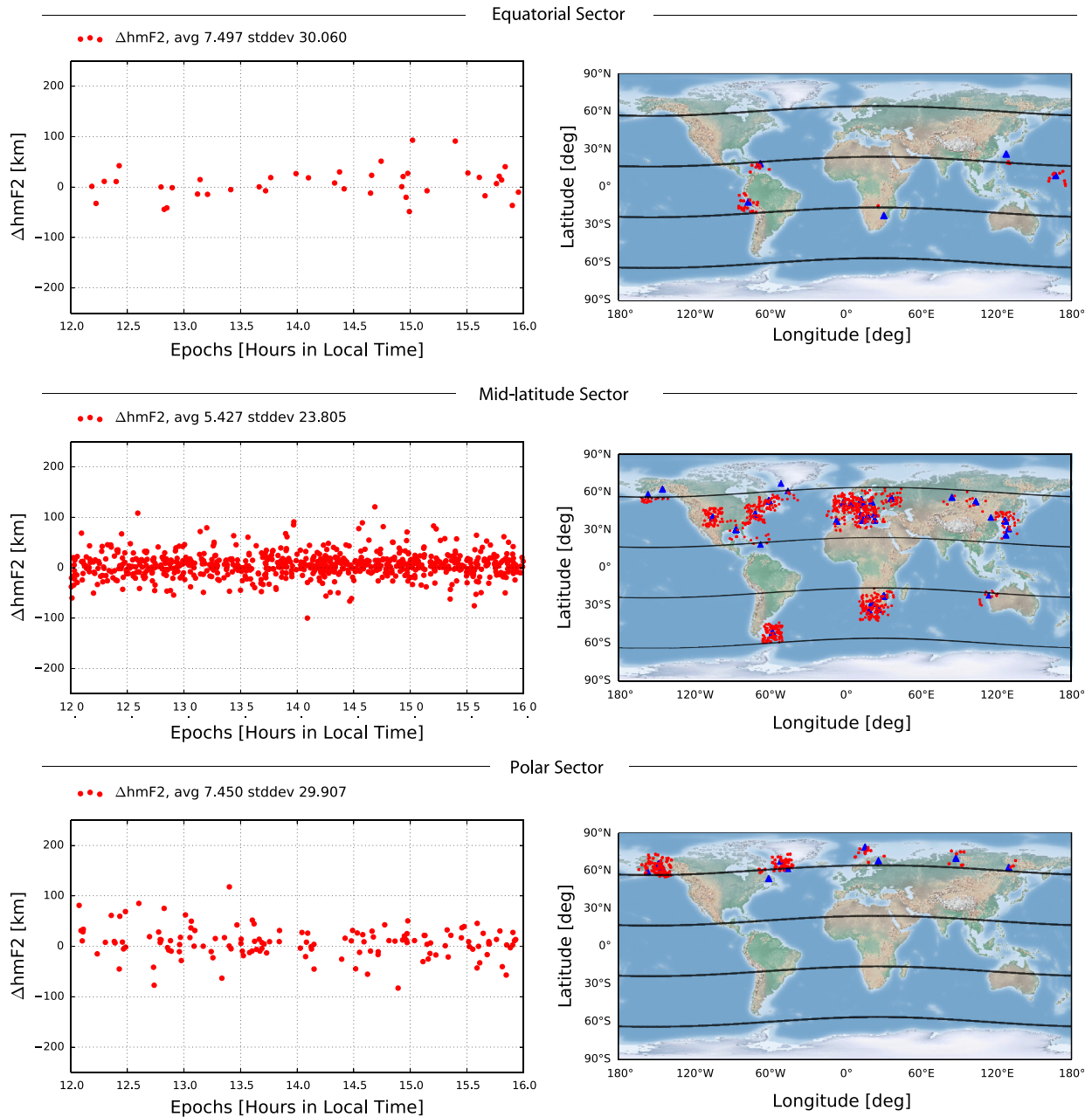


Fig. 11. Left column: Differences $\Delta hmF2$ between ionosonde observations and F2 layer peaks retrieved from F-3/C occultations. The data have been collected during the days under investigation between 10 June 2006 and 29 April 2014 within 12:00 and 16:00 LT and magnetic latitude sectors $\Delta\phi_{EQU} = \pm[0^\circ, 20^\circ]$ (top), $\Delta\phi_{MID} = \pm]20^\circ, 60^\circ]$ (center) and $\Delta\phi_{POL} = \pm]60^\circ, 90^\circ]$ (bottom). Right column: Retrieved $hmF2$ positions (red circles) and co-located ionosondes (blue triangles) within the defined magnetic latitude bands. The latitude intervals are exemplary depicted here under consideration of the magnetic North Pole from 2014.

that the $NmF2$ measurements by ionosondes are consistently lower compared to the F-3/C observations. The strongest variation can be found at the equator for all three time intervals where relative differences of 15%, 2.89%, and -6.95% are found during daytime, dawn, and night. The uncertainties in the range of 22%–29% are determined during day and dawn and 30%–35% at night.

High $NmF2$ correlations are found for all times and latitudes with marginally reduced conformity at the Poles and generally during night. In the equatorial and mid-latitude bands at day and dawn the correlations even reach values larger than 0.9. The strong correlation between ionosondes with $NmF2$ supports the outcome of [Lei et al. \(2007\)](#) where 276 co-located

value pairs between 31 globally distributed ionosondes and F-3/C measurement are analyzed and a correlation coefficient of 0.85 was found. Furthermore, a relative accuracy level of around 20% for $NmF2$ was determined by [Hajj & Romans \(1998\)](#), [Tsai et al. \(2001\)](#), and [Wu et al. \(2009\)](#). The slightly worse accuracy level resulting from this study is probably caused by the use of automatically detected ionogram peaks contained in the SPIDR database. [Schreiner et al. \(1999\)](#) compared GPS/MET $NmF2$ with ionosondes and determined variations at the magnitude of 26%, i.e., similar to the results obtained here. [Schreiner et al. \(1999\)](#) additionally found an insignificant bias of few percentages which was later confirmed by [Wu et al. \(2009\)](#) and various other authors.

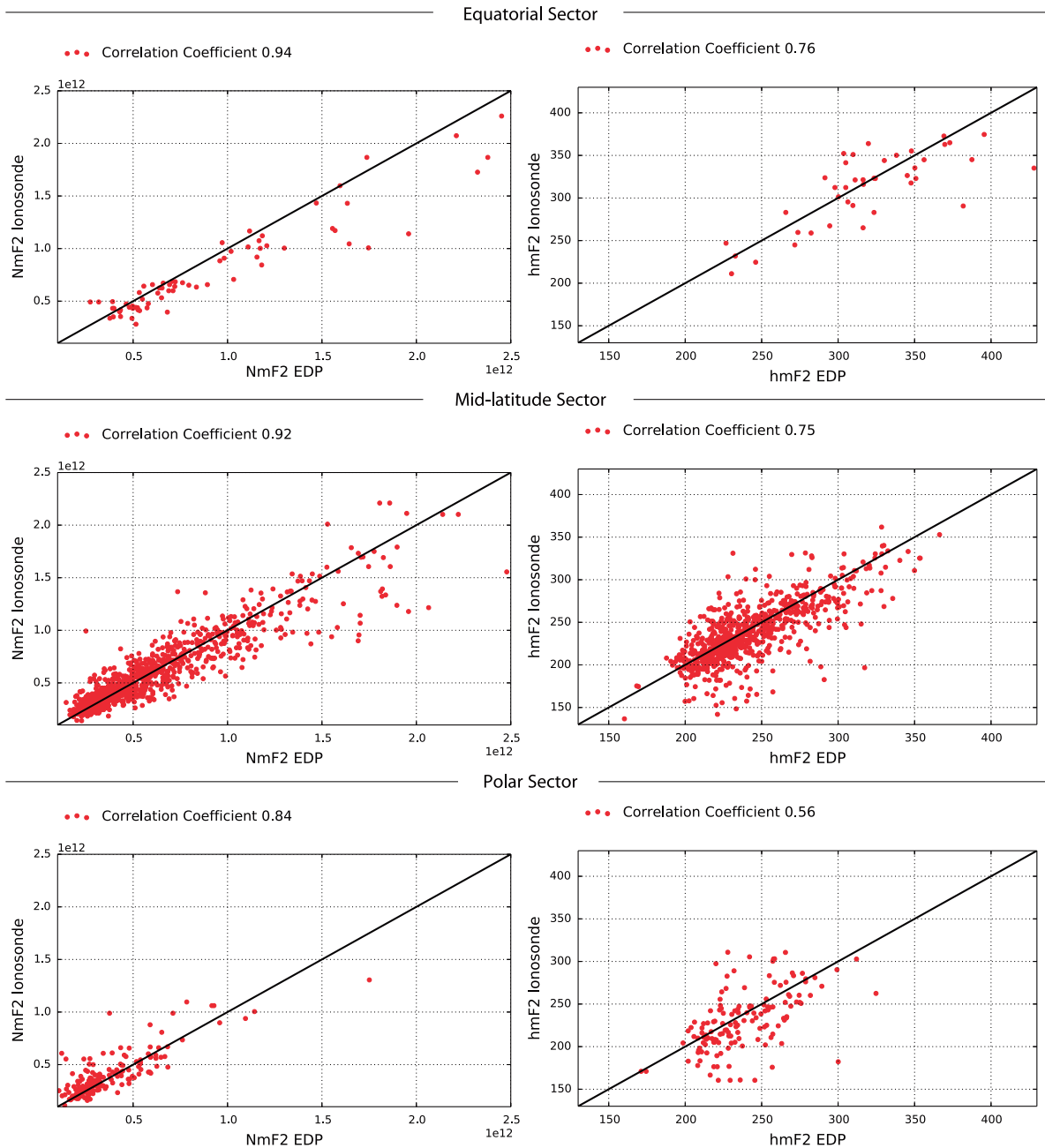


Fig. 12. Correlations between F2 layer peaks derived from F-3/C (x-axis) and ionosonde observations (y-axis) for $NmF2$ (left column) and $hmF2$ (right column). According to Figures 10 and 11, the subplots from top to bottom refer to the equatorial, mid-latitude, and polar regions.

In the case of $hmF2$, mean differences in the range of -7 km and 7.5 km with an outlier of -22 km at the Pole during night are determined. Standard deviations of the order of 24 km– 30 km discard the existence of systematic biases. Again, an outlier of 48 km standard deviation is calculated at the Pole during night. Significant differences of the variations with respect to the analyzed time intervals or latitude bands cannot be observed. Furthermore, maximum relative averages between -6% and 5% with relative standard deviations in the range of 10% – 16% are determined for $\Delta hmF2$. It can be noticed, that the largest variations are determined within the Polar Sector. Moderate correlations of around 0.7 have been found at the Equator and mid-latitudes during daytime and dawn with weaker correlations of 0.5 at the Poles. The reliability is clearly reduced during night where

correlations of 0.6 are obtained for the equatorial and mid-latitude sectors and 0.5 for the Poles.

7. Summary

The use of RO measurements and derived electron density profiles for describing the ionospheric electron density distribution helps to gain a global data distribution and to access information about the vertical N_e structure. The Formosat-3/COSMIC mission collects occultation measurements since 2006 and has been exploited for establishing a database of occultation data between 10 June 2006 and 29 April 2014 using a sampling of 30 days. This data set is compared to ionosonde measurements provided by the global SPIDR network to obtain

Table 2. Summary of the comparison between ionosonde and RO based $NmF2$ for time intervals and magnetic latitude sectors.

LT	$\Delta\varphi$	$NmF2$					
		avg (Δ) (10^{11} el/m ³)	$\sigma(\Delta)$ (10^{11} el/m ³)	avg ($\Delta\%$)	$\sigma(\Delta\%)$	Corr. coeff.	#
14:00 \pm 2	Equ	1.22	1.91	15.18	22.78	0.94	70
	Mid	0.10	1.43	2.31	22.31	0.92	1015
	Pol	-0.27	1.16	-4.11	26.08	0.84	196
08:00 \pm 2	Equ	0.07	1.39	2.89	26.04	0.92	121
	Mid	-0.07	0.95	-0.95	23.08	0.93	997
	Pol	-0.16	0.80	-4.68	29.25	0.77	140
02:00 \pm 2	Equ	-0.23	1.16	-6.95	35.30	0.85	121
	Mid	-0.18	0.88	-7.56	31.49	0.83	1062
	Pol	-0.15	0.55	-6.33	35.51	0.83	105

Table 3. Summary of the comparison between ionosonde and RO-based $hmF2$ for time intervals and magnetic latitude sectors.

LT	$\Delta\varphi$	$hmF2$					
		avg (Δ) (km)	$\sigma(\Delta)$ (km)	avg ($\Delta\%$)	$\sigma(\Delta\%)$	Corr. Coeff.	#
14:00 \pm 2	Equ	7.50	30.06	2.84	9.69	0.76	41
	Mid	5.43	23.81	3.11	11.09	0.75	751
	Pol	7.45	29.91	4.74	14.17	0.56	141
08:00 \pm 2	Equ	-7.13	29.67	-1.72	10.53	0.76	89
	Mid	-2.52	26.69	-0.16	11.08	0.67	791
	Pol	2.58	35.82	0.81	16.58	0.49	100
02:00 \pm 2	Equ	2.08	34.62	1.50	12.23	0.64	67
	Mid	0.93	29.17	0.23	9.83	0.64	824
	Pol	-21.92	47.69	-6.28	15.23	0.47	77

information about the reliability of retrieved F2 peak parameters during changing solar conditions.

In a first step, the global trend of $NmF2$ and $hmF2$ has been expressed by daily averages and compared with sunspot numbers and solar flux F10.7 indices where high correlations between 0.83 and 0.89 have been found for both parameters. Afterwards, a database of globally distributed value pairs including EDP peaks and co-located ionosonde observations has been established to determine an overall accuracy level. For this purpose, RMS values of the retrieved peak together with relative differences between ionosonde and EDP peaks have been computed. As a preliminary assessment, the overall accuracy level was determined in the range of 1×10^{11} el/m³ and 4×10^{11} el/m³ for $NmF2$ and 7 km–10 km for $hmF2$.

A more detailed assessment was provided in Section 6 where the data was separated by different latitude sectors and local time intervals. The results are summarized in the Tables 2 and 3 for $NmF2$ and $hmF2$. High correlations between ionosonde and EDP data have been found for $NmF2$. A significant systematic bias was not observed. The corresponding relative variations are determined in the range 22%–35% depending on the latitude sector and time interval. Particularly high correlations above 0.9 are found at the Equator and mid-latitudes during day and dawn. A marginally weaker agreement is observed for measurements at the Poles and generally during night.

As for $NmF2$, the absence of systematic biases can be also concluded for $hmF2$. Standard variations are found in the range of 24 km and 30 km as well as 10% and 16% referring to absolute and relative units, respectively. Good correlations of 0.7 have been obtained during day and dawn for the equatorial and mid-latitude regions. However, the correlations at the Poles and during night are significantly reduced.

The accuracies obtained in this work show quiet a good agreement with other publications that concentrated on the assessment by only few selected ionosonde stations. Generally high correlations between the F2 layer electron density peaks as derived from F-3/C occultations and ionosonde measurements have been obtained in this study. However, an extensive pre-processing and data screening was necessary for both the RO and ionosonde data to eliminate disturbances in the data and improve the data reliability. Many authors like Krankowski et al. (2011), Hu et al. (2014), Wu et al. (2009), Yue et al. (2010), and Lei et al. (2007) evaluated the accuracy of electron density peaks, retrieved from F-3/C data, either on a regional scale by means of selected ionosonde stations allowing for a manual ionogram scaling or even used synthetic data to validate the accuracy under different conditions, e.g., under the influence of varying F10.7 indices. In this work, SPIDR network data based on automatically scaled measurements are taken into account. Such observations enable the global long-term assessment but hold the potential risk of a reduced data quality. The processing algorithms of most modern ionosondes are based on the ARTIST-5 software (Galkin et al. 2008; Reinisch et al. 2009) that provide quality flags and uncertainty boundaries. Such quality indicators were not contained in the SPIDR data used here but could be of high relevance for further studies to verify the reliability of ionosondes in such validations.

In this paper, the accuracy of $NmF2$ and $hmF2$ derived from F-3/C occultations has been assessed from a global long-term study. Based on an improved retrieval technique, the potential of radio occultations for ionospheric sounding has been demonstrated. Depending on the number of LEO satellites and the geometrical constellation, a main advantage of the RO technique compared to ionosonde measurements can

be found in the global availability, in particular by providing data over the oceans. The outstanding role of occultations for multi-dimensional ionosphere modeling will be additionally strengthened with the launch of the F-3/C follow-on mission Formosat-7/COSMIC-2 scheduled for 2016.

Acknowledgements. The authors would like to thank the following services and institutions for providing the input data for this study: CDAAC and TACC (Formosat-3/COSMIC observations and orbits), IGS and CODE (GPS orbits and IONEX data) as well as NOAA/NESDIS (SPIDR ionosonde measurements and magnetic North Pole coordinates). Special thanks go to the IonSAT research group (UPC, Barcelona, Spain) for their support of any kind. Moreover, we are grateful to the editor and the reviewers for their constructive feedback and suggestions to improve the paper.

The editor thanks Ljiljana R. Cander and an anonymous referee for their assistance in evaluating this paper.

This work was supported by the German Research Foundation (DFG) and the Technische Universität München within the funding programme Open Access Publishing.

References

- Aragon-Angel, A. Contributions to ionospheric electron density retrieval. *Ph.D. Thesis*, Research Group of Astronomy and Geomatics (gAGE), Technical University of Catalonia (UPC), 53–63, 2010.
- Aragon-Angel, A., Y.-A. Liou, C.-C. Lee, B.W. Reinisch, M. Hernández-Pajares, M. Juan, and J. Sanz. Improvement of retrieved Formosat-3/COSMIC electron densities validated by ionospheric sounder measurements at Jicamarca. *Radio Science*, **46**, RS5001, 2011, DOI: [10.1029/2010RS004578](https://doi.org/10.1029/2010RS004578).
- Dow, J.M., R.E. Neilan, and C. Rizos. The International GNSS Service in a changing landscape of Global Navigation Satellite Systems. *J. Geodesy*, **83**, 191–198, 2009, DOI: [10.1007/s00190-008-0300-3](https://doi.org/10.1007/s00190-008-0300-3).
- Galkin, I.A., G.M. Khmyrov, A.V. Kozlov, B.W. Reinisch, X. Huang, and V.V. Paznukhov. The ARTIST 5. *Radio Sounding and Plasma Physics, AIP Conf. Proc.*, **974**, 150–159, 2008, DOI: [10.1063/1.2885024](https://doi.org/10.1063/1.2885024).
- García-Fernández, M., M. Hernández-Pajares, M. Juan, and J. Sanz. Improvement of ionospheric electron density estimation with GPSMET occultations using Abel inversion and VTEC information. *J. Geophys. Res.*, **108**, A9, 2003, DOI: [10.1029/2003JA009952](https://doi.org/10.1029/2003JA009952).
- Hajj, G.A., and J. Romans. Ionospheric electron density profiles obtained with the Global Positioning System: results from the GPS/MET experiment. *Radio Sci.*, **33**, 175–190, 1998, DOI: [10.1029/97RS03183](https://doi.org/10.1029/97RS03183).
- Hernández-Pajares, M., J.M. Juan, and J. Sanz. Improving the Abel inversion by adding ground data LEO radio occultations in the ionospheric sounding. *Geophys. Res. Lett.*, **27**, 2743–2746, 2000, DOI: [10.1029/2000GL000032](https://doi.org/10.1029/2000GL000032).
- Hernández-Pajares, M., J.M. Juan, J. Sanz, R. Orus, A. García-Rigo, J. Feltens, A. Komjathy, S.C. Schaer, and A. Krankowski. The IGS VTEC maps: a reliable source of ionospheric information since 1998. *J. Geod.*, **83**, 263–275, 2009, DOI: [10.1007/s00190-008-0266-1](https://doi.org/10.1007/s00190-008-0266-1).
- Hu, L., B. Ning, L. Liu, B. Zhao, G. Li, et al. Validation of COSMIC ionospheric peak parameters by the measurements of an ionosonde chain in China. *Ann. Geophys.*, **32**, 1311–1319, 2014, DOI: [10.5194/angeo-32-1311-2014](https://doi.org/10.5194/angeo-32-1311-2014).
- Krankowski, A., I. Zakharenkova, A. Krypiak-Gregorczyk, I.I. Shagimuratov, and P. Wielgosz. Ionospheric electron density observed by FORMOSAT-3/COSMIC over the European region and validated by ionosonde data. *J. Geod.*, **85** (12), 949–964, 2011, DOI: [10.1007/s00190-011-0481-z](https://doi.org/10.1007/s00190-011-0481-z).
- King, J.H., and N.E. Papitashvili. Solar wind spatial scales in and comparisons of hourly Wind and ACE plasma and magnetic field data. *J. Geophys. Res.*, **110** (A2), A02209, 2005, DOI: [10.1029/2004JA010804](https://doi.org/10.1029/2004JA010804).
- Lei, J., S. Syndergaard, A.G. Burns, S.C. Solomon, W. Wang, et al. Comparison of COSMIC ionospheric measurements with ground-based observations and model predictions: Preliminary results. *J. Geophys. Res.*, **112** (A7), A07308, 2007, DOI: [10.1029/2006JA012240](https://doi.org/10.1029/2006JA012240).
- Reinisch, B.W., I.A. Galkin, G.M. Khmyrov, A.V. Kozlov, K. Bibl, et al. New Digisonde for research and monitoring applications. *Radio Sci.*, **44**, RS0A24, 2009, DOI: [10.1029/2008RS004115](https://doi.org/10.1029/2008RS004115).
- Schreiner, W.S., S.V. Sokolovskiy, C. Rocken, and D.C. Hunt. Analysis and validation of GPS/MET radio occultation data in the ionosphere. *Radio Sci.*, **34** (4), 949–966, 1999, DOI: [10.1029/1999RS900034](https://doi.org/10.1029/1999RS900034).
- Schreiner, W.S., C. Rocken, S. Syndergaard, and D. Hunt. Estimates of the precision of GPS radio occultations from the COSMIC/Formosat-3 mission. *Geophys. Res. Lett.*, **34**, L04808, 2007, DOI: [10.1029/2006GL027557](https://doi.org/10.1029/2006GL027557).
- Tsai, L.-C., W.-H. Tsai, W.S. Schreiner, F.T. Berkey, and J.Y. Liu. Comparisons of GPS/MET retrieved ionospheric electron density and ground based ionosonde data. *Earth Planets Space*, **53**, 193–205, 2001.
- Tsai, L.-C., and W.-H. Tsai. Improvement of GPS/MET ionospheric profiling and validation using the Chung-Li ionosonde measurements and the IRI model. *Terrestrial Atmospheric and Oceanic Sciences (TAO)*, **15**, 589–607, 2004, DOI: [10.3319/TAO.2007.12.19.01\(F-3/C\)](https://doi.org/10.3319/TAO.2007.12.19.01(F-3/C)).
- Tsai, L.-C., C.H. Liu, and T.Y. Hsiao. Profiling of ionospheric electron density based on Formosat-3/COSMIC data: results from the intense observation period experiment. *Terrestrial Atmospheric and Oceanic Sciences (TAO)*, **20**, 181–191, 2009.
- Ware, R., M. Exner, D. Feng, M. Gorbunov, K. Hardy, et al. GPS sounding of the atmosphere from low Earth orbit: preliminary results. *Bull. Am. Meteorol. Soc.*, **77**, 19–40, 1996, DOI: [10.1175/1520-0477\(1996\)077<0019:GSOTAF>2.0.CO;2](https://doi.org/10.1175/1520-0477(1996)077<0019:GSOTAF>2.0.CO;2).
- Wu, X., X. Hu, X. Gong, X. Zhang, and X. Wang. Analysis of inversion errors of ionospheric radio occultation. *GPS Solut.*, **13** (3), 231–239, 2009, DOI: [10.1007/s10291-008-0116-x](https://doi.org/10.1007/s10291-008-0116-x).
- Yue, X., W.S. Schreiner, J. Lei, S.V. Sokolovskiy, D.C. Hunt, and Y.-H. Kuo. Error analysis of Abel retrieved electron density profiles from radio occultation measurements. *Ann. Geophys.*, **28**, 217–222, 2010, DOI: [10.5194/angeo-28-217-2010](https://doi.org/10.5194/angeo-28-217-2010).
- Yue, X., W.S. Schreiner, and Y.-H. Kuo. Evaluating the effect of the global ionospheric map on aiding retrieval of radio occultation electron density profiles. *GPS Solut.*, **17**, 327–335, 2012, DOI: [10.1007/s10291-012-0281-9](https://doi.org/10.1007/s10291-012-0281-9).

Cite this article as: Limberger M, Hernández-Pajares M, Aragón-Ángel A, Altadill D & Dettmering D. Long-term comparison of the ionospheric F2 layer electron density peak derived from ionosonde data and Formosat-3/COSMIC occultations. *J. Space Weather Space Clim.*, **5**, A21, 2015, DOI: [10.1051/swsc/2015023](https://doi.org/10.1051/swsc/2015023).

7.4 P-IV

Dettmering, D., Limberger, M., and Schmidt, M. (2014): Using DORIS measurements for modeling the Vertical Total Electron Content of the Earth's ionosphere. *Journal of Geodesy*, 88(12), 1131-1143, DOI 10.1007/s00190-014-0748-2.

Copyright

This work is published in *Journal of Geodesy* and available at link.springer.com.

Summary

DORIS is an excellent technique to support GNSS data in ionosphere modeling due to a rather homogeneous site distribution. P-IV contains first results of processing synchronous DORIS dual-frequency phase measurements for global TEC modeling. The TEC parametrization is based on B-spline base functions. Because of the high noise on the modulated code, the carrier phase biases have been canceled by external data where IGS VTEC has been taken into account as a reference here to adjust the observations. Jason-2, Saral, Cryosat-2 and Hy-2a data have been processed and included into a global model to assess the performance against the corresponding GPS solution. A study period of 62 days (Day Of Year (DOY) 258 - 319 in 2013) has been chosen where in particular DOY 258 has been analyzed.

The results show a good consistency of 2-3 TECU RMS with respect to the GPS solution. Additionally, model improvements are achieved by the combination of GPS with DORIS which has been confirmed by an evaluation with Jason-2 VTEC measurements.

Declaration of own contribution

The preprocessing steps including (a) the download and import of phase measurements from RINEX-3 files, (b) the download and import of satellite orbits from SP3, (c) identification of beacon coordinates and finally (c) the extraction of TEC information by means of the geometry-free linear combination has been performed by M. Limberger. Writing the manuscript paragraph about the signal preprocessing was supported by M. Limberger.

The overall own contribution is estimated at 10 %.

Table 7.4: Apportionment of own contributions for P-IV.

Criteria	Estimated own contribution
Paper concept	0 %
Computations and software development	20 %
Data analysis and interpretation of results	20 %
Design and creation of figures	0 %
Manuscript structure and writing	10 %

Confirmation by the first author

I hereby confirm the correctness of the declaration of own contribution for the publication

Dettmering, D., Limberger, M., and Schmidt, M. (2014): Using DORIS measurements for modeling the Vertical Total Electron Content of the Earth's ionosphere. Journal of Geodesy, 88(12), 1131-1143, DOI: 10.1007/s00190-014-0748-2.

Dr. Denise Dettmering

Deutsches Geodätisches Forschungsinstitut der
Technischen Universität München (DGFI-TUM),
München, Germany

Signature: *D. Dettj*

Date: *20.05.2015*

7.5 P-V

Liang, W., Limberger, M., Schmidt, M., Dettmering, D., and Hugentobler, U. (2015): Combination of ground- and space-based GPS data for the determination of a multi-scale regional 4-D ionosphere model. International Association of Geodesy Symposia, in press.

Copyright

This article will be published in the conference proceedings of the International Association of Geodesy (IAG) Scientific Assembly 2013.

Summary

P-V applies the regional electron density modeling approach published in P-I for testing the combination of TEC and electron density profiles based on a simulated and real-scenario. Target model parameter are the F2 peak parameters $NmF2$ and $hmF2$. The synthetic measurements are computed for realistic locations as obtained from GPS, CHAMP, GRACE and Formosat-3/COSMIC over South America. The results are validated on TEC basis from the comparison with CODE GIMs after integrating the signal. Furthermore, preliminary results of a multi-scale representation are presented. In addition to P-I, this paper underlines the performance of the model approach.

Declaration of own contribution

The results of this publication are computed by means of a C++ software application that has been partially developed by M. Limberger. Specific developments implemented by M. Limberger are for instance the iterative variance component estimation including the processing of different observation groups or techniques, respectively. The algorithms for preprocessing the electron density profiles and GPS data have been written by M. Limberger. Furthermore, M. Limberger helped in evaluating the results and reviewing the manuscript.

The overall own contribution is estimated at 20 %.

Table 7.5: Apportionment of own contributions for P-V.

Criteria	Estimated own contribution
Paper concept	10 %
Computations and software development	20 %
Data analysis and interpretation of results	20 %
Design and creation of figures	0 %
Manuscript structure and writing	10 %

Confirmation by the first author

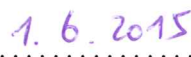
I hereby confirm the correctness of the declaration of own contribution for the publication

Liang, W., Limberger, M., Schmidt, M., Dettmering, D., and Hugentobler, U. (2015): Combination of ground- and space-based GPS data for the determination of a multi-scale regional 4-D ionosphere model. International Association of Geodesy Symposia, in press.

Wenjing Liang

Deutsches Geodätisches Forschungsinstitut der
Technischen Universität München (DGFI-TUM),
München, Germany

Signature: 

Date: 

7.6 P-VI

Liang, W., Limberger, M., Schmidt, M., Dettmering, D., Hugentobler, U., Bilitza, D., Jakowski, N., Hoque, M. M., Wilken, V., and Gerzen, T. (2014): Regional modeling of ionospheric peak parameters using GNSS data – An update for IRI. *Adv Space Res*, DOI 10.1016/j.asr.2014.12.006 (online first).

Copyright

This work is published in *Advances in Space Research* under the Elsevier Creative Common licenses. The publication is available at journals.elsevier.com.

Summary

P-VI contains the validation of F2 Chapman parameters estimated from GPS and F-3/C measurements with the model approach presented in P-I. Expanded from P-V, this work includes a two step estimator where $NmF2$ is determined in the first and $hmF2$ together with $HF2$ are estimated in a second step to ensure the stability of the adjustment system. Ionosonde data observed at the stations in Jicamarca and Port Stanley are considered for providing reference data for the validation. Comparisons are performed at low (16 July 2008), moderate (16 July 2011) and also high (1 July 2012) solar activity.

Declaration of own contribution

The results of this publication are computed by means of a C++ software application that has been partially developed by M. Limberger. Specific functionalities implemented by M. Limberger are for instance the iterative variance component estimation including the processing of different observation groups or techniques. The algorithms for preprocessing the electron density profiles and GPS data are programmed by M.limberger. Figure 3 of this publication was designed and created by M. Limberger. Furthermore, M. Limberger helped in evaluating the results and reviewing the manuscript.

The overall own contribution is estimated at 10 %.

Table 7.6: Apportionment of own contributions for P-VI.

Criteria	Estimated own contribution
Paper concept	0 %
Computations and software development	10 %
Data analysis and interpretation of results	20 %
Design and creation of figures	0 %
Manuscript structure and writing	10 %

Confirmation by the first author

I hereby confirm the correctness of the declaration of own contribution for the publication

Liang, W., Limberger, M., Schmidt, M., Dettmering, D., Hugentobler, U., Bilitza, D., Jakowski, N., Hoque, M. M., Wilken, V., and Gerzen, T. (2014): Regional modeling of ionospheric peak parameters using GNSS data — An update for IRI. Adv Space Res, DOI: 10.1016/j.asr.2014.12.006 (online first).

Wenjing Liang

Deutsches Geodätisches Forschungsinstitut der
Technischen Universität München (DGFI-TUM),
München, Germany

Signature: 梁文婧

Date: 1.6.2015

Abbreviations

A/S	Anti-Spoofing
AFRL	Air Force Research Laboratory
AU	Astronomical Unit
AVISO	Archiving, Validation and Interpretation of Satellites Oceanographic data
BDT	BeiDou Time
BLUE	Best Linear Unbiased Estimation
CDAAC	COSMIC Data Analysis and Archive Center
CGCS2000	China Geodetic Coordinate System 2000
CHAMP	Challenging Minisatellite Payload
CME	Coronal Mass Ejection
CODE	Center for Orbit Determination Europe
CORS	Continuously Operating Reference Stations
CPB	Carrier Phase Bias
Cryosat-2	Cryogenic Satellite 2
CS	Commercial Service
CSRSR	Center for Space and Remote Sensing Research
CTIM	Coupled Thermosphere-Ionosphere Model
DCB	Differential Code Bias
DCBs	Differential Code Biases
DFG	Deutsche Forschungsgemeinschaft
DGFI	Deutsches Geodätisches Forschungsinstitut
DLL	Delay Lock Loop
DLR	German Aerospace Center
DoD	Department of Defense
DORIS	Doppler Orbitography and Radiopositioning Integrated by Satellite
DOY	Day Of Year
EC	European Commission
ECEF	Earth-centered Earth-fixed
EDAM	Electron Density Assimilative Model
EGNOS	European Geostationary Navigation Overlay System
EIA	Equatorial Ionization Anomaly
EMR	Energy, Mines and Resources
EOFs	Empirical Orthogonal Functions
ESA	European Space Agency
ESM	Extended Slab Model
ESOC	European Space Operation Center
EU	European Union

EUV	Extreme Ultraviolet
F-3/C	Formosat-3/COSMIC
F-7/C-2	Formosat-7/COSMIC-2
FAIM	Fully Analytical Ionospheric Model
FLIP	Field Line Interhemispheric Plasma Model
FM	Frequency modulated
FOC	Full Operational Capability
FTP	File Transfer Protocol
gAGE	Research Group of Astronomy and Geomatics
GDR	Geophysical Data Record
GFZ	German Research Centre for Geosciences at the Helmholtz Centre Potsdam
GIM	Global Ionosphere Map
GIMs	Global Ionosphere Maps
GIOVE	Galileo In-Orbit Validation Elements
GLNT	GLONASS Time
GLONASS	Globalnaya Navigatsionnaya Sputnikovaya Sistema
GMT	Greenwich Mean Time
GNSS	Global Navigation Satellite Systems
GPS	Global Positioning System
GPST	GPS Time
GRACE	Gravity Recovery And Climate Experiment
GRSP	Geodetic Reference Service Provider
GSS	Galileo Sensor Stations
GST	Galileo System Time
GTIM	Global Theoretical Ionospheric Model
GTRF	Galileo Terrestrial Reference Frame
HoD	Hours of Day
IAG	International Association of Geodesy
IAPG	Institute for Astronomical and Physical Geodesy
ICD	Interface Control Document
ICGEM	International Centre for Global Earth Models
IDS	International DORIS Service
IERS	International Earth Rotation Service
IFM	Ionosphere Forecast Model
IGDR	Interim Geophysical Data Record
IGS	International GNSS Service
IONMON	Ionosphere Monitoring Facility
IOV	In Orbit Validation
IPP	Ionospheric Pierce Point
IRI	International Reference Ionosphere
IRO	Ionospheric Radio Occultations
ISS	International Space Station
ITRF	International Terrestrial Reference Frame
ITRS	International Terrestrial Reference System
ITU	International Telecommunications Union
ITU-R	International Telecommunication Union - Radiocommunication

JPL	Jet Propulsion Laboratory
LEO	Low Earth Orbiter
LOS	Line-of-Sight
LSTIDs	Large Scale Traveling Ionospheric Disturbances
MEO	Medium Earth Orbiter
MRR	Multi-Resolution Representation
MSLM	Modified Single Layer Mapping
MSTIDs	Medium Scale Traveling Ionospheric Disturbances
NASA	National Aeronautics and Space Administration
NAVSTAR-GPS	Navigation Satellite Timing and Ranging Global Positioning System
NCAR	National Center for Atmospheric Research
NIC09	New Ionosphere Climatology 09
NOAA	National Oceanic and Atmospheric Administration
NRCan	Natural Resources Canada
NRL	Naval Research Laboratory
NRT	Near Real Time
NSF	National Science Foundation
NSPO	National Space Organization
NTCM	Neustrelitz TEC Model
OGDR	Operational Geophysical Data Record
OS	Open Service
OSTM	Ocean Surface Topography Mission
PCA	Principal Component Analysis
PCOs	Phase Center Offsets
PCVs	Phase Center Variations
PIM	Parameterized Ionospheric Model
PLL	Phase Lock Loop
PNT	Positioning, Navigation and Timing
POD	Precise Orbit Determination
PPS	Precise Positioning Service
PRN	Pseudorandom Noise
PRS	Public Regulated Service
PVT	Positioning, Velocity and Timing
PWU	Phase Wind-Up
RA	Radar Altimetry
RINEX	Receiver Independent Exchange Format
RMS	Root Mean Square
SaR	Search and Rescue
SARAL	Satellite with Argos and Altika
SBAS	Satellite Based Augmentation System
SCC	System Control Center
SH	Spherical Harmonics
SIDC	Solar Influences Data Center
SILSO	Sunspot Index and Long-term Solar Observations

SIRGAS	Sistema de Referencia Geocéntrico para Las Américas
SLM	Single Layer Model
SoL	Safety-of-Life
SP3	Standard Product 3 Orbit Format
SPIDR	Space Physics Interactive Data Resource
SPS	Standard Positioning Service
STEC	Slant Total Electron Content
TAI	International Atomic Time
TDIM	Time Dependent Ionospheric Model
TEC	Total Electron Content
TECU	Total Electron Content Units
TIDs	Traveling Ionospheric Disturbances
TIGCM	Thermosphere Ionosphere General Circulation Model
TOMIOM	Tomographic Ionosphere Model
TP	Tangent Point
TUM	Technische Universität München
UCAR	University Corporation for Atmospheric Research
UPC	Universitat Politècnica de Catalunya
USA	United States of America
USU	Utah State University
USU-GAIM	Utah State University Global Assimilation of Ionospheric Measurements
UTC	Coordinated Universal Time
UV	Ultraviolet
VCE	Variance Component Estimation
VPL	Variance Propagation Law
VTEC	Vertical Total Electron Content
WGS-84	World Geodetic System 84

List of Figures

0.1	Interrelations of focus areas in ionosphere modeling constituting the framework of this thesis.	5
1.1	Scheme for height dependent temperature variations in the Earth atmosphere.	13
1.2	Monthly mean and daily total sunspot number, source: SILSO data/image, Royal Observatory of Belgium, Brussels (http://www.sidc.be)	14
1.3	Scheme for the interaction between features of the Sun as ionization sources and the Earth's magnetic field, inspired by a representation of the European Space Agency (http://sci.esa.in).	15
1.4	Ionospheric layer composition based on the vertical electron density distribution, here indicated by a schematical, idealized profile.	16
1.5	Composition of atmospheric layers in the temperature and ionization domain including an electron density distribution profile (red) with characteristic F2 and E peak occurrences. For comparison, orbit heights of different satellite missions, that will be described within this thesis, are provided on the right hand side. It should be noted, that this is just a sketch and the altitude as well as electron density axis is not linearly scaled.	17
1.6	Schematic representation of the photoionization process.	20
1.7	Loss of radiation intensity with respect to a path element ds or height interval dh	21
1.8	Chapman ion production profiles for different function parameters. Dependency with respect to the solar zenith angle $\chi = [0^\circ, 10^\circ, \dots, 80^\circ]$ (top left), scale height $H = [60 \text{ km}, 70 \text{ km}, \dots, 100 \text{ km}]$ (top right) and peak heights $h_0 = [200 \text{ km}, 250 \text{ km}, \dots, 400 \text{ km}]$ (bottom left) as functions of the Q/Q_{\max} ratio. The ion production Q for different maximum rates $Q_{\max} = [10^5 \text{ el/cm}^3, 2 \cdot 10^5 \text{ el/cm}^3, \dots, 6 \cdot 10^5 \text{ el/cm}^3]$ is given in the bottom right representation.	23
1.9	Scheme for a Single Layer Model.	25
2.1	Overview of selected parametrization methods that will be discussed in Chapter 2. Three schematic representations are included which show different components (zonal, sectorial, tesseral) of spherical harmonics (left), the structure of a grid-based voxel band above Earth (middle) and a basis of normalized quadratic polynomial B-splines (right). The SH structure is plotted with a visualization tool provided by ICGEM at http://icgem.gfz-potsdam.de/ICGEM/ , the voxel structure is adapted from the 2-D representation in Hernández-Pajares et al. (1999).	27
2.2	Normalized quadratic polynomial B-splines with different levels $J_\phi = 0, 1, 2, 3$ and accordingly different number of B-splines $K_\phi^J = 3, 4, 6, 10$	34
2.3	Trigonometric B-splines with different levels $J_T = 0, 1, 2, 3$ and accordingly different number of B-splines $K_T = 5, 8, 14, 26$	36
2.4	Polynomial B-splines $\phi_{k_1}^2(x_1)$ and $\phi_{k_2}^3(x_2)$ of order $m = 3$ with different levels $J_1 = 2$ and $J_2 = 3$. $\phi_3^2(x_1)$ (left), $\phi_1^2(x_1)$ (right) and $\phi_5^3(x_2)$ are emphasized to show the support area.	37

2.5	Combination of trigonometric B-splines with level $J_1 = 2$ and polynomial B-splines with level $J_2 = 3$. A specific spline combination identified by $k_1 = 5$ and $k_2 = 8$ has been highlighted and plotted in the center part of the left subplot. Accordingly, a 3-D representation of the tensor product is given on the right hand side.	38
2.6	Normalized quadratic polynomial B-spline basis spanned to an exemplary study area of $\varphi = [-30^\circ, +60^\circ]$ and $\lambda = [250^\circ, 340^\circ]$ with B-spline levels $J_1 = J_2 = 3$. Two perspectives are given by a slant viewpoint (left) and bird view (right).	39
3.1	Extended GPS core constellation with 24+3 spacecraft slots as defined by the SPS Performance Standard (graphical design inspired by http://www.gps.gov).	46
3.2	Distribution of ionospheric pierce points for specific hourly intervals 06:00-07:00 UT (top-left), 10:00-11:00 UT (top-right), 14:00-15:00 UT (bottom-left) and 18:00-19:00 UT (bottom-right) on 8 January 2015. The data is based on hourly GPS data and ultra-rapid orbits (predicted-half) provided by the IGS, available at http://igsceb.jpl.nasa.gov . The IPP colors reflect signal delays induced by the ionosphere and instrumental hardware biases. A draft of a GPS-IIF spacecraft is depicted in the top-left corner.	48
3.3	GLONASS core constellation with totally 24 spacecraft slots on three different orbital planes, i.e., eight satellites per orbit. The satellites on each plane are separated by 45° in argument of latitude.	49
3.4	Distribution of ionospheric pierce points during an one-hour timeslice between 14:00 UT and 15:00 UT at 8 January 2015 related to tracked GLONASS passes. The data is based on hourly IGS data and ultra-rapid orbits (predicted-half) available at http://igsceb.jpl.nasa.gov . A draft of a GLONASS-K spacecraft is depicted in the top-left corner.	51
3.5	Map of current DORIS ground beacon distribution. Source: IDS, International DORIS Service: http://ids-doris.org , last update on 25 November 2014.	57
3.6	Geometrical consequence of DORIS transmitter and receiver phase offsets.	59
3.7	Daily distribution of ionospheric pierce points at 15 September 2013 computed for DORIS carrier-phase measurements of different satellite missions with DGXX instrument, specifically Jason-2 (top-left), Saral (top-right), Cryosat-2 (bottom-left) and Hy-2a (bottom-right). For the mapping, a single layer model with MSLM has been taken into account. The observation leveling is based on TEC derived from IGS GIMs.	60
3.8	Raw (blue) and filtered (red) VTEC series computed from OGDR data.	61
3.9	Daily distribution of Jason-2 altimetry VTEC at 1 January 2015, computed from OGDR data. The pass plotted in Fig. 3.8 has been highlighted by red arrows with start and end time. A draft of Jason-2 has been depicted in the top-right corner.	61
4.1	Schematic representation of the radio occultation geometry between a GNSS transmitter and F-3/C receiver.	63
4.2	Global distribution of 116 electron density profiles computed from CHAMP occultations as collected during 8 January 2007. The map shows clearly the horizontal extent of the profiles. Data source: CDAAC, http://cdaac-www.cosmic.ucar.edu	65
4.3	Global distribution of 66 electron density profiles computed from GRACE occultations as collected on 8 January 2009. The map shows clearly the horizontal extent of the profiles. Data source: CDAAC, http://cdaac-www.cosmic.ucar.edu	66
4.4	Global distribution of 391 electron density profiles computed from F-3/C occultations as collected on 8 January 2015. The map shows clearly the horizontal extent of the profiles. Data source: CDAAC, http://cdaac-www.cosmic.ucar.edu	67
4.5	Schematics for the geometry of refraction on a plane (design inspired by Fjeldbo et al. (1971)).	68

4.6	Occultation geometry for bending angle computation (design inspired by García-Fernández (2004)).	71
4.7	Occultation geometry under the assumption of straight line propagation.	73
4.8	Integral discretization by means of the onion shell structure. Colored arrows illustrate the discretized integration steps between consecutive layers. This scheme shows the composition with measurements at two epochs i_1 and i_2 yielding the corresponding tangent points TP_1 and TP_2 that are located within the layers j_1 and j_2	74
4.9	Improved setup for recursive STEC inversion under consideration of the separability hypothesis. Labels and notations are similar to Fig. 4.8.	75
5.1	Categorization of ionosphere models.	77
5.2	Layer composition for the extended Gauß-Legendre integration of the electron density for the computation of TEC.	82
5.3	Geometrical ray path distribution including five SIRGAS network stations (red triangles) tracking five GPS satellites passes (blue).	83
5.4	Comparison of processing effort in computation time (blue bars) with the RMS of TEC differences (green bars) for different quadrature orders and integration step widths in a simulated scenario.	84
5.5	Flowchart of the iterative solving procedure with nested variance component estimation.	94
6.1	Climatology of $NmF2$ (left) and $hmF2$ (right) described by global averages of F2 peaks derived from F-3/C radio occultations between 2006 and 2014.	100
6.2	Left column: Collocated F2 peaks derived from ionosondes (blue triangles) and F-3/C occultations (red). Right column: Correlations between ionosonde and F-3/C $NmF2$ (top) and $hmF2$ (bottom) during daytime [12:00 LT,16:00 LT] in the mid-latitude sector, i.e., between $\pm [20^\circ, 60^\circ]$ magnetic latitude.	100
6.3	Left column: Collocated F2 peaks derived from ionosondes (blue triangles) and F-3/C occultations (red). Right column: Correlations between ionosonde and F-3/C $NmF2$ (top) and $hmF2$ (bottom) during nighttime [0:00 LT,4:00 LT] in the mid-latitude sector, i.e., between $\pm [20^\circ, 60^\circ]$ magnetic latitude.	101
6.4	2-D representation of polynomial B-splines defined by the levels $J_\lambda = 2$ and $J_\varphi = 3$ and distributed over an interval of $\lambda = [250^\circ, 340^\circ]$ and $\varphi = [-60^\circ, 30^\circ]$. The embedded transparent cuboid borders the influence zone of an exemplary vertical electron density profile that is indicated by the black solid line. In this example, altogether, $3 \times 3 = 9$ splines are affected.	103
6.5	Key parameter corrections $\Delta hmF2$, $\Delta HF2$ and $\Delta NmF2$ for a fixed time moment at 12:00 UT on 1 July 2008 are depicted along the left column. Selected F-3/C profiles that have an impact on the key parameter estimation are plotted in the right column and indicated by arrows on the key parameter maps.	104
6.6	VTEC maps referring to IRI-2007 (left), IGS GIM (middle) and the difference between IRI-2007 and IGS GIM (right) for 1 July 2008 at 13:55 UT.	105
6.7	VTEC maps referring to the model estimation (left), $\Delta VTEC$ estimation (middle) and the difference between the model estimation and CODE GIM (right) for 1 July 2008 at 13:55 UT.	105
6.8	Correlation matrices of the key parameters \mathbf{K}_{tt} at 12:00 UT on 1 July 2008 based on synthetic data (left) and F-3/C observations (right). Both matrices \mathbf{K}_{tt} represent correlations for parameters related to a grid with $\Delta\varphi = 5^\circ \times \Delta\lambda = 5^\circ$ resolution.	106
6.9	Example for the distribution of electron density profiles from F-3/C (pink dots) and F-7/C-2 (green dots) during a period of three hours, source: UCAR, http://www.cosmic.ucar.edu/cosmic2/ . A F-7/C-2 satellite draft has been depicted in the top-left corner.	109

List of Tables

2.1	Overview of the spherical harmonics parametrization for ionosphere modeling. . . .	29
2.2	Overview of the cell and voxel parametrization for ionosphere modeling.	32
2.3	Overview of the B-spline parametrization for ionosphere modeling.	41
3.1	Error sources of GNSS signals.	44
3.2	Overview on the legacy GPS signals	47
3.3	GLONASS channel allocation to the spacecraft slots (28 November 2014).	50
3.4	DORIS receiver clock biases for selected satellite missions with DGXX instrument. .	58
3.5	Overview on zenith and nadir antenna corrections due to PCOs for currently active mis- sions with DGXX receiver payload. The values have been calculated from the phase center locations published in Cerri and Ferrage (2014) under consideration of the an- tenna orientation.	59
4.1	Chronology of LEO research missions carrying radio occultation instruments as pub- lished by Mannucci et al. (2014).	64
7.1	Apportionment of own contributions for P-I.	111
7.2	Apportionment of own contributions for P-II.	126
7.3	Apportionment of own contributions for P-III.	142
7.4	Apportionment of own contributions for P-IV.	157
7.5	Apportionment of own contributions for P-V.	159
7.6	Apportionment of own contributions for P-VI.	161

Software development references

Several software packages and tools have been developed in C++ and Python as a part of this thesis. Special attention was paid to the consideration of open-source software. For this purpose, the eclipse software environment with various plugins related to C++ and Python development as well as version control tools have been used.

- **Eclipse IDE for C/C++ Developers**, Version: Kepler Service Release 2, (c) Copyright Eclipse contributors and others 2000, 2014. All rights reserved. This product includes software developed by the Apache Software Foundation.
Source: <http://eclipse.org>
- **Eclipse C/C++ Development Tools**, Version: 8.3.0.201402142303, (c) Copyright Eclipse contributors and others, 2000, 2010. All rights reserved.
Source: <http://www.eclipse.org/cdt>
- **PyDev** - Python IDE for Eclipse.
Source: <http://www.pydev.org>
- **NumPy** - Numerical Python for scientific computing.
Source: <http://www.numpy.org/>
- **SciPy** - Software for scientific computing with Python including NumPy.
Source: <http://www.scipy.org/>
- **Eclipse Subversive** - SVN Team Provider Project, (c) Copyright 2005, 2008 Polarion Software and other. All rights reserved.
Source: <http://www.eclipse.org/subversive>

The figures presented this thesis have been produced with one of the following plotting tools.

- **Generic Mapping Tools (GMT)**, Version 4.5.11, (c) Copyright 1991-2013 Paul Wessel and Walter H. F. Smith.
Source: <http://gmt.soest.hawaii.edu>
- **Matplotlib**, Version 1.3.1-1ubuntu5, Python based plotting system.
Source: <http://www.matplotlib.org>
- **yEd**, Version 3.13, Powered by the yFiles for Java Graph Visualization Library, (c) Copyright 2000-2015 yWorks GmbH. All right reserved.
Source: <http://www.yworks.com>
- **Gimp** - GNU image manipulation program, Version 2.8.10, (c) Copyright 1995-2014 Spencer Kimball, Peter Mattis and the GIMP development team.
Source: <http://www.gimp.org>
- **Corel/Ulead PhotoImpact X3**, Version 13.00.3014.0, (c) Copyright 1992-2007 InterVideo Digital Technology Corporation.

Bibliography

- Al-Fanek, O. J. S. (2013): Ionospheric Imaging for Canadian Polar Regions, Ph.D. thesis, University of Calgary, Department of Geomatics Engineering, UCGE Reports Number 20383.
- Alizadeh, M. M., Wijaya, D. D., Hobiger, T., Weber, R., and Schuh, H. (2013): Ionospheric Effects on Microwave Signals, *Atmospheric Effects in Space Geodesy*, Springer Atmospheric Sciences, pp. 35-71, DOI 10.1007/978-3-642-36932-2_2.
- Anderson, D. N. (1971): Daily variation of the ionospheric F2 equatorial anomaly in the American and Asian sectors. NCAR Coop. Ph. D. thesis, NCAR, Boulder, Colorado.
- Anderson, D. N. (1973): A theoretical study of the ionosphere F region equatorial anomaly—II. results in the American and Asian sectors. *Planetary and Space Science*, 21, 3, pp. 421-442, DOI 10.1016/0032-0633(73)90041-X.
- Anderson, D. N., Frobos, J. M., and Codrescu, M. (1989): A fully analytical low- and middle-latitude ionospheric model. *J. Geophys. Res.*, 94, 1520, DOI 10.1029/JA094iA02p01520.
- Anderson, D. N., Buonsanto, M. J., Codrescu, M., Decker, D., Fesen, C. G., Fuller-Rowell, T. J., Reinisch, B. W., Richards, P. G., Roble, R. G., Schunk, R. W., and Sojka, J. J. (1998): Intercomparison of physical models and observations of the ionosphere. *J. Geophys. Res.*, 103, A2, pp. 2179-2192, DOI 10.1029/97JA02872.
- Angling, M. J. (2004): Assimilations of radio occultation measurements into background ionospheric models. *Radio Science*, 39, DOI 10.1029/2002RS002819.
- Angling, M. J., and Khattatov, B. (2006): Comparative study of two assimilative models of the ionosphere. *Radio Science*, 41, 5, DOI 10.1029/2005RS003372.
- Angling, M. J. (2008): First assimilations of COSMIC radio occultation data into the Electron Density Assimilative Model (EDAM). *Ann. Geophys.*, 26, pp. 353-359, DOI 10.5194/angeo-26-353-2008.
- Aragón-Ángel, A. (2010): Contributions to ionospheric electron density retrieval. Ph.D. Thesis, Research Group of Astronomy and Geomatics (gAGE), Technical University of Catalonia (UPC), pp. 53-63, 2010.
- Aragón-Ángel, A., Liou, Y.-A., Lee, C.-C., Reinisch, B. W., Hernández-Pajares, M., Juan, M., and Sanz, J. (2011): Improvement of retrieved FORMOSAT-3/COSMIC electron densities validated by ionospheric sounder measurements at Jicamarca. *Radio Science*, 46, RS5001, DOI 10.1029/2010RS004578.
- Bent, R. B., Llewellyn, S. K., and Schmid, P. E. (1972): A Highly Successful Empirical Model for the Worldwide Ionospheric Electron Density Profile. DBA Systems, Melbourne, Florida.
- Bent, R. B., Llewellyn, S. K., and Walloch, M. K. (1972): Description and Evaluation of the Bent Ionospheric Model. DBA Systems, Melbourne, Florida.
- Bhuyan, P. K. and Bhuyan, K. (2008): The equatorial ionization anomaly at the topside F region of the ionosphere along 75° E. *Adv. Space Res.*, 43, pp. 1676-1682, DOI 10.1016/j.asr.2008.09.027.
- Bilitza, D. (2001): International Reference Ionosphere 2000. *Radio Sci.*, 36, 2, pp. 261-275, DOI 10.1029/2000RS002432.
- Bilitza, D., and Reinisch, B. (2008): International reference ionosphere 2007: Improvements and new parameters. *Adv. Space Res.*, 42, pp. 599-609, DOI 10.1016/j.asr.2007.07.048.
- Bilitza, D., Mckinnell, L.-A., Reinisch, B., and Fuller-Rowell, T. (2011): The international reference ionosphere today and in the future. *J. Geod.*, 85, pp. 909-920, DOI 10.1007/s00190-010-0427-x.
- Brecke, Asgeir (2013): *Physics of the Upper Polar Atmosphere*. Springer Atmospheric Sciences, Original edition published by Wiley 2013, XXVI, ISBN 978-3-642-27400-8 (Print) 978-3-642-27401-5 (Online).
- Born, M., and Wolf, E. (1999): *Principles of Optics: Electromagnetic Theory of Propagation, Interference and Diffraction of Light*. Cambridge University Press; 7th Edition (13 Oktober 1999), ISBN 978-0521642224.
- Bust, G. S., and Mitchel, C. N. (2008): History, current state, and future directions of ionospheric imaging. *Rev. Geophys.* 46, RG1003, DOI 10.1029/2006RG000212.
- Cerri, L., and Ferrage, P. (2014): DORIS satellite models implemented in POE processing. Ed. 1, Rev. 6, CNES, IDS, <ftp://ftp.ids-doris.org/pub/ids/satellites/DORISsatelliteModels.pdf>.
- Chapman, S. (1931): The absorption and dissociative or ionizing effect of monochromatic radiation in an atmosphere on a rotating earth. *Proc. Phys. Soc.*, 43, 1, p. 26 DOI 10.1088/0959-5309/43/1/305.
- Chapman, S. (1931): The absorption and dissociative or ionizing effect of monochromatic radiation in an atmosphere on a rotating earth part II. Grazing incidence. *Proc. Phys. Soc.*, 43, 5, p. 483 DOI 10.1088/0959-5309/43/5/302.
- Chapman, S., and Mian, A. M. (1942): The rate of ion-production at any height in the Earth's atmosphere: I—The spherical harmonic representation of its worldwide distribution. *Terr. Magn. Atmos. Electr.*, 47(1), pp. 31-38, DOI 10.1029/TE047i001p00031
- Chapman, S., and Mian, A. M. (1942): The rate of ion-production at any height in the Earth's atmosphere: II—The Fourier expression for its daily variation. *Terr. Magn. Atmos. Electr.*, 47(1), pp. 38-44, DOI 10.1029/TE047i001p00038.
- Ching, B. K., and Chiu, Y. T. (1973). A Phenomenological Model of Global Ionospheric Electron Density in the E-, F1-, and F2-Regions. *J. Atmos. Terr. Phys.* 35, 1615, DOI 10.1016/0021-9169(73)90180-3.

- Dach, R., Schaer, S., Lutz, S., Meindl, M., Bock, H., Orliac, E., Prange, L., Thaller, D., Mervart, L., Jäggi, A., Beutler, G., Brockmann, E., Ineichen, D., Wiget, A., Weber, G., Habrich, H., Söhne, W., Ihde, J., Steigenberger, P., and Hugentobler, U. (2012): Center for Orbit Determination in Europe (CODE). IGS Technical Report 2012, 35-46, Jet Propulsion Laboratory.
- Dach, R., Hugentobler, U., Fridez, P., and Meindl, M. (2007): Bernese GPS Software, Version 5.0. Astronomical Institute, University of Bern.
- Davies, K. (1990): *Ionospheric Radio*. IEEE Electromagnetic Waves Series 31. Peter Peregrinus, London.
- Daniell, R. E., Brown, L. D., Anderson, D. N., Fox, M. W., Doherty, P. H., Decker, D. T., Sojka, J. J., and Schunk, R. W. (1995): Parameterized ionospheric model: A global ionospheric parameterization based on first principles models. *Radio Sci.*, 30, 5, pp. 1499-1510, DOI 10.1029/95RS01826.
- Dettmering, D., Schmidt, M., Heinkelmann, R., and Seitz, M. (2011): Combination of different space-geodetic observations for regional ionosphere modeling. *J. Geodesy*, 85, pp. 989-998, DOI 10.1007/s00190-010-0423-1.
- Dettmering, D., Heinkelmann, R., and Schmidt, M. (2011): Systematic differences between VTEC obtained by different space-geodetic techniques during CONT08. *J. Geodesy*, 85, pp. 443-451, DOI 10.1007/s00190-011-0473-z.
- Dettmering, D., Schmidt, M., and Limberger, M. (2014): Contributions of DORIS to ionosphere modeling. Ouwehand L. (Ed.) *Proceedings of "20 Years of Progress in Radar Altimetry"*, IDS Workshop, Sept. 2012, Venice, Italy, ESA SP-710 (CD-ROM), ISBN 978-92-9221-274-2, ESA/ESTEC.
- Dettmering, D., Limberger, M., and Schmidt, M. (2014): Using DORIS measurements for modeling the vertical total electron content of the Earth's ionosphere. *J Geod*, 88(12), pp. 1131-1143, DOI 10.1007/s00190-014-0748-2.
- Dierckx, P. (1984): Algorithms for smoothing data on the sphere with tensor product splines. *Computing*, 32, 4, pp. 319-342, DOI 10.1007/BF02243776.
- Dow, J. M., Neilan, R. E., and Rizos, C. (2009): The International GNSS Service in a changing landscape of Global Navigation Satellite Systems. *J. Geodesy*, 83, 191-198, DOI 10.1007/s00190-008-0300-3.
- El-Rabbany, A. (2006): *Introduction to GPS: The Global Positioning System*, Second Edition. Artech House Publishers, 2nd Edition, ISBN 978-1596930162.
- Epstein, P. (1906): Zur Theorie allgemeiner Zetafunktionen. *Mathematische Annalen*, Springer, 63, 2, pp. 205-216, DOI 10.1007/BF01449900.
- Ezquer, G. R., Mosert, M. and Heredia, T. (1906): Electron density profile modeling. *Mathematische Annalen*, Springer, 63, 2, pp. 205-216, DOI 10.4401/ag-3990. *Annali Di Geofisica*, Vol. XXXIX, 3, 539-542, Italy.
- Feltens, J. (1998): Chapman profile approach for 3-D global TEC representation. *Proceeding of the IGS AC Workshop*, pp. 285-297.
- Feltens, J. (2007): Development of a new three-dimensional mathematical ionosphere model at European Space Agency/European Space Operations Centre. *Space Weather*, 5, 12, DOI 10.1029/2006SW000294.
- Feltens, J., Angling, M., Jackson-Booth, N., Jakowski, N., Hoque, M., Hernández-Pajares, M., Aragón-Ángel, A., Orús, R., and Zandbergen, R. (2011): Comparative testing of four ionospheric models driven with GPS measurements. *Radio Science*, 46, 6, DOI 10.1029/2010RS004584.
- Fjeldbo, G., Kliore, A. J., and Eshleman, V. R. (1971): The neutral atmosphere and Venus studies with the Mariner V radio occultation experiments. *Astronomical Journal*, 76, 2, DOI 10.1086/111096.
- Fu, L.-L., and Cazenave, A. (2001): *Satellite Altimetry and Earth Sciences - A Handbook of Techniques and Applications*. Academic Press Inc., ISBN 978-0122695452.
- Fuller, T. J., Rees, D., Quegan, S., Moffett, R. J., and Bailey, G. J. (1987): Interactions between neutral thermospheric composition and the polar ionosphere using a coupled ionosphere-thermosphere model. *J. Geophys. Res.*, 92, A7, DOI 10.1029/JA092iA07p07744.
- Gallagher, D. L., Craven, P. D., and Comfort, R. H. (1988): An empirical model of the earth's plasmasphere. *Adv. Space Res.*, 8, 8, pp. 15-24, DOI 10.1016/0273-1177(88)90258-X.
- Gao, Y., and Liu, Z. Z. (2002): Precise ionosphere modeling using regional GPS network data. *Journal of Global Positioning Systems*, 1, 18-24, DOI 10.5081/jgps.1.1.18.
- García-Fernández, M. (2004): Contributions to the 3D ionospheric sounding with GPS data. PhD thesis, Doctoral Program in Aerospace Science and Technology, Research group of Astronomy and Geomatics (gAGE), Depts. of Applied Mathematics IV and Applied Physics, Universitat Politècnica de Catalunya (UPC).
- Garcia-Fernandez, M., Hernández-Pajares, M., Juan, M., and Sanz, J. (2003): Improvement of ionospheric electron density estimation with GPSMET occultations using Abel inversion and VTEC information. *J. Geophys. Res.*, 108(A9), DOI 10.1029/2003JA009952.
- Ge, A. (2006): GPS Radio Occultation and the Role of Atmospheric Pressure on Spaceborne Gravity Estimation Over Antarctica. PhD thesis, Report No. 479, Geodetic Science and Surveying, Ohio State University, Columbus, Ohio 43210, School of Earth Sciences.
- Gmelig Meyling, R. H. J., and Pfluger, P. R. (1987): B-spline approximation of a close surface. *IMA J. Numer. Anal.*, 7, pp. 73-96, DOI 10.1093/imanum/7.1.73.
- Di Giovanni, G., and Radicella, S. M. (1990): An analytical model of the electron density profile in the ionosphere. *Adv. Space Res.*, 10, 11, pp. 27-30, DOI 10.1016/0273-1177(90)90301-F.
- Gorenflo, R., and Vessella, S. (2009): *Abel Integral Equations - Analysis and Applications*. Lecture Notes in Mathematics, Springer, ISBN 978-3540536680.
- Hajj, G. A. and Romans, J. (1998): Ionospheric electron density profiles obtained with the Global Positioning System. Results from the GPS/MET experiment, *Radio Sci.*, 33, pp. 175-190, DOI 10.1029/97RS03183.
- Hanse, P. C. (1996): *Regularization Tools: A Matlab Package for Analysis and Solution of Discrete Ill-Posed*

- Problems. Numer. Algo., 6, 1, pp. 1-35, DOI 10.1007/BF02149761.
- Hardy, K. R., Hajj, G. A., and Kursinski, E. R. (1993): Accuracies of atmospheric profiles obtained from GPS occultations. Proceedings of the 6th International Technical Meeting of the Satellite Division of The Institute of Navigation (ION GPS 1993), Salt Lake City, UT, September 1993, pp. 1545-1556.
- Hargraeves, J. K. (1992): The solar-terrestrial environment: An introduction to geospace - the science of the terrestrial upper atmosphere, ionosphere and magnetosphere. Cambridge University Press, ISBN 0-521-32748-2 (hardback).
- Hartmann, G., and Leitinger, R. (1984): Range errors due to ionospheric and tropospheric effects for signal frequencies above 100 MHz. Bull. Geod. 58, 2, pp. 109-136, DOI 10.1007/BF02520897.
- Heiker, A. (2012): Mutual validation of Earth orientation parameters, geophysical excitation functions and second degree gravity field coefficients. Ph.D. thesis, Hannover 2012, published in Deutsche Geodätische Kommission bei der Bayerischen Akademie der Wissenschaften, Reihe C, Nr. 697, München 2013, ISBN 978-3-7696-5109-6, ISSN 0065-5325, <http://www.dgk.badw.de>
- Hernández-Pajares, M., Juan, J. M., and Sanz, J. (1998): Global observation of the ionospheric electronic response to solar events using ground and LEO GPS data. J. Geophys. Res., 103, pp. 789-796, DOI 10.1029/98JA01272.
- Hernández-Pajares, M., Juan, J. M., and Sanz, J. (1999): New approaches in global ionospheric determination using ground GPS data. Journal of Atmospheric and Solar-Terrestrial Physics, 61, pp. 1237-1247, DOI 10.1016/S1364-6826(99)00054-1.
- Hernández-Pajares, M., Juan, J. M., and Sanz, J. (2000): Improving the Abel inversion by adding ground data LEO radio occultations in the ionospheric sounding. Geophys. Res. Lett., 27, pp. 2743-2746, DOI 10.1029/2000GL000032.
- Hernández-Pajares, M., Juan, J. M., and Sanz, J. (2007): Second-order ionospheric term in GPS: Implementation and impact on geodetic estimates. J. Geophys. Res., 112, pp. 1-16, DOI 10.1029/2006JB004707.
- Hernández-Pajares, M., Juan, J. M., Sanz, J., Orus, R., Garcia-Rigo, A., Feltens, J., Komjathy, A., Schaer, S. C., and Krankowski, A. (2009): The IGS VTEC maps: a reliable source of ionospheric information since 1998. J. Geodesy, 83, pp. 263-275, DOI 10.1007/s00190-008-0266-1.
- Hernández-Pajares, M., Juan, J. M., Sanz, J., Aragón-Ángel, A., García-Rigo, A., Salazar, D., and Escudero, M. (2011): The ionosphere: effects, GPS modeling and the benefits for space geodetic techniques. J Geod, 85, 12, pp. 887-907, DOI 10.1007/s00190-011-0508-5.
- Hernández-Pajares, M., Juan, J. M., Sanz, J., and Aragón-Ángel, A. (2012): Propagation of medium scale travelling ionospheric disturbances at different latitudes and solar cycle conditions. Radio Science, 47, 6, DOI 10.1029/2011RS004951.
- Hofmann-Wellenhof, B., Lichtenegger, H., and Wasle, E. (2008): GNSS - Global Navigation Satellite Systems. GPS, GLONASS, Galileo and more, Springer, ISBN 978-3-211-73012-6.
- Hoque, M. M., and Jakowski, N. (2012): Ionospheric Propagation Effects on GNSS Signals and New Correction Approaches. In: Global Navigation Satellite Systems: Signal, Theory and Applications, Prof. Shuanggen Jin (Ed.), InTech, ISBN 978-953-307-843-4.
- Howe, B. M., and Runciman, K. (1998): Tomography of the ionosphere: Fourdimensional simulations. Radio Science, 33, 1, pp. 109-128, DOI 10.1029/97RS02615.
- Huang, X. and Reinisch, B. W. (1996): Vertical electron density profiles from the Digisonde network. Adv. Space Res., 18, 6, pp. 121-129, DOI 10.1016/0273-1177(95)00912-4.
- Hugentobler, U., Meindl, M., Beutler, G., Bock, H., Dach, R., Jäggi, A., Urschl, C., Mervart, L., Rothacher, M., Schaer, S., Brockmann, E., Ineichen, D., Wiget, A., Wild, U., Weber, G., Habrich, H., and Boucher, C. (2008): CODE IGS Analysis Center Technical Report 2003/2004. IGS 2003-2004 Technical Reports, IGS Central Bureau.
- Modelling of DORIS instruments, Version 16.2, ftp://cdis.gsfc.nasa.gov/doris/cb_mirror/satellites/DORIS_instrument_modelling_1G_envisat.pdf.
- Jakowski, N. (2005): Ionospheric GPS radio occultation measurements on board CHAMP. GPS Solutions, 9, pp. 88-95, DOI 10.1007/s10291-005-0137-7.
- Jakowski, N., Hoque, M., and Mayer, C. (2011): A new global TEC model for estimating transionospheric radio wave propagation errors. J Geod, 85, 12, pp. 965-974, DOI 10.1007/s00190-011-0455-1.
- Jayles, C. (2009): Modeling of DORIS 2GM and Cryosat instruments. CNES/IDS technical documentation.
- Jekeli, C. (2005): Spline representations of functions on a sphere for geophysical modeling. Geodetic and Geoinformation Science, Department of Civil and Environmental Engineering and Geodetic Science, The Ohio State University, Report No. 475, Columbus.
- Juan, J., Rius, A., and Hernández-Pajares, M. (1997): A two-layer model of the ionosphere using Global Positioning System data. Geophys. Res. Lett., 24, 4, pp. 393-396, DOI 10.1029/97GL00092.
- Klobuchar, J. A. (1982): Ionospheric Corrections for the Single Frequency User of the Global Positioning System. National Telesystems Conference, NTC'82. Systems for the Eighties. Galveston, Texas, USA.
- Koch, K.-R. (1999): Parameter estimation and hypothesis testing in linear models. Springer, Berlin, ISBN 3-540-65257-4.
- Koch, K.-R., and Kusche, J. (2002): Regularization of geopotential determination from satellite data by variance components. J. Geodesy, 76, 259-268, DOI 10.1007/s00190-002-0245-x.
- Leitinger, R., Zhang, M.-L., and Radicella, S. M. (2007): An improved bottomside for the ionospheric electron density model NeQuick. Annals of Geophysics, 48, 3, DOI 10.4401/ag-3217.
- Levine, S. (1985): Derivation of the Ideal Gas Law. Journal

- of Chemical Education, 62, 5, 399.
- Liang, W., Limberger, M., Schmidt, M., Dettmering, D., Hugentobler, U., Bilitza, D., Jakowski, N., Hoque, M., Wilken, V., and Gerzen, T. (2014): Regional modeling of ionospheric peak parameters using GNSS data — An update for IRI. *Adv. Space Res.*, DOI 10.1016/j.asr.2014.12.006 (online first).
- Liang, W., Limberger, M., Schmidt, M., Dettmering, D., and Hugentobler, U. (2015): Combination of ground- and space-based GPS data for the determination of a multi-scale regional 4-D ionosphere model. *International Association of Geodesy Symposia*, in press.
- Limberger, M., Liang, W., Schmidt, M., Dettmering, D., and Hugentobler, U. (2013): Regional representation of F2 Chapman parameters based on electron density profiles. *Ann. Geophys.*, 31, pp. 2215-2227, DOI 10.5194/angeo-31-2215-2013.
- Limberger, M., Liang, W., Schmidt, M., Dettmering, D., Hernández-Pajares M., and Hugentobler, U. (2013): Correlation studies for B-spline modeled F2 Chapman parameters obtained from FORMOSAT-3/COSMIC data. *Ann. Geophys.*, 32, pp. 1533-1545, DOI 10.5194/angeo-32-1533-2014.
- Limberger, M., Hernández-Pajares, M., Aragón-Ángel, A., Altadill, D., and Dettmering, D. (2015): Long-term comparison of the ionospheric F2 layer electron density peak derived from ionosonde data and Formosat-3/COSMIC occultations. *J. Space Weather Space Clim.*, 5, A21, 2015, DOI 10.1051/swsc/2015023.
- Lyche, T., and Schumaker, L. L. (2000): A multiresolution tensor spline method for fitting functions on the sphere. *SIAM J. Sci. Comput.*, 22, pp. 724-746, DOI 10.1137/S1064827598344388.
- Manucci, A. J., Wilson, B. D., Yuan, D. N., Ho, C. H., Lindqwister, U. J., and Runge, T. F. (1998): A global mapping technique for GPS-derived ionospheric total electron content measurements. *Radio Science*, 33, 3, pp. 565-582, DOI 10.1029/97RS02707.
- Manucci, A. J., Iijima, B. A., Lindqwister, U. J., Pi, X., Sparks, L., and Wilson, B. D. (1999): GPS and Ionosphere. *URSI Review of Radio Science*, Wiley-IEEE Press, New York, ISBN 978-0-7803-6003-7.
- Manucci, A. J., Ao, C. O., Young, L. E., and Meehan, T. K. (2014): Studying the Atmosphere Using Global Navigation Satellites. *Eos, Transactions American Geophysical Union*, 95, 43, pp. 389-391, DOI 10.1002/2014EO430001.
- Martyn, D. F. (1956): Processes controlling ionization distribution in the F2 region of the ionosphere. *Australian Journal of Physics*, 9, 1, pp. 161-166, DOI 10.1071/PH560161.
- Mercier, F., Cerri, L., and Berthias, J.-P. (2010): Jason-2 DORIS phase measurement processing. *Adv. Space Res.*, 45, 12, 1141-1454, DOI 10.1016/j.asr.2009.12.002.
- Merfier, F. (2010): DORIS phase measurement and ionospheric effects. *IDS workshop, Lisbon, Portugal*, 21-22 October 2010.
- Mößmer, M. (2009): Globale drei-dimensionale Ionosphärenmodelle des VTEC. Bachelor's Thesis, Technische Universität München.
- Moldwin, M. (2008): An introduction to space weather. Cambridge University Press, ISBN 978-0-521-86149-6.
- Nava, B., Coisson, P., and Radicella, S. M. (2008): A new version of the NeQuick ionosphere electron density model. *Journal of Atmospheric and Solar-Terrestrial Physics*, 70, 15, pp. 1856-1862, DOI 10.1016/j.jastp.2008.01.015.
- Niemeier, W. (2008): *Ausgleichsrechnung - Statistische Auswertemethoden*. Walter de Gruyter GmbH & Co. KG, ISBN 978-3-11-019055-7.
- Nsumei, P., Reinisch, B. W., Huang, X., and Bilitza, D. (2012): New Vary-Chap profile of the topside ionosphere electron density distribution for use with the IRI model and the GIRO real time data. *Radio Science*, 47, RS0L16, DOI 10.1029/2012RS004989.
- Phillips, D. L. (1962): A technique for the numerical solution of certain integral equations of the first kind. *J. Assoc. Comput. Mach. (JACM)*, 9, 1, pp. 84-97, DOI 10.1145/321105.321114.
- Phinney, R. A., and Anderson, D. L. (1968): On the radio occultation method for studying planetary atmospheres. *Journal of Geophysical Research*, 73, 5, pp. 1819-1827, DOI 10.1029/JA073i005p01819.
- Radicella, S. M. (2009): The NeQuick model genesis, uses and evolution. *Ann. Geophys.*, 56, DOI 10.4401/ag-4597.
- Rangarajan, G. K., and Berreto, L. M. (2000): Long term variability in solar wind velocity and IMF intensity and the relationship between solar wind parameters and geomagnetic activity. *Earth Planets Space*, 52, 2, pp. 121-232, DOI 10.1186/BF03351620.
- Rawer, K. (1963): Propagation of decameter waves (HF-band). *Meteorological and Astronomical Influences on Radio Wave Propagation*, Ed. Landmark, B. Pergamon Press, New York.
- Ratcliffe, J. A., Schmerling, E. R., Setty, C. S. G. K., and Thomas, J. O. (1956): The Rates of Production and Loss of Electrons in the F Region of the Ionosphere. *Philosophical Transactions of the Royal Society of London, series A, Mathematical and Physical Sciences*, 248, 956, pp. 621-642, DOI 10.1098/rsta.1956.0012.
- Rayleigh, J. W. S., and Lindsay, R. B. (1945): *The Theory of Sound, Volume One: Unabridged Second Revised Edition*. Dover Books on Physics (Book 1), Dover Publications, 2nd edition (June 1, 1945) ISBN 978-0486602929.
- Reigber, C., Lühr, H., Schwintzer, P., and Wickert, J. (Eds.) (2005): *Earth Observation with CHAMP, Results from Three Years in Orbit*. Springer-Verlag Berlin, pp. 471-476, DOI 10.1007/b138105.
- Reinisch, B. W. and Huang, X. (2001): Deducing topside profiles and total electron content from bottomside ionograms. *Adv. Space Res.*, 27, 1, pp. 23-30, DOI 10.1016/S0273-1177(00)00136-8.
- Reinisch, B. W., Nsumei, P., Huang, X., and Bilitza, D. (2007): Modeling the F2 topside and plasmasphere for IRI using IMAGE/RPI and ISIS data. *Adv. Space Res.*, 39, 5, pp. 731-738, DOI 10.1016/j.asr.2006.05.032.
- Richards, P. G., and Torr, D. G. (1988): Ratios of photo-

- electron to EUV ionization rates for aeronomic studies. *J. Geophys. Res.*, 93, A5, pp. 4060-4066, DOI 10.1029/JA093iA05p04060.
- Richardson, J. D., Wang, C., and Paularena, K. I. (2001): The solar wind: From solar minimum to solar maximum. *Adv. Space Res.*, 27, 3, pp. 471-479, DOI 10.1016/S0273-1177(01)00074-6.
- Rishbeth, H. and Garriot, O. K. (1969): *Introduction to Ionospheric Physics*. Academic Press, New York, ASIN: B001RI1UA8.
- Robble, R. G., Riddles, E. C., Richmond, A. D., and Dickinson, R. E. (1988): A coupled thermosphere/ionosphere general circulation mode. *Geophys. Res. Lett.*, 15, 12, pp. 1325-1328, DOI 10.1029/GL015i012p01325.
- Schaer, S. (1999): *Mapping and predicting the Earth's ionosphere using the Global Positioning System*, Ph.D. Thesis, Bern, published in *Geod.-Geophys. Arb. Schweiz*, Vol. 59.
- Scharroo, R., and Smith, H. F. (2010): A global positioning system-based climatology for the total electron content in the ionosphere. *J. Geophys. Res.* 115, A10, DOI 10.1029/2009JA014719.
- Schmidt, M. (2007): Wavelet modeling in support of IRI. *Adv. Space Res.*, 39, pp. 932-940, DOI 10.1016/j.asr.2006.09.030.
- Schmidt, M., Bilitza, D., Shum, C. K., and Zeilhofer, C. (2008): Regional 4-D modeling of the ionospheric electron density. *Adv. Space Res.*, 42, 4, pp. 782-790, DOI 10.1016/j.asr.2007.02.050.
- Schmidt, M., Dettmering, D., Mößmer, M., Wang, Y., and Zhang, J. (2011): Comparison of spherical harmonic and B spline models for vertical total electron content. *Radio Sci.*, 46, RS0D11, DOI 10.1029/2010RS004609.
- Schmidt, M., Dettmering, D., and Seitz, F. (2015): Using B-splines expansions for ionosphere modeling. In: *Freeden W., Nashed M.Z., Sonar T. (Eds.) Handbook of Geomathematics (Second Edition)*, Springer, in press.
- Schreiner, W. S., Sokolovskiy, S. V., Rocken, C., and Hunt, D. C. (1999): Analysis and validation of GPS/MET radio occultation data in the ionosphere. *Radio Sci.*, 34, 4, pp. 949-966, DOI 10.1029/1999RS900034.
- Schumaker, L. L. (1981): *Spline functions basic theory*. John Wiley and Sons Inc., New York, ISBN 0-471-76475-2.
- Schumaker, L. L. and Traas, C. (1990): Fitting scattered data on spherelike surfaces using tensor products of trigonometric and polynomial splines. *Numer. Math.* 60, pp. 133-144, Springer.
- Schunk, R. W., Sojka, J. J., and Bowline, M. D. (1986): Theoretical study of the electron temperature in the high-latitude ionosphere for solar maximum and winter conditions. *J. Geophys. Res.*, 91, 12, A11, pp. 12041-12054, DOI 10.1029/JA091iA11p12041.
- Schunk, R. W., Scherliess, L., Sojka, J. J., Thompson, D. C., Anderson, D. N., Codrescu, M., Minter, C., Fuller-Rowell, T. J., Heelis, R. A., Hairston, M., and Howe, B. (2004): Global Assimilation of Ionospheric Measurements (GAIM). *Radio Sci.*, 39, RS1S02, DOI 10.1029/2002RS002794.
- Skone, S., and Knudsen, K. (2000): Impact of Ionospheric Scintillations on SBAS Performance, Proceedings of the 13th International Technical Meeting of the Satellite Division of The Institute of Navigation (ION GPS 2000), Salt Lake City, UT, September 2000, pp. 284-293.
- Seeber, G. (2003): *Satellite Geodesy*, 2nd completely revised and extended edition, Walter de Gruyter, ISBN 3-11-017549-5.
- Stankov, S. M., Jakowski, N., Heise, S., Muhtarov, P., Kutiev, I., and Warnant, R. (2003): A new method for reconstruction of the vertical electron density distribution in the upper ionosphere and plasmasphere. *J. Geophys. Res.*, 108(A5), 1164, DOI 10.1029/2002JA009570.
- Stankov, S. M., and Jakowski, N. (2005): Topside plasma scale height modelling based on CHAMP measurements: first results. *Earth Observation with CHAMP - Results from Three Years in Orbit*, Springer book, XVI, Springer, ISBN 3-540-22804-7.
- Stollnitz, E. J., DeRose, T. D., and Salesin, D. H. (1995): Wavelets for computer graphics: A primer, part 2. *IEEE Computer Graphics and Applications*, 15, 4, pp. 75-85, DOI 10.1109/38.391497.
- Subirana, J. S., Zornoza, J. M. J., and Hernández-Pajares, M. (2013): *GNSS data processing Volume I: Fundamentals and Algorithms*, European Space Agency (ESA), ISBN 978-92-9221-886-7.
- Tapley, B. D., Bettadpur, S., Watkins, M., and Reigber, C. (2004): The gravity recovery and climate experiment: Mission overview and early results, *Geophys. Res. Lett.*, 31, L09607, DOI 10.1029/2004GL019920.
- Thompson, D. C., Scherliess, L., Sojka, J. J., and Schunk, R. W. (2006): The Utah State University Gauss-Markov Kalman filter of the ionosphere: The effect of slant TEC and electron density profile data on model fidelity. *Journal of Atmospheric and Solar-Terrestrial Physics*, DOI 10.1016/j.jastp.2005.10.011.
- Tikhonov, A. N. (1963): Solution of incorrectly formulated problems and the regularization method. *Soviet Math. Dokl.*, 4, pp. 1035-1038; English translation of *Dokl. Akad. Nauk. SSSR*, 151, pp. 501-504.
- Tsai, L.-C., and Tsai, W.-H. (2004): Improvement of GPS/MET ionospheric profiling and validation using the Chung-Li ionosonde measurements and the IRI model. *Terrestrial, Atmospheric and Oceanic Sciences (TAO)*, 15, pp. 589-607, DOI 10.3319/TAO.2007.12.19.01(F3/C).
- Tricomi, F. G. (1985): *Integral Equations*. Dover Publications Inc. New York, ISBN 978-0-486-64828-6.
- U.S. National Imagery and Mapping Agency (2000): Department of Defense World Geodetic System 1984 - Its Definition and Relationships with Local Geodetic Systems. NIMA Technical Report 8350.2 3rd release, St. Louis, 23 June 2004, <http://earth-info.nga.mil/GandG/publications/tr8350.2/wgs84fin.pdf>.
- Vanzandt, T. E. (1967): The neutral atmosphere and the quiet ionosphere. *Physics of Geomagnetic Phenomena*, Volume 1, p. 509, Edited by Matsushita, S. and Campbell, W. H., Library of Congress Catalog Card Number 67-23168. Published by Academic Press (New York).
- Ware, R., Exner, M., Feng, D., Gorbunov, M., Hardy, K.,

- Melbourne, W., Rocken, C., Schreiner, W., Sokolovsky, S., Solheim, F., Zou, X., Anthes, A. R., Businger, S., and Trenberth, K. (1996): GPS Sounding of the Atmosphere from Low Earth Orbit: Preliminary Results. *B. Am. Meteorol. Soc.*, 77, 19-40, DOI 10.1175/1520-0477(1996)077<GSOTAF>2.0.CO;2.
- Wong, Robert F., Rollins, Craig M., Minter, Clifton F. (2012): Recent Updates to the WGS 84 Reference Frame. Proceedings of the 25th International Technical Meeting of The Satellite Division of the Institute of Navigation (ION GNSS 2012), Nashville, TN, September 2012, pp. 1164-1172.
- Wright, J. W. (1960): A model of the F region above *hmF2*. *Journal of Geophysical Research*, 65, 185-191, DOI 10.1029/JZ065i001p00185.
- Xu, G. (2010): *GPS - Theory, Algorithms and Applications*, Springer, 978-3-642-09181-0.
- Yang, Y., Hatch, R. R., and Sharpe, R. T. (2004): GPS Multipath Mitigation in Measurement Domain and its Applications for High Accuracy Navigation, Proceedings of the 17th International Technical Meeting of the Satellite Division of The Institute of Navigation (ION GNSS 2004), Long Beach, CA, September 2004, pp. 1124-1130.
- Zeilhofer, C. (2008): Multi-dimensional B-spline modeling of spatio-temporal ionospheric signals. Deutsche Geodätische Kommission, Verlag der Bayerischen Akademie der Wissenschaften, ISBN 3-7696-8203-3.
- Zeilhofer, C., Schmidt, M., Bilitza, D., and Shum, C. K. (2008): Regional 4-D modeling of the ionospheric electron density from satellite data and IRI. *Adv. Space Res.*, 43, 1669-1675, DOI 10.1016/j.asr.2008.09.033.
- Zolesi, B. and Cander, L. R. (2014): *Ionospheric prediction and forecasting*, Springer, ISBN 978-3-642-38429-5.

Acknowledgements

Completing a PhD is a formidable challenge and I would not have been able to finish this journey without the aid and support of countless people over the past years.

First of all, I want to express my gratitude towards my supervisors, Urs Hugentobler and Michael Schmidt. Thanks for your support, attention to detail and having always an open door. It has been an honor for me to research and write this doctorate under your guidance. I thank my third assessor Claudio Brunini very much for reviewing the thesis and many interesting, fruitful discussions on the terrace of DGFI. A big thank also goes to Manuel Hernández-Pajares for giving me the opportunity of a research stay in Barcelona and for his invaluable assistance, in particular while struggling with the electron density retrieval.

I would like to thank all my colleagues that accompanied me during my work in the projects "Multi-scale model of the ionosphere from the combination of modern space-geodetic satellite techniques" and "Einrichtung eines operationellen Dienstes zur Bereitstellung von Ionosphäreninformationen beim Weltraumlagezentrum". Special thanks are due to Denise Dettmering, Wenjing Liang, Murat Durmaz and Eren Erdogan who shared their experiences in ionosphere modeling through countless discussions and several shared publications.

An essential part of this cumulative PhD is composed by publications where various colleagues, reviewers and editors contributed with suggestions or comments and helped in the evaluation of the manuscripts. Thanks to all of you.

Ich möchte mich von ganzem Herzen bei meinen Eltern und Geschwistern bedanken. Ohne genau zu verstehen was ich eigentlich studiere und arbeite, habt ihr immer an mich geglaubt und mir durch Eure Unterstützung den Weg hierher geebnet.

Zuletzt möchte ich den größten Dank an meine Frau Bo-Hanna richten, die meine Höhepunkte genießen durfte, die Tiefpunkte ertragen musste und mir dabei immer mit viel Geduld, einem offenen Ohr und dem richtigen Maß an Ablenkung zur Seite gestanden hat.

Sieh nach oben und blick dem Himmel entgegen,
starker Wille spendet Kraft, treibt dich voran ...
Auf halbem Wege fast erfroren,
angetrieben von der Hoffnung auf das Ziel.

Gipfelpanorama von Juvenalis, 2010